

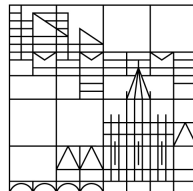
# Theoretical study of the charge and energy transport in metallic atomic-size contacts

Dissertation submitted for the degree of  
Doctor of Natural Science

Presented by  
Manuel Matt

at the

Universität  
Konstanz



Faculty of Science  
Department of Physics

Date of the oral examination: 17.02.2017

First referee: Prof. Dr. Peter Nielaba  
Second referee: Prof. Dr. Elke Scheer



# Zusammenfassung

In den vergangenen Jahrzehnten wurde die Prozessortechnologie stetig in Richtung mehr Leistung bei geringerem Verbrauch optimiert. Dabei wurde vor allem auf immer kleinere Strukturen, Stichwort „Miniaturisierung“, gesetzt. Kleinere Strukturen haben den Vorteil, dass sie kleinere Ströme zum Arbeiten benötigen und mehr Bauelemente auf einen Chip gepackt werden können. Zudem erlauben kleinere Strukturen die Verwendung höherer Taktraten [1]. Die Halbleiter-Bauelemente der aktuellsten Computer-Chips basieren auf der 14 nm Technologie. 2017 soll jedoch schon die nächste Generation auf den Markt kommen, die auf der 10 nm Technologie aufbaut [1–3].

Die Miniaturisierung kann aber nicht beliebig weit fortgesetzt werden. Mit 10 nm ist man bereits im Bereich weniger dutzend Atomschichten. Dies bringt technische Probleme mit sich, wie das Problem der Fertigungspräzision und Leckströmen [2], aber auch prinzipielle Probleme wie das Ende der Gültigkeit von Ohms Gesetz im Bereich der mittleren freien Weglänge der Elektronen (für Au  $\approx 5$  nm [4]). Der Grund dafür ist, dass der Ladungstransport rein ballistisch wird und man in den Bereich quantenmechanischer Effekte kommt [5]. Um die Strukturen trotzdem weiter verkleinern zu können, muss man zuerst die neuen Eigenschaften auf dieser Größenskala verstehen. Diese neuen Eigenschaften könnten die Grundlage neuer effizienterer Technologien darstellen, die auf makroskopischer Ebene nicht möglich wären [5].

Das ultimative Ende der Miniaturisierung stellen atomare Kontakte dar, die im Extremfall an der dünnsten Stelle nur ein Atom im Durchmesser besitzen. Während die Experimentalphysik in diesem Gebiet auf den Arbeiten von Gimzewski et al. [6] mit Rastertunnelmikroskopien, beziehungsweise Duerig et al. [7] mit Rasterkraftmikroskopien und später Muller et al. [8] mit mechanisch kontrollierten Bruchkontakten zur Bestimmung von Leitwerten und Kräften beim Ziehen von Nanodrähten aufbauen, folgt die Theorie den Arbeiten von Todorov et al. [9] und Cuevas et al. [10], die die klassische Molekulardynamik zur Bestimmung von Atomkonfigurationen und den Greensfunktionsformalismus zur Lösung der Schrödinger Gleichung für die Leitwertberechnung verbinden. Cuevas et al. [10] etablierten dabei das anschauliche Bild, dass jedes Orbital einen Leitungskanal zum Gesamtleitwert beitragen kann. Dieser Methodologie folgt auch diese Arbeit, wie bereits zuvor die Doktorarbeiten von zum Beispiel Fabian Pauly [11] und Markus Dreher [12].

Smit et al. fanden in ihren Messungen von Mg eine Peak-Struktur im Leitwerthistogramm, wie man sie von Materialien mit Leitwertquantisierung wie Au her kennt. Dabei befinden sich jedoch die Positionen der Peaks nicht an den gleichen Stellen wie bei Au [13]. Von Mg erwartet man aufgrund seiner Elektronenkonfiguration keine Leitwertquantisierung. Dafür konnten in den Simulationen auch keine Anhaltspunkte gefunden werden. Demnach wäre es ein reiner Geometrie-Effekt. Dies bedeutet, dass manche Leitwerte lediglich aus geometrischen Gründen bevorzugt werden. In den Simulationen wurde auch ein Kontakt mit parallelen Einatomkontakten und eine andere Form von parallelen Drähten gefunden, die im

Experiment einen entsprechenden Einfluss auf das Leitwerthistogramm haben könnten.

Schirm et al. entwickelten experimentell eine Methode, mit der es möglich ist, zwischen zwei definierten Plateaus im Leitwert im Bereich weniger Leitungsquanten  $G_0 = 2e^2/h$ , zum Beispiel zwischen  $1.1 G_0$  und  $1.8 G_0$ , mithilfe eines angelegten Stromes zu schalten. Im Vergleich mit unseren Simulationen konnten wir zeigen, dass zum Schalten zwischen den Plateaus in Al nur wenige Bindungen gebrochen oder erzeugt werden müssen und dabei im Wesentlichen ein Atom seine Position verändern muss [14].

Chen et al. fanden in ihren Schrotrausch-Messungen von Au bei Raumtemperatur zwei interessante Ergebnisse: Zum einen ein oszillatorisches Verhalten der Streuung der Ergebnisse als Funktion des Leitwertes, wobei die Minima dieser Oszillation bei den Maxima des Leitwerthistogrammes war und zum anderen ein erhöhtes Rauschen bei ungefähr  $G_0/2$ , was nur durch den Beitrag mehrerer Kanäle erklärt werden kann, was jedoch dem Bild des monovalenten Einatomkontaktes von Au widerspricht. Ersteres konnten wir durch das Verhalten der Kanäle in der Nähe der Maxima des Leitwerthistogrammes erklären, zweiteres durch das Auftauchen paralleler, monoatomarer Drähte die gleichzeitig gerissen sind und so jeweils einen fast geschlossenen Kanal beigetragen haben [15].

Evangelini et al. fanden ähnliche Oszillationen bei ihren Thermokraft Messungen von Au bei Raumtemperatur, was wir wiederum auf die Leitwertkanäle zurückführen konnten. Zeigen konnten wir diesen Effekt anfänglich nur für das erste Maximum im Leitwerthistogramm. Die nächsten beiden Minima der Oszillation konnten erst bei einer späteren Studie mit deutlich größeren Kontakten reproduziert werden. Ein weiteres interessantes Ergebnis ihrer Messung betraf das Vorzeichen der mittleren Thermokraft. Diese unterschied sich sowohl zwischen Festkörper und Nanokontakten, als auch zwischen den Au- und Pt- Ergebnissen. Wir konnten diese Effekte auf die unterschiedlichen Zustandsdichten und damit der unterschiedlichen Beiträge der Orbitale zurückführen [16].

Vardimon et al. machten Schrotrausch-Messungen an ferromagnetischen Metallen bei tiefen Temperaturen und fanden zwei interessante Punkte: Zum einen ein viel zu hohes Rauschen im Vergleich zu Cu, was Motts Modell von Ferromagneten widerspricht [17] und zum anderen eine Sättigung des Fano Faktors, der ein um den Leitwert (genauer dem Poisson verteilten Rauschen) normierter Wert des Schrotrauschens ist, unterhalb des Wertes für diffuse Streuung. Ersteres konnten wir darauf zurückführen, dass sich die zwei Spin Systeme anders verhalten als in dem Modell von Mott angenommen wird. Dabei spielen vor allem die  $d$  Orbitale bei den Minoritäts-Spin Elektronen eine entscheidende Rolle, denn diese verhelfen diesem Spin System zu zusätzlichen Leitwertkanälen, was wiederum zu einer negativen Spinpolarisierung führt. Diese zusätzlichen Kanäle sorgen auch für das erhöhte Rauschen im Ergebnis. Der zweite Punkt konnte auf die Verteilung der Kanäle als Funktion der Kanalöffnung zurückgeführt werden, die ab wenigen Atomen im Querschnitt fast konstant bleibt [18].

Weitere Ergebnisse der Arbeit sind, dass

- die Geschwindigkeit, mit der die Drähte gezogen werden, keinen wesentlichen Einfluss auf die Ergebnisse der Kapitel 5-8 hat (zumindest innerhalb des betrachteten Rahmens),
- die Histogramme sich glatt als Funktion der Temperatur verändern,
- der Thermostat wichtig ist, damit sich der Draht nicht zu sehr aufheizt und im Extremfall schmilzt,
- die Kristallstruktur (fcc oder bcc) keinen großen Einfluss hat,
- die Schließkurven deutlich geringer auf die Temperatur reagieren als die Öffnungskurven und sich im Wesentlichen wie Öffnungskurven bei tiefen Temperaturen verhalten, wobei bei Au lange einatomare Ketten fehlen,
- die Geometrie des Kontakts mit dem der Ziehvorgang gestartet wird, einen wesentlichen Einfluss auf die Ergebnisse haben kann (zum Beispiel bei Au auf die Häufigkeit von parallelen Drähten und damit auf die mittlere Kanalverteilung und die anderen Größen).



# Contents

<b>1. Introduction</b>	<b>13</b>
<b>2. Theoretical background / Methods</b>	<b>19</b>
2.1. Molecular dynamics . . . . .	19
2.1.1. Velocity Verlet algorithm . . . . .	20
2.1.2. Nosé-Hoover Thermostat . . . . .	20
2.1.3. Nosé-Hoover chains . . . . .	22
2.1.4. Embedded-atom-method potentials . . . . .	22
2.1.5. Minimum cross section . . . . .	23
2.2. Nonequilibrium Green's functions . . . . .	25
2.2.1. Sharvin-Weyl formula - scattering approach . . . . .	25
2.2.2. Heuristic derivation of the Landauer formula . . . . .	26
2.2.3. Green's functions . . . . .	27
2.2.4. Nonequilibrium Green's function and Keldysh formalism . . . . .	29
2.2.5. Temperature . . . . .	32
2.2.6. Application to simple transport problems . . . . .	32
2.2.7. Resulting formulas for the current through realistic systems . . . . .	35
2.2.8. Nonorthogonal basis sets . . . . .	37
2.3. Tight-binding approach . . . . .	38
2.3.1. General derivation . . . . .	38
2.3.2. Slater-Koster approximation . . . . .	39
2.3.3. NRL tight-binding method . . . . .	40
2.4. Electronic transport properties . . . . .	41
2.4.1. Shot noise and Fano factor . . . . .	41
2.4.2. Thermopower . . . . .	42
2.4.3. Electron thermal conductance . . . . .	44
2.4.4. Decimation technique for the leads . . . . .	44
<b>3. Code optimization</b>	<b>47</b>
<b>4. Model</b>	<b>49</b>
4.1. Experiments . . . . .	49
4.2. Molecular dynamics simulations . . . . .	50
4.3. Conductance calculations . . . . .	52
4.4. Figures . . . . .	53
4.5. Simple Example: Ideal Au wire(s) . . . . .	53

<b>5. Results for Au, Ag, Cu, Mg, Al and Pt at 4K</b>	<b>59</b>
5.1. Conductance . . . . .	61
5.1.1. Conductance and elongation . . . . .	61
5.1.2. Conductance histograms . . . . .	64
5.1.3. Channels . . . . .	66
5.2. Noise . . . . .	68
5.2.1. Saturation effect and comparison with diffusive regime . . . . .	71
5.3. Effect of multiple wires in parallel . . . . .	73
5.4. Thermopower . . . . .	79
5.5. Thermal conductance . . . . .	83
<b>6. Spin-polarized materials Fe, Co and Ni</b>	<b>85</b>
6.1. Conductance . . . . .	87
6.2. Noise . . . . .	94
6.3. Thermopower and thermal conductance . . . . .	97
<b>7. Results for Au, Pt and Ni at room temperature</b>	<b>99</b>
<b>8. Crystallographic elongation direction Al</b>	<b>109</b>
8.1. Elongation directions . . . . .	109
8.1.1. Conditional MCS and conductance histograms . . . . .	116
8.1.2. Rising plateaus . . . . .	118
8.2. Single-atom memory . . . . .	120
<b>9. Additional studies</b>	<b>123</b>
9.1. NVT versus NVE ensemble . . . . .	123
9.2. Temperature evolution, opening and closing curves . . . . .	127
9.2.1. Closing curves . . . . .	129
9.2.2. Closing curves of Mg, Al and Ag . . . . .	132
9.3. Influence of velocity . . . . .	136
9.4. Statistical evolution . . . . .	138
9.5. FCC versus BCC Fe lattice . . . . .	140
9.6. Doubling the size of Au contacts . . . . .	142
9.7. Geometry of initial structures of Au, Al and Pb . . . . .	148
9.7.1. Au . . . . .	148
9.7.2. Al . . . . .	155
9.7.3. Pb . . . . .	160
<b>10. Summary</b>	<b>165</b>
<b>A. Appendix</b>	<b>169</b>
A.1. Examples . . . . .	169
A.1.1. Example 1: H <sub>2</sub> . . . . .	169
A.1.2. Example 2: Semi-infinite linear chain . . . . .	171
A.1.3. Example 3: A single level coupled to electrodes . . . . .	172
A.2. Program specific data . . . . .	174
A.3. Au multiwire geometries . . . . .	179



A.4. Al geometries . . . . .	181
A.5. Histograms of channel transmissions . . . . .	182
A.6. Fano factor convergence values - overview . . . . .	183
A.7. Experimental results . . . . .	184
<b>Acknowledgments</b>	<b>185</b>
<b>Bibliography</b>	<b>187</b>

## List of Figures

1.1. STM conduction curves . . . . .	14
1.2. Sketch of MCBJ principle and transmission eigenvalues . . . . .	14
1.3. Experimental conductance histograms . . . . .	15
2.1. Mcs flow example . . . . .	24
2.2. Keldysh contour . . . . .	30
2.3. Schematic representation of a wire with two leads . . . . .	35
3.1. Scaling of TB code . . . . .	48
4.1. Sketch of MCBJ principle . . . . .	49
4.2. Evolution of simple Au wire . . . . .	51
4.3. Au results of ideal wires . . . . .	54
4.4. Au results of two parallel ideal wires . . . . .	55
4.5. Au geometries of single atom wires during time evolution . . . . .	56
5.1. Initial geometry of Au . . . . .	60
5.2. G vs displacement . . . . .	62
5.3. Au geometries with fast rupture process with G and $\tau_i$ . . . . .	63
5.4. Conductance histograms . . . . .	64
5.5. Au geometries during elongation, evolving zigzag and chain structure . . . . .	65
5.6. Mean channel distributions . . . . .	66
5.7. Au channel evolution during elongation . . . . .	67
5.8. Noise results . . . . .	68
5.9. Noise results . . . . .	69
5.10. DOS results of single atom contacts of Au, Mg, Al and Pt . . . . .	70
5.11. Single atom geometries for DOS calculations . . . . .	70
5.12. $\tau_i$ histograms at $15G_0$ . . . . .	71

5.13. Au multiple wires: G and F . . . . .	73
5.14. Au and Cu geometries at $2G_0$ and low F . . . . .	74
5.15. Au and Cu geometries at $2G_0$ and high F . . . . .	75
5.16. Au conditional histogram . . . . .	75
5.17. Au geometries during elongation process with two parallel wires . . . . .	77
5.18. Au geometries during elongation process with two parallel atoms . . . . .	78
5.19. Thermopower results at 4K . . . . .	79
5.20. Au and Pt DOS results at 4K . . . . .	80
5.21. Au and Pt geometries for DOS calculation . . . . .	80
5.22. Mean thermopower results at 4K . . . . .	82
5.23. Thermal conductance results at 4K . . . . .	83
6.1. Fe and Ni ideal geometries . . . . .	86
6.2. Ferromagnetic metals conductance vs displacement . . . . .	87
6.3. Ferromagnetic metals conductance histograms and spin polarization . . . . .	87
6.4. Co geometries of monomer and dimer structure . . . . .	88
6.5. Ferromagnetic metals mcs results . . . . .	89
6.6. Ni geometries at 4K and about $1.5G_0$ . . . . .	89
6.7. Ferromagnetic metals spin separated conductance histograms . . . . .	90
6.8. Ferromagnetic metals spin separated mean channel distributions . . . . .	91
6.9. Ni and Cu DOS . . . . .	92
6.10. Ni and Cu geometries used for DOS calculations . . . . .	93
6.11. Ferromagnetic metals Fano factor results at 4K . . . . .	94
6.12. Ferromagnetic metals $\tau_i$ histograms at $15G_0$ . . . . .	96
6.13. Ferromagnetic metals $\tau_i$ histograms at $2G_0$ . . . . .	96
6.14. Ferromagnetic metals results of thermopower at 4K . . . . .	97
6.15. Ferromagnetic metals results of $\langle S \rangle$ at 4K . . . . .	97
6.16. Ferromagnetic metals results of thermal conductance . . . . .	98
7.1. Au, Pt and Ni results of G vs. displacement at 300K . . . . .	99
7.2. Au, Pt and Ni conductance histograms at 300K . . . . .	100
7.3. Pt geometries at 300K and 3 and $3.9G_0$ . . . . .	101
7.4. Ni geometries at breaking . . . . .	102
7.5. Au, Pt and Ni channel distributions at 300K . . . . .	103
7.6. Au, Pt and Ni Fano factor results at 300K . . . . .	104
7.7. Au, Pt and Ni $\tau_i$ histograms at $15G_0$ . . . . .	105
7.8. Au, Pt and Ni thermopower results at 300K . . . . .	105
7.9. Au, Pt and Ni mean thermopower results at 300K . . . . .	106
7.10. Pt integration tests at 300K . . . . .	106
8.1. Al experimental results . . . . .	109
8.2. Al experimental results . . . . .	110
8.3. Al force results of different elongation directions . . . . .	111
8.4. Al $\langle 110 \rangle$ geometries during elongation . . . . .	112
8.5. Al force results . . . . .	113
8.6. Al force results . . . . .	113
8.7. Al results for different elongation directions . . . . .	114

8.8.	Al channel histograms at $1G_0$	115
8.9.	Al dimer DOS examples	115
8.10.	Al results of total data set as sum of elongation directions	115
8.11.	Al conditional mcs vs. $G$	116
8.12.	Al $\langle 100 \rangle$ geometries at 1.1 and $1.5G_0$	117
8.13.	Al examples with rising conductance plateaus	118
8.14.	Al DOS during rising plateau	118
8.15.	Al rising plateaus: F and S	119
8.16.	Experimental bistable switches	120
8.17.	Examples for $\langle 111 \rangle$ with $G$ , $K$ and $\tau_i$	122
9.1.	Fe $K$ and $T$ values during elongation in NVE and NVT ensembles	123
9.2.	Fe mcs results in NVE and NVT ensemble	124
9.3.	Fe geometries in context with mcs jumps	124
9.4.	Fe geometries during elongation process in NVE and NVT ensemble	125
9.5.	Fe conduction calculation results in NVE and NVT ensemble	126
9.6.	Au (56 atoms) results between 4K and 300K (opening)	127
9.7.	Au geometries during elongation at 4K with $G$ and $\tau_i$	128
9.8.	Au geometries during elongation at 300K with $G$ and $\tau_i$	128
9.9.	Au (56 atoms) results between 4K and 300K (closing)	129
9.10.	Au geometries during elongation and closing process at 4K with $G$ and $\tau_i$	131
9.11.	Results of closing curves of Mg, Al and Ag at 4K	132
9.12.	Mg geometries at $1G_0$	133
9.13.	Mg geometries with parallel wires	133
9.14.	Mg geometries with different types of parallel wires	134
9.15.	Ag geometries at $1G_0$	134
9.16.	Au (56 atoms) results at 0.4 and $8m/s$	136
9.17.	Au (56 atoms) results in statistic evolution at 4K	138
9.18.	Au (56 atoms) results in statistic evolution at 300K	139
9.19.	Ideal starting geometries of Fe in bcc and fcc	140
9.20.	Fe bcc and fcc results at 4K	141
9.21.	Ideal Au geometries	142
9.22.	Results of Au at 4K	143
9.23.	Conditional histogram of Au	144
9.24.	Conditional histogram of Au	144
9.25.	Au geometries at 4K and $3G_0$	145
9.26.	Au giant contact evolution with $G$ and $\tau_i$	146
9.27.	Ideal initial geometries of small contacts	148
9.28.	Au results at 4K	149
9.29.	Au geometries at 4K and $2G_0$ (l)	150
9.30.	Au geometries at 4K and $2G_0$ (v)	151
9.31.	Au geometries at 4K and $2.5G_0$ (l)	151
9.32.	Au results at 4K	152
9.33.	Au geometries at 300K and $2G_0$	153
9.34.	Au results at 300K	154
9.35.	Al results at 4K	156

9.36. Al geometries at 4K with 2.8 and 3.8G <sub>0</sub>	157
9.37. Al $\tau_i$ histograms between 1-8G <sub>0</sub> at 4K	157
9.38. Al results at 300K	158
9.39. Al geometries at 300K and 1G <sub>G</sub>	159
9.40. Al $\tau_i$ histograms between 1-8G <sub>0</sub> at 300K	159
9.41. Pb results at 4K	160
9.42. Pb geometries during elongation at 4K with G and $\tau_i$ (l)	161
9.43. Pb geometries during elongation at 4K with G and $\tau_i$ (v)	161
9.44. Pb results at 300K	163
9.45. Pb geometries during elongation at 300K with G and $\tau_i$ (l)	164
9.46. Pb geometries during elongation at 300K with G and $\tau_i$ (v)	164
A.1. Callgraph	178
A.2. Au geometries with parallel wires at 4K	179
A.3. Au geometry with parallel wires at 4K with $\tau_i$	179
A.4. Au geometries with parallel wires at 4K with $\tau_i$	179
A.5. Au giant geometries at 4K with $\tau_i$	180
A.6. Al geometries of a curve with $\tau_i$	181
A.7. Al geometries of a curve with $\tau_i$	181
A.8. Histograms of $\tau_i$ for different materials at 1G <sub>0</sub>	182
A.9. Histograms of $\tau_i$ for different materials at 2G <sub>0</sub>	182
A.10. Experimental results from Vardimon et al.	184

## List of Tables

5.1. Fano factor convergence results at 4K	71
5.2. channels and parallel wires of Au, Ag and Cu at 2G <sub>0</sub>	74
6.1. Ferromagnetic metals Fano factor convergence results	95
7.1. Au, Pt and Ni convergence results of Fano factor	103
8.1. Best matching geometries for Al bistable switches	121
8.2. Al geometries during elongation	122
A.1. Fano factor convergence values	183
A.2. Fano factor convergence values (ferromagnetic metals)	183

# 1. Introduction

In the last decades the development of the processor and memory technologies went toward higher performance while getting smaller and more energy-efficient. This for example allows using high performance CPUs in mobile phones. The key for this development was the miniaturization which enabled to use more transistors on one chip to increase the performance. At the same time the smaller components need less energy to work and allow for higher clock rates [1]. Electronic switches, usually realized by transistors, have been miniaturized all the way down to the atomic scale [19–27]. The latest industrial relevant technology uses 14 nm semiconductor devices to build up CPUs, but 10 nm devices are already developed and will probably go into production in 2017 [1–3].

There are several problems going further down, the precision of the fabrication and the leakage of the systems are two of them [2]. While these are technological problems, there is a more fundamental one, namely the breakdown of Ohm's law when the device dimensions become smaller than the mean free path for electrons. Below that, the electrons travel through a contact without scattering thus leading to a length-independent resistance which is dominated by the quantum mechanical properties of the materials [5]. To be able to go further down in system size, the novel properties at that scale need to be understood first. These new properties do not only have disadvantages but they open the possibility of new devices based on mechanisms which are not known from our classical, macroscopic world [5]. The field of nanoscale devices includes many research areas like carbon nanotubes [28] and biological applications like the conductance of individual DNA molecules [29–33]. The effects of quantum coherence on those systems are studied with the concept that the electrical conductance is directly equivalent to the transmission probability of incoming waves [34,35]. In contrast to nanophysics where the length of at least one dimension is below the 100 nm, this ignores the details of the atomic structures and the rich variety of chemistry involved. Another field which is directly connected with nanoscale devices tries to trace the macroscopic material properties like adhesion, friction and wear back to microscopic processes at the atomic scale [36,37].

Atomic-sized contacts, in contrast, are for example wires, in which the thinnest part consists only of one up to a few atoms in cross section. This can be achieved for example by elongating a wire till it almost breaks at one point with an MCBJ setup [8,39–41] (left side of Fig. 1.2) or by bringing a sharp STM tip in contact with a substrate [34,38,42–47].

First experiments in the direction of atomic contacts date back to the late 80's where scanning tunneling microscope (STM) measurements from Gimzewski and Möller were used to study the conductance of atomic-sized contacts [6] and Dürig et al. used an atomic force microscope (AFM) to measure the force of such systems [7]. Examples for conductance curves during the contacting and extracting of a tip in an STM setup are shown for different materials in Fig. 1.1. They have in common that all of them show kinds of plateaus as function of the tip-sample displacement, but while Au shows at least one well developed plateau at

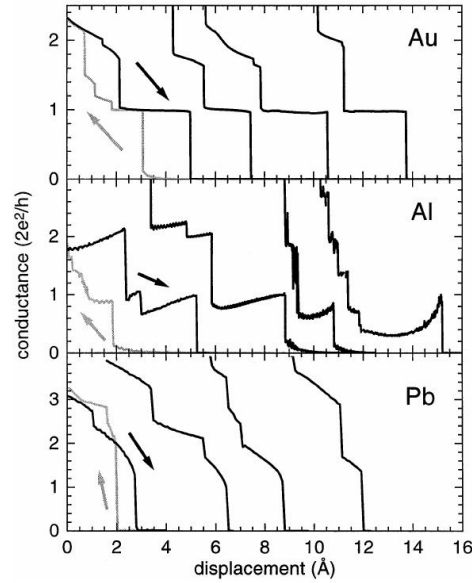


Figure 1.1.: Examples for conductance curves as function of the tip-sample displacement in STM experiments for different metals. The black curves are measured in elongation direction (extraction of the tip) and the gray curves in contraction (bringing in contact) direction. Reprinted with permission from [38]. Copyright 1998 by the American Physical Society.

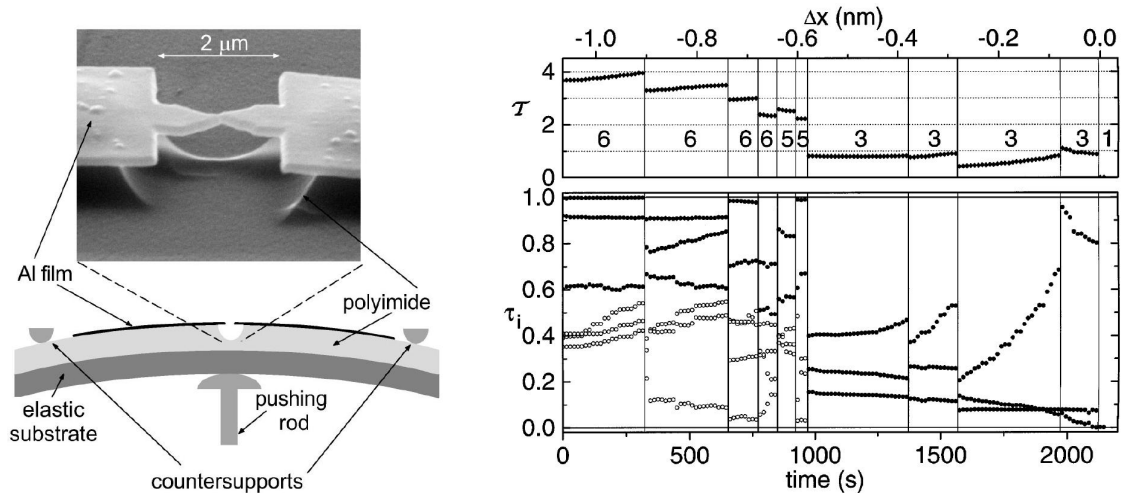


Figure 1.2.: Sketch of the working principle of the MCBJ technique with a three-point bending mechanism (left) and an example of an elongation curve of Al with total transmission (top right) and channel distributions as best fits to the measured IV curves (lower right) as function of time. Reprinted with permission from [39]. Copyright 1997 by the American Physical Society.

$G_0 = 2e^2/h$ , the other two materials, Al and Pb, show tilted plateaus at non integers of  $G_0$ . In the beginning of the 90's, a new technique called mechanically controllable break junction (MCBJ), was developed. This method uses a flexible substrate on which the wire is deposited and which is bent such that the wire gets elongated (Fig. 1.2, left). In 1992 MCBJ measurements of Pt and Nb revealed several conductance steps of the order of  $G_0$ , which were traced back to atomic structure rearrangements [8].

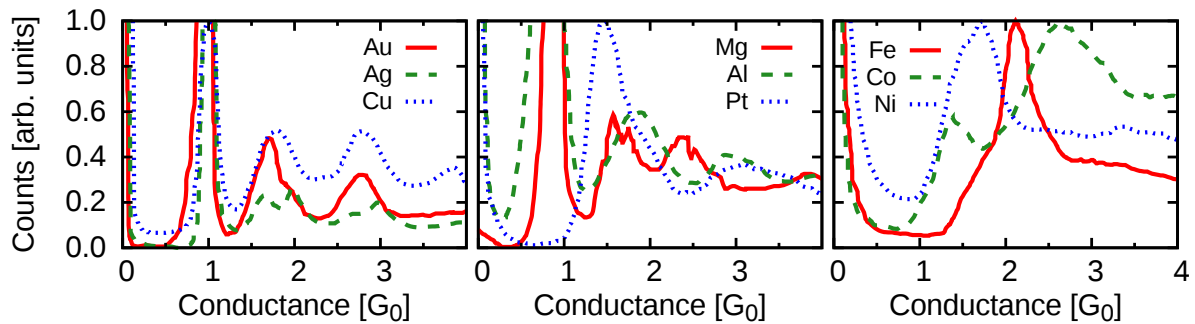


Figure 1.3.: Recent experimental conductance histograms of different metals. Au, Ag, Cu, Al and Pt are from private communications with Ran Vardimon (see sec. A.7), the ferromagnetic materials Fe, Co and Ni are from [18] and the data of Mg are from [13].

Todorov and Sutton combined molecular dynamic (MD) calculations with a tight binding description of the electronic structure to calculate the conductance of the contacts. The results supported the above interpretation of the conductance steps as results of atomic rearrangements [9]. A proof for this came from Rubio et al. in 1996 who combined force and conductance measurements to show that jumps in the conductance are correlated with jumps in the force [48]. One year later Scheer et al. [39] were able to determine the channel distribution in Al with the help of multiple Andreev reflections and discovered, that more than two channels even below a conductance of  $G_0$  (right part of Fig. 1.2). This could be explained by Cuevas et al. [10] by a picture where the number of channels is determined by the number of atomic orbitals which contribute to the current (valence orbitals). At about the same time chains of Au with a diameter of only a single atom were discovered [34, 49, 50] and new techniques like electromigration [51] were developed to create atomic contacts and to contact single molecules to electrodes. Those new methods made it possible to show that single molecule devices can exhibit physical phenomena like Coulomb blockade or the Kondo effect [45, 52], that they could act as single-electron transistors [53] or as molecular switches [24, 54–59].

At the beginning single conductance curves as function of displacement or time like on the right side of Fig. 1.2 were investigated and compared with each other. But as each curve has its own characteristics and not all conductance plateaus are at multiples of  $G_0$ , statistics of curves in the form of conductance histograms have been introduced [44, 60, 60, 61]. These histograms show metal specific preferred conductance values, which are not compatible with the free electron models. Examples of such histograms for different materials from MCBJ measurements at low temperatures are shown in Fig. 1.3.

Despite a huge amount of work that followed the line of Todorov, Sutton, Cuevas and others [9, 10, 38, 62–69, 69–75], there are still a lot of open questions. Many of them include the correlation between geometrical and conductance properties with (high) statistics which is still a challenging problem in computer science. There are for example peaks in the conductance histograms which need a statistical treatment of the problem in theory for each material separately. Attempts in that direction were done for example by Cuevas, Nielaba, Pauly and coworkers [68–70]. These simulations were able to reproduce some experimental features like the first peak in the conductance histograms of Au, the evolution of Au chains

with one atom in diameter and the opening of the second channel of Au starting with  $1 G_0$ . They also showed the relation between the cross section of a contact and its conductance and the sensitivity of the conductance to the position of the atoms near the narrowest part of the wires for different materials. Open questions remained concerning the positions of the higher conductance peaks, especially of Au which were not reproducible in a sufficient manner from theory so far. A related question was the opening of the higher channels of Au which open in experiments in average much more step-like than in the theoretical results.

A comprehensive review with a lot more references to theoretical and experimental studies was published by Agraït et al. [5] in 2003 and a more recent overview of the whole area with introductions to the basic experimental and theoretical approaches can be found in the book of Juan Carlos Cuevas and Elke Scheer [4].

Apart from the electrical conductance, other transport properties have been studied in the context of metallic atomic-size contacts. Thus for instance, in recent years the study of the thermopower is attracting a lot of attention. Thermopower is a measure for the ability of a material to convert a voltage drop into a temperature gradient and vice versa. The observation that nanostructured materials may enhance their efficiency makes it to an interesting research area [76–79]. Low temperature calculations from Pauly et al. showed for example an almost vanishing average thermopower of Au, Ag and Pt [73] which is consistent with experimental results from Ludoph et al. [80]. The deviations of the mean values, on the other hand, were underestimated by far. Looking more closely at the data one could ask if the slight variation of the mean thermopower toward negative values for Au and toward positive ones for Pt is only a statistical point or a significant result which would be in contrast to the bulk properties of this materials. Recent thermopower measurements of atomic contacts at room temperature showed indeed mean values which are clearly negative for Au and positive for Pt with minima at the maxima of the conductance histograms [16, 81].

Another interesting transport property is shot noise. Shot noise measurements are an interesting tool to get more insights into the quantum properties of contacts far beyond what is extractable from the conductance measurements [20–24, 28, 35]. As it is connected with the distribution of transmission eigenvalues it can be even used to extract ranges of possible values of those [82]. Recent shot noise measurements of Au contacts at room temperatures by Chen et al. [15] showed suppression of the deviation of the noise at the maxima of the conductance histograms and a peak in the tunneling regime at about  $G_0/2$ . The latter point is specially interesting because it implies that more than one channel contributes to the conductance which contradicts the picture of the monovalent Au atom with its  $s$  orbital supporting exactly one channel.

As for non-magnetic metals there have been many experimental STM and break-junction-based studies of ferromagnetic materials [45, 52, 83–114]. But a lot of work has also been done from the theory side to investigate the transport properties of those ferromagnetic atomic contacts [69, 72, 115–142]. The reported theoretical results clearly suggest that in the atomic scale ferromagnetic contacts, contrary to their macroscopic ones, the  $d$  orbitals play a fundamental role for the transport properties. Shot noise measurements from Vardimon et al. [18] of ferromagnetic materials and Cu at 4 K showed much larger shot noise values for the ferromagnetic materials compared to the  $s$  conductor Cu. This supports the theoretical findings and contradicts the semi-classical description of ferromagnetic metals by Mott [17] where the  $s$  orbitals should dominate the conductance properties and the  $d$  orbitals the



magnetic ones. But at that point mainly individual experimental and theoretical works have been done and a systematic comparison was missing. Vardimon et al. also found a saturation of the Fano factor, which is the shot noise normalized by the poissonian (classical, uncorrelated) noise and which can be expressed in terms of transmission eigenvalues  $\tau_i$  by  $F = (\sum_i \tau_i(1 - \tau_i)) / (\sum_i \tau_i)$ , far below the 1/3 one expects in the diffusive limit [143, 144]. Smit et al. found a peak structure in the histograms of Mg contacts similar to Au although with less peaks at different positions [13]. But as member of the alkaline earth metals it should not show conductance quantization effects at all.

As already mentioned, there have been a lot of papers of atomic or molecular switches published [24, 54, 55, 57–59, 83]. For example Schirm et al. [14] showed in their experiments that it is possible to switch with a current between two well defined conductance values in a cyclic manner at least hundreds of times. As the current was small and the transition very sharp and well defined the question is if the transition is triggered by a single atom or are there more atoms involved? And does it play a role in which crystallographic direction the wires are elongated or grown? - One could expect differences in the results, maybe the switch is only possible in some directions and not in others?

All these questions are addressed by theoretical simulations because the experiments are not able to give full answers on their own. In this sense the comparison between theory and experiments is very important and only in the combination most questions can be answered. This is the aim of this work. Following the line of Todorov, Sutton, Cuevas, Pauly, Dreher and others, the open questions will be addressed using the combination of MD for the structure calculations and Green's functions based on TB parametrizations to calculate conductance properties of wires which are much larger than what was addressable before in theory with much larger statistics and for more metals.

For the understanding of the following work a deep knowledge of the literature is not required. Many properties partly known since up to more than one decade like the building of long Au chains with only a single atom in cross section will be reproduced and determined in a straight forward way.

The script is organized as follows. In **chapter 2** the basic theory is described following mainly the lines of [4] and [145]. **Chapter 3** shortly presents some details of the code and why it is able to go beyond what was done before in other works. In **chapter 4** the used model with application details is shown (examples for input and parameter files can be found in the appendix). There are also a few experimental techniques shortly described. More profound descriptions can be found in many textbooks like [4]. Two simple academic examples are finally shown to demonstrate the approach.

**Chapters 5-8** show the main results of the work. They include low temperature calculations of the monovalent metals Au, Ag and Cu but also for Mg, Al and Pt (**chapter 5**). The low temperature results are separated into the individual properties under investigation like conductance histograms, channel distributions, noise and so on. The second one (**chapter 6**) shows the results for the ferromagnetic materials Fe, Co and Ni. The third one (**chapter 7**) shows room temperature results of Au, Pt and Ni and the last one of them (**chapter 8**) analyses Al in more detail to answer the questions in context of the bistable switches of Schirm et al. and the influence of the elongation direction onto the results.

**Chapter 9** is devoted to questions concerning the simulation parameters like the influence

of the thermostat in the MD calculations onto the results, the influence of the velocity which is orders of magnitude higher than in experiments and the size and form of the initial wires. Finally **appendix A** includes some simple examples for the application of the Green's function technique which are also summarized from [4] and some further information like additional geometries, histograms, an overview of Fano factor convergence values and unofficial experimental results from Vardimon et al. which were published in other formats.

## 2. Theoretical background / Methods

Within this work, we want to achieve two things. First of all we want to have metallic wires with atomic resolution as realistic as possible. To achieve this point we use (classical) molecular dynamics (MD) simulations with a velocity Verlet kind of time integration schema and pseudo potentials from the embedded atom method to elongate initially ideal wires until they break. The details of the methods needed for this part are described in section 2.1.

The second part is the determination of the electronic properties of the geometries obtained in the MD simulations. To these properties belong the conductance (inverse electrical resistance) of the wire-geometry, their channel distribution, shot noise, thermopower and electronic contribution to the thermal conductance. To get access to those, we use a nonequilibrium Green's function technique combined with a tight-binding description of the atoms, which will be introduced together with the different properties in sections 2.2 and 2.3.

### 2.1. Molecular dynamics

Molecular dynamics (MD) is a method to derive transport and equilibrium properties of many-body systems using laws of classical dynamics (e.g. solving Newton's equations of motion). In classical MD quantum mechanical effects are ignored or included in an approximated manner into the potentials used to describe the interactions between the particles. Here, a particle is an abstract object and could be an atom, a molecule or actually a macroscopic object. For most practical purposes this is usually a good approximation. But the quality of the results depend strongly on the potentials used.

An important quantity of a system under investigation is its temperature  $T$ , whether it is kept fixed, manipulated or an outcome of the system itself<sup>1</sup>. Though temperature is a macroscopic, thermodynamic quantity<sup>2</sup>, it has its origins in the microscopic behavior of the particles of the macroscopic body or volume. Therefore a kind of temperature can be defined there, too. From the thermal equilibrium one has a definition of the temperature  $T$  through the average kinetic energy per degree of freedom  $\langle \frac{1}{2}mv_\alpha^2 \rangle = \frac{1}{2}k_B T$  where  $\alpha$  is a component of the velocity  $v$  of a given particle with mass  $m$  and  $k_B$  is the Boltzmann constant. In MD one can define an instantaneous (time  $t$  dependent) temperature  $T(t)$  (usually not in equilibrium) as

$$T(t) = \frac{1}{k_B N_f} \sum_{i=1}^N \sum_{\alpha}^3 m v_{\alpha,i}^2(t) \quad (2.1)$$

---

<sup>1</sup>For example heating or cooling due to atomic reorganizations.

<sup>2</sup>And quasi-stationary equilibrium.

where  $N$  is the number of particles and  $N_f$  is the number of degrees of freedom. The following sections are based on Chapter 4 and 6 of [145].

### 2.1.1. Velocity Verlet algorithm

A widely used algorithm for time integration is the velocity Verlet algorithm. Here the coordinates are updated using a Taylor-like expansion

$$\mathbf{r}(t + \Delta t) = \mathbf{r}(t) + \mathbf{v}(t)\Delta t + \frac{\mathbf{f}(t)}{2m}\Delta t^2 \quad (2.2)$$

$$\mathbf{v}(t + \Delta t) = \mathbf{v}(t) + \frac{\mathbf{f}(t + \Delta t) + \mathbf{f}(t)}{2m}\Delta t \quad (2.3)$$

The velocity  $\mathbf{v}$  of the new time  $t + \Delta t$  can only be calculated after one has calculated the new positions which are needed for the new forces  $\mathbf{f}$ .

### 2.1.2. Nosé-Hoover Thermostat

The Nosé-Hoover thermostat goes back to papers from Nosé [146] and Hoover [147]. The goal is to fix the temperature somehow to a constant value generating a canonical distribution. To do this, they start from the Lagrangian formulation of classical mechanics and added an additional coordinate  $s$  with effective mass  $Q$  to the N-body system

$$\mathcal{L}_{Nose} = \sum_{i=1}^N \frac{m_i}{2} s^2 \dot{\mathbf{r}}_i^2 - V(\mathbf{r}^N) + \frac{Q}{2} \dot{s}^2 - \frac{L}{\beta} \ln(s) \quad (2.4)$$

with inverse temperature  $\beta = \frac{1}{k_B T}$  and  $L$  is a parameter to be fixed. Here,  $V(\mathbf{r}^N)$  is an external potential. With  $\mathbf{p}_i \equiv \frac{\partial \mathcal{L}}{\partial \dot{\mathbf{r}}_i} = m_i s^2 \dot{\mathbf{r}}_i$  and  $p_s \equiv \frac{\partial \mathcal{L}}{\partial \dot{s}} = Q \dot{s}$ , the Hamiltonian of the system can be written as

$$\mathcal{H}_{Nose} = \sum_{i=1}^N \frac{\mathbf{p}_i^2}{2m_i s^2} + V(\mathbf{r}^N) + \frac{p_s^2}{2Q} + \frac{L}{\beta} \ln(s) \quad (2.5)$$

$$= \sum_{i=1}^N \frac{\mathbf{p}'_i{}^2}{2m_i} + V(\mathbf{r}^N) + \frac{p_s^2}{2Q} + \frac{L}{\beta} \ln(s) \quad (2.6)$$

$$= \mathcal{H}(\mathbf{p}'_i, \mathbf{r}) + \frac{p_s^2}{2Q} + \frac{L}{\beta} \ln(s) \quad (2.7)$$

where  $\mathbf{p}'_i = \mathbf{p}_i/s$  is the scaled momenta of particle  $i$  of a microcanonical ensemble with  $6N + 2$  degrees of freedom. At the same time one has to scale the time variable  $\Delta t' = \Delta t/s$ . The primed variables are called the real one (see equation 2.7) and the unprimed ones are called virtual. Due to the time scaling, one can assume that the virtual or the real time step fluctuates with  $s$ , depending on which one is kept fix. The partition function of the system now reads (assuming only conservation of energy)

$$Q_{Nose} = \frac{1}{N!} \int dp_s ds d\mathbf{p}'^N d\mathbf{r}^N s^{3N} \delta(E - \mathcal{H}_{Nose}) \quad (2.8)$$

$$= \frac{C}{N!} \int d\mathbf{p}'^N d\mathbf{r}^N \exp[-\beta \mathcal{H}(\mathbf{p}'_i, \mathbf{r})] \quad (2.9)$$

Here one has to set  $L$  to  $3N + 1$  if virtual time is kept constant, or to  $3N$  if real time is kept constant. Now, assuming the latter case, the ensemble average of a variable  $A(\mathbf{p}/s, \mathbf{r})$  amounts to

$$\frac{\langle A(\mathbf{p}/s, \mathbf{r})/s \rangle}{\langle 1/s \rangle} = \frac{\int d\mathbf{p}'^N d\mathbf{r}^N A(\mathbf{p}/s, \mathbf{r}) \exp[-\beta\mathcal{H}(\mathbf{p}', \mathbf{r})]}{\int d\mathbf{p}'^N d\mathbf{r}^N \exp[-\beta\mathcal{H}(\mathbf{p}', \mathbf{r})]} \quad (2.10)$$

$$= \langle A(\mathbf{p}/s, \mathbf{r}) \rangle_{NVT} \quad (2.11)$$

and the equations of motions can be written as

$$\frac{d\mathbf{r}'_i}{dt'} = s \frac{d\mathbf{r}'_i}{dt} = \frac{\partial \mathcal{H}_{Nose}}{\partial \mathbf{p}_i} = \frac{\mathbf{p}_i}{m_i s} = \frac{\mathbf{p}'_i}{m_i} \quad (2.12)$$

$$\frac{d\mathbf{p}'_i}{dt'} = s \frac{d\mathbf{p}_i/s}{dt} = -\frac{\partial \mathcal{H}_{Nose}}{\partial \mathbf{r}_i} - \frac{\mathbf{p}_i}{s} \frac{ds}{dt} = -\frac{\partial V(\mathbf{r}^N)}{\partial \mathbf{r}'_i} - \mathbf{p}'_i \frac{sp'_s}{Q} \quad (2.13)$$

$$\frac{1}{s} \frac{ds}{dt'} = \frac{s}{s} \frac{ds}{dt} = \frac{\partial \mathcal{H}_{Nose}}{\partial p_s} = \frac{sp'}{Q} \quad (2.14)$$

$$\frac{d(sp'_s/Q)}{dt'} = \frac{s}{Q} \frac{dp_s}{dt} = -\frac{s}{Q} \frac{\partial \mathcal{H}_{Nose}}{\partial s} = \frac{1}{Q} \left( \sum_i \frac{p_i'^2}{m_i} - \frac{L}{\beta} \right) \quad (2.15)$$

Introducing the thermodynamic friction coefficient  $\xi = sp'_s/Q$ , omitting the primes and writing time derivatives as dots, one can rewrite the equations above as

$$\dot{\mathbf{r}}_i = \frac{\mathbf{p}_i}{m_i} \quad (2.16)$$

$$\dot{\mathbf{p}}_i = -\frac{\partial V(\mathbf{r}^N)}{\partial \mathbf{r}_i} - \xi \mathbf{p}_i \quad (2.17)$$

$$\frac{\dot{s}}{s} = \frac{d \ln(s)}{dt} = \xi \quad (2.18)$$

$$\dot{\xi} = \frac{1}{Q} \left( \sum_i \frac{p_i^2}{m_i} - \frac{L}{\beta} \right) \quad (2.19)$$

The quantity for the energy

$$\mathcal{H}'_{Nose}(\mathbf{r}, \mathbf{p}, s, p_s) = \sum_{i=1}^N \frac{\mathbf{p}_i^2}{2m_i} + V(\mathbf{r}^N) + \frac{s^2 p_s^2}{2Q} + \frac{L}{\beta} \ln(s) \quad (2.20)$$

is conserved in the sense that  $\dot{\mathcal{H}}'_{Nose} = 0$ . The energy in the physical system (including heat bath) has to be preserved.

In practice, the used program (LAMMPS [148]) uses a Liouville-Parrinello-Raman scheme to solve the equations of motion from the Nosé-Hoover chain formalism with a Velocity-Verlet like schema [149–151].

### 2.1.3. Nosé-Hoover chains

While the above described Nosé-Hoover thermostat generates a canonical distributions if one has external forces and/or the center of mass remains fixed. Due to the conservation of  $\mathcal{H}'_{Nose}$ , there are problems if these constrains are not fulfilled. A case where this thermostat fails to generate the correct behavior is the harmonic oscillator. To overcome all these problems, Martyna et al. [152] proposed a method where they coupled more than one Nosé-Hoover thermostat to a chain of thermostats. The equations of motion of a system with  $N$  particles coupled to a Nosé-Hoover chain with  $k = M$  thermostats read then

$$\dot{\mathbf{r}}_i = \frac{\mathbf{p}_i}{m_i} \quad (2.21)$$

$$\dot{\mathbf{p}}_i = -\frac{\partial V(\mathbf{r}^N)}{\partial \mathbf{r}_i} - \frac{p_{\xi,1}}{Q_1} \mathbf{p}_i \quad (2.22)$$

$$\dot{\xi}_k = \frac{p_{\xi,k}}{Q_k} \quad k = 1, \dots, M \quad (2.23)$$

$$\dot{p}_{\xi,1} = \left( \sum_i \frac{p_i^2}{m_i} - \frac{L}{\beta} \right) - \frac{p_{\xi,2}}{Q_2} p_{\xi,1} \quad (2.24)$$

$$\dot{p}_{\xi,k} = \left( \frac{p_{\xi,k-1}^2}{Q_{k-1}} - \frac{1}{\beta} \right) - \frac{p_{\xi,k+1}}{Q_{k+1}} p_{\xi,k} \quad (2.25)$$

$$\dot{p}_{\xi,M} = \left( \frac{p_{\xi,M-1}^2}{Q_{M-1}} - \frac{1}{\beta} \right) \quad (2.26)$$

With a chain-length of 1, the original thermostat is recovered. The related conserved energy is

$$\mathcal{H}_{NHC}(\mathbf{r}, \mathbf{p}, \xi, p_\xi) = \mathcal{H}(\mathbf{r}, \mathbf{p}) + \sum_{k=1}^M \frac{\mathbf{p}_{\xi,k}^2}{2Q_k} + \frac{L}{\beta} \xi_1 + \sum_{k=2}^M \frac{\xi_k}{\beta} \quad (2.27)$$

### 2.1.4. Embedded-atom-method potentials

A further thing one needs is a model for the interactions between the particles (atoms in our case). In classical molecular dynamics one usually uses so-called pseudo potentials. They have functional forms or are tabulated and they can be empirical or fitted to experimental and/or higher level theories (e.g. DFT<sup>3</sup> calculations). The simplest pseudo potentials are pair potentials which model pure two body interactions. They are only distance dependent<sup>4</sup>. More complex ones try to include the effects of more atoms, e.g. three-body potentials<sup>5</sup>.

In the following, the Finnis-Sinclair embedded-atom-method (EAM) type potentials [153] will be described which were used in our simulations. It is a higher order potential in the

<sup>3</sup>Density Functional Theory.

<sup>4</sup>An example is the Lennard-Jones potential which successfully describes the noble gases.

<sup>5</sup>An example is the Stillinger-Weber potential, which successfully describes the surface reconstruction of Si.

sense that it includes the effects of multiple atoms within a cut-off region. The functional form of the total energy can be written as [154–156]

$$E_{tot} = \sum_{i,j} \phi(r_{ij}) + \sum_i F(n_i) \quad (2.28)$$

$$n_i = \sum_j \varrho(r_{ij}) \quad (2.29)$$

Here  $\phi(r_{ij})$  is the pair potential energy between atom  $i$  and  $j$  (which is purely distant dependent as mentioned above),  $\varrho(r_{ij})$  is the density functional describing the electron density contribution of atom  $j$  at position of atom  $i$  and  $F(n_i)$  is the embedding energy which describes the modification of the energy landscape due to the presence of electron densities from (other) atoms.

Different realizations of this schema have different drawbacks, some are known to be too soft, others too stiff [157].

In most calculations we used the potentials from Sheng et al. [156]. They used DFT calculations of a few hundred atomic configurations with about a hundred atoms each to get statistical data of the potential-energy surface (PES) against which the above formula was fitted. They included effects of crystal structures, defects, deformations, melting, liquids and cooling processes and tested them against experimental data. This scheme aims at getting the best transferable potentials, applicable to low and high coordinated geometries.

### 2.1.5. Minimum cross section

In this thesis, wires with a diameter up to a few  $nm$  and a length (defined as  $z$ -direction, see Fig.2.1) in the same order of magnitude will be analyzed. A characteristic value of such a wire is its minimal cross section (mcs) perpendicular to the  $z$ -direction. Classically it's an interesting value because Ohm's law connects the resistance (or inverse conductance) of a macroscopic wire with its cross section. The equivalent for microscopic system is the Sharvin-Weyl formula (see section 2.2.1).

But in microscopic systems, the mcs can not be uniquely defined. In the following, three different approaches to define a mcs are presented.

The simplest way to calculate a cross section is to project the atoms modeled as spheres with radii  $r = \sqrt{3}a_0$ , where  $a_0$  is the lattice constant, onto the  $z$ -axes (assuming the wire is stretched along the  $z$ -axes). The smallest of the values along the axes is the mcs. Divided by  $\pi \cdot r^2$ , the mcs corresponds to the number of atoms in the constriction. In the elongated case where only the ends of two spheres are overlapping in the constriction<sup>6</sup>, this value can be between 0 and 1.

A second possibility is described and used in the dissertation of Markus Dreher [12] and goes back to [62]. It is based on the assumption of a symmetric wire cross section and the calculated radii represents the effective radii of a cylinder representing the volume of the atoms at that position. Therefore, one first determines the volume of the wire at position

<sup>6</sup>In context of electrons this regime is called "tunneling regime".

$z \pm \Delta z/2$  build up of atoms with radius  $r_0 = (2/\pi)^{1/3} \cdot a_0$ , where  $a_0$  is the lattice constant (the atoms fill the whole unit cell). The volume of that disk  $V_d$  is now compared with the volume of a cylinder (with length  $\Delta z$ ) and one gets the effective radius as

$$r_{eff} = \sqrt{\frac{V_d}{\pi \cdot \Delta z}} \quad (2.30)$$

Going to bigger wires, both approaches have a big disadvantage: They are not able to correctly distinguish between multiple discontinuous connections between the leads, which can break individually. If those regions exist, these two approaches will lead to wrong results and would have to be somehow modified by a more complex algorithm.

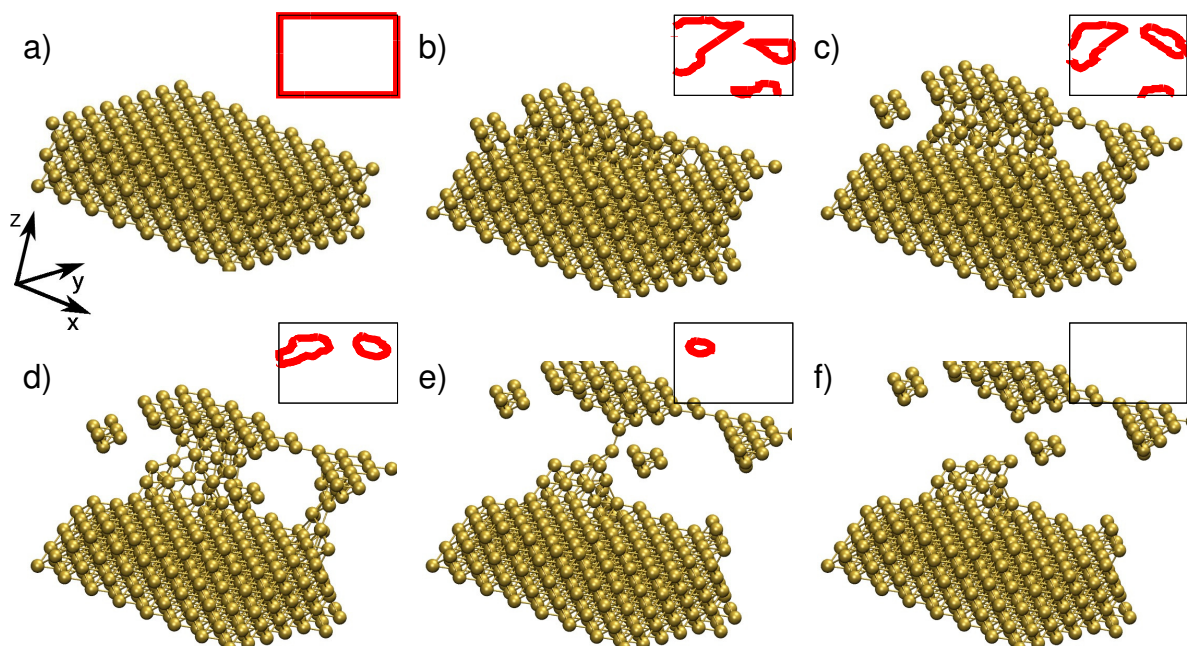


Figure 2.1.: A wire can consist out of more than one connection between the two leads. a)-d) show the evolution of a Au wire which breaks into three connections (see b) and c)) which break individually during the elongation process. In the upper parts the corresponding borders of the projections of the connections calculated by the cellular automata program (see text) are shown.

A different algorithmic approach is by using cellular automata to simulate a flow through the constriction. In this realization, the atoms are mapped as spheres onto a fine three dimensional grid<sup>7</sup>. Each grid point (cell) can be part of an atom or not, having the value ‘0’ or ‘1’. The rules for a cell A are as follows: Assuming it is occupied by a flow particle (electron), then search for a cell to put the electron in. The possibilities are (in that order): to the cell below, to one of the other four cells adjacent below or to one of the four cells in the same height. As precondition the target cell has to be empty and has to be part of an atom. If a target cell B is found, the flow particle goes from cell A to cell B, emptying cell A and filling cell B. If no target cell can be found, or cell A is not occupied by a flow particle, nothing happens.

<sup>7</sup>So each atom is represented by a couple of grid points in all three spatial directions.



The rules have to be applied to all cells, beginning from bottom to top again and again till a steady state is achieved. The restrictions are now projected onto the lowest area of cells. Adding up all flow particles there and dividing the result by the number of cells of the cross section of an atom leads again to a mcs describing the number of atoms in the restricted region.

In this context the flow simulation has a further advantage: It can count the number of connections between the leads. This can be achieved by looking again at the lowest area of cells and counting the number of closed areas containing only filled cells. To do so one counts the number of closed borders which is equivalent if one assumes that there are no simple holes.

The evolution of such a wire where multiple connections appear, is shown in Fig. 2.1.

In this thesis, the last definition of mcs with cellular automata will be used if not written different.

## 2.2. Nonequilibrium Green's functions - The way from the Hamiltonian to the conductance

In the following section the basic formulas used to calculate the conductance from the Hamilton operator are introduced and their derivations are described. It is meant as a summary of the relevant chapters of the textbook from Juan Carlos Cuevas and Elke Scheer [4]. More specialized descriptions of some topics can be found in the dissertations of Fabian Pauly [11] and Markus Dreher [12]<sup>8</sup>.

### 2.2.1. Sharvin-Weyl formula - scattering approach

From Ohm's law, it is known that the (electrical) conductance  $G$  of a macroscopic metallic wire with cross section area  $S$ , length  $L$  and conductivity  $\sigma$  is given by

$$G = \sigma \frac{S}{L} \quad (2.31)$$

In 1965 Sharvin approximated the propagation of electrical current through a ballistic contact where the length is smaller than the mean free path of the electrons, with the flow of classical gas through an orifice. With a net current of  $I = ne\Delta v S$ , where  $e$  is the electron charge,  $S = \pi R^2$  the cross section area with radius  $R$  and  $\Delta v = \pm eV/(\hbar k_F)$  the velocity change of the electrons through a potential difference of  $eV$ , the Fermi wave vector  $k_F$  and the electron density  $n = k_F^3/(3\pi^2)$ , Sharvin ended up with a conductance given by

$$G = G_0 \left( \frac{k_f R}{2} \right)^2 \quad (2.32)$$

where  $G_0 = \frac{2e^2}{h}$  is the quantum of conductance. The result also includes a factor of 2 for the spin and a factor of  $\frac{3}{8}$  for the correct integration of  $\Delta v$  through the orifice.

---

<sup>8</sup>In German.

For narrow contacts ( $2k_F R \gg 1$ ), the so-called Weyl correction takes into account that the Heisenberg uncertainty principle influences the Fermi electrons:

$$G = G_0 \left( \frac{k_f R}{2} \right)^2 \left( 1 - \frac{2}{k_F R} + \dots \right) \quad (2.33)$$

### 2.2.2. Heuristic derivation of the Landauer formula

In quantum mechanics, one can write the (one dimensional) current (considering a plane wave  $e^{ikx}$ ) through a potential barrier from left to right as

$$J_{L \rightarrow R} = \frac{e}{L} \sum_k v(k) \tau(k) f_L(k) [1 - f_R(k)] \quad (2.34)$$

where  $\frac{e}{L} v(k) \tau(k) = J_k$  is the electron current density for a given  $k$  with  $e$  the electron charge,  $L$  the length of the barrier,  $v(k) = \hbar k/m$  the group velocity,  $\tau(k) = |t|^2$  the transmission probability with the transmission amplitude  $t$  and  $f_{L/R}(k)$  the Fermi function of the left/right electron reservoir.

Going from the sum  $(1/L) \sum_k$  to the integral form  $1/(2\pi) \int dk$  and with  $E = \hbar^2 k^2 / (2m)$  from  $dk$  to  $dE$ , one gets

$$J_{L \rightarrow R} = \frac{e}{h} \int dE \tau(E) f_L(E) [1 - f_R(E)] \quad (2.35)$$

and the total current  $I(V)$  (with a factor 2 for the spin)

$$I(V) = J_{L \rightarrow R} - J_{R \rightarrow L} \quad (2.36)$$

$$= \frac{2e}{h} \int dE \tau(E) [f_L(E) - f_R(E)] \quad (2.37)$$

$$\approx \frac{2e^2}{h} \cdot \tau(E = E_F) \cdot V \quad \text{for low } V \text{ at } T=0\text{K} \quad (2.38)$$

$$= G_0 \cdot \tau(E = E_F) \cdot V \quad (2.39)$$

$$= G \cdot V \quad (2.40)$$

Here the fact was used, that  $f_L(E) - f_R(E)$  at  $T = 0\text{K}$  is equal to one in the interval  $[E_F - eV, E_F + eV]$  and zero elsewhere.

If the transmission amplitude  $t(E = E_F)$  is not a scalar but a matrix (operator)  $\hat{t}(E = E_F)$ , one has to sum up all its eigenvalues  $\tau_n$  to get the total conductance  $\tau$ :

$$G = G_0 \tau = G_0 |t|^2 \rightarrow G = G_0 \text{Tr}\{\hat{t}^\dagger \hat{t}\} = G_0 \sum_n \tau_n \quad (2.41)$$

The  $\tau_n$ 's are in the range  $[0, 1]$  and are also called (individual) channel transmissions because each physically available channel (e.g. overlap between electronic orbitals) is represented by one eigenvalue  $\tau_n$  and can contribute up to  $1 G_0$  to the total conductance. Equation (2.41) is known as multi channel Landauer formula.

### 2.2.3. Green's functions

With the help of Green's functions one can derive the Landauer formula in a more formal way. To do so, let us start with the Schroedinger equation of motion

$$i\hbar\Psi_s(t) = \mathbf{H}\Psi_s(t) \quad (2.42)$$

$$\Psi_s(t) = e^{-\frac{i}{\hbar}\mathbf{H}(t-t_0)}\Psi_s(t_0) \quad (2.43)$$

with the time-evolution operator  $\mathbf{S}_s = e^{-i\mathbf{H}(t-t_0)}$ . The time independent Schroedinger equation can be solved with the Green's function (propagator)  $\mathbf{G}$ <sup>9</sup>

$$H(x)\Psi(x) = E\Psi(x) \rightarrow [E - H(x)]G(x, x') = \delta(x - x') \quad (2.44)$$

$$H(x) = \frac{p^2}{2m} + V(x) = -\frac{\hbar^2}{2m}\partial_x^2 + V(x) \quad (2.45)$$

In the case of free electrons the potential is constant ( $V(x) = V_0$ ) and one gets an exact solution for  $G$ :

$$G(x - x', E) = \mp \frac{i}{V} e^{\pm ik|x-x'|} \quad (2.46)$$

with  $k = m \cdot v = \sqrt{2m(E - V_0)}$ . The upper sign corresponds to the retarded and the lower one to the advanced Green's function. The function  $G(x - x', E)$  can be interpreted as propagation amplitude of an electron, moving from  $x'$  to  $x$  at energy  $E$ . Retarded/advanced means that the propagation is forward/backward in time. The Green's functions with the corresponding signs have an superindex  $r/a$  for retarded/advanced.

To solve the problem of divergencies an infinitesimal imaginary part  $E \rightarrow E \pm i\eta$  is introduced. The sign of the imaginary part shows the direction in time: positive for forward (retarded) and negative for backward (advanced):

$$\lim_{\eta \rightarrow 0} [(E \pm i\eta) - H(x)] G^{r,a}(x, x') = \delta(x - x') \quad (2.47)$$

or as an operator identity

$$\mathbf{G}^{r,a}(E) = \lim_{\eta \rightarrow 0} [(E \pm i\eta)\mathbb{1} - \mathbf{H}]^{-1} \quad (2.48)$$

$$= \sum_n \frac{|\Psi_n\rangle \langle \Psi_n|}{(E \pm i\eta) - \varepsilon_n} \quad (2.49)$$

where  $\mathbb{1}$  is the identity operator, and  $\varepsilon_n$  and  $|\Psi_n\rangle$  are the eigenvalues and eigenfunctions of  $\mathbf{H}$ , respectively. For simplicity, the limit  $\eta \rightarrow 0$  is from now on implicitly assumed and no longer explicitly written.

Equation (2.48) is often referred to as direct definition of  $\mathbf{G}$  (within this context), while (2.49) is referred to as spectral representation.

<sup>9</sup>In following for simplicity one dimensional.

If one can divide the Hamiltonian  $\mathbf{H}$  into an unperturbed  $\mathbf{H}_0$  and an arbitrary single-particle perturbation  $\mathbf{V}$

$$\mathbf{H} = \mathbf{H}_0 + \mathbf{V} \quad (2.50)$$

then there exists a third representation for  $\mathbf{G}$ :

$$\mathbf{G}^{r,a}(E) = [(E \pm i\eta)\mathbb{1} - \mathbf{H}_0 - \mathbf{V}]^{-1} \quad (2.51)$$

$$= \mathbf{g}^{r,a}(E) + \mathbf{g}^{r,a}(E)\mathbf{V}\mathbf{G}^{r,a}(E) \quad (2.52)$$

$$\mathbf{g}^{r,a}(E) = [(E \pm i\eta)\mathbb{1} - \mathbf{H}_0]^{-1} . \quad (2.53)$$

Equation (2.52) is known as Dyson's equation, where  $\mathbf{g}^{r,a}(E)$  is the Green's function of the unperturbed system  $\mathbf{H}_0$ .

Later, the perturbation  $\mathbf{V}$  will be replaced by the so-called self-energy  $\mathbf{\Sigma}$  which describes the coupling of the considered system to the environment (e.g. walls).

With the Green's function one can calculate the local density of states (LDOS) in a given position  $\mathbf{r}$

$$\varrho(\mathbf{r}, E) = \mp \frac{1}{\pi} \text{Im} \{G^{r,a}(\mathbf{r}, E)\} \quad (2.54)$$

To see this, one can compare the LDOS in the form known from quantum mechanics (2.55) with the Green's function in the spectral representation (2.56) and use the Cauchy principal value  $\mathbb{P}$  (2.57):

$$\varrho(\mathbf{r}, E) = \sum_n |\langle \mathbf{r} | \Psi_n \rangle|^2 \delta(E - \varepsilon_n) \quad (2.55)$$

$$\mathbf{G}^{r,a}(\mathbf{r}, E) = \sum_n \frac{\langle \mathbf{r} | \Psi_n \rangle \langle \Psi_n | \mathbf{r} \rangle}{(E \pm i\eta) - \varepsilon_n} \quad (2.56)$$

$$\frac{1}{E \pm i\eta} = \mathbb{P} \left( \frac{1}{E} \right) \mp i\pi \delta(E) \quad \text{with} \quad E \rightarrow E - \varepsilon_n \quad (2.57)$$

For a discrete basis of atomic orbitals with atom (sites)  $i$ , one ends up with

$$\varrho_i(E) = \mp \frac{1}{\pi} \text{Im} \{G_{ii}^{r,a}(E)\} \quad (2.58)$$

instead of (2.54).

### 2.2.4. Nonequilibrium Green's function and Keldysh formalism

Up to now, time did not play any role. But to go forward to nonequilibrium Green's functions, one has to introduce time to order the processes. This can be done within the framework of the Keldysh formalism. Let us see how this works (Chapter 7 of [4]).

First of all, one needs the time evolution operator in the interaction picture  $\mathbf{S}(t, t_0)$  with

$$\Psi_s(t) = e^{-i\mathbf{H}(t-t_0)}\Psi_s(t_0) \quad (2.59)$$

$$\Psi_I(t) = e^{i\mathbf{H}_0 t}\Psi_s(t) = \mathbf{S}(t, t_0)\Psi_I(t_0) \quad (2.60)$$

$$\mathbf{S}(t, t_0) = e^{i\mathbf{H}_0 t}e^{-i\mathbf{H}(t-t_0)}e^{-i\mathbf{H}_0 t_0} \quad (2.61)$$

where index  $s$  denotes the Schroedinger and index  $I$  the interaction picture.

The equations of motion are

$$i\frac{\partial}{\partial t}\Psi_I(t) = \mathbf{V}_I(t)\Psi_I(t) \quad (2.62)$$

$$\mathbf{V}_I(t) = e^{i\mathbf{H}_0 t}\mathbf{V}e^{-i\mathbf{H}_0 t} \quad (2.63)$$

where  $\mathbf{V} = \mathbf{H} - \mathbf{H}_0$  is the considered perturbation (interaction). Equation (2.62) can be rewritten in integral form as

$$\Psi_I(t) = \Psi_I(t_0) - \int_{t_0}^t dt' \mathbf{V}_I(t')\Psi_I(t') \quad (2.64)$$

which can be solved iteratively. One ends up with

$$\begin{aligned} \Psi_I(t) = & \left[ 1 + \sum_n (-i)^n \int_{t_0}^t dt_1 \mathbf{V}_I(t_1) \cdot \int_{t_0}^{t_1} dt_2 \mathbf{V}_I(t_2) \right. \\ & \left. \cdots \int_{t_0}^{t_{n-1}} dt_n \mathbf{V}_I(t_n) \right] \Psi_I(t_0) \end{aligned} \quad (2.65)$$

$$= \mathbf{S}(t, t_0) \Psi_I(t_0) \quad (2.66)$$

$$\mathbf{S}(t, t_0) = \sum_{n=0}^{\infty} \frac{(-i)^n}{n!} \int_{t_0}^t dt_1 \int_{t_0}^{t_1} dt_2 \cdots \int_{t_0}^{t_{n-1}} dt_n \mathbf{T}[\mathbf{V}_I(t_1)\mathbf{V}_I(t_2)\cdots\mathbf{V}_I(t_n)] \quad (2.67)$$

with the time ordering operator  $\mathbf{T}$  who arranges the operators in the correct order in time from right to left ( $t > t_1 > \cdots > t_n > t_0$ ) and takes care of the anticommutator relation for fermions. The expectation value of an operator  $\mathbf{A}$  now reads

$$\langle \mathbf{A} \rangle = \frac{\langle \Psi_I | \mathbf{A}_I(t) | \Psi_I \rangle}{\langle \Psi_I | \Psi_I \rangle} \quad (2.68)$$

$$= \frac{\langle \phi_0 | \mathbf{S}(-\infty, t) \mathbf{A}_I(t) \mathbf{S}(t, -\infty) | \phi_0 \rangle}{\langle \phi_0 | \mathbf{S}(-\infty, t) \mathbf{S}(t, -\infty) | \phi_0 \rangle} \quad (2.69)$$

Here one assumes an adiabatically on and off switching of the perturbation  $\mathbf{V}(t) \rightarrow \exp\{-\varepsilon|t|\}\mathbf{V}(t)$  at  $t = \pm\infty$  and a noninteracting state  $|\phi_0\rangle$ . The generalization of (2.68) to non equilibrium systems in (2.69) has the disadvantage that the time-evolution can not be written in a single operator any more. To overcome this, one introduces the *Keldysh contour* which divides the

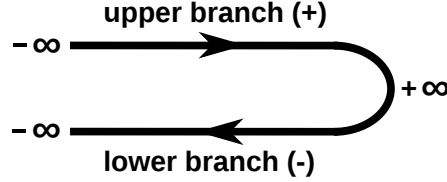


Figure 2.2.: The Keldysh contour with an upper and a lower branch as usually shown in textbooks [4].

timeline into two branches: an upper branch going from  $-\infty$  to  $+\infty$  and a lower one going from  $+\infty$  to  $-\infty$  (Fig. 2.2). They are connected at  $+\infty$ . Introducing an index  $+/-$  to indicate if the operator is defined in the upper/lower branch and a time ordering operator for the Keldysh contour  $\mathbf{T}_c$  one gets

$$\langle \mathbf{A} \rangle = \frac{\langle \phi_0 | \mathbf{T}_c [\mathbf{A}_I(t) \mathbf{S}_-(-\infty, \infty) \mathbf{S}_+(\infty, -\infty)] | \phi_0 \rangle}{\langle \phi_0 | \mathbf{S}_-(-\infty, \infty) \mathbf{S}_+(\infty, -\infty) | \phi_0 \rangle} \quad (2.70)$$

$$= \frac{\langle \phi_0 | \mathbf{T}_c [\mathbf{A}_I(t) \mathbf{S}_c(\infty, -\infty)] | \phi_0 \rangle}{\langle \phi_0 | \mathbf{S}_c(\infty, -\infty) | \phi_0 \rangle} \quad (2.71)$$

$$\mathbf{S}_c(\infty, -\infty) \equiv \mathbf{S}_-(-\infty, \infty) \mathbf{S}_+(\infty, -\infty) \quad (2.72)$$

with the time-evolution operator  $S_c$  along the Keldysh contour. With the creation and annihilation operators of a particle (electron) on site  $i$ ,  $\mathbf{c}_i^\dagger$  and  $\mathbf{c}_i$ , there exist four possibilities for the Green's functions

$$G_{i,j}(t_\alpha, t'_\beta) = -i \frac{\langle \Psi_H | \mathbf{T}_c [\mathbf{c}_i(t_\alpha) \mathbf{c}_j^\dagger(t'_\beta)] | \Psi_H \rangle}{\langle \Psi_H | \Psi_H \rangle} \quad (2.73)$$

with  $\alpha, \beta$  equals  $+$  or  $-$  for the upper/lower branch. For  $G_{i,j}^{\alpha\beta}$  (assuming  $\langle \Psi_H | \Psi_H \rangle = 1$ ) this leads to

$$t = t_+ \text{ and } t' = t'_+ : G_{i,j}^{++}(t, t') = -i \left\langle \mathbf{T} \left[ \mathbf{c}_i(t) \mathbf{c}_j^\dagger(t') \right] \right\rangle \quad (2.74)$$

$$t = t_+ \text{ and } t' = t'_- : G_{i,j}^{+-}(t, t') = i \left\langle \left[ \mathbf{c}_j^\dagger(t') \mathbf{c}_i(t) \right] \right\rangle \quad (2.75)$$

$$t = t_- \text{ and } t' = t'_+ : G_{i,j}^{-+}(t, t') = -i \left\langle \left[ \mathbf{c}_i(t) \mathbf{c}_j^\dagger(t') \right] \right\rangle \quad (2.76)$$

$$t = t_- \text{ and } t' = t'_- : G_{i,j}^{--}(t, t') = -i \left\langle \bar{\mathbf{T}} \left[ \mathbf{c}_i(t) \mathbf{c}_j^\dagger(t') \right] \right\rangle \quad (2.77)$$

where  $\bar{\mathbf{T}}$  has the opposite time ordering as  $\mathbf{T}$ . They can be summarized in a  $2 \times 2$  matrix  $\check{\mathbf{G}}$ :

$$\check{\mathbf{G}} = \begin{pmatrix} \mathbf{G}^{++} & \mathbf{G}^{+-} \\ \mathbf{G}^{-+} & \mathbf{G}^{--} \end{pmatrix} \quad (2.78)$$

With that, Dyson's equation in the nonequilibrium looks like

$$\check{\mathbf{G}}(t, t') = \check{\mathbf{g}}(t, t') + \int dt_1 \int dt_2 \check{\mathbf{g}}(t, t_1) \check{\Sigma}(t_1, t_2) \check{\mathbf{G}}(t_2, t') \quad (2.79)$$

where  $\check{\mathbf{g}}$  is the Green's function of the unperturbed system. The self-energy  $\check{\Sigma}$  has the same  $2 \times 2$  form as  $\check{\mathbf{G}}$ .

In many stationary systems, where everything only depends on time differences, one can get the form of equation (2.52) (with Fourier transformation of equation (2.79))

$$\check{\mathbf{G}}(E) = \check{\mathbf{g}}(E) + \check{\mathbf{g}}(E) \check{\Sigma}(E) \check{\mathbf{G}}(E) \quad (2.80)$$

For a system with  $N$  noninteracting electrons in a time dependent external potential  $V(t)$

with  $\mathbf{H} = \mathbf{H}_0 + \sum_{i=1}^N V(\mathbf{r}_i, t)$  the self-energy gets the (trivial) form

$$\check{\Sigma}(\mathbf{r}, t) = \begin{pmatrix} V(\mathbf{r}, t) & 0 \\ 0 & -V(\mathbf{r}, t) \end{pmatrix} \quad (2.81)$$

To have off-diagonal elements, one would need inelastic events like electron-electron or electron-phonon interaction.

The four Green's functions (2.74)-(2.77) are not independent from each other. This can be used to reduce their number to three independent Green's functions

$$\mathbf{G}^r = \mathbf{G}^{++} - \mathbf{G}^{+-} = \mathbf{G}^{-+} - \mathbf{G}^{--} \quad (2.82)$$

$$\mathbf{G}^a = \mathbf{G}^{++} - \mathbf{G}^{-+} = \mathbf{G}^{+-} - \mathbf{G}^{--} \quad (2.83)$$

$$\mathbf{G}^K = \mathbf{G}^{++} + \mathbf{G}^{--} = \mathbf{G}^{+-} + \mathbf{G}^{-+} \quad (2.84)$$

where  $\mathbf{G}^{r/a}$  are the retarded/advanced Green's functions and  $\mathbf{G}^K$  is the Keldysh Green's function. The self-energies can be written accordingly

$$\Sigma^r = \Sigma^{++} + \Sigma^{+-} = -(\Sigma^{-+} + \Sigma^{--}) \quad (2.85)$$

$$\Sigma^a = \Sigma^{++} + \Sigma^{-+} = -(\Sigma^{+-} + \Sigma^{--}) \quad (2.86)$$

$$\Sigma^K = \Sigma^{++} + \Sigma^{--} = -(\Sigma^{+-} + \Sigma^{-+}) \quad (2.87)$$

The related Dyson equations are

$$\mathbf{G}^{r,a} = \mathbf{g}^{r,a} + \mathbf{g}^{r,a} \Sigma^{r,a} \mathbf{G}^{r,a} \quad (2.88)$$

$$\mathbf{G}^\beta = \mathbf{g}^{+-} + \mathbf{g}^\beta \Sigma^a \mathbf{G}^a + \mathbf{g}^r \Sigma^r \mathbf{G}^\beta + \mathbf{g}^r \Sigma^\beta \mathbf{G}^a \quad (2.89)$$

$$= (\mathbf{1} + \mathbf{G}^r \Sigma^r) \mathbf{g}^\beta (\mathbf{1} + \Sigma^a \mathbf{G}^a) + \mathbf{G}^r \Sigma^\beta \mathbf{G}^a \quad (2.90)$$

where  $\beta$  is  $K$  ( $\mathbf{G}^K$ ),  $+-$  ( $\mathbf{G}^{+-}$ ) or  $-+$  ( $\mathbf{G}^{-+}$ ).

### 2.2.5. Temperature

Having a look on  $G^{+-}$  in time domain

$$G_{ij}^{+-}(t) = \iota \langle \mathbf{c}_j^\dagger(0) \mathbf{c}_i(t) \rangle \quad (2.91)$$

one gets for  $i = j$  and  $t = 0$

$$G_{ii}^{+-}(0) = \int_{-\infty}^{\infty} \frac{dE}{2\pi} \cdot G_{ii}^{+-}(E) \quad (2.92)$$

$$= \iota \langle \mathbf{n}_i \rangle \quad (2.93)$$

$$= \int_{-\infty}^{\infty} \frac{dE}{2\pi} \cdot 2\pi \iota \rho_i(E) f(E) \quad (2.94)$$

with  $\langle \mathbf{n}_i \rangle$  the mean occupation number on site  $i$ .  $f(E) = [\exp\{(E - \mu)/k_B T\} + 1]^{-1}$  is the Fermi function,  $\mu$  the chemical potential,  $k_B$  the Boltzmann factor and  $T$  the temperature. This implies that

$$G_{ii}^{+-}(E) = 2\pi \iota \rho_i(E) f(E) \quad \propto f(E) \quad (2.95)$$

and equivalently

$$G_{ii}^{-+}(E) = -2\pi \iota \rho_i(E) [1 - f(E)] \quad \propto 1 - f(E) \quad (2.96)$$

Generalizing these proportionalities and using the general relation  $\mathbf{G}^a(t) - \mathbf{G}^r(t) = \mathbf{G}^{+-}(t) - \mathbf{G}^{-+}(t)$ , one gets

$$\mathbf{G}^{+-}(E) = [\mathbf{G}^a(E) - \mathbf{G}^r(E)] f(E) \quad (2.97)$$

$$\mathbf{G}^{-+}(E) = -[\mathbf{G}^a(E) - \mathbf{G}^r(E)] [1 - f(E)] \quad (2.98)$$

These formulas are also true for the unperturbed (non-interacting) Green's functions  $g^{+-}/g^{-+}$  or in a basis  $|i\rangle$  for  $g_{ij}^{+-}/g_{ij}^{-+}$ .

### 2.2.6. Application to simple transport problems

Before advancing to the results for realistic systems, it is a good idea to make the formalism a bit more transparent by using a few simple examples. They can be found in section 7.4 and 7.4.1 of [4] and are the basis for the understanding of the realistic system.

Simple examples for equilibrium Green's functions (an  $H_2$  molecule, a semi-infinite linear chain and a single level coupled to electrodes, all from section 5.3 of [4]) can be found in the appendix (A.1).

1) Consider a linear chain with the tight-binding Hamiltonian

$$\mathbf{H} = \sum_i \varepsilon_i \mathbf{n}_i + \sum_{ij} t_{ij} (\mathbf{c}_i^\dagger \mathbf{c}_j + \mathbf{c}_j^\dagger \mathbf{c}_i) \quad (2.99)$$

$$= \sum_i \varepsilon_i \mathbf{n}_i + t \sum_i (\mathbf{c}_i^\dagger \mathbf{c}_{i+1} + \mathbf{c}_{i+1}^\dagger \mathbf{c}_i) \quad (2.100)$$



where only next neighbor interactions and a constant hopping parameter  $t$  between the neighbors are considered. The current through a point between site  $i$  and site  $i + 1$  can then be calculated via

$$\mathbf{I}(t) = \frac{iet}{\hbar} \left( \mathbf{c}_i^\dagger(t) \mathbf{c}_{i+1}(t) - \mathbf{c}_{i+1}^\dagger(t) \mathbf{c}_i(t) \right) \quad (2.101)$$

The mean value of that current operator is now just

$$\langle \mathbf{I}(t) \rangle = \frac{iet}{\hbar} \left( \langle \mathbf{c}_i^\dagger(t) \mathbf{c}_{i+1}(t) \rangle - \langle \mathbf{c}_{i+1}^\dagger(t) \mathbf{c}_i(t) \rangle \right) \quad (2.102)$$

$$= \frac{iet}{\hbar} \left( G_{i+1,i}^{+-}(t,t) - G_{i,i+1}^{+-}(t,t) \right) \quad (2.103)$$

$$\langle \mathbf{I} \rangle = \frac{iet}{\hbar} \int_{-\infty}^{\infty} \frac{dE}{2\pi} \left( G_{i+1,i}^{+-}(E) - G_{i,i+1}^{+-}(E) \right) \quad (2.104)$$

where  $\langle \mathbf{I} \rangle$  is the Fourier transform of  $\langle \mathbf{I}(t) \rangle$ . The Fourier transformation is possible if a stationary state is achieved.

2) Consider two leads,  $\mathbf{H}_L$  (left) and  $\mathbf{H}_R$  (right), which touch each other at only one point (one atom of each lead) which leads to a coupling  $\mathbf{H}_C$ . The tight-binding Hamiltonian can be written as

$$\mathbf{H} = \mathbf{H}_L + \mathbf{H}_R + \mathbf{H}_C \quad (2.105)$$

$$= \mathbf{H}_L + \mathbf{H}_R + t \left( \mathbf{c}_L^\dagger \mathbf{c}_R + \mathbf{c}_R^\dagger \mathbf{c}_L \right) \quad (2.106)$$

The resulting current in the point contact is (assuming a stationary state)

$$I = \langle \mathbf{I} \rangle = \frac{iet}{\hbar} \int_{-\infty}^{\infty} dE \left( G_{RL}^{+-}(E) - G_{LR}^{+-}(E) \right) \quad (2.107)$$

One now has to make a choice for the perturbation. The external potential as perturbation is not a good idea, because the voltage drops through the whole system. A better choice is to make the coupling the perturbation and to introduce the voltage by shifting the corresponding chemical potential (e.g.  $\mu_L = eV$  and  $\mu_R = 0$ ). The corresponding self-energy for the latter choice is then

$$\Sigma_{LR}^{r,a} = \Sigma_{RL}^{r,a} = t \quad (2.108)$$

$$\Sigma^{+-} = \Sigma^{-+} = 0 \quad (2.109)$$

Using equation (2.89) in two equivalent forms with  $\Sigma^{+-} = 0$  (in energy space) leads to

$$G_{LR}^{+-} = g_{LR}^{+-} + tg_{LL}^{+-} G_{RR}^a + tg_{LL}^r G_{RR}^{+-} \quad (2.110)$$

$$G_{RL}^{+-} = g_{RL}^{+-} + tG_{RR}^{+-} g_{LL}^a + tG_{RR}^r g_{LL}^{+-} \quad (2.111)$$

Together with equation (2.90) for  $\mathbf{G}^{+-}$  and  $\mathbf{G}^{-+}$  and the general relations  $\mathbf{G}^a - \mathbf{G}^r = \mathbf{G}^{+-} - \mathbf{G}^{-+}$  and  $\mathbf{G}^a = [\mathbf{G}^r]^\dagger$  one ends up at

$$I = \frac{e}{h} \int_{-\infty}^{\infty} dE t^2 [g_{LL}^{+-}(E)G_{RR}^{-+}(E) - g_{LL}^{-+}(E)G_{RR}^{+-}(E)] \quad (2.112)$$

$$= \frac{e}{h} \int_{-\infty}^{\infty} dE t^2 |1 + tG_{RL}^r(E)|^2 \cdot [g_{LL}^{+-}(E)g_{RR}^{-+}(E) - g_{LL}^{-+}(E)g_{RR}^{+-}(E)] \quad (2.113)$$

$G_{RL}^r$  can be calculated by using the  $RL$  and  $LL$  component of Dyson's equation (2.88). Taking into account that  $\mathbf{g}$  is purely diagonal ( $g_{RL} = 0$ ) and  $\mathbf{\Sigma}$  is purely off-diagonal, one gets

$$G_{RL}^r = g_{RR}^r \Sigma_{RL}^r G_{LL}^r = t g_{RR}^r G_{LL}^r \quad (2.114)$$

$$G_{LL}^r = g_{LL}^r + g_{LL}^r \Sigma_{LR}^r G_{RL}^r = g_{LL}^r + t g_{LL}^r G_{RL}^r \quad (2.115)$$

$$\Leftrightarrow 1 + tG_{RL}^r = [1 - t^2 g_{RR}^r g_{LL}^r]^{-1} \quad (2.116)$$

together with (2.95) and (2.96) the current reads (remembering the shifts from the chemical potential)

$$I = \frac{e}{h} \int_{-\infty}^{\infty} dE \frac{4\pi^2 t^2 \varrho_L(E - eV) \varrho_R(E)}{|1 - t^2 g_{LL}^r(E - eV) g_{RR}^r(E)|^2} \cdot [f(E - eV) - f(E)] \quad (2.117)$$

$$= \frac{e}{h} \int_{-\infty}^{\infty} dE \tau(e, V) \cdot [f(E - eV) - f(E)] \quad (2.118)$$

where  $\varrho_{L/R}$  is the local density of states of the two leads (projected onto sites  $L/R$ ). For sufficient low voltages, the current depends only linearly on  $V$

$$I(E_F, V = 0) \approx \frac{e}{h} \cdot \tau(E_F, V = 0) \cdot V \quad (2.119)$$

$$= G \cdot V \quad (2.120)$$

$$= \frac{G_0}{2} \cdot \tau(E_F, V = 0) \cdot V \quad (2.121)$$

The prefactor is only  $\frac{G_0}{2}$  because the spin dependency was ignored here without compensating it by a factor of two.

In the tunneling limit, where  $V \neq 0$  but  $t$  goes to zero, the denominator of  $\tau$  goes to one and the current becomes

$$I = \frac{e}{h} \int_{-\infty}^{\infty} dE 4\pi^2 t^2 \varrho_L(E - eV) \varrho_R(E) \cdot [f(E - eV) - f(E)] \quad (2.122)$$

The differential conductance (in opposite to the linear one in (2.119)) is given by the derivative of the current by the applied voltage. Assuming that the left lead is for example an

STM (Scanning tunneling microscope) tip with a constant density of states near the Fermi energy  $\varrho_L(E_F)$ , then  $G(V)$  is proportional to the local density of states of the sample  $\varrho_R$ :

$$G(V) = \frac{dI}{dV} \quad (2.123)$$

$$= \frac{e}{h} 4\pi^2 t^2 \varrho_L(E_F) \varrho_R(E_F + eV) \quad (2.124)$$

$$\propto \varrho_R(E_F + eV) \quad (2.125)$$

Here  $\frac{\partial f(E-eV)}{\partial V} = \delta(E_F - (E - eV))$  was used.

### 2.2.7. Resulting formulas for the current through realistic systems

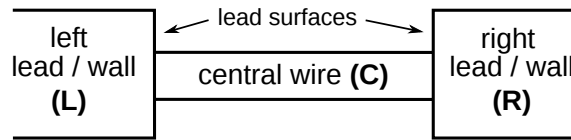


Figure 2.3.: Schematic representation of a system with a wire (C) connected to two leads (L) and (R).

Up to now the formalism of the nonequilibrium Green's functions was derived and their usability for a few simple systems was demonstrated. Now we want to derive the formulas applicable to realistic systems: three dimensional wires consisting of atoms with orbitals (tight-binding approach without inelastic interactions):

$$\mathbf{H} = \sum_{ij,\alpha\beta,\sigma} h_{i\alpha,j\beta} \mathbf{c}_{i\alpha,\sigma}^\dagger \mathbf{c}_{j\beta,\sigma} \quad (2.126)$$

The atoms are labeled with  $i, j$  with orbitals  $\alpha, \beta$ . Spin  $\sigma$  was included here for completeness and  $h_{i\alpha,j\beta}$  are the hopping matrix elements.

The goal is to calculate the current  $J$  through a wire. To get there one first divides the system into three regions (Fig. 2.3): a semi infinite wall (electrode/lead/reservoir) on the left side (index  $L$ ), a semi infinite wall on the right side (index  $R$ ) and a piece of wire connecting those two walls (index  $C$ ). This is similar to the second example in the last part (two leads, touching at one point).

Assuming that the walls do not couple directly to each other (they are separated far enough), one can write the Hamiltonian as

$$\mathbf{H} = \begin{pmatrix} \mathbf{H}_{LL} & \mathbf{t}_{LC} & \mathbf{0} \\ \mathbf{t}_{CL} & \mathbf{H}_{CC} & \mathbf{t}_{CR} \\ \mathbf{0} & \mathbf{t}_{RC} & \mathbf{H}_{RR} \end{pmatrix} \quad (2.127)$$

where the main diagonal consists of the Hamiltonians of the three subsystems which couple through the  $\mathbf{t}$ 's.

Using the hopping matrices  $\mathbf{t}_{CX}$  and  $\mathbf{t}_{XC}$  with  $X = L, R$  defined as

$$(\mathbf{t}_{XC})_{i\alpha,j\beta} = h_{i\alpha,j\beta} \quad \text{with } i \in X; j \in C \quad (2.128)$$

$$(\mathbf{t}_{XC}) = (\mathbf{t}_{XC})^\dagger \quad (2.129)$$

the (mean) current can be written as (looking only at the interface  $LC$ )

$$I = \frac{ie}{\hbar} \sum_{i \in L; j \in C; \alpha\beta\sigma} \left[ h_{i\alpha,j\beta} \langle \mathbf{c}_{i\alpha,\sigma}^\dagger \mathbf{c}_{j\beta,\sigma} \rangle - h_{j\beta,i\alpha} \langle \mathbf{c}_{j\beta,\sigma}^\dagger \mathbf{c}_{i\alpha,\sigma} \rangle \right] \quad (2.130)$$

$$= \frac{e}{\hbar} \sum_{i \in L; j \in C; \alpha\beta\sigma} \left[ h_{i\alpha,j\beta} G_{j\beta,i\alpha}^{+-,\sigma\sigma}(t, t) - h_{j\beta,i\alpha} G_{i\alpha,j\beta}^{+-,\sigma\sigma}(t, t) \right] \quad (2.131)$$

$$= \frac{2e}{\hbar} \text{Tr} \{ \mathbf{G}_{CL}^{+-}(t, t) \mathbf{t}_{LC} - \mathbf{t}_{CL} \mathbf{G}_{LC}^{+-} \} \quad (2.132)$$

Summing up over the spin degrees of freedom resulted in a factor of two (spin degeneracy leads to equal contribution from each spin).

Following the same arguments as in subsection 2.2.6, one ends up with

$$I = \frac{2e}{h} \int_{-\infty}^{\infty} dE 4 \text{Tr} \{ \mathbf{G}_{CC}^r \mathbf{t}_{CR} \text{Im} \{ \mathbf{g}_{RR}^a \} \mathbf{t}_{RC} \mathbf{G}_{CC}^a \mathbf{t}_{CL} \text{Im} \{ \mathbf{g}_{LL}^a \} \mathbf{t}_{LC} \} \times (f_L - f_R) \quad (2.133)$$

with the Fermi functions  $f_{L/R}$  of the walls and the Green's functions of the non-interacting walls  $\mathbf{g}_{LL/RR}$ . The influence of the right wall, which was not clearly visible in equation 2.132, was introduced by using Dyson's equation for  $\mathbf{G}_{CL/LC}^{+-}$  and following up for  $\mathbf{G}_{CC}^{+-/-+}$ , where  $\mathbf{G}_{CC}$  is influenced by the interaction with both walls. Using the self-energy  $\Sigma$  and the scattering rate matrix  $\Gamma$  with

$$\Sigma_X^{r,a} = \mathbf{t}_{CX} \mathbf{g}_{XX}^{r,a} \mathbf{t}_{XC} \quad (2.134)$$

$$\Gamma_X \equiv \text{Im} \{ \Sigma_X^a \} \quad (2.135)$$

where  $X$  is  $L$  or  $R$  one gets

$$I = \frac{2e}{h} \int_{-\infty}^{\infty} dE T(E, V) \times (f_L - f_R) \quad (2.136)$$

$$\tau(E, V) \equiv 4 \text{Tr} \{ \Gamma_L \mathbf{G}_{CC}^r \Gamma_R \mathbf{G}_{CC}^a \} \quad (2.137)$$

$$= \text{Tr} \{ \mathbf{t}^\dagger(E, V) \mathbf{t}(E, V) \} \quad (2.138)$$

$$\mathbf{t}(E, V) = 2 \Gamma_L^{\frac{1}{2}} \mathbf{G}_{CC}^r \Gamma_R^{\frac{1}{2}} \quad (2.139)$$

$T(E, V)$  is the energy- and voltage-dependent total transmission probability of the system and  $\mathbf{t}(E, V)$  its transmission matrix. To use  $\Gamma^{\frac{1}{2}}$  is possible, because  $\Gamma$  is positive definite.

In the linear regime and for zero temperature the standard Landauer formula is recovered

$$G = \frac{2e^2}{h} \text{Tr} \{ \mathbf{t}^\dagger(E_F, 0) \mathbf{t}(E_F, 0) \} \quad (2.140)$$

$$= \frac{2e^2}{h} \sum_{i=1}^N \tau_i \quad (2.141)$$

with  $\tau_i$  the eigenvalues of  $\mathbf{t}^\dagger \mathbf{t}$ . In principle, the number of channels  $N$  is the dimension of the matrix  $\mathbf{t}^\dagger \mathbf{t}$ , but as this is a somewhat arbitrary size (one could make the wire a bit longer or shorter while the current should be the same), it should be clear, that this is only the upper bound. Actually, the (real) number of channels with non-vanishing transmission<sup>10</sup> is determined by the narrowest part of the wire.

In the end, one has to calculate the Green's functions of the central region  $\mathbf{G}_{CC}$  and the self-energies due to the corresponding leads  $\Sigma_{L,R}$ . The first one results in

$$\mathbf{G}_{CC}^a = (\mathbf{G}_{CC}^r)^\dagger = [(E - i0^+) \mathbb{1} - \mathbf{H}_{CC} - \Sigma_L^a - \Sigma_R^a]^{-1} \quad (2.142)$$

and the second one needs through equation (2.134) the knowledge of the uncoupled (ideal and semi-infinite) leads  $\mathbf{g}_{XX}$ . The leads are usually described as ideal, material dependent surfaces and computed using special recursive techniques (e.g. the decimation technique of section 2.4.4).

### 2.2.8. Nonorthogonal basis sets

Going from an orthogonal basis set to a nonorthogonal one, as is regularly used in molecular electronics because of better transferability, one has to introduce the overlap matrix  $\mathbf{S}$  with  $S_{ij} = \langle i | j \rangle$ . In the orthogonal case one gets the identity matrix

$$S_{ij} = \langle i | j \rangle = \delta_{ij} \quad (2.143)$$

$$\mathbf{S} = \mathbb{1} \quad (2.144)$$

For the nonorthogonal case where  $\mathbf{S} \neq \mathbb{1}$  one has to generalize the eigenstate equation  $\mathbf{H} - E\mathbb{1} = \mathbf{0}$  to  $\mathbf{H}_N - E\mathbf{S} = \mathbf{0}$  where the index  $N$  denotes the nonorthogonal basis set. Rewriting this equation a bit, the same expression as before can be regained

$$\mathbf{H}_N - E\mathbf{S} = \mathbf{H}'_N - E\mathbb{1} \quad (2.145)$$

$$\mathbf{H}'_N = \mathbf{H}_N - E(\mathbf{S} - \mathbb{1}) \quad (2.146)$$

That means, the on-site energies remain unchanged while the hopping matrix elements get an energy dependent modification

$$h'_{ij} = h_{ij} - ES_{ij} \quad (2.147)$$

---

<sup>10</sup>Larger than a certain threshold  $\varepsilon$ .

The Green's functions have to be transformed equivalently

$$\mathbf{G}_{CC,N}^{r,a} = [(E \pm i0^+) \mathbf{S}_{CC} - \mathbf{H}_{CC,N} - \Sigma_{L,N}^{r,a} - \Sigma_{R,N}^{r,a}]^{-1} \quad (2.148)$$

$$\mathbf{t}'_{XC} = \mathbf{t}_{XC} - E \mathbf{S}_{XC,N} \quad , \quad X = L, R \quad (2.149)$$

In practice, one often uses the so-called Löwdin transformation to transform an operator  $O$  from an orthogonal to a nonorthogonal basis set

$$\mathbf{O}_N = \mathbf{S}^{\frac{1}{2}} \mathbf{O} \mathbf{S}^{\frac{1}{2}} \quad (2.150)$$

## 2.3. Tight-binding approach

The following section is based on Chapter 9 of [4].

To be able to calculate the Green's functions of atomic systems, one needs a way to describe its Hamiltonian. In our work, the so called NRL<sup>11</sup> tight-binding method developed by Cohen, Mehl and Papaconstantopoulos [158] was used<sup>12</sup>. This is a non-orthogonal tight-binding scheme which is more transferable than orthogonal ones and uses the Slater-Koster two-center approximation.

### 2.3.1. General derivation

The tight-binding method is closely related to the LCAO (linear combination of atomic orbitals) method. Assuming that the localized orbitals  $\phi_{i\alpha}(\mathbf{r}) = \phi_{\alpha}(\mathbf{r} - \mathbf{R}_i)$  are centered around the positions  $\mathbf{R}_i$  of the atom  $i$ , the Hamiltonian  $\mathbf{H}$  of the system reads

$$\mathbf{H} = \sum_{ij,\alpha\beta} H_{i\alpha,j\beta} \mathbf{c}_{i\alpha}^{\dagger} \mathbf{c}_{j\beta} \quad (2.151)$$

$$H_{i\alpha,j\beta} = \int d\mathbf{r} \phi_{\alpha}^*(\mathbf{r} - \mathbf{R}_i) \left[ -\frac{\hbar^2}{2m} \nabla^2 + V(\mathbf{r}) \right] \phi_{\beta}(\mathbf{r} - \mathbf{R}_j) \quad (2.152)$$

where the potential  $V(\mathbf{r})$  describes the Coulomb interaction between the electrons and the ions. This choice of the matrix elements  $H_{i\alpha,j\beta}$  neglects the many-body interactions like the electron-electron interaction.

The integrals are usually not solved directly, but given as parameters which were calculated approximately or fitted to experimental data or other theories. The approach on how to get these parameters is the main difference between different tight-binding methods.

In a finite system the Hamiltonian can be diagonalized by rewriting the wave function

$$\Phi_{i\alpha} = \sum_{j\beta} c_{i\alpha,j\beta} \phi_{j\beta}(\mathbf{r}) \quad (2.153)$$

<sup>11</sup>Naval Research Laboratory, <http://www.nrl.navy.mil/mstd/branches/6390/computational-methods>

<sup>12</sup>Unfortunately the parameters can not be found on the nrl homepage any longer.

which leads to a set of equations for the coefficients  $c_{i\alpha,j\beta}$  with energy  $E$  and overlap matrix elements  $S_{i\alpha,j\beta}$

$$0 = \sum_{j\beta} [H_{i\alpha,j\beta} - ES_{i\alpha,j\beta}] c_{i\alpha,j\beta} \quad (2.154)$$

$$S_{i\alpha,j\beta} = \int d\mathbf{r} \phi_{\alpha}^*(\mathbf{r} - \mathbf{R}_i) \phi_{\beta}(\mathbf{r} - \mathbf{R}_j) \quad (2.155)$$

The problem has non-trivial solutions if the determinant  $\det(\mathbf{H} - E\mathbf{S}) = 0$ . The roots of this equation are the eigenenergies and the corresponding eigenfunctions are the wavefunctions of the finite system.

The atomic-like functions can be written as a product of a radial function and spherical harmonics

$$\phi_{nlm}(\mathbf{r}) = \phi_{nl}(|\mathbf{r}|) \cdot Y_{lm}(\mathbf{r}/r) \quad (2.156)$$

$$S^+ = (Y_{lm} + Y_{lm}^*)/\sqrt{2} \quad (2.157)$$

$$S^- = (Y_{lm} - Y_{lm}^*)/(i\sqrt{2}) \quad (2.158)$$

The  $S^{\pm}$  were defined to have real angular functions. The index  $n$  labels different functions with the same angular momentum  $l$  ( $s, p, d, \dots$ ).  $m = 0, \pm 1, \pm 2, \dots, \pm l$  ( $\sigma, \pi, \delta, \dots$ ) denotes the quantum number of the z-component of the orbital angular momentum. The (real) orbitals are labeled as

$$s \quad (l = 0, m = 0) \quad (2.159)$$

$$p_z \quad (l = 1, m = 0) \quad (2.160)$$

$$p_x/p_y \quad (l = 1, m = \pm 1) \quad (2.161)$$

$$d_{3z^2-r^2} \quad (l = 2, m = 0) \quad (2.162)$$

$$d_{yz}/d_{xz} \quad (l = 2, m = \pm 1) \quad (2.163)$$

$$d_{xy}/d_{x^2-y^2} \quad (l = 2, m = \pm 2) \quad (2.164)$$

### 2.3.2. Slater-Koster approximation

In the integral equations (2.152) and (2.155) for  $H_{i\alpha,j\beta}$  and  $S_{i\alpha,j\beta}$  appear one-, two- and three-center integrals, depending on the positions of the orbitals  $\alpha$  and  $\beta$  and the ion. For the overlap and the kinetic part of equation (2.152) only the positions of the two orbitals ( $i\alpha, j\beta$ ) are relevant. They can have one center (orbitals are on the same atom; on-site elements) or two centers (orbitals are on different atoms). In addition, the potential part of equation (2.152) also includes the position of an ion-potential which can be the same as the one of one or both of the orbitals (the ion of one of the orbitals: one- or two-center integrals), or somewhere else (three-center integrals).

The two center matrix elements  $K_{lm,l'm'}$  of the states  $lm$  and  $l'm'$  is diagonal in  $m$  if the z-axis is chosen to lie in the line connecting the two centers  $K_{lm,l'm'} = K_{l'm} \delta_{m,m'}$ . With  $s, p$

and  $d$  orbitals, there are 10 irreducible  $K_{l'm}$  (SK-) parameters. If the quantization axis is fixed in space, the functions have to be transformed to use the SK-parameters. Each function can be expressed as linear combination of SK-parameters. Now, using only the two-center form fitted to other data (experimental or other theoretical ones), all matrix elements have the same symmetry as in free space.

### 2.3.3. NRL tight-binding method

The question at this stage is how the parameters should be chosen to get results for total energies, energy bands and geometrical structures as good as possible and at the same time transferable. The problem is that effects of the three-center terms, which have to be somehow integrated into the two-center matrix elements, are structure sensitive. The NRL approach uses the density-functional-theory ansatz for the total energy

$$E = \int \frac{d^3\mathbf{k}}{(2\pi)^3} \sum_n \varepsilon_n(\mathbf{k}) + F[n(\mathbf{r})] \quad (2.165)$$

and shifts the potential in such a way, that the density dependent functional  $F[n(\mathbf{r})]$  becomes constant

$$V_0 = F[n(\mathbf{r})]/N_e \quad (2.166)$$

$$E = \int \frac{d^3\mathbf{k}}{(2\pi)^3} \sum_n \varepsilon_n(\mathbf{k}) + N_e V_0 \quad (2.167)$$

$$= \int \frac{d^3\mathbf{k}}{(2\pi)^3} \sum_n (\varepsilon_n(\mathbf{k}) + V_0) \quad (2.168)$$

$$= \int \frac{d^3\mathbf{k}}{(2\pi)^3} \sum_n \varepsilon'_n(\mathbf{k}) \quad (2.169)$$

For a set of eigenvalues  $\varepsilon(\mathbf{k})$  and total energies  $E$  for different crystal structures and volumes one determines  $V_0$  and with that the shifted eigenvalues  $\varepsilon'(\mathbf{k})$ . Now one has to find a set of parameters for the Hamiltonians which reproduce the energies and eigenvalues of the different structures.

The TB-parameters are constructed as follows:

The density of atom  $i$  is constructed as

$$\rho_i = \sum_j e^{-\lambda^2 R_{ij}} F(R_{ij}) \quad (2.170)$$

$$F(R_{ij}) = \Theta(R_c - R_{ij}) \cdot [1 + e^{(R_{ij} - R_c)/L + 5}]^{-1} \quad (2.171)$$

where the sum over atoms  $j$  runs within a cut-off distance  $R_c$  around the position of atom  $i$ , weighted with the cut-off function  $F(R_{ij})$  with the length-scale  $L$ .  $R_{ij}$  is the distance between the atoms  $i$  and  $j$ . While  $L$  and  $R_c$  are given,  $\lambda$  is the first fitting parameter. The angular-momentum ( $l$ ) dependent on-site terms are fitted by

$$h_{il} = a_l + b_l \rho_i^{\frac{2}{3}} + c_l \rho_i^{\frac{4}{3}} + d_l \rho_i^2 \quad (2.172)$$



The  $a_l$ ,  $b_l$ ,  $c_l$  and  $d_l$  with  $l = 0, 1, 2$  ( $s, p, d$ ) are 12 fitting parameters. With 10 independent (SK) parameters  $H_{ll'm}$  ( $m = \sigma, \pi, \delta$ )<sup>13</sup> all two-center hopping integrals can be constructed. These parameters are constructed as polynomial times exponential decay times cut-off function

$$H_{ll'm}(R_{ij}) = [e_{ll'm} + f_{ll'm}R_{ij} + g_{ll'm}R_{ij}^2] \cdot e^{-h_{ll'm}^2 R_{ij}} \cdot F(R_{ij}) \quad (2.173)$$

$$S_{ll'm}(R_{ij}) = [p_{ll'm} + q_{ll'm}R_{ij} + r_{ll'm}R_{ij}^2] \cdot e^{-s_{ll'm}^2 R_{ij}} \cdot F(R_{ij}) \quad (2.174)$$

$S_{ll'm}$  are a set of SK overlap functions for the non-orthogonal tight-binding which have the same structure as the hopping parameters.

$H_{ll'm}$  and  $S_{ll'm}$  include 80 fitting parameters ( $e, f, g, h, p, q, r, s$ ).

In total, there are 93 fitting parameters to reproduce the database of energies and eigenvalues mentioned above.

## 2.4. Electronic transport properties

Up to now it was shown how to calculate the conductance of an (atomic) system. But with this method, one has access to more transport properties, such as shot noise, Fano factor, thermopower and the electronic contribution to the thermal transport. These properties are sometimes easier to measure in experiments than the channel distributions or energy dependent transmissions they are derived from in theory.

In the following, these three properties will be introduced shortly. It is meant as a summary of the Chapters 4.7, 4.8 and 19 of [4].

### 2.4.1. Shot noise and Fano factor

In conductors, eliminating all sources of spurious noise, there remain two types of noise measured as temporal fluctuations  $P$  of the electrical current, namely the thermal noise and the shot noise. The thermal noise is due to the thermal motion of the electrons and is also known as Johnson-Nyquist noise. Within a broad frequency range ( $\hbar\omega \ll k_B T$ ) it has a white power spectrum (frequency independent) and is directly proportional to temperature  $T$  and conductance  $G$  ( $V = 0$ ,  $T \neq 0$ )

$$P_{thermal} = 4k_B T G \quad (2.175)$$

The shot noise, in contrast, has its origin in quantum mechanics. Electrons have a finite probability for being transmitted or reflected within the sample in the non-equilibrium situation (finite current). This noise is highest if the transmission of the electron is most uncertain. That is achieved at half open channels ( $\tau_i = 0.5$ ). If a channel is more or less open as one half, it contributes less to the total shot noise. Fully open or closed channels ( $\tau_i = 0$  or  $1$ ) have no uncertainty and thus do not contribute to shot noise. For very low temperatures, the shot noise power reads

$$P_{shot-noise} = 2eVG_0 \sum_n \tau_n (1 - \tau_n) \quad (2.176)$$

<sup>13</sup>10 independent combinations of  $l, l'$  and  $m$ :  $ss\sigma, sp\sigma, pp\sigma, pp\pi, sd\sigma, pd\sigma, pd\pi, dd\sigma, dd\pi, dd\delta$ .

In the following  $\sum_n \tau_n(1 - \tau_n)$  will be referenced as shot noise<sup>14</sup>.

Shot noise is maximal if the electrons are transmitted randomly and therefore follow the Poisson statistics

$$P_{Poisson} = 2eI = 2eVG_0 \sum_n \tau_n \quad (2.177)$$

The factor  $\tau_n(1 - \tau_n)$  represents the suppression of the noise due to correlation effects (Pauli principle) which reduce uncertainty. That also means that shot noise is a measure of correlation effects in the system and together with the total transmission, the experimental results of shot noise also provide information for conclusions on the transmission coefficients [82].

The total (temperature and voltage dependent) noise is a combination of thermal and shot noise<sup>15</sup>

$$P(T, V) = G_0 \left[ 2k_B T \sum_n \tau_n^2 + eV \coth \left( \frac{eV}{2k_B T} \right) \sum_n \tau_n(1 - \tau_n) \right] \quad (2.178)$$

Normalizing the shot noise by the poissonian (classical, uncorrelated) noise, gives at zero temperature

$$F = \frac{P_{shot-noise}}{P_{Poisson}} = \frac{\sum_n \tau_n(1 - \tau_n)}{\sum_n \tau_n} \quad (2.179)$$

This normalized version is called Fano factor.

## 2.4.2. Thermopower

The thermopower (or Seebeck coefficient)  $S$  is a more complicated matter. It is in general a measure of the magnitude and sign of a thermoelectric voltage induced by a temperature difference along the system. In that way it is defined for small temperature differences  $\Delta T$  as

$$S \approx -\frac{\Delta V}{\Delta T} \quad (2.180)$$

where  $\mu$  is the chemical potential and  $\Delta V$  the (measured) thermoelectric voltage. Here the usual system geometry is assumed, where the central system is coupled to two leads, one at each end. Then the temperature gradient is achieved by heating or cooling one lead while keeping the other one at a constant temperature.

As for shot noise, there are two contributions to thermopower: phonons (lattice vibrations) and an electronic part. The phonons transport heat from the hot to the cold part of the system (lead/reservoir) but also interact with the electronic part of the system. Because phonons contribute not directly to the thermopower but by dragging electrons along, the phononic contribution is called phonon drag. For point contacts it is believed to be very small and is therefore neglected.

<sup>14</sup>If one wants to compare it with experiments, one has to introduce units.

<sup>15</sup> $\coth(x) \approx \frac{1}{x}$

The electronic contribution (without inelastic scattering) to the thermopower can be written as

$$S = -\frac{1}{eT} \frac{\int_{-\infty}^{\infty} (E - \mu) \tau(E) \frac{\partial f(E, T)}{\partial E} dE}{\int_{-\infty}^{\infty} \tau(E) \frac{\partial f(E, T)}{\partial E} dE} \quad (2.181)$$

$$\approx -\frac{\pi^2 k_B^2 T}{3e} \frac{\tau'(E_F)}{\tau(E_F)} \quad (2.182)$$

with the zero-bias transmission function  $\tau(E)$  ( $G = G_0 \tau(E_F) = G_0 \sum_n \tau_n(E_F)$ ). Here  $f(E, T) = [\exp\{(E - \mu)/k_B T\} + 1]^{-1}$  is the Fermi function with chemical potential  $\mu \approx E_F$ . For zero temperature it achieves a delta function around the Fermi energy  $E_F$ . In this sense, equation (2.182) is the leading term of the Sommerfeld expansion of the thermopower for low temperatures.

At this point it is useful to introduce the coefficients  $K_n$  with

$$K_n = \int_{-\infty}^{\infty} (E - \mu)^n \tau(E) \left(-\frac{\partial f(E, T)}{\partial E}\right) dE \quad (2.183)$$

With these coefficients one can express the conductance  $G$  and the thermopower  $S$  as

$$G = \frac{2e^2}{h} K_0 \quad \text{and} \quad S = -\frac{K_1}{eTK_0} \quad (2.184)$$

In (bulk) wires the transport mechanism is fully incoherent and relevant is the energy dependence of the (macroscopic) conductivity. As both electrons and holes contribute to the thermopower voltage but partially cancel each other, an electron-hole asymmetry is needed to gain a finite  $S$  and the sign of  $S$  can be used to determine which charge carriers dominate the electrical transport.

In contrast, for atomic contacts the transport mechanism is expected to be coherent and relevant is the energy dependence of the transmission  $\tau(E)$ . But assuming a two dimensional electron gas (2DEG) with a restrictive potential perpendicular to the current direction one gets, depending on the potential, a stepwise or quasi stepwise<sup>16</sup>  $\tau(E)$  where the slope is always  $\geq 0$ . The result is a thermopower which is always  $\leq 0$ . But this simple picture is incomplete, ignoring completely the influence of the orbital structure of the electronic system, different for each metal. This again leads to a material specific sign, amplitude and spread of  $S$  where again the electron-hole asymmetry is important to gain a finite value.<sup>17</sup>

<sup>16</sup>Like the Fermi function at zero or higher temperature.

<sup>17</sup>That the thermopower can have different signs for different materials and within the spread of one material (different geometric configurations) was experimentally found for example in [16].

### 2.4.3. Electron thermal conductance

Another important transport property that can be calculated within this approach is the electronic contribution to the thermal conductance  $\kappa_{el}$ . It describes how much thermal energy per unit of time and cross-section area flows induced by a temperature gradient

$$\kappa_{el} = -\frac{Q}{\Delta T} \quad (2.185)$$

Via  $K$  from above (equation 2.183) it can be written as

$$\kappa_{el} = \frac{2}{hT} \left( K_2 - \frac{K_1^2}{K_0} \right) \quad (2.186)$$

$$\approx L_0 T G \quad (2.187)$$

with the Lorentz number  $L_0 = (k_B/e)^2 \pi^2/3$ . The last term is again the Sommerfeld expansion for the integrals in  $K_n$  to lowest order in  $k_B T/\mu$ , valid for smooth functions  $\tau(E)$ . The approximation is known as Wiedemann-Franz relation and describes the relation between thermal and electrical conductance.

### 2.4.4. Decimation technique for the leads

As one wants to calculate the transmission from one lead to another through the interesting central part, at some point at the beginning of the calculations one has to calculate the (unperturbed) Green's functions of the (semi-infinite, ideal) leads.

In the following the decimation technique of Guinea et al. [159] will be shortly described as the technique of choice. It is well described in the appendix D.2 of [11] and we will use the notation from there (which is consistent with what was used up to now).

In general, one has to solve the equation for the Green's function

$$[(E + i\eta)\mathbf{S} - \mathbf{H}] \mathbf{G}^r = \mathbb{1} \quad (2.188)$$

The leads are then described by (super) layers parallel to the surface

$$\begin{aligned} & [(E + i\eta)\mathbf{S}_{m,m} - \mathbf{H}_{m,m}] \mathbf{G}_{m,l}^r \\ & + \sum_{n \neq m} [(E + i\eta)\mathbf{S}_{m,n} - \mathbf{H}_{m,n}] \mathbf{G}_{n,l}^r = \delta_{m,l} \end{aligned} \quad (2.189)$$

where  $m, l$  are the layer index with  $m, l \in \{0, n_l\}$  where  $n_l$  is the last layer considered (the layer  $n_{l+1}$  is not coupled to the surface layer 0 any more). A super layer may contain more than one layer, depending on the structure and the order of interaction considered. This will be neglect here for simplicity.

Using translational symmetry, equation (2.189) can be written as

$$\mathbf{W}\mathbf{G}_0^r + \tau_1 \mathbf{G}_1^r = \mathbb{1} \quad (2.190)$$

$$\tau_2 \mathbf{G}_{m-1}^r + \mathbf{W}\mathbf{G}_m^r + \tau_1 \mathbf{G}_{m+1}^r = 0 \quad (2.191)$$

where  $\mathbf{W}$ ,  $\tau_1$  and  $\tau_2$  are the coupling matrices containing the  $(E + \eta)\mathbf{S} - \mathbf{H}$  terms.

In the decimation technique, one first eliminates all Green's functions with odd layer numbers ( $\mathbf{G}_1^r, \mathbf{G}_3^r, \mathbf{G}_5^r, \dots$ ). Next, every second Green's function with even layer number ( $\mathbf{G}_2^r, \mathbf{G}_6^r, \mathbf{G}_{10}^r, \dots$ ) is eliminated. Equations (2.190) and (2.191) can be formally regained for the  $n$ 'th step by using

$$\mathbf{W}_s^{(n)} = \mathbf{W}_s^{(n-1)} - \tau_1^{(n-1)} \left( \mathbf{W}_b^{(n-1)} \right)^{-1} \tau_2^{(n-1)} \quad (2.192)$$

$$\mathbf{W}_b^{(n)} = \mathbf{W}_b^{(n-1)} - \tau_1^{(n-1)} \left( \mathbf{W}_b^{(n-1)} \right)^{-1} \tau_2^{(n-1)} - \tau_2^{(n-1)} \left( \mathbf{W}_b^{(n-1)} \right)^{-1} \tau_1^{(n-1)} \quad (2.193)$$

$$\tau_1^{(n)} = -\tau_1^{(n-1)} \left( \mathbf{W}_b^{(n-1)} \right)^{-1} \tau_1^{(n-1)} \quad (2.194)$$

$$\tau_2^{(n)} = -\tau_2^{(n-1)} \left( \mathbf{W}_b^{(n-1)} \right)^{-1} \tau_2^{(n-1)} \quad (2.195)$$

$\mathbf{W}_s$  is now the effective matrix of  $[(E + \eta)\mathbf{S} - \mathbf{H}]$  for the first renormalized (surface) layer (equation (2.190)) while  $\mathbf{W}_b$  is the equivalent for the other layers (bulk,  $n=1: 4, 8, \dots$ )<sup>18</sup>. The new  $\tau$ 's measure the effective interactions between the renormalized layers ( $n=1$ : between layer 0 and 4, 4 and 8,  $\dots$ )<sup>19</sup>.

This procedure can now be repeated until the effective interactions of the renormalized surface layer 0 ( $\tau_1^{(\nu)}$ ) with the first remaining renormalized bulk layer  $2^\nu$  ( $\tau_2^{(\nu)}$ ) can be neglected, or the  $W$ 's are converged in the sense that the difference between  $\mathbf{W}_{s/b}^{(\nu-1)}$  and  $\mathbf{W}_{s/b}^{(\nu)}$  is negligible.

After the convergence of  $\mathbf{W}_s$  and  $\mathbf{W}_b$  is achieved, one can write equations (2.190) and (2.191) as

$$\mathbf{W}^{(\nu)} \mathbf{G}_0^r = \mathbb{1} \quad (2.196)$$

$$\mathbf{W}^{(\nu)} \mathbf{G}_{2^\nu}^r = \mathbb{0} \quad (2.197)$$

and the resulting Green's functions for surface and bulk are

$$\mathbf{G}_s^r = \left( \mathbf{W}_s^{(\nu)} \right)^{-1} \quad (2.198)$$

$$\mathbf{G}_b^r = \left( \mathbf{W}_b^{(\nu)} \right)^{-1} \quad (2.199)$$

The correctness of equation (2.199) can be seen if one repeats the formalism with a layer sufficiently deep in the bulk.

In principle this has to be done for both leads, but if the leads are identical, one can use the results of one lead for both.

<sup>18</sup>for  $n=2$  it would be: 8, 16,  $\dots$

<sup>19</sup>for  $n=2$ : between 0 and 8, 8 and 16,  $\dots$



### 3. Code optimization

The tight-binding code to calculate the transport through a wire goes back to different codes from Carlos Cuevas and Fabian Pauly. One of them was used in the work of Markus Dreher [12]. Within this work, the programs have been merged and optimized in the context of sparse matrices (reduction of RAM usage of 80% and more, depending on the size of the wire) and parallelized within the framework of openmp (shared memory  $\rightarrow$  up to one node) and mpi (distributed memory  $\rightarrow$  multi-node calculations). Furthermore the input was optimized for better readability and comparability with the program code LAMMPS which was used for the MD-simulations.

For the memory optimization the non-zero entries of the most sparse matrices (mainly the Hamilton and Overlap matrix) are saved in a small matrix together with their index-pointer instead of the linear ordering with all zeros<sup>1</sup>.

The openmp parallelization was realized partly by parallelizing independent loops but mostly indirect by using MKL-routines for the matrix operations which are openmp parallelized. The loops are mainly MPI parallelized which partly needs the Scalapack package instead of the lapack package for the matrix operations. Using the MKL versions of it enables both parallelization methods in parallel even within the matrix operations which need most of the computer time (see section A.2 in the appendix). The calculation of the energy dependent transmission is parallelized in two ways, each loop individually and by loops (one has to choose which one should be used). The first one would be perfect but the current implementation is not very efficient<sup>2</sup> so the second one is the default. This has the disadvantage that the scalability of the code ends with the number of mpi processes equal to the number of energy points which are calculated.

The program interface in the form of a parameter file which includes all necessary parameters for the current run has been optimized in the form that most options have a default value and all possible options are addressed via option-names. All options not known and anything after '#' are ignored. An example of such a parameter file with explanations of the options is given in the appendix (A.2).

The real time needed to calculate the transport of one point with a wire of 1125 atoms in the central part<sup>3</sup>, beginning with the creation of the Green's functions of the walls till the writing of the data, is shown in Fig. 3.1 as function of the number of used nodes<sup>4</sup>. The speedup is the time needed to calculate the test case with a low number processes (cores or nodes) (here two nodes) divided by the time needed to calculate it with a higher number of

---

<sup>1</sup>Usually the matrix entries are stored in a linear manner, one row after the other. That way the position of an entry (index-pointer) is defined by the position within that line of numbers and the shape of the matrix.

<sup>2</sup>Because of a bug of the used hybrid parallelized lapack routine, a workaround has to be made which ruins the efficiency.

<sup>3</sup>See sec. 4.3.

<sup>4</sup>The nodes had 24 cores each which were used within the openmp (shared memory) environment.

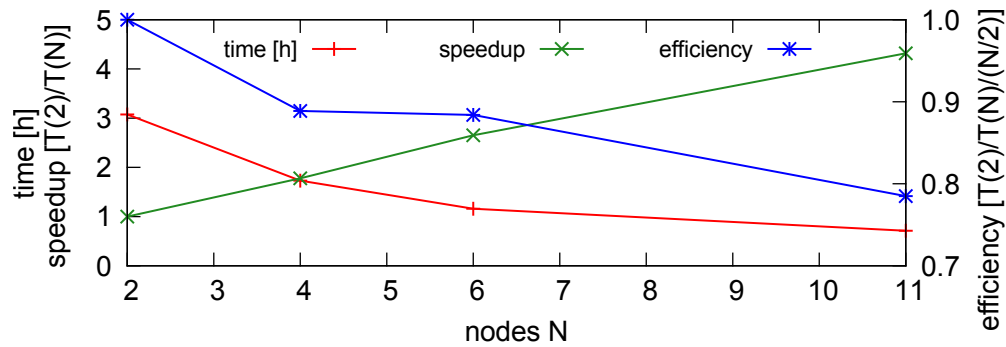


Figure 3.1.: Scaling of the TB transport code for the calculation of one point of a wire with 1125 atoms in the central part.

processes<sup>5</sup>. Ideally it grows with the same factor as the number of processes. In this case the parallelization would not lead to overhead due to additional communications between the cores and no timeouts of cores due to asynchronous distributions of calculations<sup>6</sup>. The efficiency normalizes the speedup with the number of cores to get a process independent number. Ideally it should be one. An efficiency of almost 0.8 with 11 nodes is still a very good one. Smaller systems do not parallelize that far that good.

<sup>5</sup>An alternative to the strong scaling shown here would be the weak scaling where the system size per process is kept fix. This makes sense for problems which scale strictly linear with system size.

<sup>6</sup>CPU load.



# 4. Model

## 4.1. Experiments

There are different ways to get experimental access to few atom contacts. One of these is the so called 'mechanically controllible break junction' (MCBJ) [39]. Fig. 4.1 shows a sketch of the working principle: A nanobridge is suspended on a flexible substrate which gets bent in a three-point bending mechanism (here the central point is fixed while the two arrows on the sides bend the substrate downwards). By this, the nanobridge gets elongated and thinned down until it breaks.

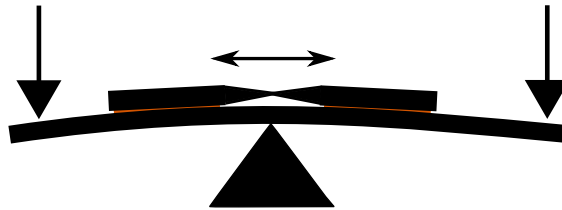


Figure 4.1.: Sketch of the working principle of the MCBJ technique.

To some extent, MCBJs were used in all experiments of our cooperation partners. An alternative method would be to use electromigration where one uses the force of the electric current to move the atoms [51]. This was used in the group of Elke Scheer to establish a bistable switch after preparing the samples with an MCBJ technique. One can also use scanning electron microscopes (STM), atomic force microscopes (AFM) or a combination of them to create (metal) atomic contacts by bringing the tip of the microscope in contact with or even press it into the sample and measure current (with STM) and force (AFM). With (high resolution) transmission electron microscopes (TEM) it is possible to image atomic contacts with atomic resolution. This can be done by putting an STM into a TEM or by using the incident energy of the TEM electrons to locally heat up the sample and burn holes in it. More information and further references for these techniques can be found in [4, Chapter 2].

### Fano factor

Different to the total noise power  $S_I$  which is the Fourier transform of the voltage fluctuations produced by the junction, shot noise as part of the total noise power and therefore the Fano factor  $F$  is experimentally not directly accessible. But following Kumar et al. [35] one can determine it with a set of measurements. Therefore they introduced a reduced noise

$$Y(V) = \frac{S(V) - S(0)}{S(0)} \quad (4.1)$$

and a parameter

$$X(V) = \frac{eV}{2k_B T} \coth \frac{eV}{2k_B T} \quad (4.2)$$

with which the total noise reduces to the linear relation

$$Y(V) = [X(V) - 1]F \quad (4.3)$$

The curve  $Y(X(V), V)$  can now be fitted onto a set of noise power measurements. This method was used in the group of Oren Tal [18].

## Channel distribution

There are currently at least two principal ways to determine the channel distribution  $\tau_i$  from experiments: Utilizing the nonlinear properties which appear when using superconducting leads and by fitting the channel distribution to the Fano factor and conductance values.

The first one uses that the multiple Andreev reflection in the superconducting state leads to nonlinearities in the I-V curves. They can be fitted which leads to a set of channels [39, 63, 160]. The precision of the transmission of each channel is about  $\pm 0.05$  (see SI of [14]). The procedure has the great disadvantage that one has to stay at very low temperatures and has to deal with superconducting leads. Having access to the Fano factor one can overcome this problem. The second method uses the relation between the Fano factor, conductance and channel distribution of a contact [82]

$$G = \sum_i \tau_i \quad (4.4)$$

$$F = \frac{\sum_i \tau_i (1 - \tau_i)}{G} \quad (4.5)$$

Depending on the problem the two parameters  $G$  and  $F$  are not sufficient to determine the channel distribution exactly but to give a range of possible values for each channel. The interpretation of the result for a transmission coefficient (channel) as mean value with standard deviation, which would be the usual interpretation if looking on statistical results as one does here, is not totally correct here because every value in the range is equally likely (the highest value in the resulting range has equal probability than every other point within the range). The resulting uncertainty is much larger than in the first method (see for example Fig. 3 of [82] or Fig. 6d of [18]).

## 4.2. Molecular dynamics simulations

The experimental techniques are so called top-down approaches, where one has something very big (a piece of wire) and makes it smaller to get to the right dimensions (nanobridge). In the theory on the other hand, one uses bottom-up approaches, where one builds up the wanted structure (nanobridge) from smaller units (atoms). This difference in the approaches causes problems fitting theory and experiments together. One problem is, that besides a tiny region around the few atom contact, the experimental wires have orders of magnitude

more atoms than the theory is able to handle. One consequence is discussed later to explain experimental findings not compatible with the theoretical findings at that stage (see sec. 5.2).

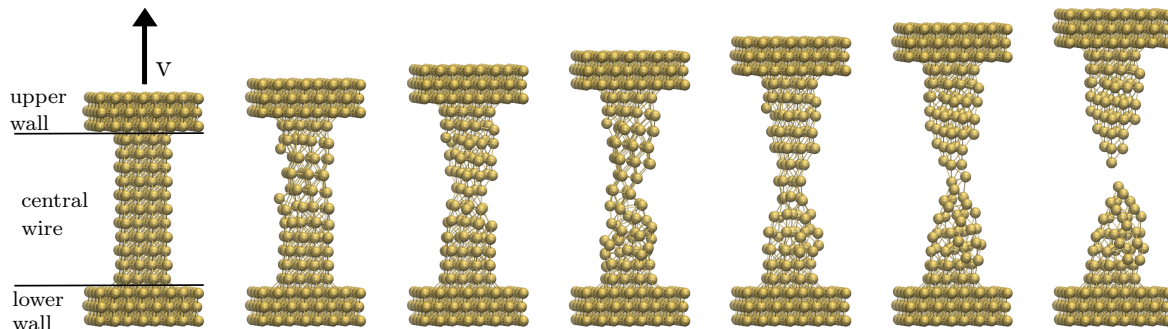


Figure 4.2.: Evolution of a simple Au wire during elongation. The upper wall is therefore pulled away with a constant velocity of  $0.4 \text{ m/s}$ . The frame rate is  $(0.5 \text{ ns})^{-1}$ .

In our approach we build a system separated into three parts, two walls and the central wire (Fig. 4.2). Every part is build up by atoms described by EAM-potentials in the MD-part (see sec. 2.1) and by Slater-Koster tight-binding parametrizations to describe the electronic structure in the calculation of the conductance (see sec. 2.2). The coordinates are those of an ideal lattice (fcc except for Fe which is bcc) with the corresponding lattice constants. In the MD-part, which is done with the open source code LAMMPS (Large-scale Atomic/Molecular Massively Parallel Simulator) [148, 161] the atoms in the walls are kept fixed (they do not move) and the upper wall is pulled away by a constant velocity of around  $1 \text{ m/s}$  (see Fig. 4.2)<sup>1</sup>. The velocity seems to be very high, but compared with the speed of sound in such systems, which is in the order of  $10^3 \text{ m/s}$ , it is still very slow. The initial velocities of the atoms in the central wire are chosen randomly with a Gaussian distribution to yield the wanted average temperature.

If it is not marked differently, a Nosé-Hoover thermostat keeps the average temperature constant to ensure an NVT-ensemble and a time-step of  $1 \text{ fs}$  ensures a stable calculation.

Before the elongation starts, a thermalisation has to be done<sup>2</sup>. It is required to relax possible stress at the surfaces due to the ideal lattice within the finite geometry<sup>3</sup>. During the elongation several snapshots of the atomic coordinates with a frequency typically between one in 10 and one in 100 ps are written out. Besides the coordinates of the atoms one has access to data like energies, pressures and forces and can calculate thermodynamic- or global-mean properties like temperature and the force needed to elongate the wire at the constant velocity.

An example input file for LAMMPS can be found in the appendix in section A.2.

<sup>1</sup>In most cases about  $0.4 \text{ m/s}$ .

<sup>2</sup>We found  $100 \text{ ps}$  to be sufficient.

<sup>3</sup>Although surface reconstruction does not play a role with the materials we looked at.

### 4.3. Conductance calculations

To calculate the nine by nine elements per atom in the Hamiltonian and overlap matrix<sup>4</sup> within the tight-binding ansatz, only the positions of the atoms and their relative orientations to each other are needed. Those coordinates are taken from the snapshots of the MD calculations.

The system is divided as in the MD part. The atoms in the walls are not taken explicitly as the ones of the central wire, but they are used to calculate a surface Green's-function to approximate the walls as semi-infinite (perfect) walls.

During the calculation the central wire is forced to be charge-neutral. It has to be done because the tight-binding parameters are designed for bulk, not for low-coordinated structures. We use a self consistent manner by alternately shifting the local potentials of the atoms (the so called 'on-site shift') and recalculating the densities until it is neutral up to a certain epsilon [162]<sup>5</sup>.

As results of the conductance calculations one gets the energy dependent channel transmissions  $\tau_{i,\sigma}(E)$ <sup>6</sup> and with that the total conductance

$$G(E) = \frac{e^2}{h} \sum_{\sigma} \text{Tr}\{\mathbf{t}_{\sigma}^{\dagger} \mathbf{t}_{\sigma}\} = \frac{e^2}{h} \sum_{i,\sigma} \tau_{i,\sigma}(E) = \frac{e^2}{h} \sum_{\sigma} \tau_{\sigma}(E) = \frac{e^2}{h} \tau(E) = \frac{G_0}{2} \tau(E) \quad (4.6)$$

with the quantum of conductance  $G_0 = \frac{2e^2}{h} = (12.9 \text{ k}\Omega)^{-1}$ , the total spin dependent transmission  $\tau_{\sigma}(E)$  and the total transmission  $\tau(E) = \sum_{\sigma} \tau_{\sigma}(E)$  for each snapshot.  $\mathbf{t}_{\sigma}$  is the transmission matrix of spin  $\sigma$ . For some materials (for example Au) the spin ( $\sigma$ ) dependence is omitted, leading to  $\tau_{\uparrow} = \tau_{\downarrow} = \frac{1}{2}\tau$ . In this situations  $\tau := \tau_{\sigma}$ , leading to  $G(E) = G_0\tau(E)$ .

The energy dependent density of states at the positions of atoms (the so called local DOS or LDOS) can also be calculated within the Green's-function formalism.

The channel transmissions  $\tau_{i,\sigma}$  are the input values for the post-processing, where one calculates the properties one is interested in, like the conductance histogram as simple histogram of the total conductance values at the Fermi energy  $G(E_f)$ , the mean channel distribution at the Fermi energy  $\langle \tau_{i,\sigma}(E_f) \rangle$ , the Fano factor as normalized noise of the channels at the Fermi energy

$$F = \frac{\sum_{i,\sigma} \tau_{i,\sigma}(E_f)(1 - \tau_{i,\sigma}(E_f))}{\sum_{i,\sigma} \tau_{i,\sigma}(E_f)}, \quad (4.7)$$

the thermopower

$$S = -\frac{K_1}{eTK_0} \quad (4.8)$$

with

$$K_n = \int_{-\infty}^{\infty} (E - \mu)^n \tau(E) \left( -\frac{\partial f(E, T)}{\partial E} \right) dE \quad (4.9)$$

<sup>4</sup>Double with spin.

<sup>5</sup>If the convergence is slow ( $\gtrsim 5$  iterations) then the charge neutrality loop is the most time consuming part of the calculation.

<sup>6</sup>Also called 'transmission coefficients' or 'transmission eigenvalues'.

and the (electron) thermal conductance

$$\kappa_{el} = \frac{2}{hT} \left( K_2 - \frac{K_1^2}{K_0} \right) \quad (4.10)$$

(see sec. 2.4.1 and 2.4.2). For  $S$  and  $\kappa_{el}$  one needs, differently to the rest, the energy dependent total transmission  $\tau_\sigma(E)$ , but not its decomposition into channels  $\tau_{i,(\sigma)}(E)$ .

Because of the window function one only needs a small (temperature dependent) energy range around the Fermi energy  $E_f$ <sup>7</sup>. In the calculations we restrict ourselves to 11 transmission points to approximate the energy dependency. As the Hamiltonian has to be inverted several times during the conductance calculations, where the Hamiltonian grows roughly with  $N^2$ , where  $N$  is the number of atoms in the central region, the conductance calculations take between one and two orders of magnitude more time than the MD calculations<sup>8</sup>.

An example parameter file for the calculations of the transport can be found in the appendix in section A.2.

## 4.4. Figures

If one does statistics one has to think about presenting a lot of data in a simple way. The three forms used in this thesis and in most publications are

- histograms: counting the number of events having a specific value (conductance) as function of that value. One has to weight resolution against statistics (higher resolution means less average statistics per value).
- scatter plots: plotting every data point or
- density plots: (discretized) scatter plots as 2-dimensional histograms, the height of each point is coded in color.

Density plots are discretized scatter plots with the advantage that overlapping data points do not lead to a loss of information. The histograms are projections of scatter plots (or density plots) onto the corresponding axis, losing information of one axis, but having a simpler overview of the remaining one, for example the projection of the conductance versus elongation density plot (Fig. 5.2) onto the conductance axis gives the conductance histogram (Fig. 5.4).

## 4.5. Simple Example: Ideal Au wire(s)

The simplest geometry one can think of is an ideal one-atomic wire between two walls as can be seen on top of figure 4.3 for the cases of three (first and second column) and eight atoms (last two columns) in the wire. But besides the length of the wire, the position of the wire in relation to the borders has to be chosen. In the following examples the stablest lattice position next to the  $\langle 100 \rangle$  surface of an Au fcc lattice was used.<sup>9</sup>

<sup>7</sup>The relevant window at 4 K is about 0.0005 Ryd and at 300 K about 0.0294 Ryd.

<sup>8</sup>With the MD-parameters we used.

<sup>9</sup>This means that the corresponding Au atom in the chain has 4 next neighbors in the wall against one in the chain which causes the stable point to be much closer to the wall than the lattice point we consider.

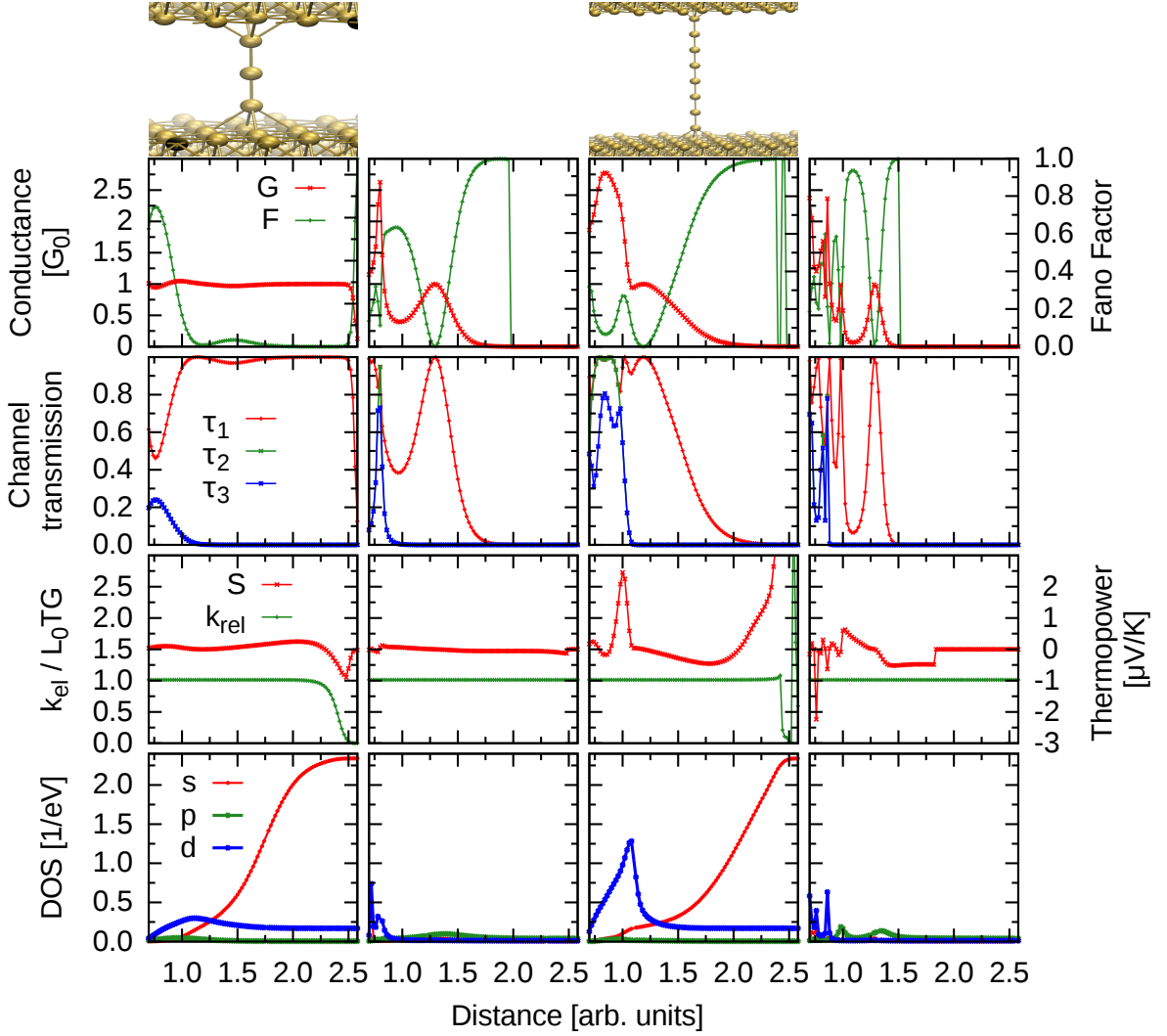


Figure 4.3.: Results for ideal wires with three atoms (first and second column) and eight atoms (third and fourth column) as function of the displacement between the atoms in the wires. 1.0 arb.units corresponds to a distance of about 0.245 nm. In column one and three the charge neutrality condition was used and it was disabled in the other two columns. The pictures on top of columns one and three show the corresponding wires with three and eight atoms. In row one the total conductance (red) and Fano factor (green), in row two the three contributing channels ( $\tau_2$  and  $\tau_3$  are degenerated), in row three  $\kappa_{rel}$ , the quotient of the thermal conductance  $\kappa_{el}$  and the Wiedemann-Franz relation (red) and the thermopower (green) and in row four the DOS of the central atom in the wire are plotted.

In figure 4.3 all physical properties relevant in this thesis are shown as overview. The properties were introduced in the theory section and will be discussed in more detail in the following sections. In the first and third column the charge neutrality condition was used while it was disabled for the calculations in columns two and four. This condition directly influences the density of states (DOS) which is shown for the central atom in row four and leads to less features of the transmission properties (conductance, channel distributions and Fano factor) as function of the displacement between the atoms in the wire. The drastically

increased value of the s-orbital leads, e.g., to an almost constant transmission value up to relative high distances compared to the results without the neutrality condition. In contrast to the s-orbital, the p-orbitals lose their influence due to the charge neutrality, which is the cause for the loss of features in the transmission properties of the wires. Due to the much higher number of atoms (and therefore orbitals), the features of the long wire without charge neutrality are much more pronounced than in the case of the short wire. What is more interesting is the behavior of the long wire with charge neutrality: The transmission for short distances is much enhanced compared to the short wire. This is due to the enhanced DOS in the d-orbitals which leads to an enhancement of the second and third channel.

Of course, the wires are only stable within a small range around 1.0 (about 0.245 nm).<sup>10</sup> The exact range depends on the number of atoms in the wire (the longer the less stable) and its temperature (the higher the less stable).

In a second example one can look what happens if there are two identical wires next to each other. Here, because of the topological properties of the walls, a continuous separation of the wires is not possible. But as it is only to demonstrate the effects qualitatively here, in Fig. 4.4 only stable positions of the individual wires were used. The points with index  $s$  are from a single wire for comparison.

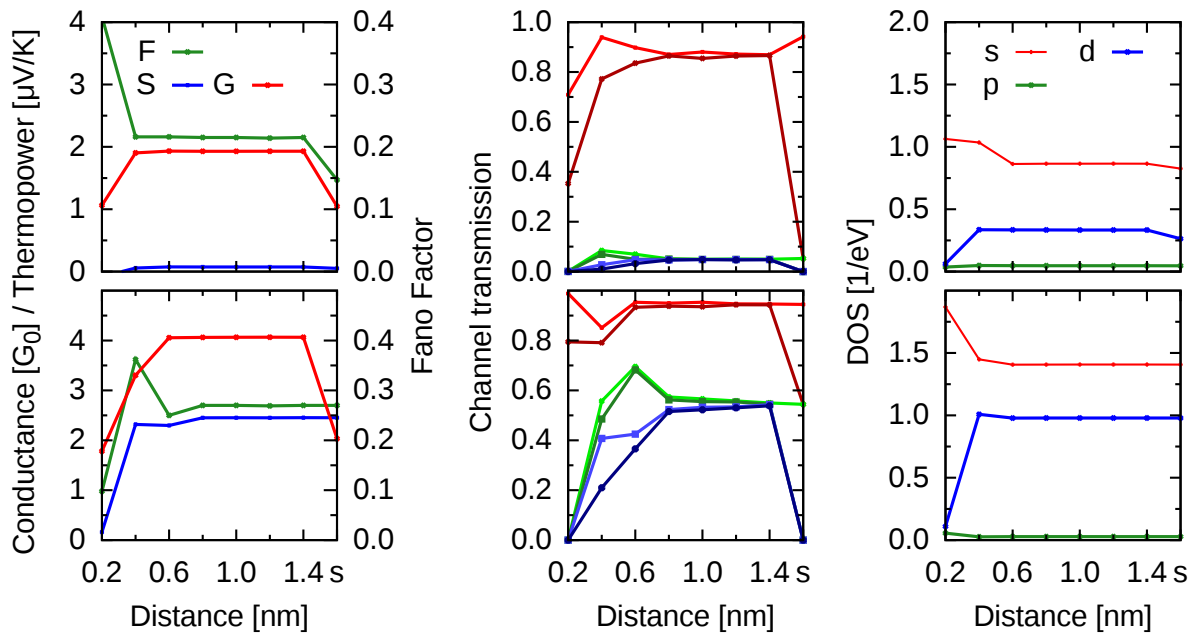


Figure 4.4.: Results of two parallel ideal wires with three atoms per wire (upper row) and eight atoms per wire (lower row) as function of their distance. The results for a single wire are included as reference (last point, x-tic position is marked by 's'). The distance of the atoms within one wire is 0.245 nm ( $\hat{=}$  1.0 arb.units in Fig. 4.3). The properties are like in Fig. 4.3, except for  $\kappa_{rel}$  which is not shown and equal to one for all points.

At short distances the total conductance is suppressed below the conductance of a single wire (left column of Fig. 4.4). But with increasing distance the conductance rises to the sum of two single wires. Not all properties regain the values of individual wires (which means the

<sup>10</sup>The distance was taken from an elongation process where a long single atom chain (7 atoms long) appeared.

same values as one individual wire) at the same distance as the conductance. The channel distribution and with it the Fano factor are slightly more sensitive and need more distance to show the values of individual wires where every channel of the individual wire is doubled. This is explained by a look at the DOS which shows that at low distances the DOS of the d-orbitals are suppressed while the DOS of the s-orbitals are slightly enhanced.

While this description is qualitatively true for both lengths of the wires, there are differences in the details. The short chains (upper row) are according to the conductance already almost separated at a distance of 0.4 nm, while it takes about 50 % longer (0.6 nm) for the long chains. A second point is more remarkable: The saturated Fano factor is not the same as the one of the single chain. Following this further one sees that the channels are not as open as in the single chain case while the DOS of the central atom is higher. The problem at this point is the charge neutrality condition which modifies the two cases differently<sup>11</sup>. Deactivating the charge neutrality condition leads to the assumed behavior (although different results, not shown).

This problem arises because of the tiny extent of the system (only 3 atoms per chain). The longer chain is more stable against such problems such that no visible effect can be seen (although 8 atoms are still very few).

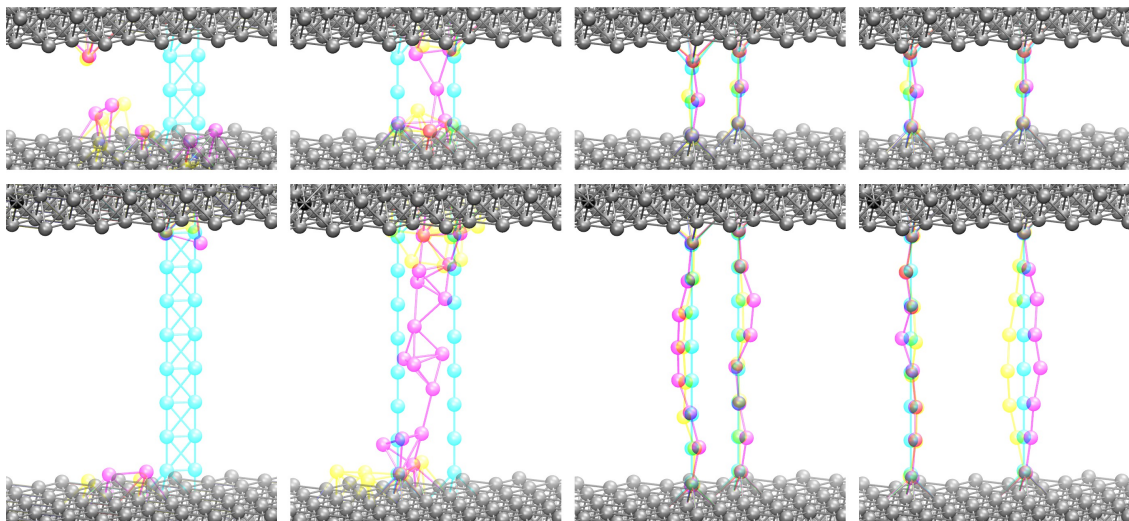


Figure 4.5.: The figures on top belong to the first four data points in the plots of Fig. 4.4, where the wires in the upper row have three and in the lower row eight atoms each. The figures include three time-steps evolved with MD encoded in colors (0, 5, and 10 ps).

The figures in 4.5 present not only the ideal wire configurations which were used to calculate the transmission values, but also a short time evolution in 5 ps time-steps encoded in different colors. The atoms of the walls do not move, so the colors add up to gray. The other atoms move to a certain degree, leading to partially overlapping or totally separated color-coded atoms.

Both studied wire-lengths, three and eight atoms, behave similar. Small separations of about

<sup>11</sup>This is no convergence problem.



0.2 nm generate high repulsive forces leading to an explosive behavior. The doubled separation is not explosive any more, but the configuration is not stable enough to prohibit the fusion of the two wires. The fused wire is still not stable and breaks in-between 5 and 10 ps. Displacing further to 0.6 nm is far enough to suppress the attractive (and repulsive) forces such that the individual wires stay stable<sup>12</sup>. This was also the point in the discussion of the conductance values where the mutual influence of the wires seemed to have almost vanished.

These examples show how experimentally accessible values like conductance and Fano factor can be supplied with insights from experimentally not accessible properties like DOS and channel distributions. The second example will also become important to explain observations from an experiment shown later.

In the following sections the results of larger and more realistic systems up to a few hundred of atoms in the wire and dozens of atoms in the cross section will be shown for different materials.

---

<sup>12</sup>For at least 10 ps.



# 5. Results for Au, Ag, Cu, Mg, Al and Pt at 4 K

In recent years a lot of work has been done to investigate the properties of atomic-size contacts, both in theory and experiments. Examples are studies of conductance quantization [39, 163], energy dissipation in atomic ballistic wires [83], electron–phonon interaction modifications to the shot noise [28, 35], flicker noise in metal junctions [29] and Joule heating in the electrodes [30]. Most of these works use statistical analysis methods like conductance histograms [31, 36, 37, 164] to average over the microscopic variability of junction configurations. Similar tools are density plots of for example the conductance as function of the elongation of the wire [56, 165, 166], current-voltage characteristics [167–169] and mechanical stiffness versus elongation [170]. Two dimensional cross-correlation methods also use entire ensembles to get more detailed information about motifs of junction formations [75, 112, 171]. They showed that transport properties such as the conductance [19, 172], shot noise [20–24], or thermopower [26, 39] are different from those known of macroscopic wires.

There have also been considerable efforts to go beyond the ensemble-averaged analysis methods. Using superconducting leads, the theory of multiple Andreev reflections allows the determination of the individual transmission channels [39, 64]. The channel transmissions are much more sensitive to the atomic configurations near the thinnest part of the wire than their sum [10, 39, 71]. It is also known for example that non-integer transmission coefficients are characteristic for multivalent metals [5, 10, 39, 64, 71].

The shot noise is directly coupled to the behavior of the channels and can therefore be used as tool to get for example information about ranges of transmission values [82].

At the same time, there have also been many advances from theoretical side. Particularly the combination of molecular dynamic simulations with quantum transport calculations enabled the possibility to establish a direct comparison of theoretical and experimental results [9, 68, 69, 74].

Despite the huge amount of work from experiments and theory not all questions could be answered yet. There are for example the well known higher conductance peaks of Au which could not be well reproduced in calculations or the appearance of an enhanced shot noise at about  $G_0/2$  in Au experiments which indicates the presence of multiple channels where only one should contribute to the conductance [15].

In this chapter the main results of this work for the not explicitly spin-polarized (nonmagnetic) materials<sup>1</sup> Au, Ag, Cu, Mg, Al and Pt at 4 K are presented and compared with experiments to answer some of the open questions. The six investigated elements will be grouped into noble (monovalent<sup>2</sup>) metals (Au, Ag and Cu) and the rest (Mg, Al and Pt)<sup>3</sup>.

---

<sup>1</sup>Spins are considered as degenerated and not explicitly taken into account.

<sup>2</sup>With an unpaired electron in the s-orbital of the outermost shell.

<sup>3</sup>Pt belongs to the transition metals.

In the following they will be referred to as spin independent materials.

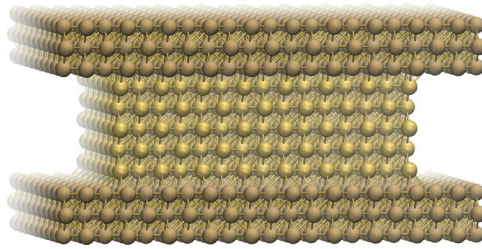


Figure 5.1.: Initial geometry of Au for the elongation calculations of the next sections. The walls were colored in a darker shade than the central wire.

The initial geometry of these systems are like the example in Fig. 5.1 of Au<sup>4</sup>. They all have an fcc lattice with the same initial geometry with 563 atoms in the central region, but different lattice parameters. The target temperature of the thermostat for the calculation of the geometries was set to 4 K and the wires were elongated with a speed of 0.4 m/s. Statistics is typically made out of 100 elongation curves.

The results for Cu presented in this section were partially<sup>5</sup> published together with experimental results from Vardimon et al. in [18].

---

<sup>4</sup>The lattice constants have to be adjusted for each element.

<sup>5</sup>Conductance histogram, mean channel distribution and Fano factor.

## 5.1. Conductance

The easiest value to measure in experiments and therefore the best value to compare with is the conductance. Unfortunately one can not compare directly single calculations with single measurements because the systems are not that well defined in experiments. Even the crystallographic direction in which the wire is elongated is often not known. However, even if we would know all those details the temperature is larger than 0 K, which means that one also would have to know the velocities of all atoms. But that is experimentally not achievable in sufficient detail.

As consequence one has to compare statistics with each other. For that one uses the figure types explained in section 4.4.

### 5.1.1. Conductance and elongation

The first thing we want to look at are the correlations between the conductance and the displacements they were calculated at. Here one has to keep in mind that in principle the displacement is not defined in a unique way. In theory one has a well defined initial structure, so one uses the displacement from the upper wall with comparison to that. But in experiments the initial structure is not well defined so another way has to be used. There one uses the first event where the conductance achieves  $1 G_0$  as basis<sup>6</sup>.

The results of our theory curves are plotted as density plots in Fig. 5.2.

One can see similarities and differences between the metals. Within 1 nm of elongation, for example, most contacts drop down from 10 to  $0 G_0$  where  $0 G_0$  means that the contact is broken. But how that happens in detail is different. The transition into the tunneling regime (the exponentially decaying curves below about  $1/2 G_0$ ) is visible in all contacts, but best pronounced in Al. That observation gives insight into the rupture behavior: Taking into account that the data points are calculated at the same discrete spacing in time (and therefore elongation), there have to be different fast rupture processes involved.

To get a feeling for that, Fig. 5.3 shows one example each for a fast and a slow process. In the left plots the conductance (red) of the geometries and the force (green) needed to elongate the geometries further is plotted as function of the displacement. On the right side two geometries each demonstrate what happens. The upper row shows a sudden rupture such that the conductance and force drop down to zero immediately. The geometries on the right show that a mono-atomic wire has formed which snaps back in a very short timescale after the rupture which leads to a drastic increase in distance between the nearest atoms of each half of the former wire.

This is an extreme case because not every Au wire develops such a mono-atomic wire. But similar results can be seen from structures whose atoms in the vicinity of the neck-hole have slightly stretched bonds. Breaking the contact leads to a sudden loss of the constraint and the atoms relax on a short timescale, leading to similar conductance and force curves. To work that way several atoms have to contribute to sum up to a large enough effect. The result of both effects is that the tunneling regime can not be well represented in the elongation plots.

<sup>6</sup>This means that this events always happen at a displacement of e.g. 0 nm.

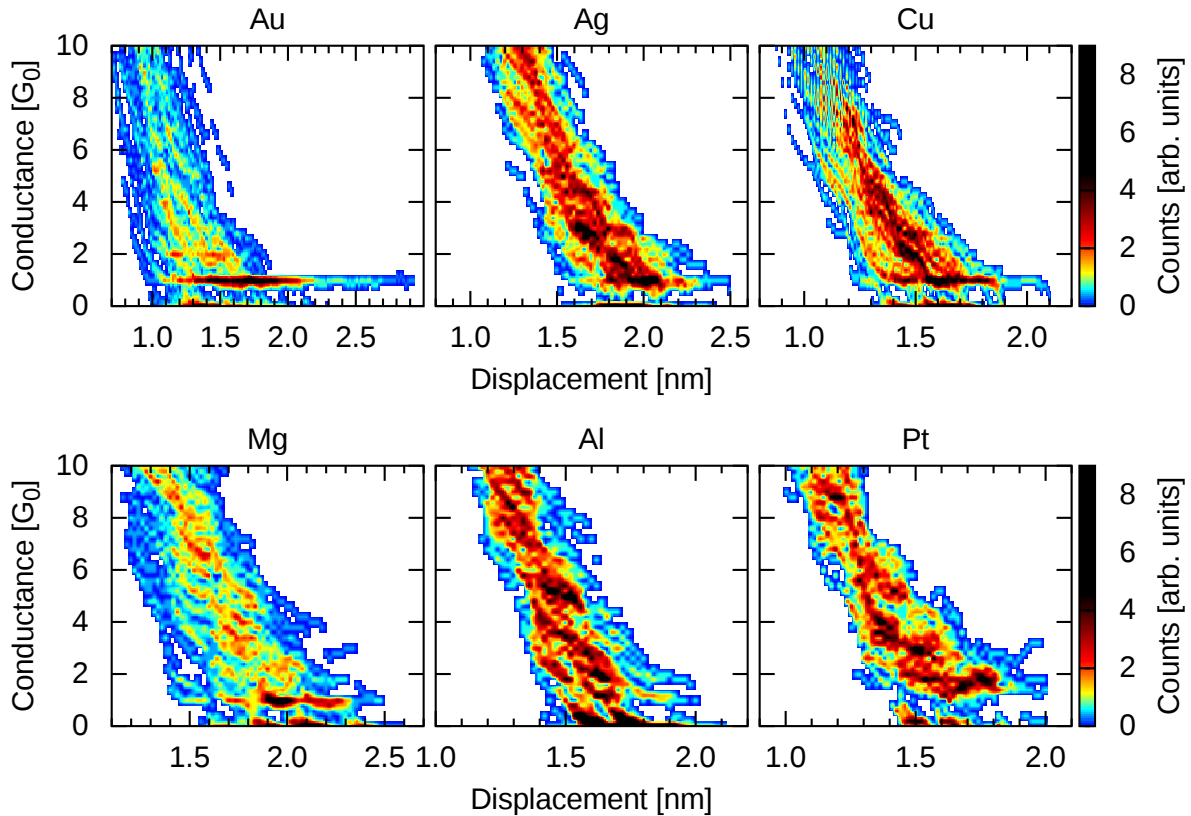


Figure 5.2.: Density plots of the total conductance data of 100 elongation curves as function of the displacement of their upper walls to the initial positions. The densities are normalized to an upper limit of 9.

Ag and Cu which don't form long wires (see below) have sufficiently soft potentials to show the second behavior and therefore do not map the tunneling regime very well.

The second row in Fig. 5.3 shows a slow rupture process of an Au example: The two halves separate from each other without geometric reordering and the number of elongated bonds is too low to displace the atoms of the two halves far enough after the breaking of the last bond to leave the tunneling regime. Nevertheless, the breaking is visible as step in the force. Because of a high conductance value at the breaking of the contact of about  $1.7 G_0$ , the example in the lower row in Fig. 5.3 for Al shows a very smooth process below  $1 G_0$ . This high conductance value is due to contributions from  $s$  and  $p$  orbitals instead of only  $s$  orbitals as for Au. Here the two halves are more pyramidal formed, leading to two rigid structures after breaking. The two resulting halves are stable enough such that the last plateau at about  $1.8 G_0$  gets recovered if one reverses the elongation direction of the wall (the closing curve is not shown).

Pt more likely shows the direct jump from short structures (about  $1.5 G_0$ ) by breaking to  $0 G_0$ , but it also shows the slower breaking process like Al with cone like halves.

Another noticeable behavior of the monovalent metals Au, Ag and Cu is the creation of a clear plateau at  $1 G_0$ . This is specially pronounced in Au where, as shown in Fig. 5.3, long (more than one or two atoms) mono-atomic wires can develop which have about constant conductance during the chain expansion. The constant conductance is visible as plateau

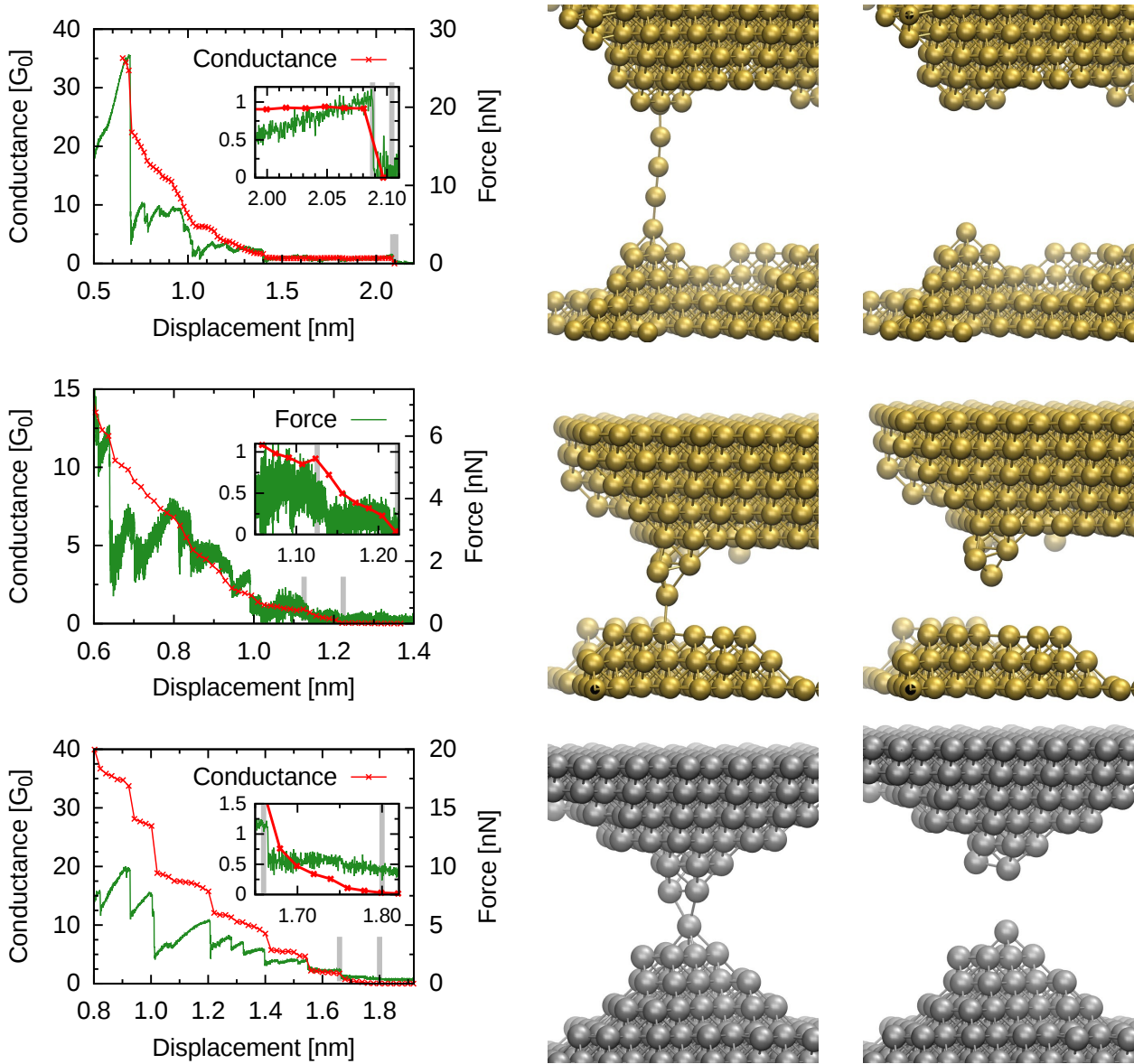


Figure 5.3.: Examples for a fast rupture process of Au (upper row), a slower one of Au (second row) and a slow one of Al (lower row). The geometries are at displacements of 2.09 nm ( $0.9 G_0$ ) and 2.10 nm ( $0 G_0$ ) (upper row), 1.13 nm ( $0.9 G_0$ ) and 1.22 nm ( $0 G_0$ ) (second row) and 1.66 nm ( $1.7 G_0$ ) and 1.80 nm ( $0 G_0$ ) (lower row). The vertical gray bars in the figures mark the positions of the geometries of the right side.

between about 1.4 and 2.1 nm (red) while the force (green) shows multiple jumps similar to the one in the inset.

### 5.1.2. Conductance histograms

In Fig. 5.2 different preferred conductance values for each material can be estimated. The  $1G_0$  plateau for the monovalent metals was already mentioned, but there are more. To analyze this further one projects the data of the density plots onto their conductance axes and thus gets the corresponding conductance histograms (Figs. 5.4).

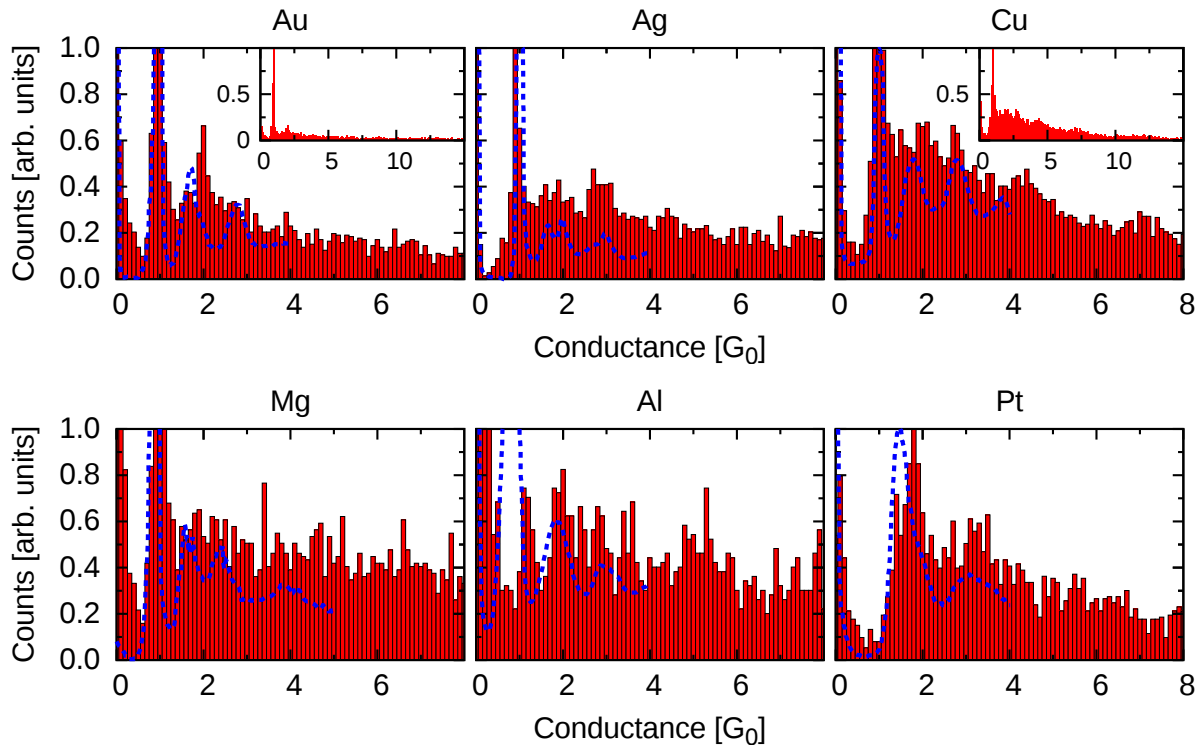


Figure 5.4.: Conductance histograms of 100 elongation curves each. The main histograms of Au, Cu and Mg are cropped in height (see insets). The bin size is  $0.1 G_0$ . The dotted blue lines are from experiments from the group of van Ruitenbeek<sup>7</sup> [13] (Mg) and the group of Tal<sup>8</sup> [18] (rest, see also section A.7).

As expected there is a dominant peak<sup>9</sup> at about  $1 G_0$  for the monovalent metals. This peak is very sharp in contrast to the peak of Mg which also has a peak at  $1 G_0$ . Al has its first peak at about  $1.2 G_0$  and Pt at about  $1.8 G_0$ . The higher values are due to contributions from other orbitals than the  $s$  orbital, namely the  $p$  orbital for Al and the  $d$  orbitals for Pt. The first peak of this metals between  $1 G_0$  and  $2 G_0$  is build up mainly by monomers, dimers and in the case of Au also mono-atomic chains. Examples for this can be found in Fig. 5.5 and Fig. 5.3.

<sup>7</sup>The experiments in the group of van Ruitenbeek were done with the MCBJ technique at 4.2K and  $< 10^{-5}$  mbar at a separation speed of the leads of 100 nm/s. The statistics includes  $3 \cdot 10^3$  traces.

<sup>8</sup>The experiments in the group of Tal were done with the MCBJ technique at 4.2K and  $10^{-5}$  mbar with notched wires. The experiments were done by Ran Vardimon.

<sup>9</sup>A peak has to consist out of more than only a single bar to distinguish it from statistical noise. For example the first peak of Au is build up by at least 5 peaks, but the actual number depends strongly on the resolution and noise of the histogram.



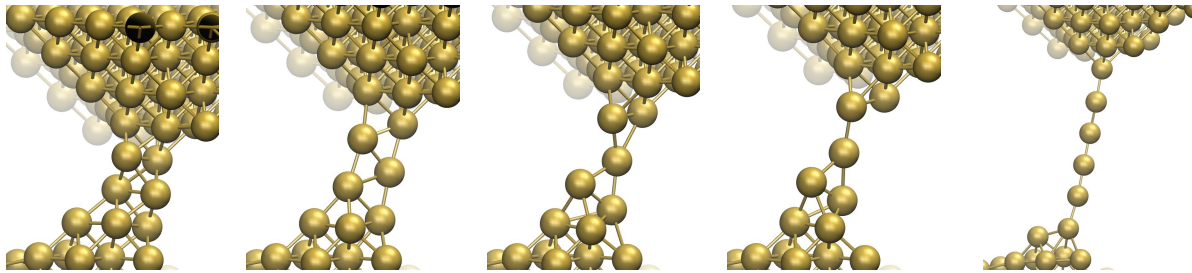


Figure 5.5.: Evolution of a Au contact from  $2.0 G_0$  with 3 channels ( $\tau_i > 0.01$ , first geometry), a zigzag structure with  $1.2 G_0$  and 2 channels (second geometry), a monomer with  $0.7 G_0$  and 2 channels (third geometry), a dimer with  $0.8 G_0$  and 1 channel (fourth geometry) to a long wire with  $0.9 G_0$  and 1 channel.

Further peaks are visible, if not every time very clear separated from the rest. The monovalent metals show more clearly separated peaks than the others but they are much broader than their first ones. An exception is Au where also the second peak is very sharp. The reason for the difference in Au is the possibility of the creation of parallel mono-atomic wires which have  $1 G_0$  each. This is an important point understanding different properties of Au nanocontacts. Therefore it will be discussed later in a separate section (sec. 5.3).

The results of the conductance histograms are in very good agreement with recent experiments (blue curves in Fig. 5.4<sup>10</sup>). The experimental results of the monovalent metals show well established peaks at slightly below multiples of  $G_0$ . Ag shows an indicated double peak structure at about  $1.8 G_0$  and  $2.0 G_0$  which is also reproduced by the theory. The individual peaks were created from the same kind of geometries but not from the same curves. The second of the double peak in Ag has additional contributions from wires with three atoms in diameter, while the plateaus of the first one are solely build up by geometries with two atoms in the constriction.

Conductance quantization if existent shows itself as sharp peaks in the conductance histogram at multiple of  $G_0$  [60]. This can be recognized in the histograms of the monovalent metals in Fig. 5.4. The other materials show deviations in peak positions and width of the peaks.

Mg low temperature results from Smit et al. [13] (blue curve in Fig. 5.4) aroused the question of quantization despite it not belonging to the monovalent metals. But the results here do not show quantization effects. Except the first peak which is very broad compared to the first peaks of the monovalent metals, the following peaks are at wrong positions and too broad to be resolved individually<sup>11</sup>. The first experimental Al conduction peak is about  $0.3 G_0$  lower than the theoretical one while the second one fits quite well. The difference between the experimental and theoretical results of Al will be discussed later in section 8. The two visible peaks in Pt fit quite well in theory and experiment to each other.

<sup>10</sup>See also section A.7 and [18] for more details.

<sup>11</sup>The second and third experimental peak overlap in the theory results to one noisy peak.

### 5.1.3. Channels

Another way to see conductance quantization is to look at its channel distributions.

The transmission eigenvalues (channel openings)  $\tau_i$  tell us how the total transmission (the sum of the eigenvalues) is built up from different 'channels' (and their eigenvalues) through the wire. Each atomic orbital can hold one channel and contribute therefore at most one quantum of conductance ( $G_0$ ). This would correspond to a fully open channel ( $\tau_i = 1$ ). But to be able to contribute the orbital has to overlap with an orbital from another atom, and this overlap does not have to be perfect, leading to a partially open channel ( $\tau_i < 1$ ). The distribution of the  $\tau_i$  are often referenced to as 'channel distribution' and it can be averaged by multiple realizations (for example different elongation processes with the same conductance value) to get the 'mean channel distribution'.

Conductance quantization appears in the mean channel distribution as step wise opening (one by one) of the individual channels as function of the conductance, meaning that ideally all channels except one have zero or full transmission.

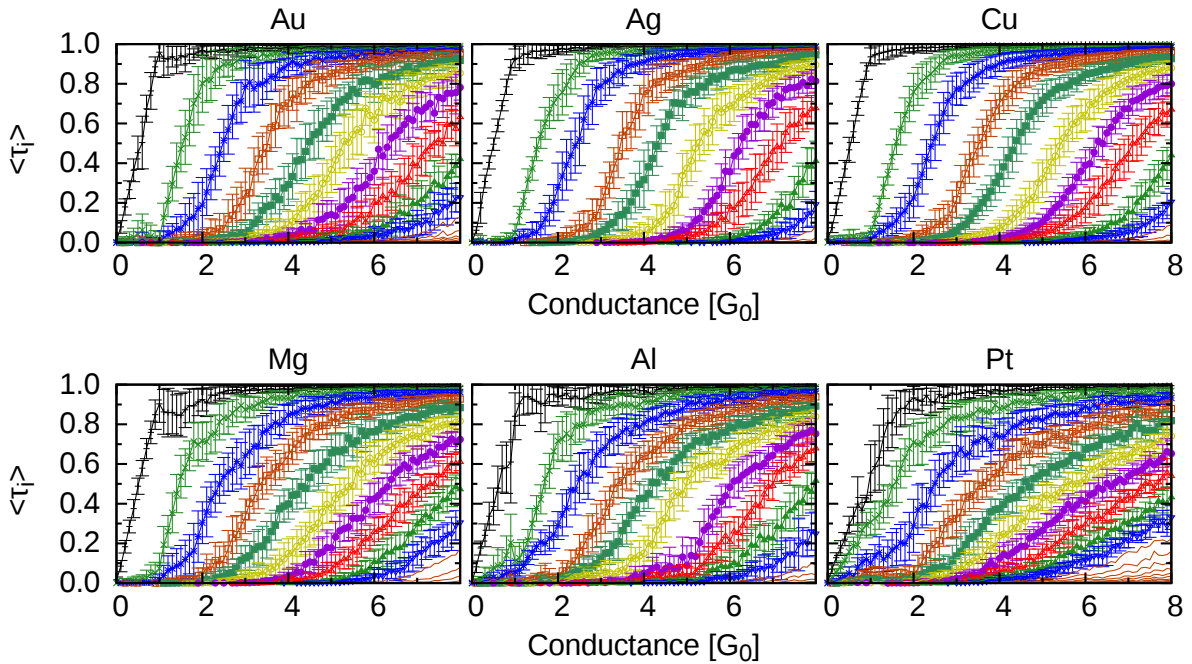


Figure 5.6.: Mean channel distributions with standard deviations of the 10 highest channels of 100 elongation curves each as function of the total conductance.

This distribution is experimentally not easy to measure because one has to couple the system to superconducting electrodes or use the estimation via shot noise measurements (see sec. 4.1). For Mg the calculations do not show a clear step wise opening (Fig. 5.6). For the monovalent metals this looks different, at least the first channel opens almost fully before the second one starts to rise noticeable. But also the higher channels saturate much faster than for Mg. Al with contributions from  $p$  orbitals shows from the beginning multiple channels as does Pt with contributions from  $d$  orbitals. But while Al has a dominant channel, the channels in Pt are more similar in transmission. So Al and Pt do clearly not show conductance quantization.

Noise suppression as fingerprint of the channel distributions will be a further indication

whether a metal shows quantization or not. The noise distributions of these metals will be discussed in section 5.2.

The small peak in the Au distribution at about  $0.5 G_0$  will be discussed later in section 5.3 in the context of parallel wires.

Going back to Fig. 5.5 one finds two further interesting structures, a so called zigzag structure (second geometry) and a stacked version of it where two zigzag structures lie on top of each other (here in the out of plane direction, first geometry). The zigzag structure has a conductance of above  $1.2 G_0$ , much lower as one could expect for a geometry which looks like two parallel wires touching each other. But looking deeper one finds a small difference of  $0.015 \text{ nm}$  between the bond length along the wire (about  $0.28 \text{ nm}$ ) and the ones following the zigzag structure (about  $0.26 \text{ nm}$ - $0.27 \text{ nm}$ ). And looking at its channel distribution in Fig. 5.7 (second gray vertical line) one indeed finds two channels, one making  $2/3$  of the total transmission and the second making the residual  $1/3$ . Thus it can be thought of a folded chain where the dominant transmission still goes through the mono-atomic wire. This structures are experimentally well known for Au [173].

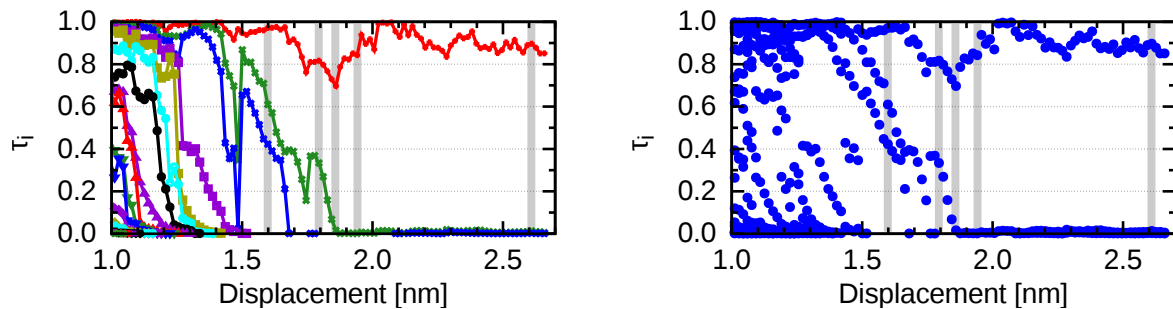


Figure 5.7.: Channel transmissions of a Au wire as function of the displacement of the walls. On the left, the transmission eigenvalues (channels) are connected according to their order in the set of eigenvalues with transmission  $\tau_i > 0.001$ . The vertical lines mark the positions of the Au geometries of Fig. 5.5.

The stacked zigzag structure has with  $2 G_0$  not the doubled transmission compared to one zigzag structure. This can be explained by the arguments given in section 4.5: Destructive interference leads to a decrease of the total conductance from the expected  $2.4 G_0$  down to  $2.0 G_0$ .

In Fig. 5.7 the channel distribution during the elongation process is shown in two ways. The version on the left side is as usual in publications: the channels are connected and color coded according to their size with respect to the others of that geometry. But this is somewhat misleading, adding information about the time-line of the individual channels one does not have. In truth one only has the information given in the plot on the right side. The problem is that one can not be sure that two points connected in such a way are really from the same ‘physical channel’ (two lines could cross). In simple examples this point plays no role but in more complex ones (for example the channel distribution in Fig. 5.17), the progress is not unambiguous. The problem can be avoided using finer time resolutions where the needed resolution depends on the problem<sup>12</sup>.

<sup>12</sup>The evolution of the channels would need to be quasi continuous.

## 5.2. Noise

Coming from the channel distribution one has access to a value which is experimentally much easier to measure: Shot noise. In the linear regime the zero-frequency shot noise can be calculated as  $S_I = \sum_{i,\sigma} \tau_{i,\sigma}(1 - \tau_{i,\sigma}) = 2eIF$  with current  $I$  and Fano factor  $F$  (see section 2.4.1). The Fano factor which is defined as noise normalized by its full poissonian value  $2eI$ , can be written as

$$F = \frac{\sum_{i,\sigma} \tau_{i,\sigma}(1 - \tau_{i,\sigma})}{\sum_{i,\sigma} \tau_{i,\sigma}} \quad (5.1)$$

It is not only a measure of the correlation between the electrons [174] but also allows conclusions about the channel distribution within some range of possibilities<sup>13</sup>. As one does not need superconducting electrodes this method is in principle not only applicable at low temperatures but able to give experimentally access to channel information for wires at higher temperatures than 4.2K. But on the other hand the shot noise contribution to the measured excess noise gets more and more negligible with higher temperatures against the contributions from the Johnson–Nyquist noise [175].

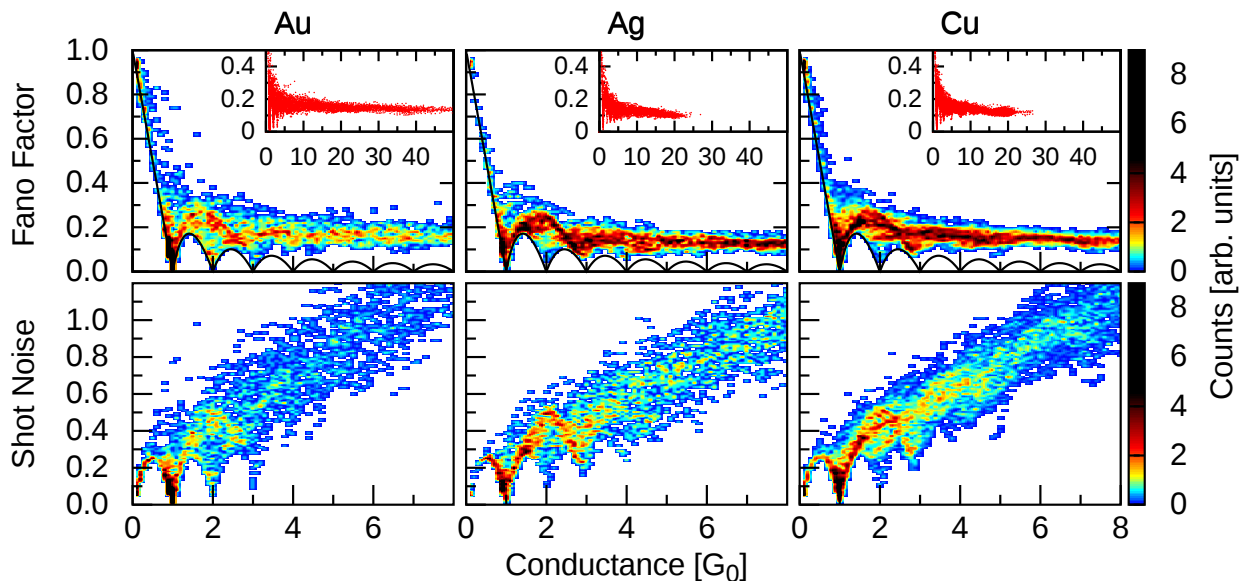


Figure 5.8.: Density plots of the Fano factor and the corresponding shot noise from data of 100 elongation curves each as function of the total conductance. The densities are normalized to an upper limit of 9. The insets are scatter plots of the data points. The overlap of the data points in the density plot below the black lines ( $F_{min}$ ) is an plotting artifact<sup>14</sup>. Experimental results can be found in the appendix (sec. A.7).

The results of the calculations of the spin independent materials are shown in Figs. 5.8 and 5.9. The shot noise is here only presented as examples of how it looks like. Later on it will be omitted because it includes no information not already contained in the Fano factor data<sup>15</sup>.

<sup>13</sup>See sec. 4.1 for more details.

<sup>14</sup>It's actually at that point not possible to have data points below  $F_{min}$  (forbidden region).

<sup>15</sup>It is the Fano factor times a straight line as can be seen in equation 5.1.

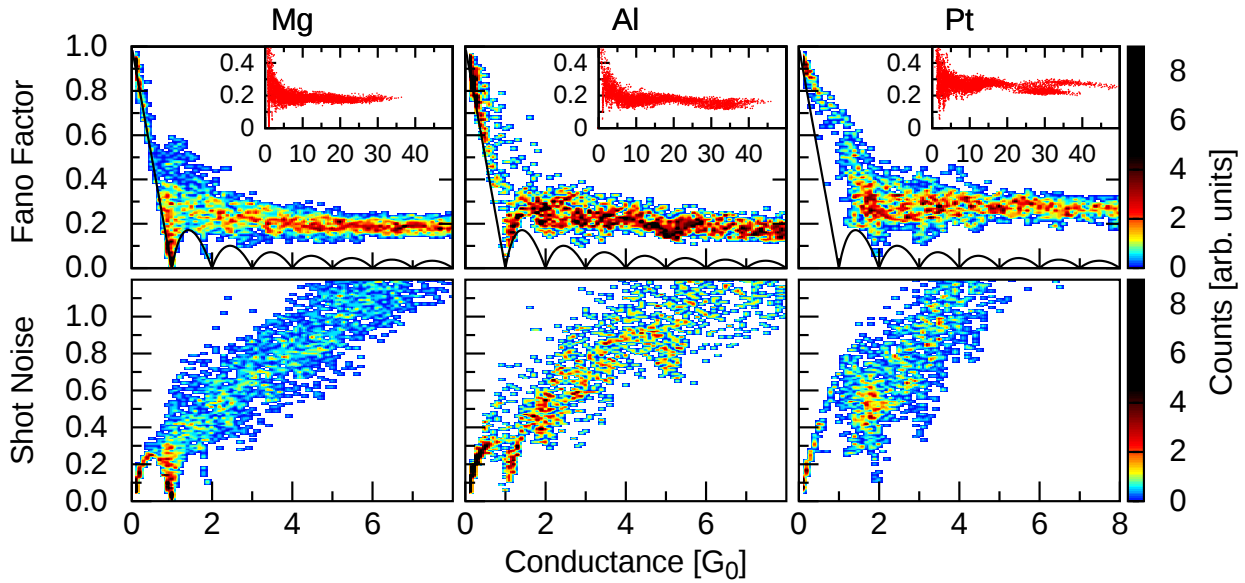


Figure 5.9.: Same as Fig. 5.8 for Mg, Al and Pt.

The black line in the Fano factor plots present the minimal values possible with spin-degeneracy. It is given by

$$F_{min} = 1 - \frac{1}{G} [int(G) + \{G \cdot 1 - int(G)\}^2] \quad (5.2)$$

where  $int(G)$  means the next lower value to  $G$ .<sup>16</sup> The dips to zero at integer multiple of  $G_0$  are due to the possibility to have only fully open ( $\tau_i = 1$ ) and fully closed ( $\tau_i = 0$ ) channels. Between two integer values one needs at least one channel between zero and one, leading to a finite Fano factor.

Except for Pt all materials show the first dip at  $1 G_0$  to some extent. This is expected from the mean channel distributions shown in the last section. The deviations from the minimal noise are due to the fact that the structures are not ideal, meaning that there is a great variation in angles and distances between the atoms (disorder) leading to the same conductance but with higher noise (more channels with less transmission each due to worse overlap of the orbitals)<sup>17</sup>. The higher the conductance the more the steps are smeared out, but the general effect remains up to relative high values (see insets of Fig. 5.8). For the non-monovalent metals the contributions from other orbitals lead to multiple partially open channels which also contribute to the noise. This can be seen in Fig. 5.10 where the DOS contributions of the orbitals (upper row) and resulting transmissions (lower row) for single atom contacts of Au as representative for the monovalent metals, Mg, Al and Pt are shown. While Au is an almost pure  $s$  conductor, Mg has already large contributions from  $p$  orbitals despite it has no unpaired  $p$  electrons. With an unpaired electron in the  $3p$  orbital the conductance of Al is as expected dominated by  $p$  orbitals. Pt on the other side has like Au an unpaired  $6s$  orbital but also an unpaired  $5d$  orbital<sup>18</sup>. In this Pt example  $d$  dominates by

<sup>16</sup>Equivalent to  $\text{floor}(G)$ .

<sup>17</sup>Even the ideal wire at the beginning is not ideal in this sense, because they are finite structures with surfaces.

<sup>18</sup> $[Xe]4f^{14}5d^96s^1$

far, but in another example shown below (Fig. 5.20) the local density of states in  $s$  and  $d$  are similar in size.

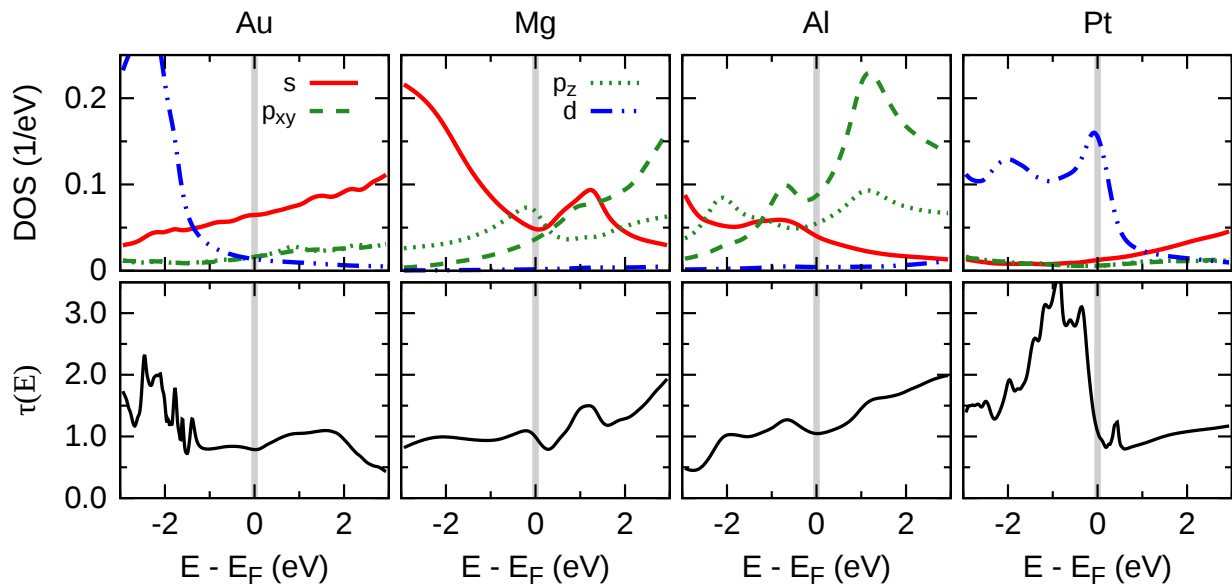


Figure 5.10.: Projection of the density of states (DOS) onto the bridging atom in a single atom contact (upper row) as function of the energy-difference to the Fermi energy  $E_F$ . The orbitals are grouped in contributions from  $s$ ,  $p$  and  $d$  orbitals and normalized by the number of the corresponding orbitals. In the second column the total transmissions  $\tau(E)$  of the same geometries are plotted.

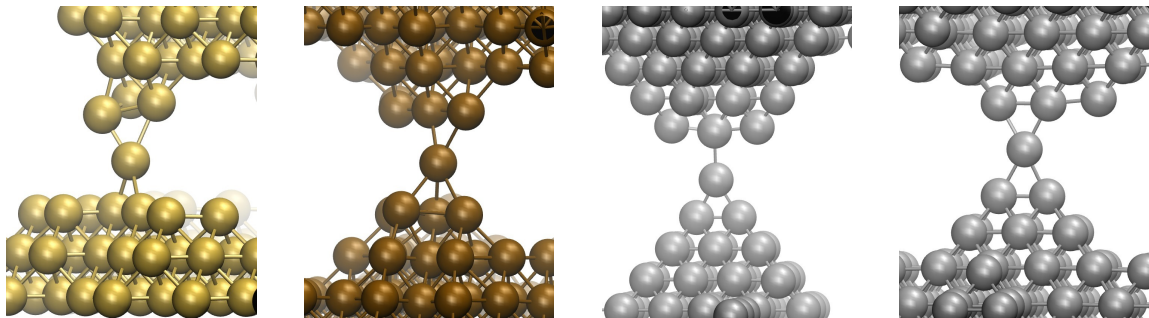


Figure 5.11.: Geometries used for the calculations of the (energy dependent) DOS and transmission in Fig. 5.10.

### 5.2.1. Saturation effect and comparison with diffusive regime

There is a second interesting point visible in the plots of the Fano factor results: a material dependent saturation somewhere below 0.2. The values of the saturation are presented in Table 5.1. They are gained by fitting the data above  $5G_0$  by a horizontal line ( $f(x) = a$ ). The standard deviations are in all cases about the same, but the mean values start from low values of the monovalent metals (0.12 for Ag to 0.16 for Au) up to large values from Pt (0.27). Mg and Al are with 0.18 to 0.17 more close to the noble metals than to Pt.

Au	Ag	Cu	Mg	Al	Pt
$0.16 \pm 0.02$	$0.12 \pm 0.02$	$0.14 \pm 0.02$	$0.18 \pm 0.02$	$0.17 \pm 0.02$	$0.27 \pm 0.03$

Table 5.1.: Overview of the convergence results. The results are gained by fitting the Fano values above  $5G_0$  by a horizontal line.

The saturation values are interesting because they are material dependent and (much) smaller than the  $1/3$  one would expect in the metallic diffusive regime of large structures<sup>19</sup> [143,144]. The expected reduction from 1 to  $1/3$  is due to the contribution of open channels with vanishing noise. The underlying distribution has a bimodal form [176]:

$$P(\tau) = \frac{G}{G_0} \cdot \frac{1}{2\tau\sqrt{1-\tau}} \quad (5.3)$$

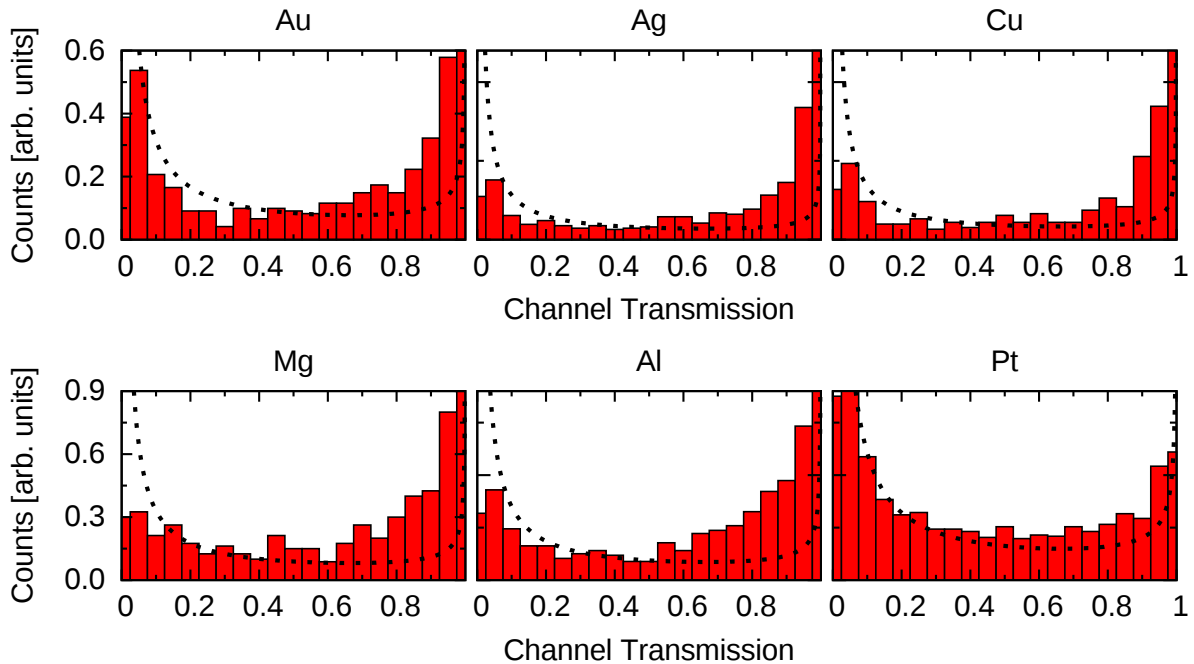


Figure 5.12.: Histograms of the transmission coefficients at a conductance of  $15 \pm 0.125 G_0$ . The lines are the fitted bimodal distributions  $P(\tau)$  (equation 5.3).

This distribution can also be compared with the calculated data. For better visual comparison the prefactor  $G/G_0 = x$  was used as fitting parameter for the data at  $15 \pm 0.125 G_0$ . The results are shown in Fig. 5.12.

<sup>19</sup>Diffusive regime means: mean free path  $\ll$  sample length  $\ll$  localization length.

Despite Pt all materials are at  $15 G_0$  far away from the bimodal distribution (dotted lines). The results for Al get slightly closer to the bimodal distribution going to  $40 G_0$ , but not by much<sup>20</sup>. The Au distribution does not change visibly. For Ag and Cu no data are available for such high conductance values. The results from the distributions at  $15 G_0$  are in perfect agreement with the saturation values from Table 5.1. Pt, the only one near the bimodal distribution, has by far the highest saturation value but lies still below  $1/3$ .

This can be explained looking at the orbital structures discussed in the context of Fig. 5.10 above: The conductance of monovalent metals is  $s$  dominated which are due to their spherical symmetry the most symmetric ones, for Mg and Al  $p$  orbitals play also an important role and for Pt the  $d$  orbitals play the most important role which are the most anisotropic and therefore geometry sensitive ones.

In summary, the saturation of the Fano factor at higher conductance values has most likely nothing to do with the diffusive regime. It's more likely a steady state for low conductance values and contains some information about the orbital origin of the noise. But depending on the orbital structure (see Pt) the result can be near to diffusive.

---

<sup>20</sup>And the statistics is much worse, because we concentrated the computational effort onto low conductance values.



### 5.3. Effect of multiple wires in parallel

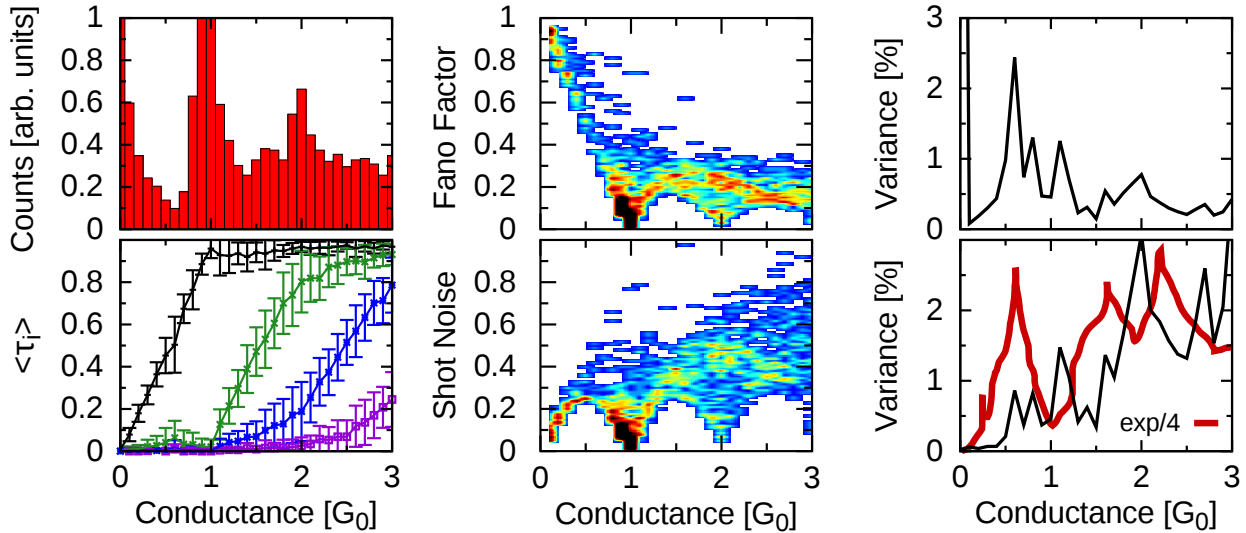


Figure 5.13.: Zoom into the Au data: Conductance histogram and Fano factor with variance ( $\langle F^2 \rangle - \langle F \rangle^2$ ) (upper row) and mean channel distribution and shot noise with variance (lower row). The experimental curve of the variance of the shot noise (red curve) is a (rough) mean of the data in [15, Fig. 1e] divided by 4.<sup>21</sup> The experiments were done in the group of Douglas Natelson at room temperature<sup>22</sup>.

As already seen in the last sections Au plays a special role within this materials because it can build long chains [49, 68]. Fig. 5.13 shows a zoom into the four already seen figures and additionally the variance of the Fano factor and shot noise data. The most interesting observations here are

- the suppression of the Fano factor and shot noise and their variances at  $1 G_0$  which is reflected as suppression of all channels but the first in the channel distribution at that point,
- the high peak in the conductance histogram at  $2 G_0$  which is combined with two "main ways" in the Fano factor and shot noise distributions, one with high and one with suppressed noise and the corresponding peak in their variances (Ag and Cu show only the upper "way") while the experimental data shows a dip in the variance there,
- and the appearance of higher channels at around  $0.5 G_0$  which is reflected as shoulder (peak) in the Fano factor (shot noise) data and a peak in their variances.

The suppression at  $1 G_0$  was already discussed above as a consequence of the orbital structure<sup>23</sup> which is directly visible by the single atom contacts which lead to  $1 G_0$ . The reduction

<sup>21</sup>The amplitude of the variance in the experiment depends strongly on the used bias voltage. Compare therefore (e) and (f) of Fig. 1 of [15].

<sup>22</sup>The experiments were done with an STM setup at room temperature in air with a bias of 180 mV. The statistics include 816 traces.

<sup>23</sup>Mainly  $s$  orbitals contribute.

in the variance only supplies this.

	total counts	2 channels		2 wires
		> 0.1	> 0.2	
Au (4K)	24	33%	63%	29%
Au (300K)	17	1%	29%	0%
Ag (4K)	11	0%	18%	0%
Cu (4K)	52	10%	31%	0%

Table 5.2.: Curves with data at  $2 \pm 0.1 G_0$  for the different materials. A curve is counted if the condition is achieved at least three times during the elongation process. The total counts are the total number of curves found with data at  $2 \pm 0.1 G_0$ . 2 channels > 0.1 means that exactly 2 channels have transmission eigenvalues greater than 0.1. The values of the last column are relative to the contributing curves (total counts).

To have deeper insight into what happens at  $2 G_0$  table 5.2 shows how many curves contribute with at least three data points<sup>24</sup> and how many of the contributing curves have only two channels greater than 0.1 or greater than 0.2. Only two channels with  $\tau_i > 0.1$  means that the two channels have to be near 1 to sum up to  $2 G_0$ . This could imply that there are two independent wires.

Indeed, looking at the last row which presents the number of curves with parallel wires<sup>25</sup>, one finds that for Au at low temperatures only one curve with  $\tau_i > 0.1$  was not seen as geometry with two individual wires (second example in Fig. 5.14).

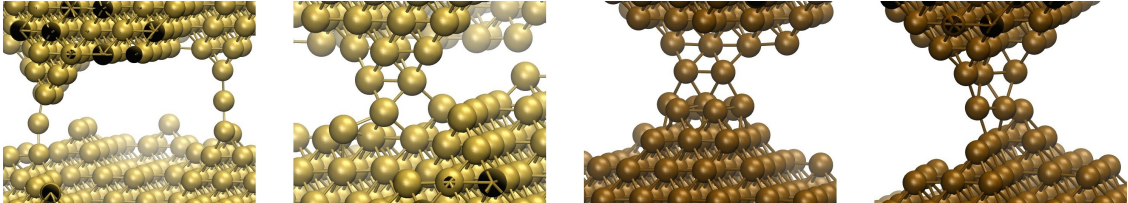


Figure 5.14.: Geometries of Au and Cu at about  $2 G_0$ . From left to right:

- Au:  $1.96 G_0$ ,  $\tau_1 = 0.99$ ,  $\tau_2 = 0.95$ ,  $\tau_3 = 0.02$ ,  $F = 0.046$ ,
- Au:  $2.03 G_0$ ,  $\tau_1 = 1.00$ ,  $\tau_2 = 0.92$ ,  $\tau_3 = 0.04$ ,  $F = 0.088$ ,
- Cu:  $2.02 G_0$ ,  $\tau_1 = 0.99$ ,  $\tau_2 = 0.89$ ,  $\tau_3 = 0.08$ ,  $F = 0.117$ ,
- Cu:  $2.03 G_0$ ,  $\tau_1 = 1.00$ ,  $\tau_2 = 0.96$ ,  $\tau_3 = 0.04$ ,  $F = 0.050$ .

Fig. 5.14 shows examples for Au and Cu at  $2 G_0$  with  $\tau_1 > 0.1$  and  $\tau_2 > 0.1$  but  $\tau_3 < 0.1$ . The first example shows two parallel wires. The second one is the one of eight Au contacts in table 5.2 which was not detected as contact with two wires. Cu does not show parallel wires, the same is true for Au at room temperature. For Ag no geometry has been found showing this channel distribution.

Two geometries of Cu with  $\tau_3 < 0.1$  are shown on the right half of Fig. 5.14, a highly symmetric one (first one) and a completely asymmetric example (second one). Interestingly

<sup>24</sup>To be not a very short fluctuation or transition state.

<sup>25</sup>Optically separated.

it is the asymmetric example which has a very low noise. The reason is the third channel which is available only at the geometry with higher symmetry where other channels have closed only a few steps before.

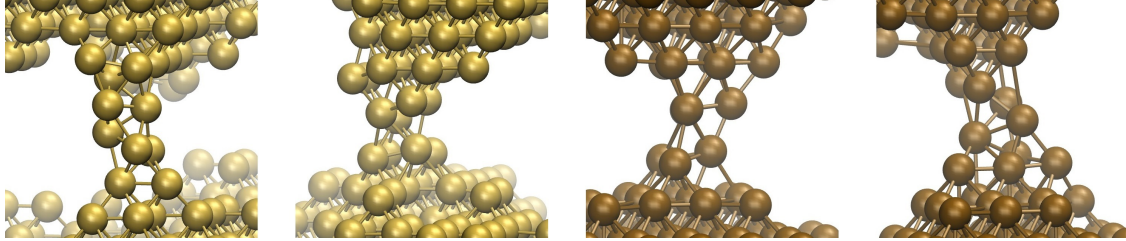


Figure 5.15.: Geometries of Au and Cu at about  $2 G_0$ . From left to right:

Au:  $2.04 G_0$ ,  $\tau_1 = 0.99$ ,  $\tau_2 = 0.59$ ,  $\tau_3 = 0.46$ ,  $F = 0.250$ ,  
 Au:  $2.01 G_0$ ,  $\tau_1 = 0.99$ ,  $\tau_2 = 0.53$ ,  $\tau_3 = 0.48$ ,  $F = 0.262$ ,  
 Cu:  $1.99 G_0$ ,  $\tau_1 = 0.98$ ,  $\tau_2 = 0.55$ ,  $\tau_3 = 0.47$ ,  $F = 0.264$ ,  
 Cu:  $2.00 G_0$ ,  $\tau_1 = 0.99$ ,  $\tau_2 = 0.53$ ,  $\tau_3 = 0.48$ ,  $F = 0.253$ .

The extreme opposite in terms of noise at  $2 G_0$  is shown in Fig. 5.15, again for two Au and two Cu examples. Similar between the geometries is the form of the minimal cross sections which can be set somewhere between triangular and rectangular (first, second and fourth geometry). The third geometry, which has a minimal cross section of only two atoms and which more looks like the first Cu example in Fig. 5.14, has a plane with three atoms in a triangular cross section connecting the minimal part with the lower lead. Whether it is the geometry which leads to bad overlap of the orbitals or destructive interference between channels, the two half open channels contribute almost maximal to the noise.

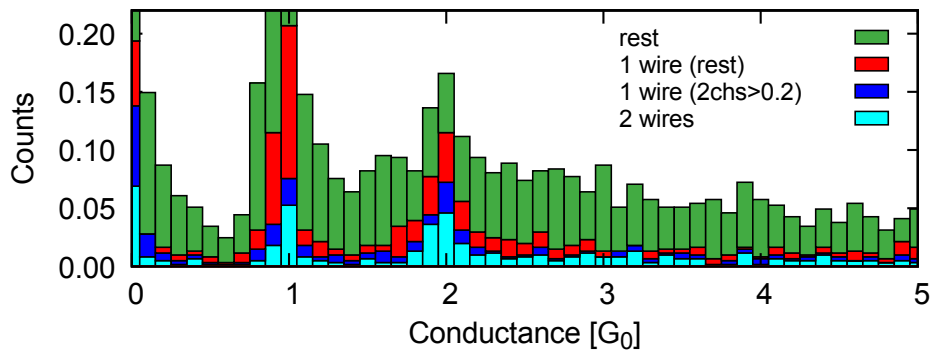


Figure 5.16.: Conditional transmission histograms of Au at 4 K. The total transmission histogram is divided into contributions from one wire with only two open channels  $> 0.2$  (blue), the contributions from the rest with only one wire (red), the contributions from two parallel wires (cyan) and the rest which fulfills none of the above conditions (green). The condition had to be fulfilled at  $2.0 \pm 0.1 G_0$  for at least 3 data points during the elongation process.

The effect of the results of Au at 4 K in table 5.2 onto its conduction histogram is shown in Fig. 5.16. Here the green histogram is the difference between the three conditional histograms in the foreground and the total conductance histogram. Interesting is the relative strong correlation between the first and second peak in the histogram, meaning that the curves building up the second peak also contribute with at least the same amount to the first

peak and there are only relative few points in-between. For the parallel wires (cyan) this is plausible because the conductance gets reduced by breaking one of the two chains leading to a sudden decrease to  $1 G_0$ . This effect also explains why the peak at  $1 G_0$  has a steep edge coming from higher values while the other one has the usual decay. In contrast, single wires with more than two channels (red) like the examples shown in Fig. 5.15 show a sharp plateau at  $1 G_0$ , a broad peak at  $2 G_0$  and a large background in-between. This means that the corresponding configurations are not very stable and that the transition is more continuous. The cause for this can be (locally) enhanced disorder like in the chain in the first geometry of Fig. 5.15.

In the conditional transmission histogram it can be nicely seen that the contribution from the defined single and parallel wires is only  $2/3$  of the total height of the  $2 G_0$  peak, the remaining  $1/3$  is background. Background means elongation curves that do not show plateaus next to  $2 G_0$  with more than two data points. This should be visible in the difference between opening and closing histograms<sup>26</sup>. As it is statistically very unlikely that two parallel wires survive the breaking and reconnection process, but the background and the contribution from the single wires should remain, the peak at  $2 G_0$  would still be visible but reduced by the contribution of the parallel wires.

In total it seems to be clear how the two main ways of Fano factors at  $2 G_0$  arise for Au. Cu on the other hand seems to be more complex and the geometries with low and high Fano factors are not easy distinguishable. The observations made in Ag are similar to the ones in Cu but with much reduced probabilities (see table 5.2).

A problem arises when comparing this results with the experimental findings (Fig. A.10). In contrast to the theoretical results, in experiments the low noise branch dominates by far the picture. For Au this could mean that for much greater sample sizes<sup>27</sup>, the probability to find parallel wires forming the second peak should be much larger than for the sizes which are manageable by theory. For Ag and Cu no parallel wires were found so far. This does not mean that they do not exist in experiments, our sample sizes are probably just too small to be able to show them. As long as the dimensions of the calculated structures are much smaller than in the experiments, it is not possible to exclude the possibility of parallel wires.

The most likely origin for the discrepancy seems to be the creation of the geometries which were taken during an elongation with very high speed compared to experiments and with semi-empirical potentials to describe the interactions, where small changes in the geometries can have large effects in the transport properties [68]. The effect of velocity was checked to play no important role within reasonable<sup>28</sup> ranges. It will be shortly discussed in section 9.3. But there are also other possibilities which could cause differences to the experimental findings which are worth mentioning: The small system size and its connection to the leads could cause additional noise, the parametrization of the tight-binding approach could be too inaccurate or even the Landauer approach could be insufficient in some, yet unknown, sense.

The last item in the list of interesting observations, namely the appearance of higher channels

<sup>26</sup>Elongation and compression (negative elongation), see section 9.2 for more details.

<sup>27</sup>The experimental samples are much larger.

<sup>28</sup>Accessible with MD and statistics.

at  $0.5 G_0$ , was part of the discussion in [15]. The point is interesting because originally it was thought that Au would not be able to show such a behavior. The reason for this is the picture of a wire which breaks after forming a single atom contact. But as Au is a pure  $s$  conductor one atom should only be able to connect one channel.

But before it was never thought of the existence of parallel wires. This is again the key to solve the point: Multiple wires like the ones already shown in Fig. 5.14 who led to the low noise values at  $2 G_0$  can break at the same time, leading to two channels having about the same values.

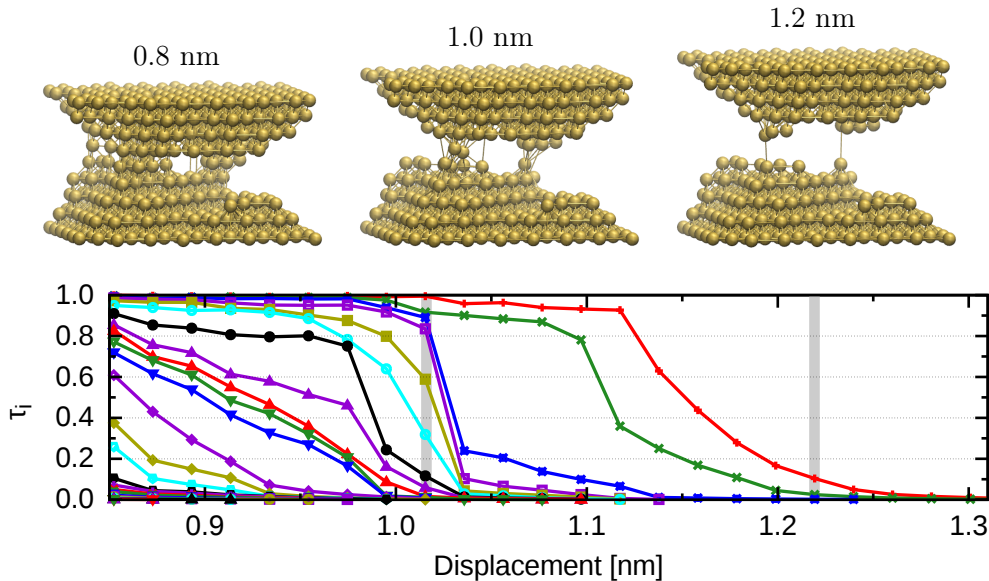


Figure 5.17.: Evolution of a Au structure at 4K ending in two parallel wires breaking at the same time. The conductance values of the above geometries are  $12.7 G_0$ ,  $4.8 G_0$  and  $0.13 G_0$  with 22, 10 and 2 channels having at least a value of 0.01. The transmission eigenvalues of the last geometry are 0.10 and 0.03. Below: Channel distribution of the elongation process.

Another example is shown in Fig. 5.17. The vertical bars in the channel distributions in the bottom of the figure mark the positions of the right two geometries from atop<sup>29</sup>.

An interesting behavior is the bunching of channels following the same trend (for example channel 5 and 6 at the position of the first vertical bar in Fig. 5.17). This is not totally unexpected because every compact region (separated part in cross section) of the wire which breaks on its own has its open channels, its closed channels and a channel in-between. With this interpretation the number of half open channels would give the number of compact regions. But looking at the next example (Fig. 5.18) this interpretation seems not to be very stringent.

Following the last two channels in both examples one can see that the wires do not break perfectly at the same time but one slightly before the other<sup>30</sup>. Thermal fluctuations and phonons can cause such differences even if the two wires would be (geometrically) identical.

<sup>29</sup>To present the channel distribution of the left geometry makes not much sense because a confusing number of channels (22) are contributing.

<sup>30</sup>If one of the wires would be a long one, then a slightly displaced breaking would not lead to this behavior because with high probability it would break too fast.

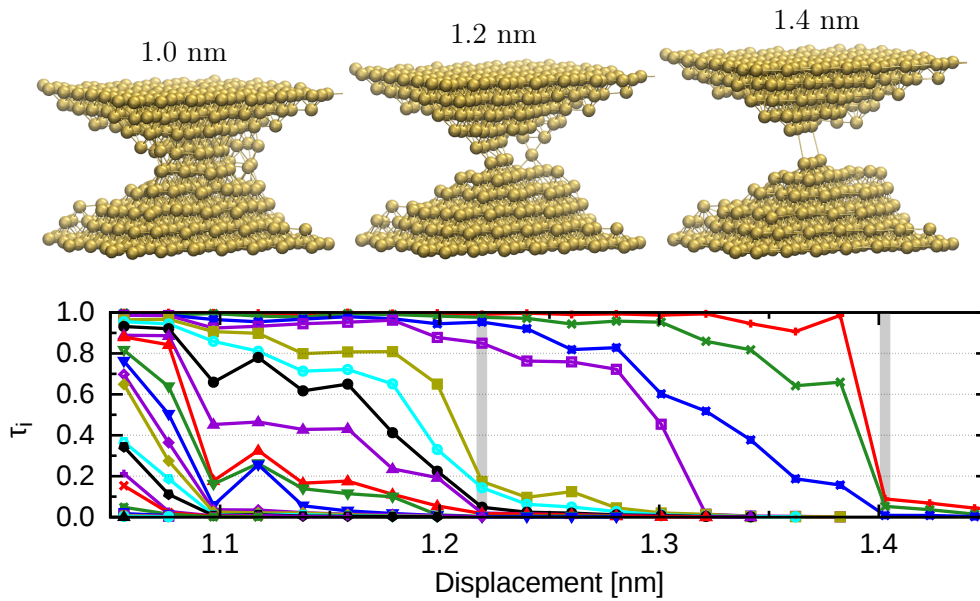


Figure 5.18.: Evolution of a Au structure at 300 K ending in parallel atoms breaking at the same time. The conductance values of the above geometries are  $13.3 G_0$ ,  $4.2 G_0$  and  $0.15 G_0$  with 22, 9 and 2 channels having at least a value of 0.01. The transmission eigenvalues of the last geometry are 0.09 and 0.05. Below: Channel distribution of the elongation process.

But wires do not have to be separated that far laterally. Indeed, they even can be neighboring atoms. Such an example for Au at room temperature with the corresponding channel distribution is shown in Fig. 5.18. Here the wires break edgewise, not like a thin wire. In principle this could lead to a high number of slightly open channels, but at the end there are usually slight variations in the distance, leading to channels closing faster than others. While at low temperatures both possibilities contribute, at room temperatures no separated wires were found. The explanation therefor could be that the individual wires at room temperatures were too likely to fuse at the small distances possible in this calculations and that it is energetically more unlikely to find two stable single atom wires. This difference between room and low temperatures was already visible in the results of table 5.2 where the question of parallel wires at  $2 G_0$  was discussed.

## 5.4. Thermopower

Extending the calculations of the transmission from  $\tau(E_F)$  to  $\tau(E)$ , where the energy  $E = E_F \pm \Delta E$  is within a temperature dependent energy window  $\Delta E$  around the Fermi energy, one has direct access to the thermopower (or Seebeck coefficient)  $S$  which describes a potential difference which appears as response to an applied temperature difference ( $S = \Delta T / \Delta V$ ; see section 2.4.2). The default number of integration points in this calculations for  $S$  is 11 ( $E_F \pm 5$  points). This number is a compromise between getting an accurate description of the energy dependency of the transmission around the Fermi energy and the calculation effort needed for additional points<sup>31</sup>.

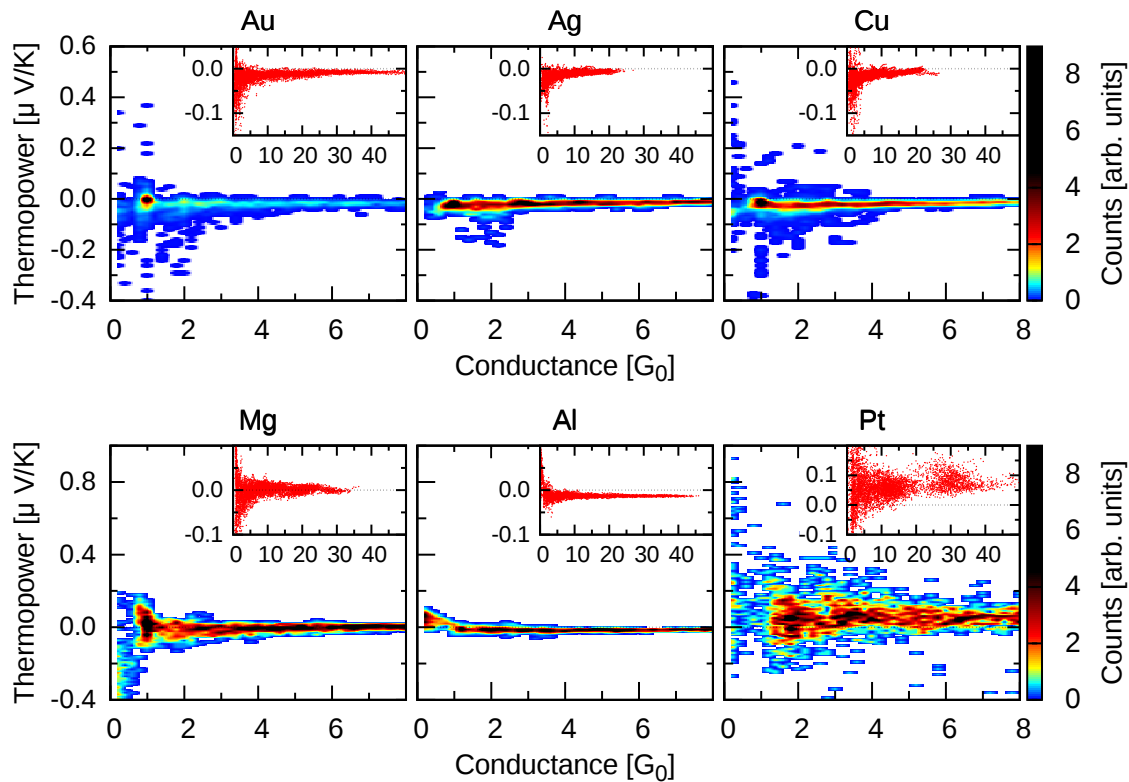


Figure 5.19.: Density plots of the thermopower data of 100 elongation curves each as function of the total conductance. The densities are normalized to an upper limit of 9. The insets are scatter plots of the data points.

The results are summarized as density plots with scatter plots for higher conductance values as insets (Fig. 5.19). The monovalent metals and Al show a negative thermopower while Pt has a positive one. Mg has a vanishing average thermopower.

The behavior of Au and Pt at that scale are interesting because they behave opposite to each other and to what is known from bulk [16]. The sign can be explained with the energy dependent DOS and the resulting slope of  $\tau(E)$  near the Fermi energy. In Fig. 5.20 a Au and a Pt example of the DOS for an atom in the constriction with only few atoms (around

<sup>31</sup>It does not scale directly with the number of data points because the charge neutrality loop which is in most cases the most time consuming part of the calculation ( $\gg 80\%$  is not unusual), has to be done only once.

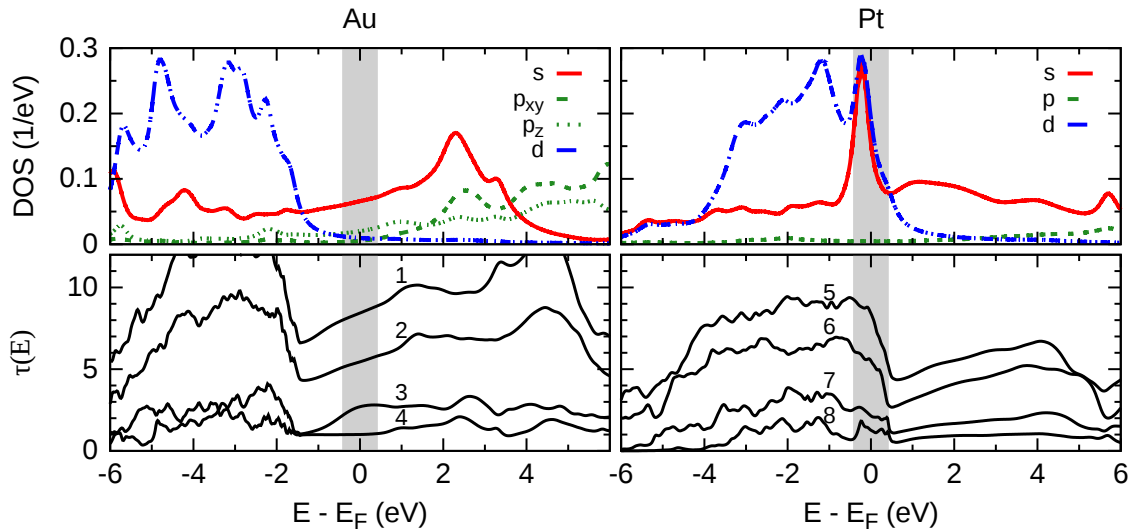


Figure 5.20.: Projection of the density of states (DOS) onto the central atom in a single atom contact (upper row) as function of the energy-difference to the Fermi energy  $E_F$ . The orbitals are grouped in contributions from  $3d$ ,  $4s$  and  $4p$  orbitals and normalized by the number of the corresponding orbitals. In the second column the total transmission  $\tau(E)$  of 4 Au and Pt geometries are plotted as function of  $E - E_F$ . The geometries are shown in Fig. 5.21 and the position of the atom for the DOS calculation is each marked by an arrow.

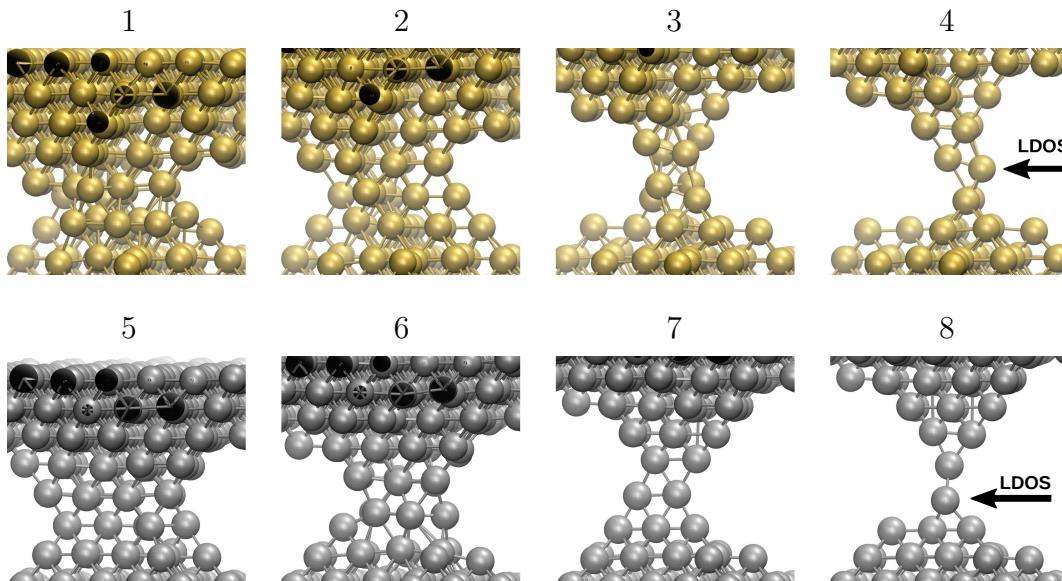


Figure 5.21.: Au (top) and Pt (bottom) geometries at 300 K used for the calculation of the curves in the bottom row of Fig. 5.20. The number on top of each geometry corresponds to the numbering of the curves in Fig. 5.20. The last geometry in each row was used for the calculation of the DOS, the corresponding atom is marked by an arrow.

$1 G_0$ ) of geometries achieved at room temperature as shown in [16] are presented<sup>32</sup>. Other examples of monomers at 4 K were already shown in Fig. 5.10 of section 5.2.

<sup>32</sup>The explanation is equivalent for geometries achieved at low temperatures.



The density of the dominant  $s$  orbital of Au is (monotonously) rising. So do the densities of the  $p$  orbitals (specially  $p_z$ ) contribute to the increasing transmission. The sign of the thermopower, which is inverse to the sign of the slope of the energy dependent transmission, is hence negative.

Pt on the other side has additionally large  $d$  contributions and near the Fermi energy both,  $s$  and  $d$  are decreasing with increasing energy. As both contributions are on a falling flank the absolute slope of the  $\tau(E)$  curve is relative large compared with the one of Au, which is reflected in the relatively large thermopower data of Pt. The monomer in Fig. 5.10 shows a slightly different behavior of  $s$ : It has a positive slope opposite to  $d$ . But in total dominates the high negative slope of  $d$  and the transmission again has a negative slope which results in a positive thermopower.

The explanation for the signs of Mg and Al are similar to each other (see Fig. 5.10). The density of the  $p$  orbitals of Mg near the Fermi energy show almost a plateau while  $s$  has a minima next by. The resulting slope of the transmission and therefore the thermopower is very sensitive to the exact position of the Fermi energy with respect to this minima of  $s$ . Hence it is reasonable to find a vanishing thermopower with a tendency to negative values (Fig. 5.22).

For Al the negative slope of  $s$  competes with the positive one of  $p$  where for geometries larger  $1 G_0$   $p$  dominates the behavior of the transmission.

The results for the evolution of Au and Pt are in good agreement with the experimental results from the group of Nicolás Agraït [16] measured at room temperature<sup>33</sup> (Fig. 7.9). But they also found that for Au the thermopower oscillates for small contacts with a frequency of about  $1 G_0$ , where the minima of the absolute values of the mean thermopower are at the maxima of the conductance histogram<sup>34</sup>.

The explanation is the same as for the minima in the Fano values: the opening of the channels one by one. Due to that the transport at multiples of  $G_0$  is dominated by fully open channels which leads to a flat evolution of the  $\tau(E)$  curve near the Fermi energy<sup>35</sup> and with that to the suppression of the thermopower.

To analyze the theoretical results with respect to these oscillations, the mean thermopower with standard deviation together with the conductance histogram are plotted in Fig. 5.22. Unfortunately the experimental findings can not be reproduced very well. One can recognize a reduction of the absolute value of the thermopower around  $1 G_0$ , but this is not satisfying because there are sharp peaks before and after the maximum of the conductance histogram which is not what is seen in the experiments. The first peak could be a problem of statistics which is very low there.

A different point is the temperature. The measurements we compare here with were done at room temperature while the theoretical ones are at 4 K and the relation could be more difficult than just linear. And indeed the results shown later for 300 K (Fig. 7.9 in section 7) show minima of the absolute value of the thermopower at about the first and second maxima of the conductance histogram. The temperature modifies two things, the geometries probed during the elongation and the energy window relevant for the integration of the transmission. As the transmission behaves smooth and monotonous in a wide range around the Fermi

<sup>33</sup>One has to keep in mind that the thermopower is in first order linear in temperature.

<sup>34</sup>Similar experimental results at room temperature were found before from [81].

<sup>35</sup>Wouldn't it be flat, then the channel distribution wouldn't show this behavior (too unstable).

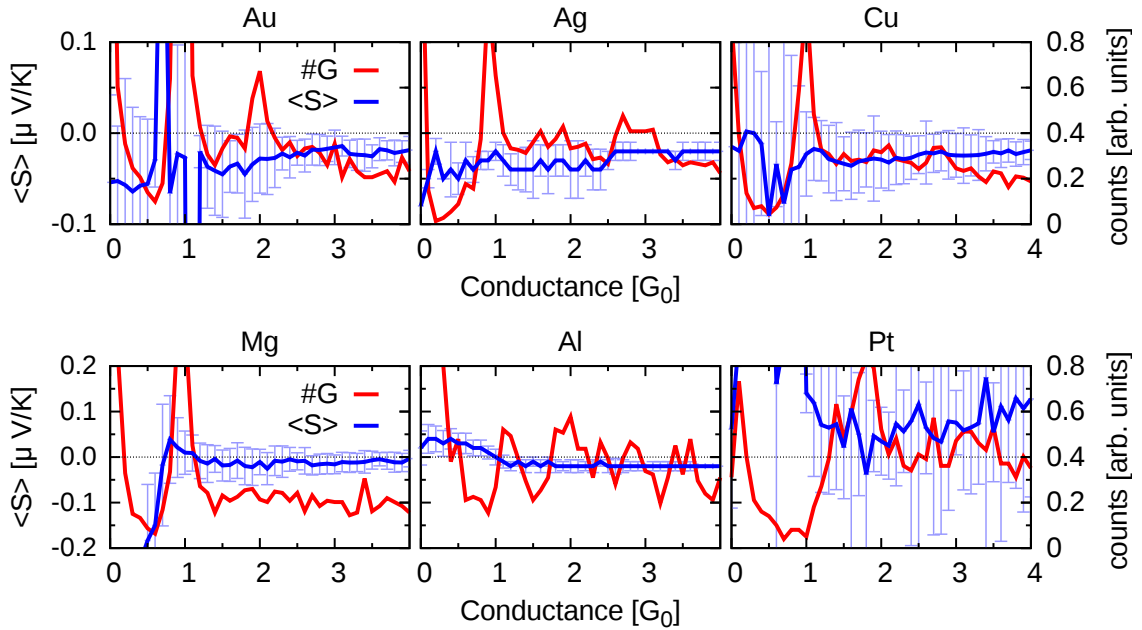


Figure 5.22.: Conductance histogram (red) and mean thermopower (blue) with standard deviation (light blue) as function of the total conductance.

energy, this means that at room and low temperatures different geometries are probed (at least dominantly). Our results are mainly consistent with the ones from Pauly et al. [73] who found in their calculations at 4.2 K a vanishing thermopower with the tendency to negative values and with measurements from Ludoph et al. [80] at low temperatures who observed a random distribution of the thermopower around zero.

But there is a second possibility: The system is too small. The influence of system size and geometry will be discussed later, but indeed, for larger systems the two minima are again at about  $1 G_0$  and  $2 G_0$  (Fig. 9.22). The sharp peaks have also vanished or are much reduced in amplitude. Going the other way to smaller contacts the results for 4 K get worse (Fig. 9.28). But the reduction of thermopower at  $1 G_0$  remains. At 300 K the small contacts are behaving smooth, but the reduction at  $2 G_0$  vanished (Fig. 9.34).

In total, both the temperature and the system size play an important role by explaining the behavior of the thermopower.

The other two monovalent metals show a small dip near  $1 G_0$ . While the dip in Ag is at  $1 G_0$  as is the peak in the conductance histogram, the dip in Cu is very broad and slightly shifted to higher values.

For non-monovalent metals this behavior is not expected and especially not for Pt where the dominant  $d$  orbitals are very sensitive to local disorder<sup>36</sup>, resulting in larger fluctuations in the thermopower.

<sup>36</sup>Because of their anisotropy.

## 5.5. Thermal conductance

The electronic part of the thermal conductance can be calculated using the same data as before for the thermopower (see section 2.4.3).

$$\kappa_{el} = \frac{2}{hT} \left( K_2 - \frac{K_1^2}{K_0} \right) \quad (5.4)$$

The dimension of  $\kappa_{el}$  is  $[W/K]$ . To get the thermal conductivity in units of  $\frac{W}{K \cdot m}$  one has to multiply  $\kappa_{el}$  with the length of the system and divide it by its cross section. But this is unusual for nanoscale systems because the cross section and in experiments also the length of the system are not well defined. The resulting prefactor for the (ideal) initial geometry where the three dimensions are well defined in the simulations is about  $\frac{1}{10 \text{ nm}} = 10^8 \frac{1}{\text{m}}$ .<sup>37</sup>

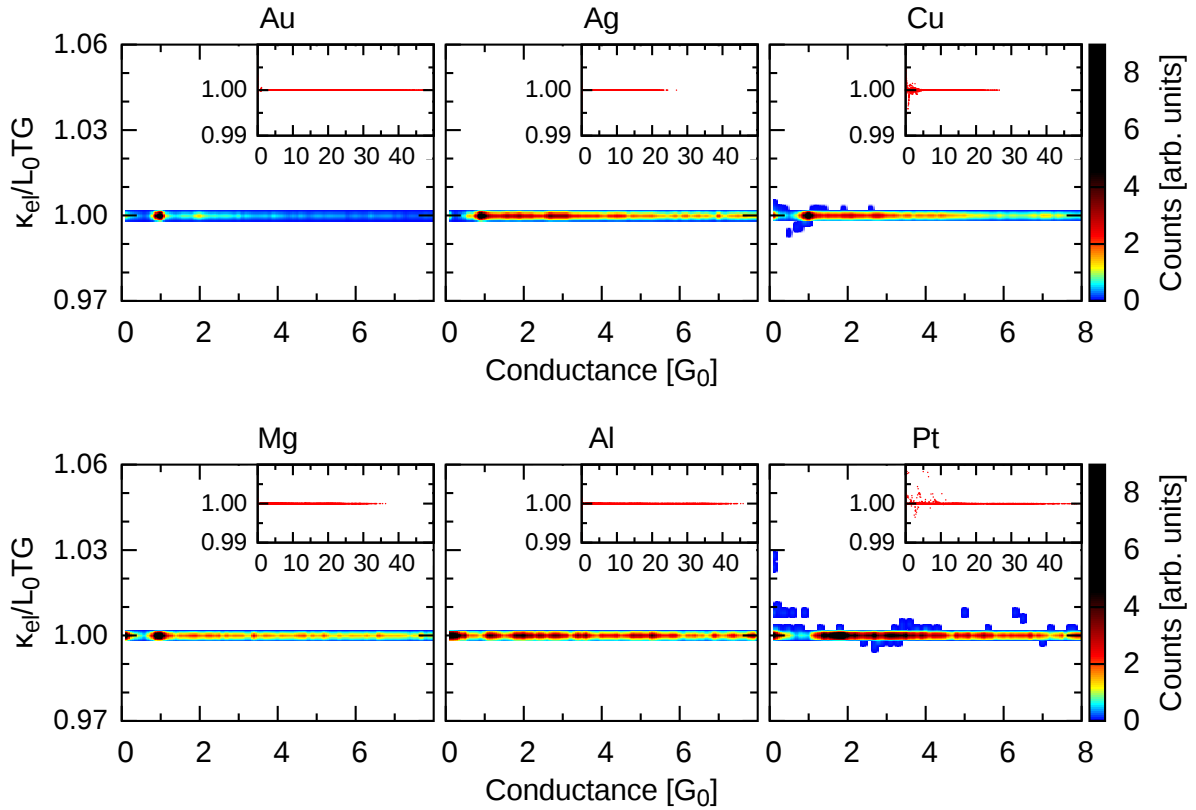


Figure 5.23.: Density plots of the ratio of  $\kappa_{el}$  to  $L_0TG$  of data from 100 elongation curves each as function of the total conductance. The densities are normalized to an upper limit of 9. The insets are scatter plots of the data points. The impression that the uncertainty has a well defined limit ( $1.0 \pm \Delta$ ) is due to the plotting scheme which has a finite resolution and the data points are represented by Gaussian with a fixed extend.

The question asked in this context is whether it differs from the linear regime as function of the conductance known as Wiedemann-Franz relation

$$\kappa_{el} = L_0TG \quad (= L_0TG_0K_0) \quad (5.5)$$

<sup>37</sup>For Au at 4 K it's about  $0.08 \frac{W}{K \cdot m}$  and at 300 K about  $5.6 \frac{W}{K \cdot m}$ ,  
for Pt at 4 K it's about  $0.12 \frac{W}{K \cdot m}$  and at 300 K about  $8.2 \frac{W}{K \cdot m}$ .

with the Lorentz number  $L_0 = (k_B/e)^2 \pi^2/3$ . To answer this the ratio of the two formulas above is plotted in Fig. 5.23 for the different materials.

The results show no significant deviations from 1.00. The small and rare deviations in Cu and Pt can be traced back to numerical problems which were negligible (in amplitude and numbers) for the other properties<sup>38</sup>.

A problem could be that the integration points for the calculation of the charge are optimized for special Au geometries. A hint in this direction is the observation that doing the charge neutrality starting from a modified point (compared to the one which led to the results with deviations) leads to the correct (linear) result. To prevent this problem one would have to use a finer grid which would need a lot of extra computer time and only 0.8% of the calculated Pt points (as worst example here) are beyond an error of 0.1%.

In total, at low temperatures within the resolution of the calculations no significant deviations from the Wiedemann-Franz law could be found.

---

<sup>38</sup>1% deviation of the conductance at  $1 G_0$  would mean an error in the order of  $0.01 G_0$ .

## 6. Spin-polarized materials Fe, Co and Ni

Up to now the spin did not play any role in the calculations. But for ferromagnetic materials like Fe, Co and Ni the spin plays a crucial role. This is known in the macroscopic world (for example magnets) but as will be shown below it also plays an important role in the understanding of properties of nanoscale materials.

In the semi-classical description of ferromagnetic materials by Mott [17] the current is divided into electrons from two independent spin bands, the majority-spin and minority-spin electrons. In this description it is assumed that the  $s$  orbitals dominate the conduction properties while the  $d$  orbitals are localized and are responsible for the net magnetization. Mott's theory is based on the Drude formula which is based on the electron density of the conduction band which is assumed to be spin-independent and the inelastic scattering (relaxation) time which is assumed to be spin-dependent. The relaxation time of the majority-spin electrons is similar to that of spin-independent materials while that of the minority-spin electrons is reduced by the scattering of electrons from  $s$  states to partially filled  $d$  states. The reduced relaxation time of the minority-spin electrons is responsible for low conductivity values compared to noble metals. Furthermore, the majority-spin electrons dominated conduction leads in this model to a positive spin-polarization of the current.

As for spin independent (non-magnetic) metals there have been many experimental STM and break-junction-based studies of ferromagnetic materials [45, 52, 83–114]. Some concentrated on the observation of peaks in the conductance histograms at half-integer multiples of  $G_0$  [84, 98–103]. They were interpreted as evidence for the theory that only spin-split fully open channels contribute to their conductance. But experiments from Untiedt et al. [104] for Fe, Co and Ni with break junctions under cryogenic vacuum conditions put this interpretation in question. They didn't find evidence for a fractional conductance quantization but found a broad peak at  $1 G_0$  instead. They suggested that the observed peaks at half-integer values in the conductance histograms could be due to contamination.

Another discussion has to do with the observations that the anisotropic magnetoresistance (AMR), which is an effect that shows a variance in the resistance as function of the relative orientation between current direction and magnetization and is based on the spin-orbit interaction, exhibits an anomalous angular dependence in Fe [110] and Co [84] atomic contacts. But they also found the occurrence of conductance jumps upon the rotation of the magnetization which were interpreted as an effect of the so-called ballistic AMR. However, as ferromagnetic atomic contacts are not expected to be ballistic this interpretation is questionable [72]. Shi et al. suggested that sudden atomic rearrangements could be the origin for these jumps [177, 178].

Both effects, half-integer quantization and ballistic AMR are not expected from the picture of the conductance in these atomic contacts which is based on the Landauer approach [10, 64]. Due to these controversies and the large interest in spin-dependent transport of nanoscale

contacts, several theoretical groups have investigated the transport properties of ferromagnetic atomic contacts [69, 72, 115–142]. Besides the conductance and the AMR, these studies have addressed aspects like the electronic structure of ideal systems (for example monoatomic wires), the influence of domain walls on electronic and transport properties, or the magnetic structure.

In total, the reported theoretical results clearly suggest that in the atomic scale ferromagnetic contacts, contrary to their macroscopic ones, the  $d$  orbitals play a fundamental role for the transport properties. They also find no fundamental reason to expect conductance quantization or full spin polarization.

However, these studies lack a systematic one-to-one comparison with experiments which is difficult because it requires a simultaneous description of the detailed atomic structure and transport properties of the contacts. A problem from the experimental side is the lack of information about the channel distributions. This was an important step for the understanding of the conductance of spin independent metals, but the method which uses superconducting leads [64, 179] is not usable in the case of ferromagnetic contacts. Therefore no generally accepted picture for electrical conduction in ferromagnetic atomic contacts could be established.

Recently Vardimon et al. [18, 82] were able to surpass this problem by extracting the needed data to determine the channel distribution of different ferromagnetic materials from shot noise measurements at cryogenic temperature and vacuum conditions (see sec. 4.1 for details of the method).

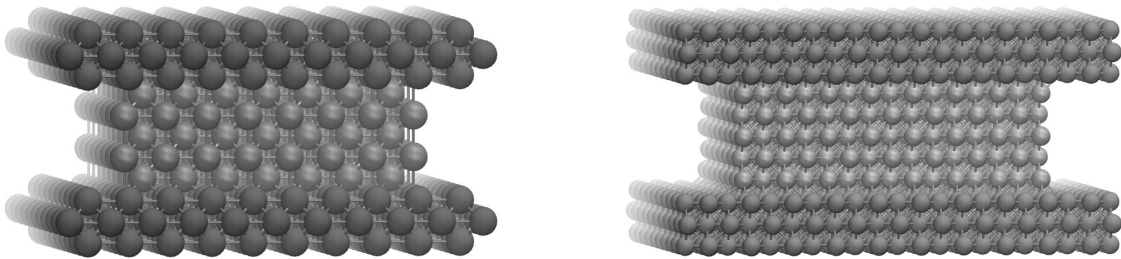


Figure 6.1.: Ideal start geometries of bcc Fe (left) and fcc Ni (right).

In this section the three ferromagnetic materials Fe, Co and Ni will be investigated and compared systematically with the experiments from Vardimon et al. The experimental and theoretical results were published in [18]. In the calculations the spins have different TB-parameters and are considered as independent except for the determination of the charge in the charge neutrality loop. The results can therefore be divided into the spin components and the total as sum of those. The natural unit is now  $G_0/2 = e^2/h$  instead of  $G_0 = 2e^2/h$  but for the most time the factor 2 will be put into the value<sup>1</sup> resulting again in units of  $G_0$ . The initial geometries will be the same as before but while Ni and Co also have an fcc lattice Fe has a bcc lattice (Fig. 6.1). The results of fcc and bcc Fe do not differ drastically. This will be shown in a later section (sec. 9.5).

<sup>1</sup>As before for the results of the spin independent materials.

In the following a similar analysis will be done as for the spin independent materials.

## 6.1. Conductance

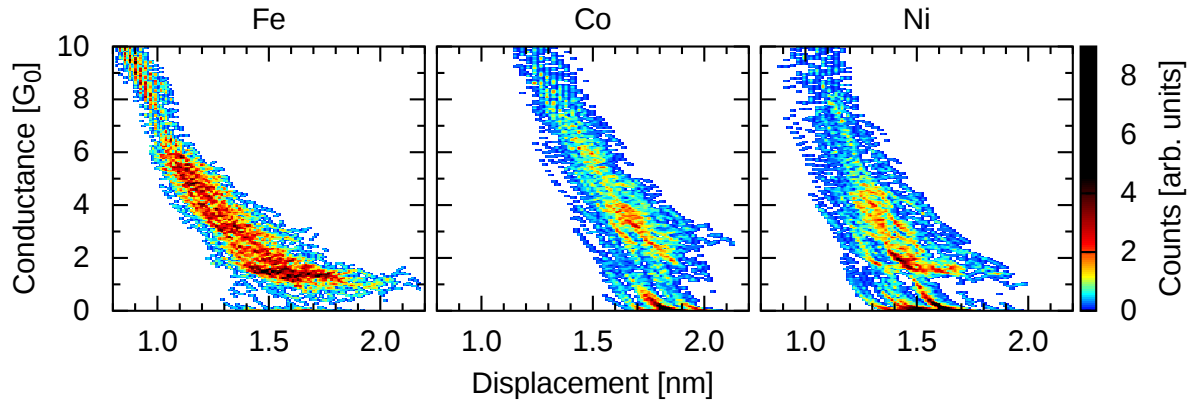


Figure 6.2.: Density plots of the total conductance data of 100 elongation curves as function of the displacement of their upper walls to the initial positions for the spin polarized materials Fe, Co and Ni at 4K. The densities are normalized to an upper limit of 9.

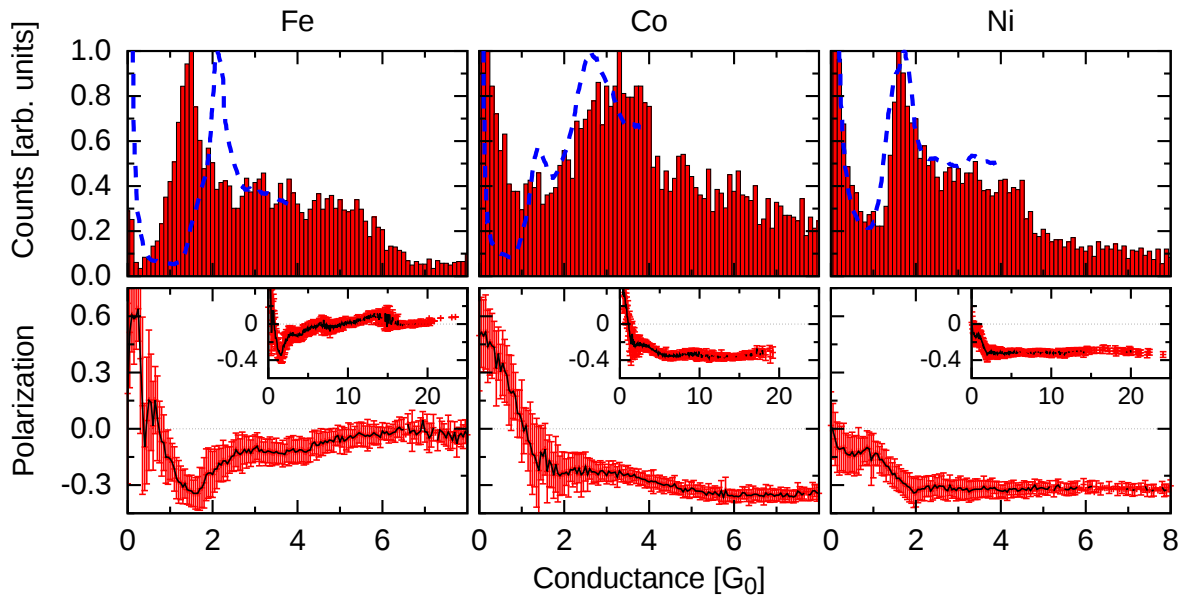


Figure 6.3.: Conductance histograms (upper row) and mean spin polarization with standard deviation (lower row) of 100 elongation curves each at 4K. The blue dashed lines are experimental results from the group of Oren Tal<sup>2</sup> [18].

In Figs. 6.2 and 6.3 the results for the conductance are shown in the known ways as function of the elongation and as histograms. The density plot of Fe seems to be smeared out with

<sup>2</sup>The experiments in the group of Tal were done with the MCBJ technique at 4.2 K and  $10^{-5}$  mbar with notched wires. The experiments were done by Ran Vardimon.

a large accumulation with a broad width at low conductance values which is reflected in the histogram as broad peak between 1 and  $2G_0$ . In the histogram additional peaks at 3 and  $4G_0$  could be interpreted as such. The first peak is shifted downwards with respect to the experimentally observed one by roughly  $G_0/2$  (blue dashed line). The reason is still unclear. Fe is the only bcc structure under investigation, but the fcc-calculations give similar results (see section 9.5). So do the calculations with lower velocities. One uncertainty remains in the parametrization of the MD-potential and the TB-parameters. While the TB-parametrizations are all from the same source, the Fe potential had to be taken from a different (much older) source than the others. But different MD potentials were tested without much effect onto the conductance histogram<sup>3</sup>. An explanation for these could be that while the potentials from Sheng et al. were derived by including huge amounts of DFT calculations, the older potentials found were limited to experimental data only. As consequence the older potentials could lead to slightly wrong energy landscapes in the vicinity of low coordinated structures like few atom contacts, which would lead to a wrong mapping of the different possible geometries.

As the Fano factor results (section 6.2) fit quite well to the experimental findings,<sup>4</sup> [18] the TB-parameters seem not to be the main problem and therefore the results should be valid also for the other electronic properties investigated here.

In contrast to Fe, Co and Ni show more clearly decay paths within the density. Also clear transitions into the tunneling regime are visible, similar or even better than for Al, meaning that the resulting geometries are very rigid and the last breaking bond does not lead to a sudden jump in distance (see the discussion in section 5.1.1).

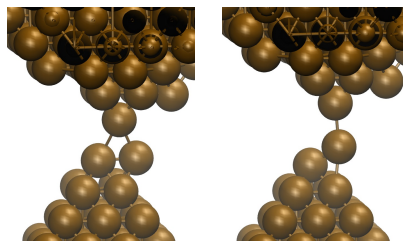


Figure 6.4.: Co in monomer and dimer structure. They are from the same curve and 0.09 nm of elongation separated from each other. The conductance values are:  $1.5G_0$  with 3 and 5 channels in the two spin systems ( $\tau_{\sigma,i} \geq 0.01$ ) and  $1.3G_0$  with 3 and 4 channels.

The peaks at about  $1.3G_0$  and  $2.9G_0$  with a shoulder to higher values for Co and at about  $1.6G_0$  for Ni fit very well to the experimental results (blue dashed line).

The first peak in Fe and Ni are as before in the spin independent materials the most dominant ones. The first peak in Co at about  $1.3G_0$  is an exception, which means that these geometries are much less stable than in other materials. It is built up by one-atom contacts, monomers (one atom connects both halves of the former wire) and dimers (the two halves are connected by a single bond) which is the usual mix for the first peak. An example for each of those two types is shown in Fig. 6.4.

<sup>3</sup>Especially onto the peak-positions.

<sup>4</sup>The Fano factor is not totally independent of the results of the conductance histogram, but under the assumption that the geometries (angles, distances, ...) found in theory are not much different from the ones in experiment, only the frequency of occurrence (histograms) would be wrong.



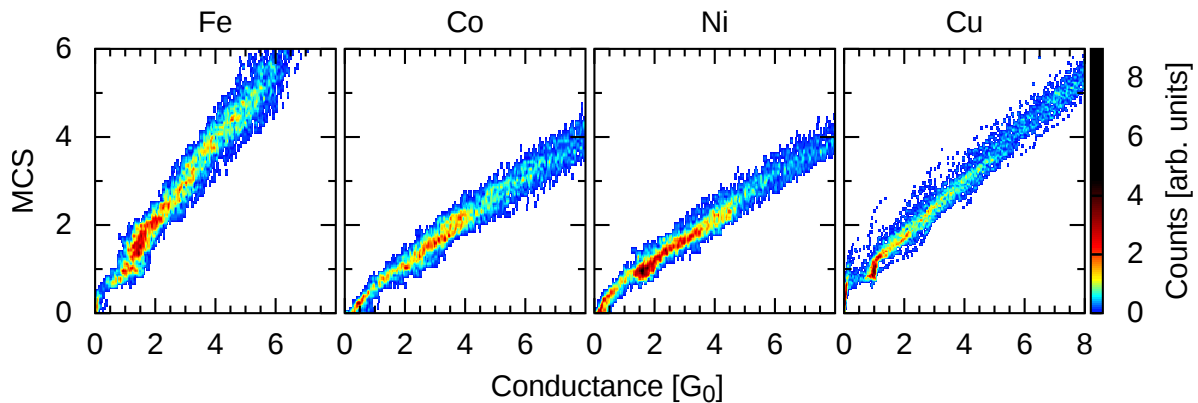


Figure 6.5.: Density plots of the minimal cross section (MCS) as function of the conductance. The slopes for a linear fit ( $ax + b$ ) are 0.91 (Fe), 0.50 (Co), 0.49 (Ni) and 0.59 (Cu).<sup>5</sup>

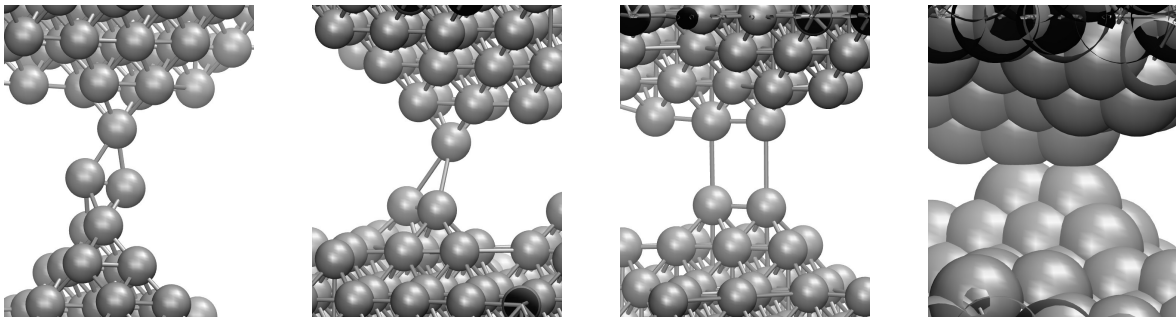


Figure 6.6.: Geometries of Ni contributing to the first peak in the conductance histogram. The values are:  $1.9G_0$  with  $MCS = 1.1$  (first),  $1.5G_0$  with  $MCS = 0.7$  (second) and  $1.3G_0$  with  $MCS = 0.9$  (third). The last geometry is the same as the third but with enhanced diameter of the spheres representing the atoms.

In Fig. 6.5 the relation between the minimal cross section (MCS) and the conductance of the structures is shown for all three materials including Cu as comparison. The relation is interesting because according to the Sharvin formula (see sec. 2.2.1) there should be a univocal relation between both. The figure shows how uncertain the mapping to one another is. While it still fits quite well for Cu, the conductance values are much more spread for a given MCS value (and vice versa) for the ferromagnetic contacts.

A second problem exists in the mapping between MCS value and geometry, which is also not unique. These problems are demonstrated on an example in Fig. 6.6. All three shown Ni geometries contribute to the (relative broad) first peak in the conductance histogram. While the MCS vs conductance works fine within the range of single atom contacts (first and second geometry), it fails to include the third one which constitutes out of parallel atoms in an elongated state. The low MCS value in that geometry is due to only small overlap of the two parallel atoms to their opposite ones as is depicted in the last column of Fig. 6.6. But despite these deviations, the linear relation expected from Sharvin's formula does work on average, but not for the individual geometries.

<sup>5</sup>Using  $ax$  instead would give: 0.98 (Fe), 0.52 (Co), 0.54 (Ni) and 0.64 (Cu)

In the second row of Fig. 6.3 the spin polarization of the conductance (or current) as relative difference between the spin channels is shown. It is defined as

$$Polarization = \frac{I_{\uparrow} - I_{\downarrow}}{I_{\uparrow} + I_{\downarrow}} \quad (6.1)$$

According to the Mott theory the spin polarization should be positive because the transport should be dominated by the majority-spin ( $\uparrow$ ) electrons. While this was experimentally shown to be correct for larger structures<sup>6</sup> [180], this is not what can be seen in Fig. 6.3. Co and Ni have a strictly negative polarization above the single atom contact regime and relative large fluctuations below. The polarization saturates slightly below  $-30\%$ . In contrast Fe saturates at vanishing spin polarization after it exhibits a sign change at about  $5G_0$ . The results in the single atom range (around  $2G_0$ ) are similar to the others, but below that, the fluctuations are even higher. This can be explained by the relative small contribution of the spin-down (minority spin) compared to the other ferromagnetic materials (see discussion of channels below)<sup>7</sup>.

It is interesting to note that the presence of spin-down  $d$  states at the Fermi energy (see Fig. 6.9) leads to a reduction of the conductance of the minority-spin in the bulk case and therefore, to a positive spin polarization, but in the case of few atom contacts of all three materials to additional channels resulting in an enhanced conductance of the minority-spin and therefore a negative spin polarization.

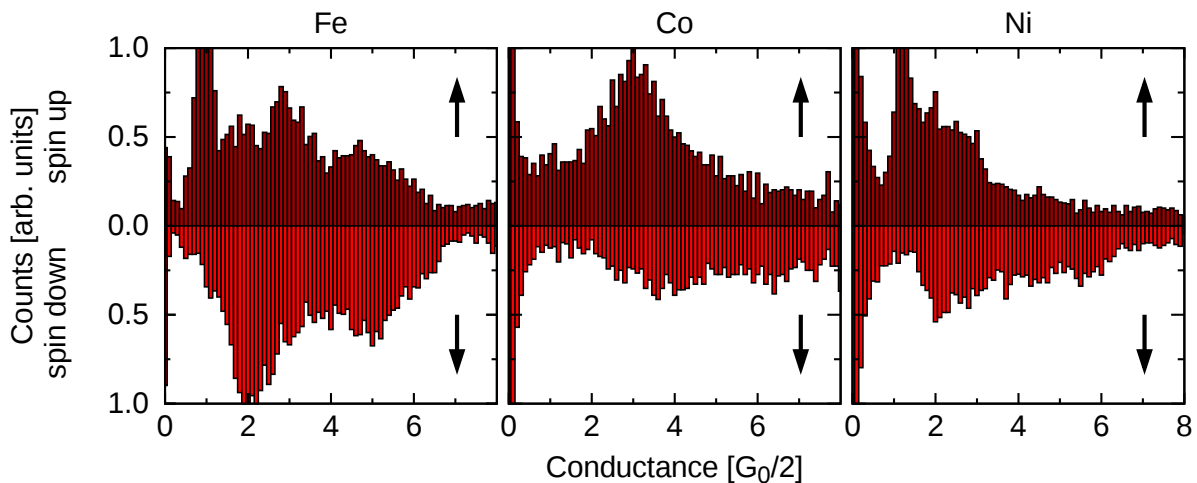


Figure 6.7.: Conductance histograms for the same data set than in Fig. 6.3, but for each spin separately. The unit is therefore  $\frac{1}{2}G_0$ . The histograms of Fe and Ni are cut at 30% and 60% of their particular total height to enhance smaller peaks (like for Au and Cu in Fig. 5.4). The scaling factor is the same for the spin-up and the spin-down histograms.

Fig. 6.7 shows the histograms of the spin-up and spin-down components separately<sup>8</sup>. One can see that for example the broad Fe peak at about  $1.7G_0$  is built up by a relative sharp spin-up peak at about  $1.0G_0/2$  and a broad peak at about  $2.0G_0/2$ .

<sup>6</sup>Larger means far away from the range of single atom contacts.

<sup>7</sup>Compare for example the heights and numbers of spin-up and down channels at  $8G_0$  between Fe, Co and Ni in Fig. 6.8. The sum of the values of the spin-up and spin-down channels has to be the same ( $\tau = \sum_{i,\sigma} \tau_{i,\sigma} = 8$ ).

<sup>8</sup>The sum of both histograms does not correspond to the histogram of the total conductance in Fig. 6.3.

The behavior of the two spin systems are in general very interesting, while the spin-up histograms of Fe and Ni look like Au, their spin-down histograms look more like Pt (see Fig. 5.4). This observation will be discussed more deeply looking at the Fano factors of these materials. Co seems to be more difficult.

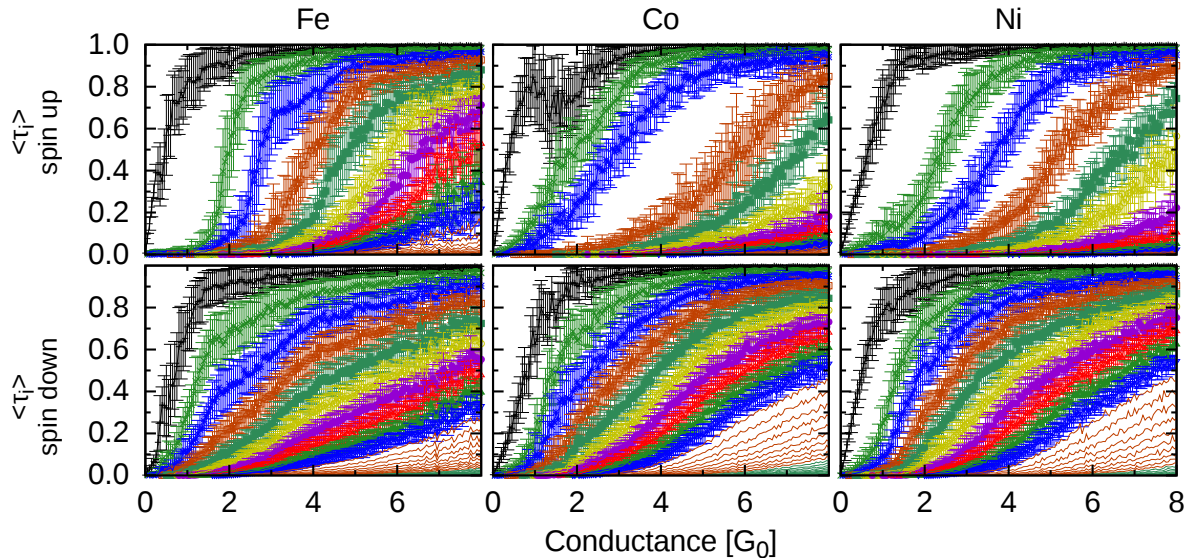


Figure 6.8.: Mean channel distributions of the spin up (upper row) and spin down (lower row) channels with standard deviations of the 10 highest channels of 100 elongation curves each as function of the total conductance.

As already noted in previous chapters the channel distribution gives hints to the polarization and the orbital nature of the spin system. For Fe the transmission is first dominated by the first channel of the spin-up system leading to a positive polarization. But at  $1 G_0$  there are already more than three spin-down channels partially open, while there is still only one in the spin-up system leading to a negative spin-polarization. But because of relative low slopes of the spin-down channels the polarization tends to an unpolarized system at  $8 G_0$ . Co first behaves similar, but at  $1 G_0$  there are about the same number of spin-up channels and spin-down channels leading to an unpolarized system. But while there is a gap between the third and fourth spin-up channel, there is none in the spin-down system leading again to a negative spin-polarization. For Ni the first spin in both subsystems behave at the beginning similar but at about  $1 G_0$  spin-down again dominates the conductance with more available channels than the spin-up system.

So in total the channel distributions of the two spin systems evolve in all three materials very similar leading to very similar polarization as function of the total conductance. Deviations are at very small conductance values and due to different slopes of the channels in the spin-down system at higher conductance values.

The opening of the spin-up channels especially in Ni resembles that of the monovalent metals which are  $s$  dominated conductors. The spin-down channels on the other side remembers more on Pt which has large  $d$  contributions.

This can be analyzed further by looking at the spin dependent DOS calculations of Ni as example for the ferromagnetic materials and of Cu as example for the monovalent metals. Fig. 6.9 shows for both metals the DOS of a monomer and the one of bulk [18].

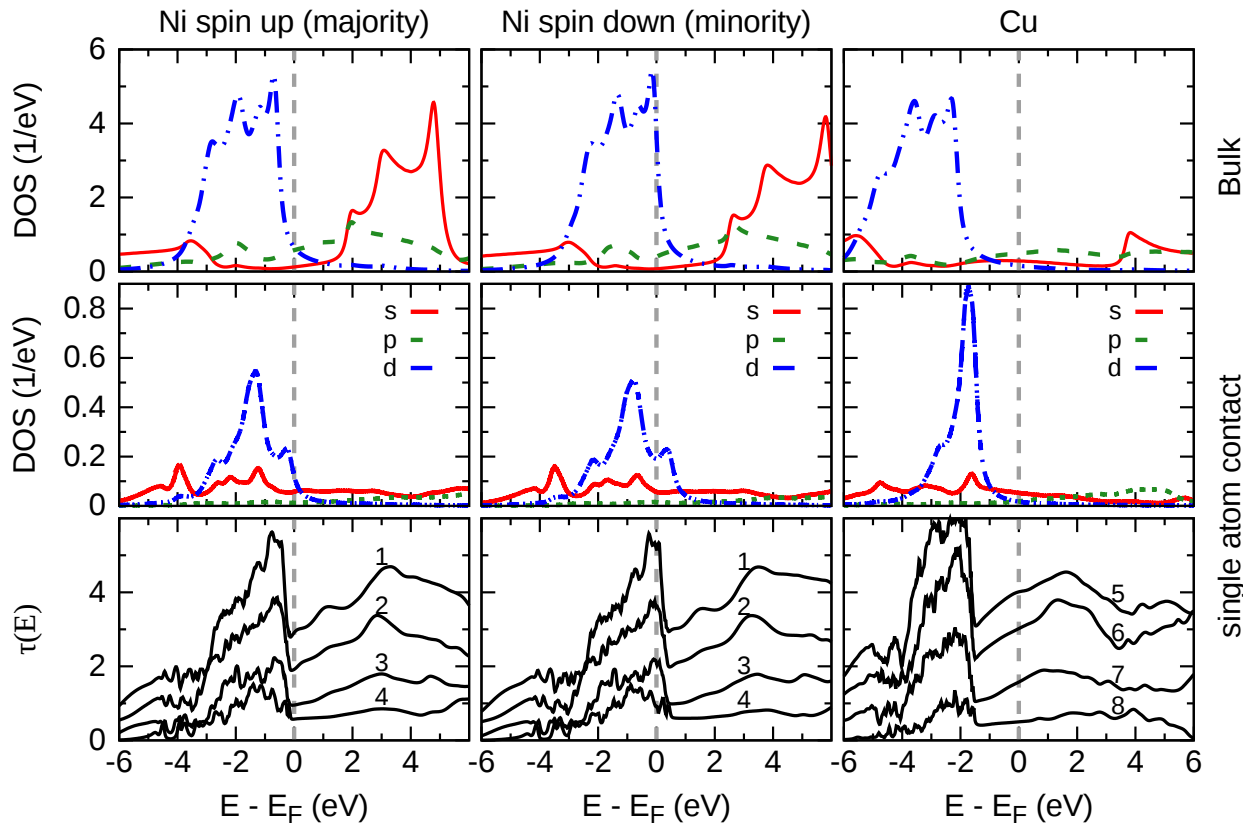


Figure 6.9.: Density of states (DOS) for bulk (upper row) and its projection onto the central atom in a single atom contact (middle row) as function of the energy-difference to the Fermi energy  $E_F$ . The first two columns are Ni, divided into spin up and spin down electrons and the third column is Cu. The orbitals are grouped in contributions from  $3d$ ,  $4s$  and  $4p$  orbitals and normalized by the number of the corresponding orbitals. In the third column the total transmission  $\tau(E)$  of 4 Ni and Cu geometries are plotted as function of  $E - E_F$ . The transmission of Ni is as in row one and two divided into the two spin directions. The geometries are shown in Fig. 6.10 and the position of the atom of the DOS in row two is marked by an arrow. The bulk data are from private communication from Juan Carlos Cuevas.

While for Ni bulk in both spin directions the  $d$  orbitals play the most important and the  $s$  orbitals a minor role (first row), for spin up the situation changes considerably going to one atom contacts (second row) where both contribute similar. In contrast, the spin down  $d$  orbitals are shifted energetically with respect to the Fermi energy resulting in a still  $d$  dominated regime. This is reflected in the total transmission functions (bottom row) which shows that for spin up the Fermi energy is on the right side of the flank and for spin down at its peak.

Cu shows a similar behavior for the few atom contacts as the spin up part of Ni. This is in contrast to the bulk behavior, where the Fermi energy of Cu is still far on the right side of the DOS for the  $d$  orbitals, different to Ni. Having a look at Fig. 5.20 where on the right part the results for Pt are shown, one finds similarities with the spin down results of Ni, as already hinted. But the similarities are only for the  $d$  orbitals and the total transmission, not the contributions from  $s$  orbitals. The  $s$  orbitals show the same behavior and contributions

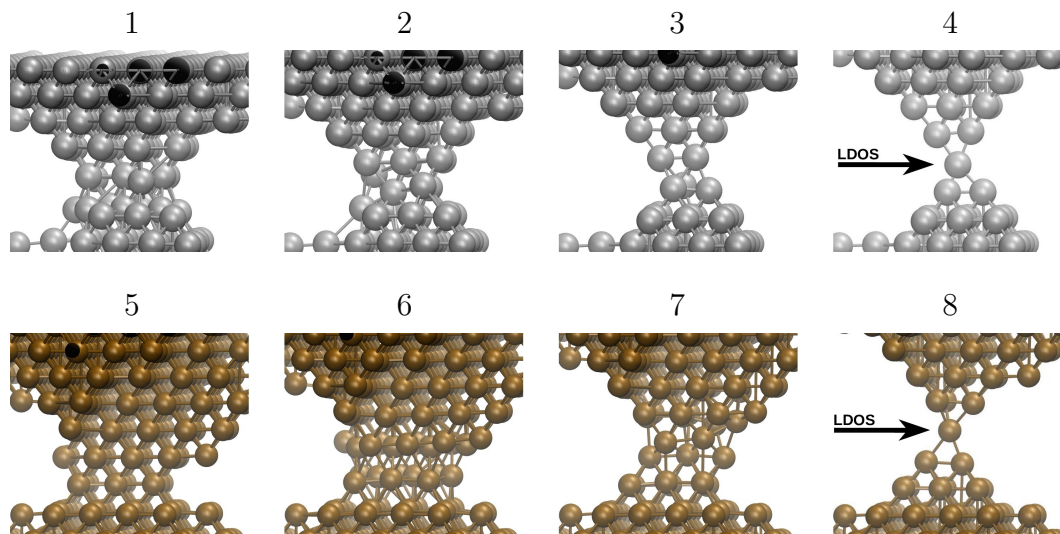


Figure 6.10.: Ni (top) and Cu (bottom) geometries at 4 K used for the calculation of the curves in the bottom row of Fig. 6.9. The number on top of each geometry corresponds to the number of the curves. The last geometry in each row was used for the calculation of the DOS, the corresponding atom is marked by an arrow.

than the  $d$  orbitals in Pt while for Ni the  $d$  orbitals contribute three times more in average<sup>9</sup>. The different transmission curves in the last row show that this explanation is not only valid for the monomer for which the density is shown, but also for higher conductance values of thicker wires.

The  $p$  orbitals were not discussed here because they do not contribute significantly in the few atom contacts (in contrast to the bulk, but this behavior is similar in all three cases).

In total the different behavior of the spin directions can be traced back to a relative shift in energy of the orbitals with respect to each other. In the shown example the relative shift is in the order of  $1/2$  eV.

<sup>9</sup>The orbitals are normalized by their numbers, so 1 for  $s$ , 3 for  $p$  and 5 for  $d$ .

## 6.2. Noise

Similar to the spin independent metals the Fano factor gives access to information about the channel distributions. The experiment has only access to the total Fano factor ( $F = \sum_{i,\sigma} \tau_{i,\sigma}(1 - \tau_{i,\sigma}) / (\sum_{i,\sigma} \tau_{i,\sigma})$ ), but the theory is able to divide it again into the two spin-systems ( $F_\sigma = \sum_i \tau_{i,\sigma}(1 - \tau_{i,\sigma}) / (\sum_i \tau_{i,\sigma})$ ). So while the total Fano factor is important to compare with experiments, the spin dependent plots give more insight into the physical backgrounds.

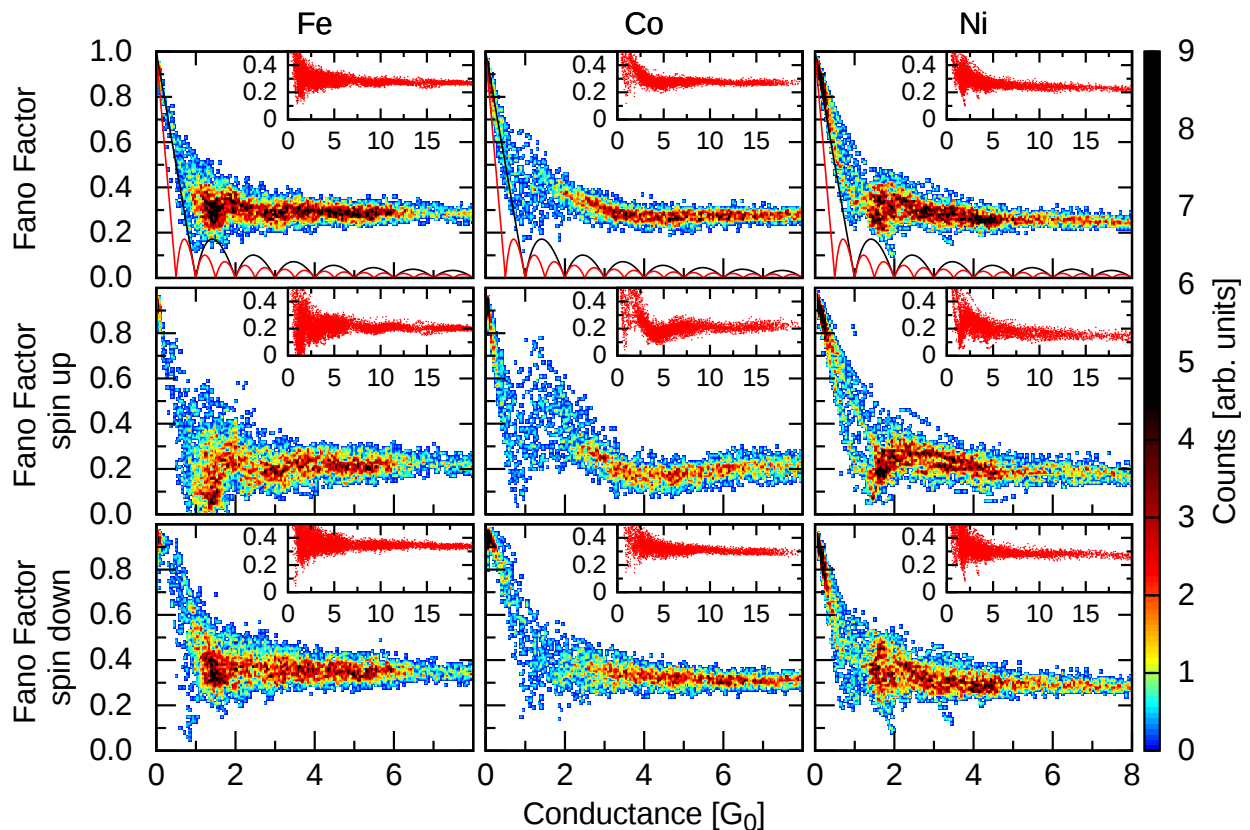


Figure 6.11.: Density plots of the Fano factor data of 100 elongation curves each as function of the total conductance. The upper row is the Fano factor of all channels, the lower two rows show the Fano factor of the individual channels normalized by their channel conductance. The densities are normalized to an upper limit of 9. The insets are scatter plots of the data points.

Different to the spin independent metals the total Fano factor of the spin dependent metals have a second line (red) which presents the minimal Fano factor for full spin-polarization ( $F_{min}^{pol}$ ), which is lower than the unpolarized one ( $F_{min}$ ). They are given as function of the total transmission  $\tau$  by

$$F_{min}(\tau) = 1 - [int(1\tau) + \{\tau \cdot 1 - int(1\tau)\}^2] / [1\tau] \quad (6.2)$$

$$F_{min}^{pol}(\tau) = 1 - [int(2\tau) + \{\tau \cdot 2 - int(2\tau)\}^2] / [2\tau] \quad (6.3)$$

They are derived using the assumption that the channels open one by one up to full trans-

mission<sup>10</sup> (lowest possible Fano values). This means that the measured Fano factor can already give a hint for spin-polarization. Even the (minimal<sup>11</sup>) degree of polarization can be estimated if the measured point is below the  $F_{min}$  curve [181, Fig. 4].

The results in Fig. 6.11 show a few data points of Fe in the tunneling regime below  $1 G_0$  and at about  $1.3 G_0$  between the  $F_{min}$  and the  $F_{min}^{pol}$  lines. Co only shows data points between the two lines in the tunneling regime and Ni does not show such points. The experimental results from Vardimon et al. [18] (and in Fig. A.10) do not show any hint of polarization.

The spin resolved results reveal two interesting points, namely that the spin-up values are much lower than the spin-down ones and that the spin-up results show regions with largely suppressed Fano factors and large spread at the same time while the spin-down results don't show this in a significant manner. This reminds again of the difference between the results for the monovalent metals and Pt. While the monovalent metals show suppression at multiples of  $G_0$  and a bridging<sup>12</sup> of the dip at  $2 G_0$ , Pt shows mainly a suppression at  $2 G_0$  and has in total much higher values.

	Fe	Co	Ni
total	$0.28 \pm 0.02$	$0.27 \pm 0.02$	$0.24 \pm 0.02$
spin up	$0.21 \pm 0.02$	$0.21 \pm 0.02$	$0.16 \pm 0.03$
spin down	$0.35 \pm 0.02$	$0.30 \pm 0.02$	$0.28 \pm 0.02$

Table 6.1.: Overview of the convergence results. The results are gained by fitting the Fano values above  $5 G_0$  by a horizontal line. Compare Table 5.1 for the values of the spin independent materials.

To get values which are more easy to compare one can look at the convergence fits (table 6.1). There the spin-up values converge near 0.2 (Au was at 0.16) and the spin-down values around 0.3 (Pt was at 0.27).

Ni is with 0.16 for spin-up and 0.28 for spin-down within the error at the values of Au and Pt. The other two have slightly higher noise values.

Related to this is the question of how close to the bimodal distribution the channel distributions at  $15 G_0$  are (Fig. 6.12). As result one can say that they are all closer than the results shown for the spin independent metals except for Pt. The spin-up results of Fe and Ni deviate most from the bimodal distribution as could be expected from the convergence results of the Fano factor, but Co spin-up which has the same convergent value as Fe spin-up looks almost perfectly fit to the black line. That the spin-down results fit quite well to the bimodal distribution could again have been suspected.

Looking at the evolution of this histograms by making one at  $2 G_0$  one finds that the spin-down results of all three materials still look similar, having a sharp and strong peak at very low transmissions and a broad peak below and above one half and no contributions from fully open channels.

<sup>10</sup>For example  $\tau = 1.9$  would mean  $\tau_1 = 1, \tau_2 = 0.9$ .  $\tau = 2.1$  would mean  $\tau_1 = 1, \tau_2 = 1, \tau_3 = 0.1$ .

<sup>11</sup>Spin-polarization lowers the Fano factor, but even full spin-polarization could lead to values above the  $F_{min}$  curve (it is only the minimal possible value).

<sup>12</sup>The 'two ways'.

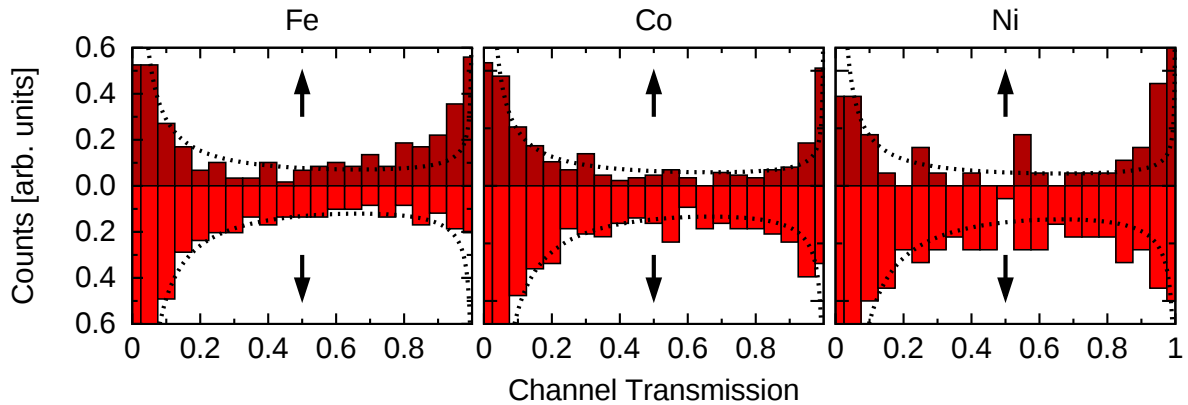


Figure 6.12.: Histograms of the transmission coefficients at a total conductance of  $15 \pm 0.125 G_0$ . The results are separated into the contributions from the spin-up channels (up) and spin-down channels (down). The lines are the fitted bimodal distributions  $P(\tau)$  (equation 5.3).

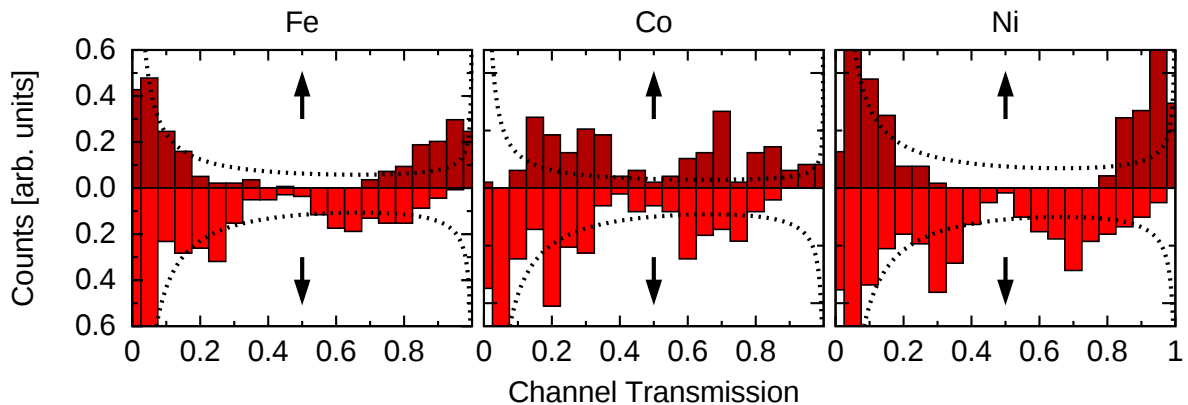


Figure 6.13.: Histograms of the transmission coefficients at a total conductance of  $2 G_0$ .

In contrast the spin-up histograms of Fe and Ni have a low and a high conductance peak with fully open channels. So the negative spin-polarization is due to a high number of slightly open spin-down channels which oppose a small number of fully and almost closed spin-up channels. The Co spin-up histogram is again more similar to the spin-down one but having no peak at very low eigenvalues. Instead it has fully open channels like in the other two materials.

This information can partially be seen in the mean channel distributions of Fig. 6.8, too.

The Fe and Ni spin-up histograms are already similar to the Au results, but not for Au at  $2 G_0$  but rather at  $1 G_0$  (see Figs. A.8 and A.9 in the appendix). This can be understood by considering the effect of the spin-polarization of about  $-0.3$  at  $2 G_0$  (Fig. 6.3) which means that spin-down contributes on average with about  $2.6 G_0/2$  and spin-up with about  $1.4 G_0/2$ , which is near  $1 G_0$ .<sup>13</sup>

<sup>13</sup>In the spin independent picture both spin directions would contribute  $2 G_0/2 = 1 G_0$ .



### 6.3. Thermopower and thermal conductance

Thermopower and thermal conductance are gained by integrating the energy dependent transmission (with some prefactors) around the Fermi energy (equation 2.181). Therefore these values are very sensitive to the orbital structure of the materials. In the earlier sections we have seen that the  $d$  orbitals play an important role in the understanding of the properties of these ferromagnetic metals. As this was also the case for Pt we expect similar results.

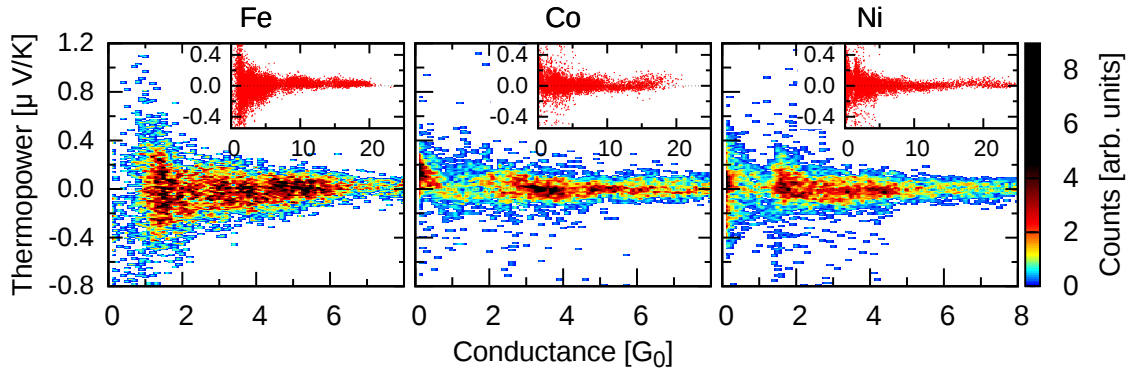


Figure 6.14.: Density plots of the thermopower data of 100 elongation curves each as function of the total conductance. The densities are normalized to an upper limit of 9. The insets are scatter plots of the data points.

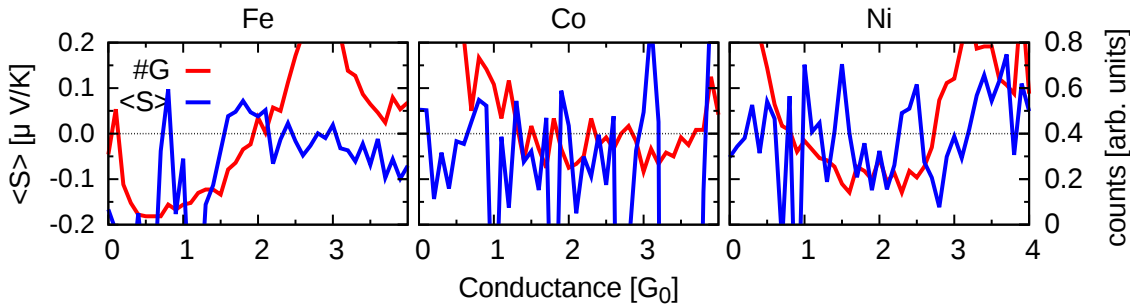


Figure 6.15.: Conductance histogram (red) and mean thermopower (blue) as function of the total conductance.

And indeed, comparing Figs. 6.14 and 6.15 of the ferromagnetic metals with Pt in Figs. 5.19 and 5.22 one finds very similar results: a large spread of the density around zero and huge fluctuations of the mean. But while the mean of Pt still had a positive preference, it fluctuates around zero for the ferromagnetic materials with a slight tendency to negative values.

Similar results for the thermal conductance (Fig. 6.16), while Pt was prone to numerical problems so are Co and Ni. Fe interestingly not. The problems arise as before for Pt only in the limit of a few  $G_0$ . In numbers, about 1.4% of Co and 0.2% of Ni data points (above  $0.1 G_0$ ) have a deviation greater than 1%. But without explicit testing one can not exclude all points as numerical cases but the tests done so far indicate that at least most of the points deviate due to numerical issues. Therefore the Wiedemann-Franz law is perfectly fulfilled for (almost) all points.

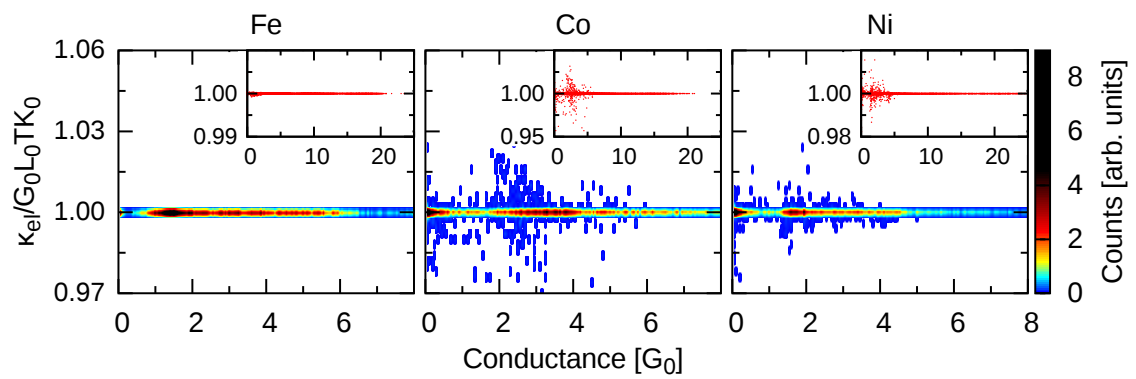


Figure 6.16.: Density plots of the ratio of  $\kappa_{el}$  to  $L_0TG$  of data from 100 elongation curves each as function of the total conductance. The densities are normalized to an upper limit of 9. The insets are scatter plots of the data points.

## 7. Results for Au, Pt and Ni at room temperature

Most applications in daily life are not designed to work at very low temperatures, but rather at room temperature where no cooling is needed. Room temperature means in our case 300 K. Some experiments at room temperature were already mentioned. Examples are the ones on thermopower which found non-vanishing average values for Au with oscillations as function of the contact size [16,81] which contradicts the low temperature experiments and calculations [73,80]. For bulk materials it is known that different to low temperatures where the phonon drag contribution plays an important role, the thermopower is dominated by the electron diffusion contribution [17,182]. Thus the sign and magnitude of the thermopower of bulk metals at room temperature depends mainly on the energy dependence of the conductance around the Fermi energy and therefore on the characteristic density of states around the Fermi energy. But as we already have seen in the last sections, the density of states of few atom contacts differ clearly from those of bulk systems. Hence it is reasonable that the sign and amplitude of the thermopower results could depend on both, size and temperature. Other recent room temperature experiments looked for example for the conductance and shot noise and their variances [183–185].

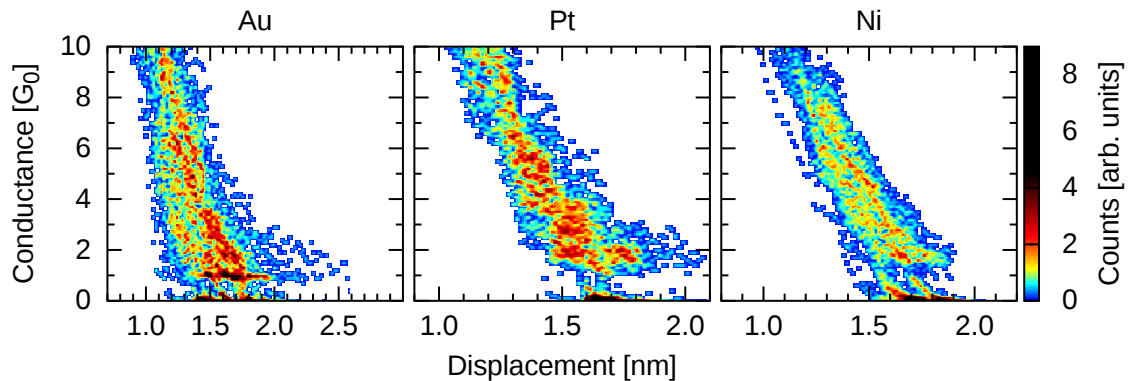


Figure 7.1.: Density plots of the total conductance data of 100 elongation curves each as function of the displacement of their upper walls to the initial positions. The densities are normalized to an upper limit of 9.

Temperature in the context of theoretical simulations means first of all the kinetic energy in the MD calculation which should modify the behavior of the materials during the elongation process. It should make configurations less stable because more energy is available to overcome barriers, but also geometries not known from low temperatures could be possible [5]. This modifications in the geometries are the basis for the modifications in the statistical results.

A second point where the temperature explicitly is included is the energy window needed for the calculations of the thermopower and the thermal conductance. The thermal conductance has in addition an explicit temperature dependence<sup>1</sup>.

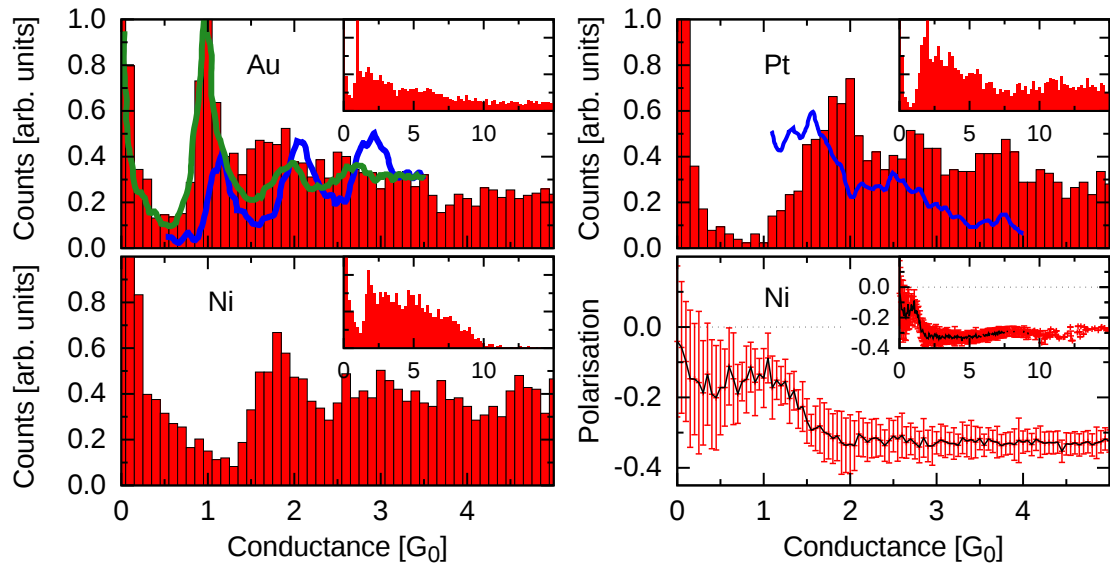


Figure 7.2.: Conductance histograms (upper row and lower row left) and polarization of Ni (lower row right) of 100 elongation curves each as function of the total conductance. The blue curves are the experimental results from the group of Nicolás Agraït<sup>2</sup> [16] and the green ones are from the group of Douglas Natelson<sup>3</sup> [15], both at room temperature. The insets show the same theoretical results up to 15  $G_0$ .

The analyzes of the effects were done for three materials Au, Pt and Ni that were studied in previous sections at low temperatures. The initial geometries with 563 atoms in the central wire are the same as in the 4K studies and the results will be presented in the following in an equivalent manner.

The total conductance results as function of the displacement are similar to those at low temperatures, but for Au the plateau at 1  $G_0$  is much shorter and in total much less pronounced (Fig. 7.1). This is also reflected in the conductance histograms (Fig. 7.2), but there it is visible that it does not only concerns Au, but the first peak of all three materials. That can be explained in terms of kinematics where energy barriers, separating different geometric configurations, can be more easily overcome<sup>4</sup> at higher temperatures (energies). This effect also leads to less variation in the paths seen in the displacement curves and should lead

<sup>1</sup>See section 2.4.2 and 2.4.3 for further details.

<sup>2</sup>The experiments in the group of Agraït were done with an STM setup with notched wires at room temperature. The temperature differences for the corresponding thermopower measurements were chosen between 20 and 40 K. The statistics include 909 Au and 216 Pt traces. The experiments were done by Charalambos Evangelis and Laura Rincón-García.

<sup>3</sup>The experiments in the group of Natelson were done with an STM setup at room temperature in air with a bias of 180 mV. The statistics include 816 traces.

<sup>4</sup>Atomic reorganizations.

to less pronounced higher peaks in the histograms. But for Pt, in contrast, peaks at about  $2.0 G_0$ ,  $2.7 G_0$  and  $3.8 G_0$  are visible while in the low temperature results only a peak at  $1.8 G_0$  clearly appears. The mechanism behind it is unclear. It seems that at higher temperatures Pt is able to achieve more stable configurations not easily accessible at low temperatures.

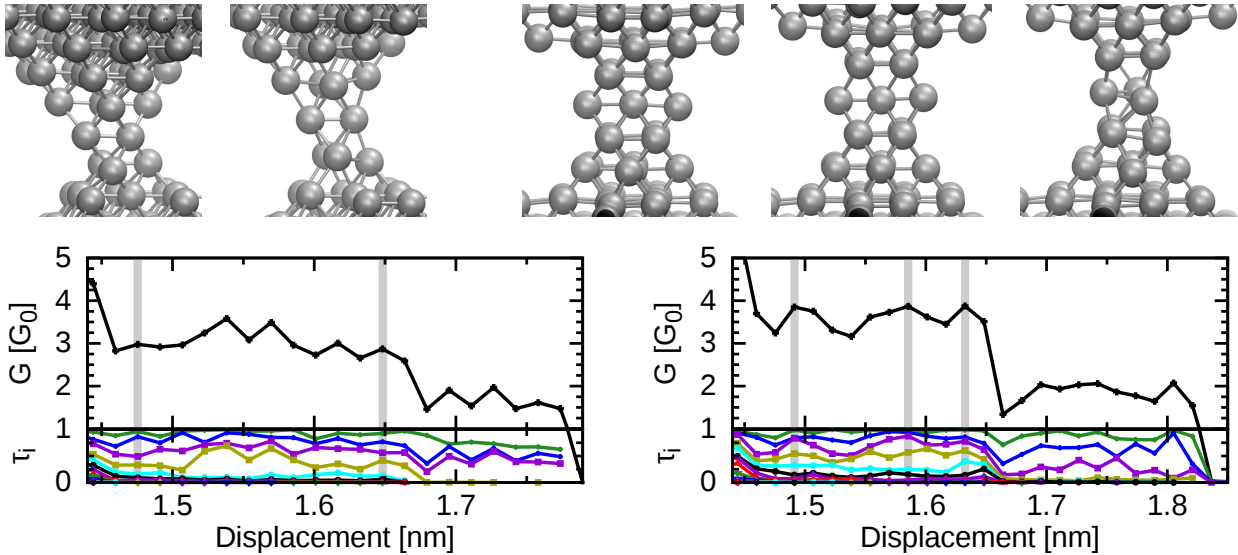


Figure 7.3.: Geometries of Pt at 300 K with  $3.0 G_0$  and  $2.9 G_0$  (first and second geometry, belonging to one curve) and  $3.8 G_0$ ,  $3.9 G_0$  and  $3.9 G_0$  (geometries 3 to 5, belonging to one curve). The first two geometries are separated by  $0.17 \text{ nm}$ , geometry three and four are separated by  $0.09 \text{ nm}$  and four and five by  $0.05 \text{ nm}$  of elongation<sup>5</sup>. Below are the conductance and channel transmissions of the two curves. The gray bars mark the positions of the geometries above.

Pt geometries of two curves with long lifetimes, one at the second peak and one at the third peak, are plotted in Fig. 7.3. The difference between the two geometries of the first curve are only elastic elongation of the bonds between the atoms. In this way the geometry is very stable and survives more than  $0.17 \text{ nm}$  of elongation<sup>6</sup>. The same can be told about the first two geometries of the second curve. But the third geometry of the second curve which still has about the same conductance looks different and is not very stable. It gets modified several times during the  $0.06 \text{ nm}$  of elongation during which the plateau exists.

For Ni the situation is different. There the higher temperature seems to reduce the range of elongation paths: It takes about  $0.1 \text{ nm}$  longer to reduce the conductance below  $10 G_0$  and about  $0.2 \text{ nm}$  more to break compared to the low temperature results. At the same time the time needed to fall below  $10 G_0$  stays similar and for breaking even reduces slightly by  $0.1 \text{ nm}$ .

The difference can be explained with the geometries shown in Fig. 7.4: The higher temperature of  $300 \text{ K}$  and with that the higher kinetic energy allows a reconstruction of the surfaces during the elongation process, leading to two conical halves touching each other at

<sup>5</sup>The corresponding times are:  $440 \text{ ps}$  (geometries 1 and 2),  $240 \text{ ps}$  (geometries 3 and 4) and  $120 \text{ ps}$  (geometries 4 and 5). The conductance time-step is  $40 \text{ ps}$ , the MD time-step is  $1 \text{ fs}$ .

<sup>6</sup>Elongation means elongation of the walls.

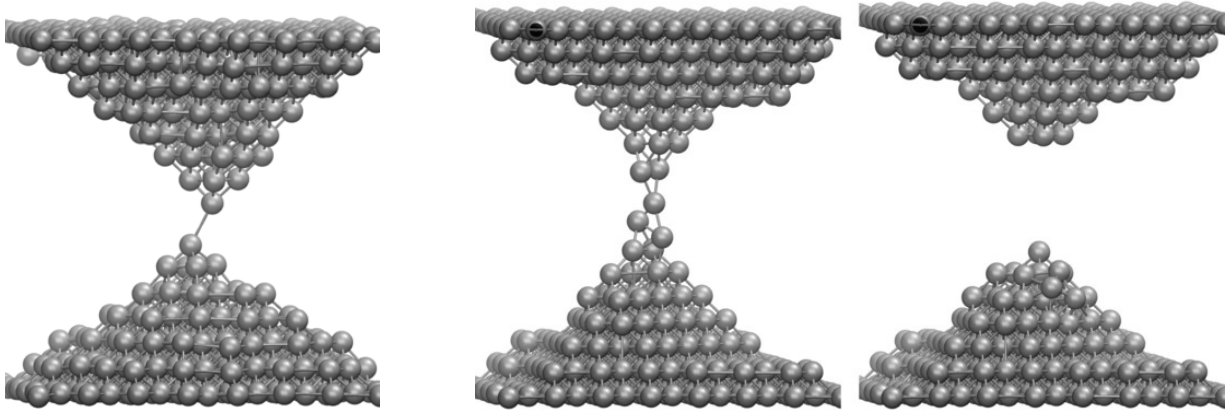


Figure 7.4.: Left: A typical geometry of Ni at 300 K shortly before rupture. The rupture proceeds smoothly, meaning that the two halves keep their geometries while the one bond connecting the parts breaks in a continuous way. Right: A geometry before and after breaking which was only found at 4 K. Here the rupture process is not smooth, but it breaks in a very short timescale in connection with a snapping back of the atoms in the connection onto the lower part.

their tips (left geometry in Fig. 7.4). At low temperatures, on the other hand, the kinetic energy is not high enough for this reconstruction, leading to surfaces which are locally well ordered. Furthermore, at low temperatures it is possible to create small wires with two atoms in diameter, leading to the second geometry in Fig. 7.4 shortly before rupture. At room temperature the geometry would have been relaxed to an energetically more preferable (broken) configuration. This elongated structure rips in the way already seen for Au chains in Fig. 5.3 of section 5.1 (right geometry in Fig. 7.4).

This faster decay compared to low temperatures leads to a reduction of data points at low conductance values which is visible in the overall height of the conductance histogram but also in the density plots like for the Fano factor or thermopower data.

The mean polarization of Ni has not changed in comparison to the low temperature calculations.

The room temperature results from Evangelini et al. (blue lines in Fig. 7.2) show clear peaks in the Au histogram at about  $1.2 G_0$ ,  $2.1 G_0$  and  $2.9 G_0$  which is slightly shifted upwards by about  $0.2 G_0$  with respect to the theoretical ones here. The results for Pt in the same work show small and broad peaks at about  $1.6 G_0$  and  $2.5 G_0$ . This time the shift is in the opposite direction by about the same amount of  $0.2 G_0$ . Similar is the crossing in the relative peak heights between the experimental and theoretical histograms: While the experimental Au histograms show the better pronounced ones, for Pt they are better pronounced in theory. Other experimental results from the literature (for example the green line in Fig. 7.2) show much better agreement with our theoretical results.

The Ni histogram<sup>7</sup> was investigated by Moriguchi et al. [186] in 2012 with the MCBJ technique at room temperature<sup>8</sup>. Their histogram shows weak and very broad peaks at about

<sup>7</sup>Together with Fe and Co.

<sup>8</sup>The experiments of Moriguchi et al. were done with the MCBJ technique at room temperature with a pressure of  $2 \cdot 10^{-10}$  mbar and at a separation speed of the leads of 0.7 pm/s. The bias was set constantly

$2.5 G_0$  and  $5 G_0$  which they interpreted as background. This is in contrast to the theoretical results in Fig. 7.2 where at least one clear peak at about  $1.8 G_0$  can be found<sup>9</sup>.

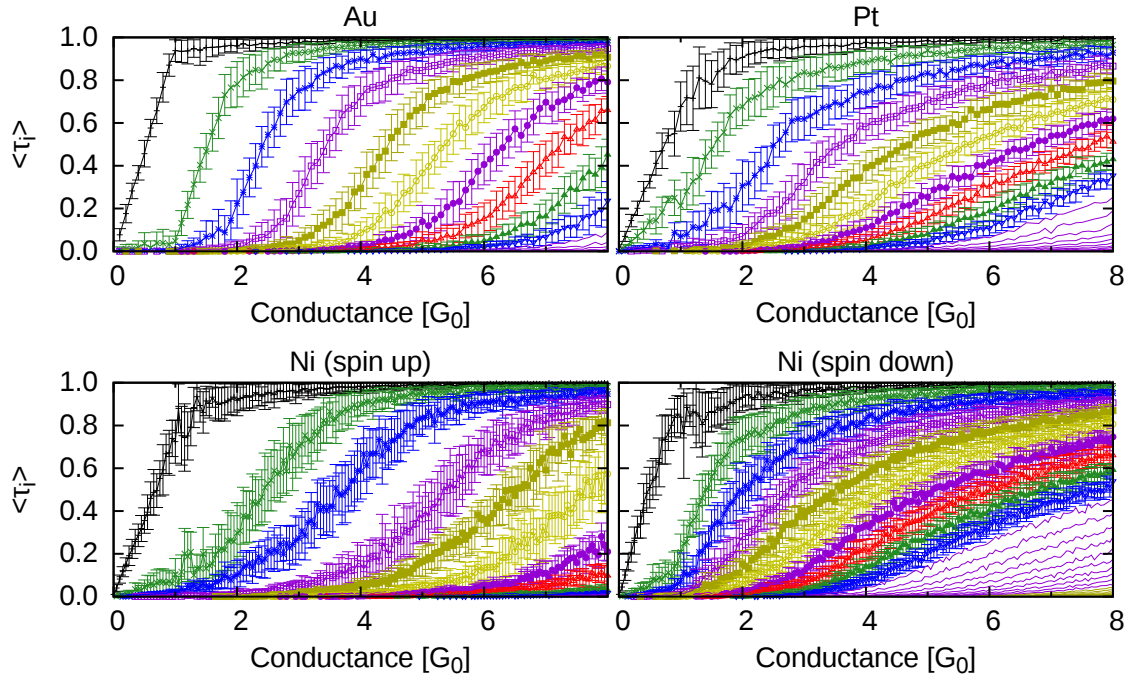


Figure 7.5.: Mean channel distributions with standard deviations of the highest 10 channels of 100 elongation curves each as function of the total conductance.

The mean channel distributions (Fig. 7.5) are almost identical to their counterparts at low temperature. An exception is Au at about  $0.5 G_0$  where the peak of the second channel is much less pronounced at room temperature. This is due to the already discussed reduced probability of parallel wires (see section 5.2).

Au	Pt	Ni (total)	Ni (spin up)	Ni (spin down)
$0.15 \pm 0.02$	$0.27 \pm 0.02$	$0.25 \pm 0.02$	$0.16 \pm 0.02$	$0.29 \pm 0.02$

Table 7.1.: Overview of the convergence results. The results are gained by fitting the Fano values above  $5 G_0$  by a horizontal line.

The Fano factor shown in Fig. 7.6 for room temperature looks very much the same as for those materials at low temperatures with a few exceptions. The tendency goes to slightly smaller values of about 0.01. This could mean that the geometries are slightly more relaxed, meaning that they achieve energetically more preferable configurations as compared to their low temperature counterparts. This is reasonable considering the higher kinetic energy with respect to the energy barriers between different local minima in the configuration space and was already discussed for Pt above in context of Fig. 7.4.

The results for the fitted horizontal lines for the plateaus at higher conductance values (Table 7.1) are within the error the same as for the low temperature cases which is also reasonable

to 100 mV. The statistics includes 5100 traces on 4 specimens.

<sup>9</sup>In the experimental histogram a small peak at about  $1.7 G_0$  could be interpreted as real, but it is more likely noise.

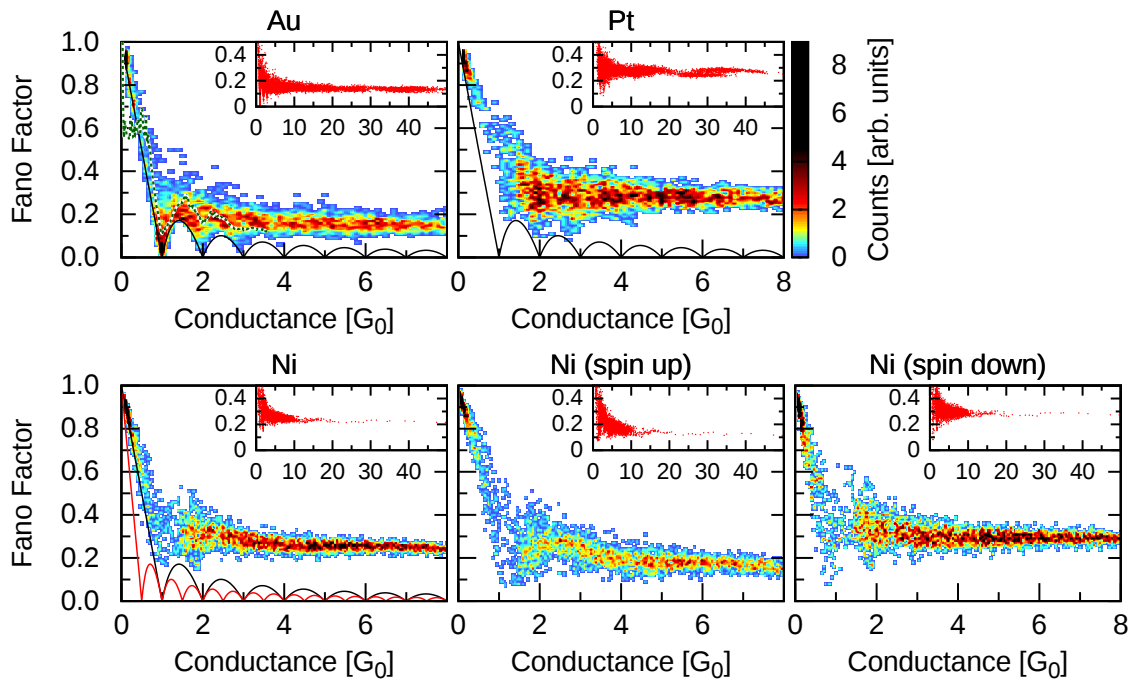


Figure 7.6.: Density plots of the Fano factor data of 100 elongation curves each as function of the total conductance. Ni is divided into three panels: the total Fano factor (lower left) and the Fano factor of the individual channels normalized by their channel conductance each as function of the total conductance. The densities are normalized to an upper limit of 9. The insets are scatter plots of the data points. The green-white dotted line in the Au plot presents the mean results from experiments of the group of Douglas Natelson [15].

because the larger structures<sup>10</sup> are more stable against temperature compared to the ones with only few atoms in the bottleneck at small conductance values. Therefore one expects only small modifications of the available configuration space<sup>11</sup> at room temperature, far below the melting temperature of about 1337 K for Au ([187])<sup>12</sup>.

For Au the ‘two ways’ going from  $1 G_0$  to  $3 G_0$  discussed intensively for the low temperature Fano factor results are smeared out as expected for higher temperatures and the very low branch is now missing. The latter is again due to the loss of parallel wires summing up to  $2 G_0$ .

The distribution of the transmission coefficients at  $15 G_0$  is as expected qualitatively the same as at 4 K (Figs. 5.12 and 6.12): Au and Ni spin-up are far away from the bimodal distribution while Pt and Ni spin-down are more close. The Ni histograms constitute of only relative few data points, but at least the trend is visible.

The thermopower results shown in Fig. 7.8 look similar to the results at low temperatures taking in account the different scaling because of the approximately linear dependence of the thermopower from temperature. An exception is Ni where a shift to positive values can be seen. The mean thermopower in Fig. 7.9 shows more: For Au the strange peaks around  $1 G_0$  are gone and there are clear minima in the amplitude at the positions of the

<sup>10</sup>Needed to get higher conductance values.

<sup>11</sup>Geometries

<sup>12</sup>Pt: 2041 K, Ni: 1728 K [187].



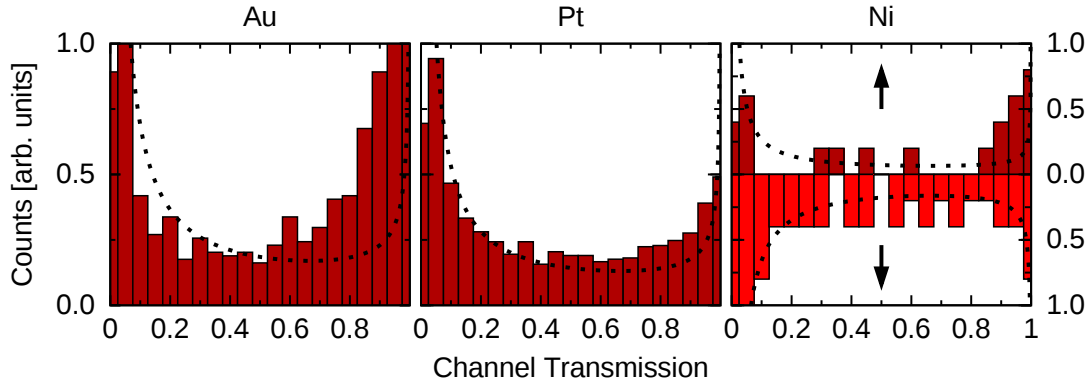


Figure 7.7.: Histograms of the transmission coefficients at a conductance of  $15 \pm 0.125 G_0$ . Ni is separated into the contributions from the spin-up channels (up) and spin-down channels (down). The lines are the fitted bimodal distributions  $P(\tau)$  (equation 5.3).

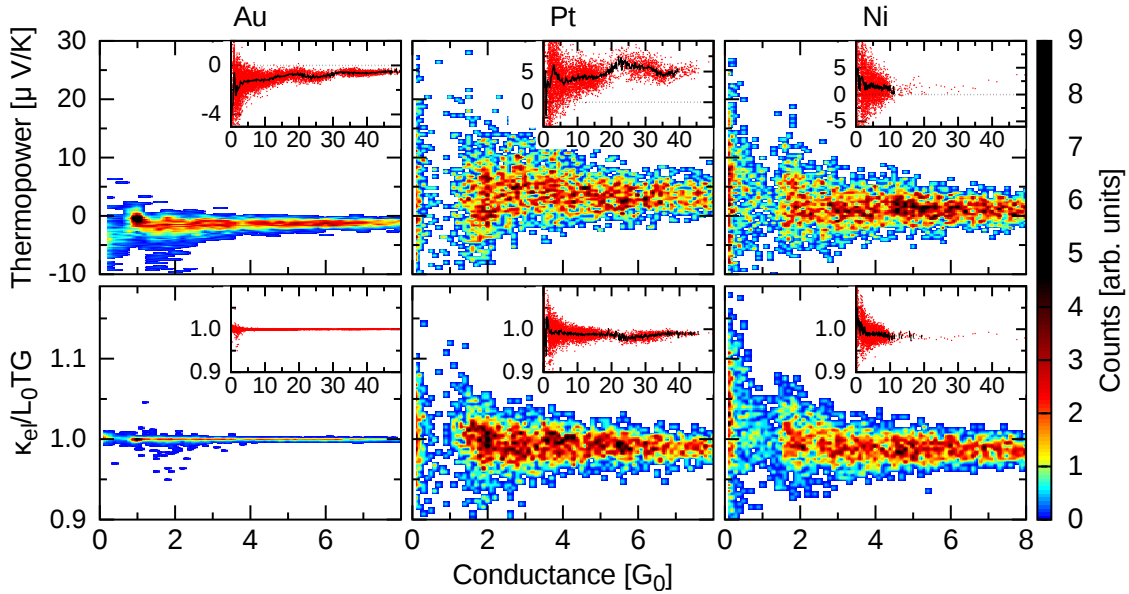


Figure 7.8.: Density plots of the thermopower (upper row) and the ratio of  $\kappa_{el}$  to  $G_0 L_0 T K_0$  (lower row) data of 100 elongation curves each as function of the total conductance. The densities are normalized to an upper limit of 9. The insets are scatter plots of the data points with its mean values as black line. As guide for the eye a black dotted line is plotted into the thermopower insets.

maxima of the conductance histogram. Especially at  $1 G_0$  the thermopower almost vanishes. This is consistent with the experimental results from Evangelini et al. [16] (dotted lines) and was already discussed in the context of the results at low temperatures (section 5.4). For Pt the mean values are strictly positive without the dip at  $1.8 G_0$  which was seen at low temperature, consistent with the experimental findings (dotted lines).

Finally Ni has changed its oscillatory behavior around 0 at low temperature to a finite, positive mean thermopower with large fluctuations.

The results for the thermal conductance of Pt and Ni (second row of Fig. 7.8) shows large enhanced deviations compared to their low temperature results. Au on the other side shows

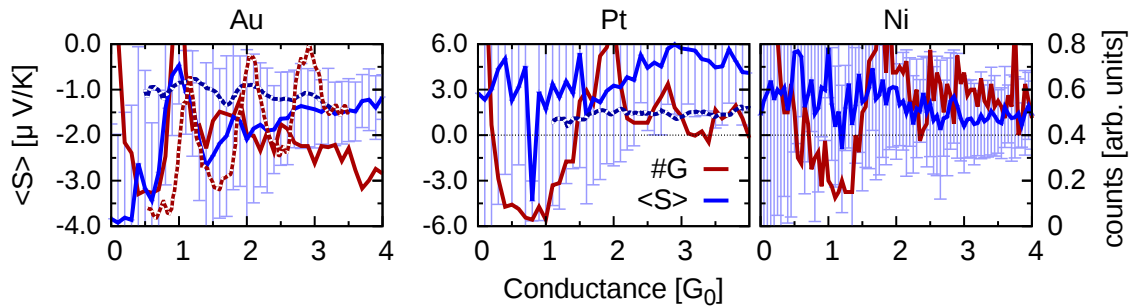


Figure 7.9.: Conductance histogram (red) and mean thermopower (blue) with standard deviation (light blue) as function of the total conductance. The dotted lines are the experimentally determined results for the conductance of Au (red) and thermopower of Au and Pt (blue) from the group of Nicolás Agraït<sup>2</sup> [16].

again almost the perfect linear conductance dependence of the Wiedemann-Franz law.

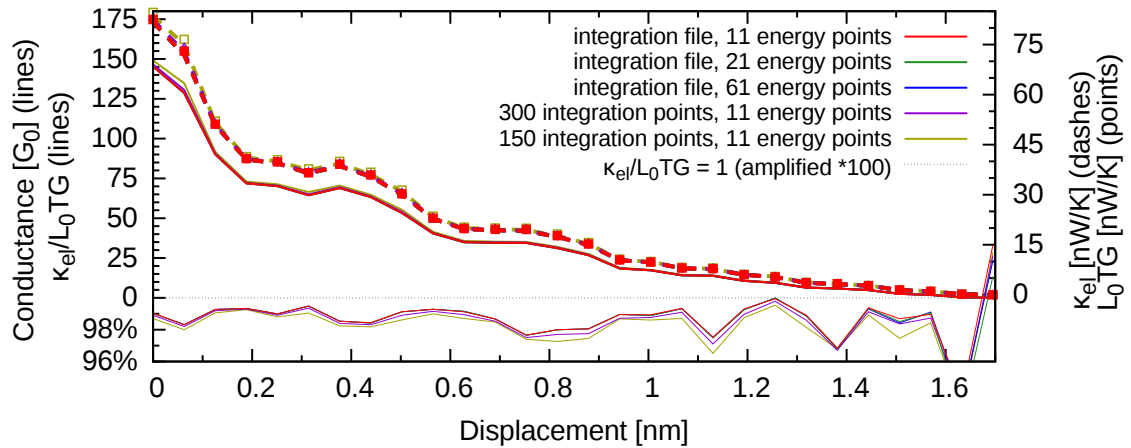


Figure 7.10.: Parameter tests for the calculation of the conductance and thermal conductance for a Pt elongation curve. The red curve is with 149 optimized sampling points for the integration of the (energy dependent) density (file) in the charge neutrality loop and 11  $\tau(E)$  points ( $E_F \pm 5$  points) for the calculation of the thermopower and thermal conductance (the default). The relation between  $\kappa_{el}$  and  $L_0TG$  is plotted with an offset to be centered around 0 instead of 1 as in the plots before and the deviation to 1 is enhanced by a factor of 1000 according to the left axes. The black dotted line at 0 is a guide for the eye.

To test if this is again only a numerical problem, a Pt opening curve was calculated using the default file with 149 sampling points with optimized positions along the integration line for the calculation of the (energy dependent) density in the charge neutrality loop with different numbers of the total transmission as function of energy for the calculation of the thermopower and thermal conductance. Further more two sets of equally spaced sets of integration points for the density were tested. The results are presented in Fig. 7.10. The features are in all sets the same. Most deviation shows the yellow one which is with 150 equally spaced integration points the most imprecise one. The effect of the number of total transmission points is negligible.

As result one can state that the deviations from the Wiedemann-Franz law are, different to

those at 4 K, no numerical artifacts, but physically relevant results.

This result can be expected looking at the energy dependence of the transmission near the Fermi energy (Figs. 5.10 and 5.20). While it is relative flat on a longer range in Au, it is strongly energy dependent in Pt. The latter is also the case for Ni (Fig. 6.9). While the important energy window increases with increasing temperature, the non-linearity grows in importance with growing temperature and leads to deviations from the linear law.



## 8. Influence of the crystallographic elongation direction on AI

Up to now every wire was elongated in the  $\langle 100 \rangle$  direction. But is it really the experimental relevant case and what is the difference if one elongates into other directions?

This questions arose in the context of electromigration experiments from Christian Schirm et al. who established bistable switches of Al at the nanoscale with conductance values of the plateaus in the order of a few  $G_0$  [14]. The theoretical analysis shows that this switches can be realized by geometric configurations who have to switch only the position of one atom or to break/reconnect a few bonds. While in the context of [14] this was only demonstrated in the  $\langle 111 \rangle$  direction, this will be shown in the following also in the  $\langle 100 \rangle$  and  $\langle 110 \rangle$  directions. To do this 500 curves of each direction were calculated at a temperature of 0.25 K.

Additional analysis like in the sections before will be presented to compare the three directions with each other and with known experimental data.

### 8.1. Comparison between elongation directions and with experimental data

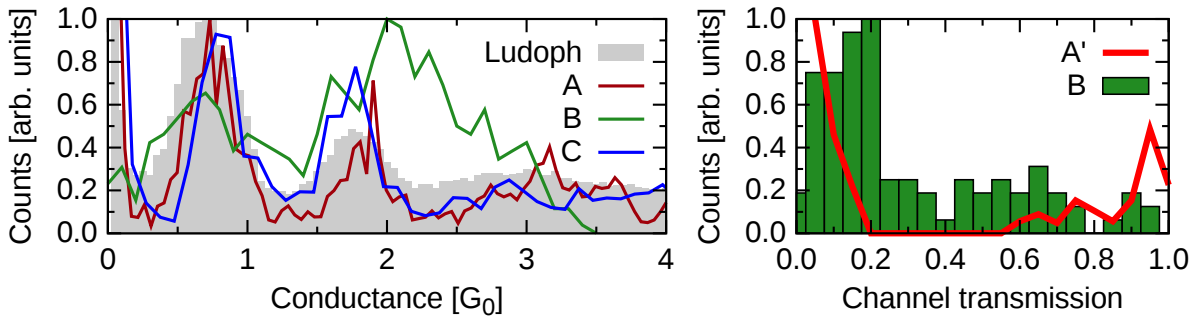


Figure 8.1.: Experimental conductance histograms (upper row) and channel transmission histograms at  $1 \pm 0.125 G_0$ . Samples A (28863 points at 0.25 K), B (433 points at 0.25 K) and C (7855 points at 10 K [188]) are from the group of Elke Scheer. The histogram in the background is from B. Ludoph et al. [189] and includes 2800 traces. Sample A' is a subset of A where besides the conductance the channel transmission was determined.

Some experimental (MCBJ) results are summarized in Figs. 8.1 and 8.2. The aim of sample B was to get good channel measurements in combination with electromigration experiments (see next section). They are mainly from the group of Elke Scheer, but also data from other groups are included for comparison. The histograms show peaks at around  $0.7 G_0$  and  $1.8 G_0$ . The mean channel distributions around  $1 G_0$  show mainly small channel openings, some intermediate ones and (almost) no fully open ones. The effect of this channel distribution is

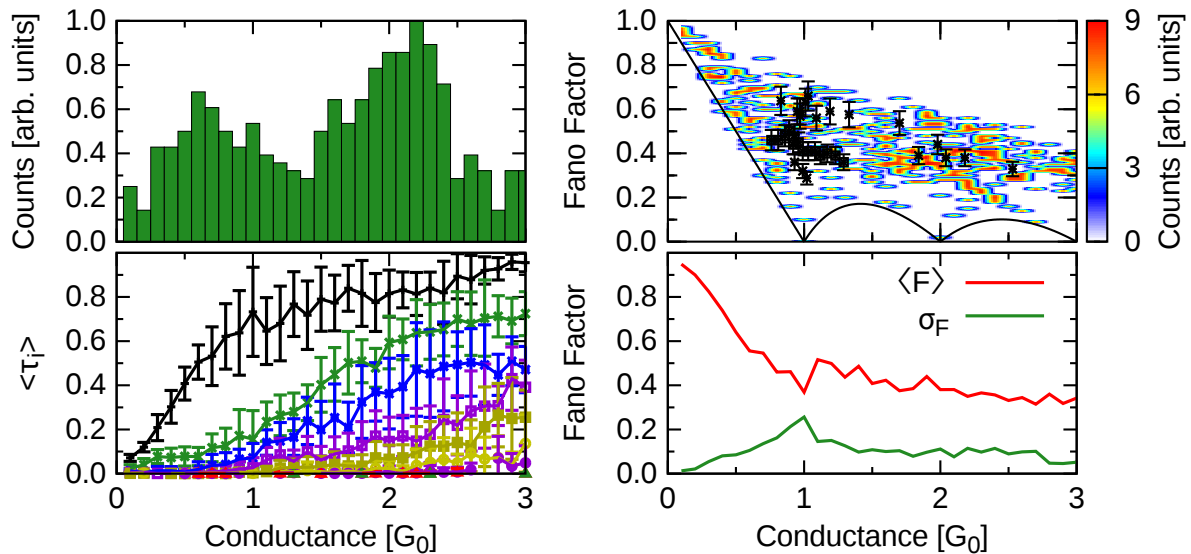


Figure 8.2.: Experimental conductance histogram (upper left), mean channel distribution (lower left) and Fano factor density (upper right) with mean value  $\langle F \rangle$  and standard deviation  $\sigma_F$  (lower right) from sample B. The results are partly published in the supporting information of [14]. In the Fano factor density results from Brom et al. from [190] are included as points with error bars.

that at  $1 G_0$  the first channel is in mean far from completely open (shown for sample B in Fig. 8.2). The slow opening of the first channel is compensated by a bunch of other channels opening at the same time. The corresponding Fano factor distribution shows relative high values (consistent with the direct measurement of Brom et al. [190]) with only a small dip of the mean and a peak of the standard deviation at  $1 G_0$ .

Beginning the theoretical results as usual with the conductance versus displacement density plots (upper part of Fig. 8.3) one finds three very different behaviors for the three different elongation directions and they differ all by what was shown for the larger contacts elongated into the  $\langle 100 \rangle$  direction (Fig. 5.2). Most significant is the position and spread in displacements at which the contacts break. While it was with roughly  $0.5 \text{ nm}$  relative sharp for the large contacts between about  $1.5$  and  $2.0 \text{ nm}$ , the small ones break with an about three times larger spread starting at about  $1.0 \text{ nm}$  in the  $\langle 100 \rangle$  and  $\langle 111 \rangle$  and at about  $1.5 \text{ nm}$  in the  $\langle 110 \rangle$  direction. Because of the smaller structures the shift to smaller displacements at rupture was expected. The  $\langle 100 \rangle$  direction has the smallest spread of this three and the  $\langle 111 \rangle$  the largest.

The force needed to elongate the wire further (bottom line in Fig. 8.3) shows as expected a roughly linear decay<sup>1</sup> with large spread.

An exception is the  $\langle 110 \rangle$  direction below about  $1.2 \text{ nm}$  which shows an increase with very low spread. This can be explained with the example shown in Fig. 8.4: The first rupture at  $0.11 \text{ nm}$  leads to grain boundaries (blue circle in geometry 2) moving towards the walls with every rupture (geometry 2 to 4). The new phase under tension is also fcc-like, but with a different orientation. The following geometric reorganizations need less force and due to the symmetry of the processes about the same amplitude. This changes after about  $1.4 \text{ nm}$

<sup>1</sup>With decreasing cross section in the bottleneck the number of bonds which have to be elongated also decreases.

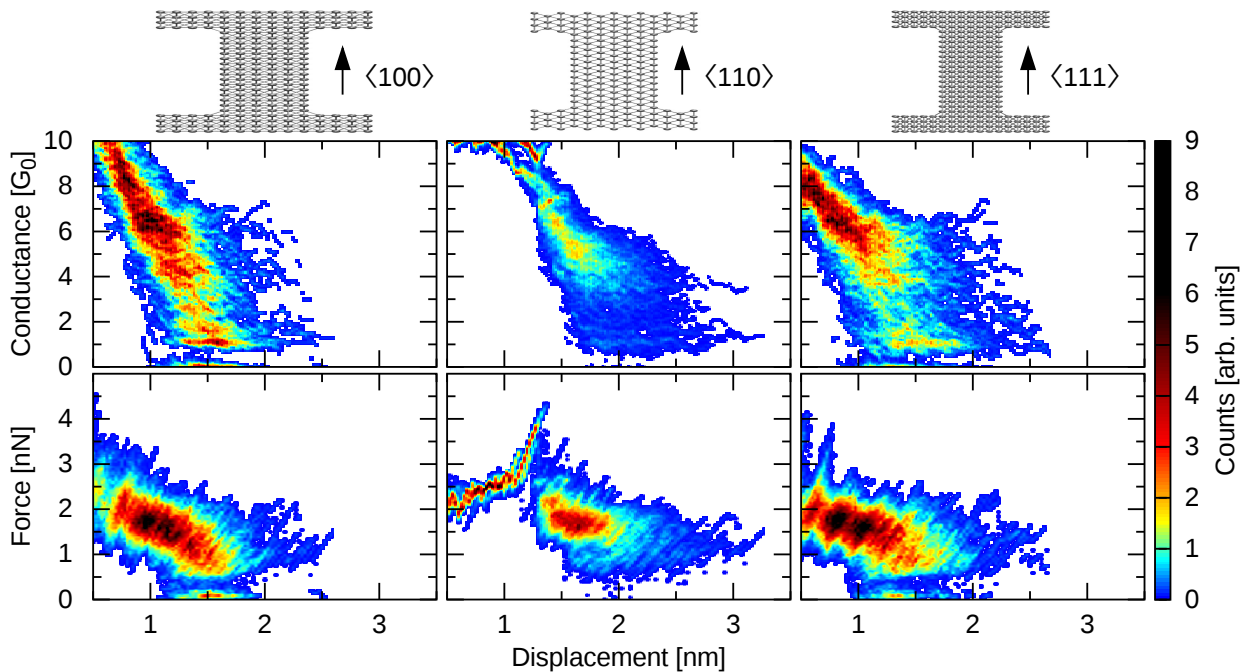


Figure 8.3.: Density plots of the total conductance (upper row) and force (lower row) data of 500 elongation curves with about 300 atoms (288 for  $\langle 100 \rangle$  (first column), 316 for  $\langle 110 \rangle$  (second column), 301 for  $\langle 111 \rangle$  (third column)) in the central wire each as function of the displacement of their upper wall to its initial position for Al. The densities are normalized to an upper limit of 9.

(geometry 5) where the rupture does not modify the borders between the two highly symmetric phases any more but leads to a constriction with disorder (blue circle) which behaves as known from other materials and the other two elongation directions. Geometries 3 and 4 are similar in symmetry and hence have very similar conductance values. The range in between shows several geometric rearrangements and therefore no flat conductance plateau. The new phase which seems to be energetically preferred with tension disappears after the breaking (geometry 7).

As most properties are not shown as function of the displacement but as function of the conductance<sup>2</sup> Fig. 8.5 shows again the force needed to elongate the wire further, but this time as function of the total conductance with mean value and standard deviation. Starting from  $1 G_0$  upwards, the relation between those two properties is mostly linear<sup>3</sup>.

But the detailed mapping is not so easy as the example in Fig. 8.6 shows. There are well defined regions as for example the increase in force going from  $14 G_0$  to  $13 G_0$  which is just the region around geometry 2 in Fig. 8.4 and shows an elastic deformation<sup>4</sup> in combination with a decreasing conductance till a plastic deformation<sup>5</sup> leads to an abrupt decrease in the force curve. But there are also regions for example around  $4.5 G_0$  (after about 1.8 nm) or  $10.5 G_0$  (between geometry 3 and 4) which show loops. They arise because of increasing

<sup>2</sup>As already discussed the displacement is not uniquely defined in experiments.

<sup>3</sup>Below  $1 G_0$  starts somewhere the tunneling regime.

<sup>4</sup>Elongation of bonds.

<sup>5</sup>Reorganization of atoms/breaking of bonds.

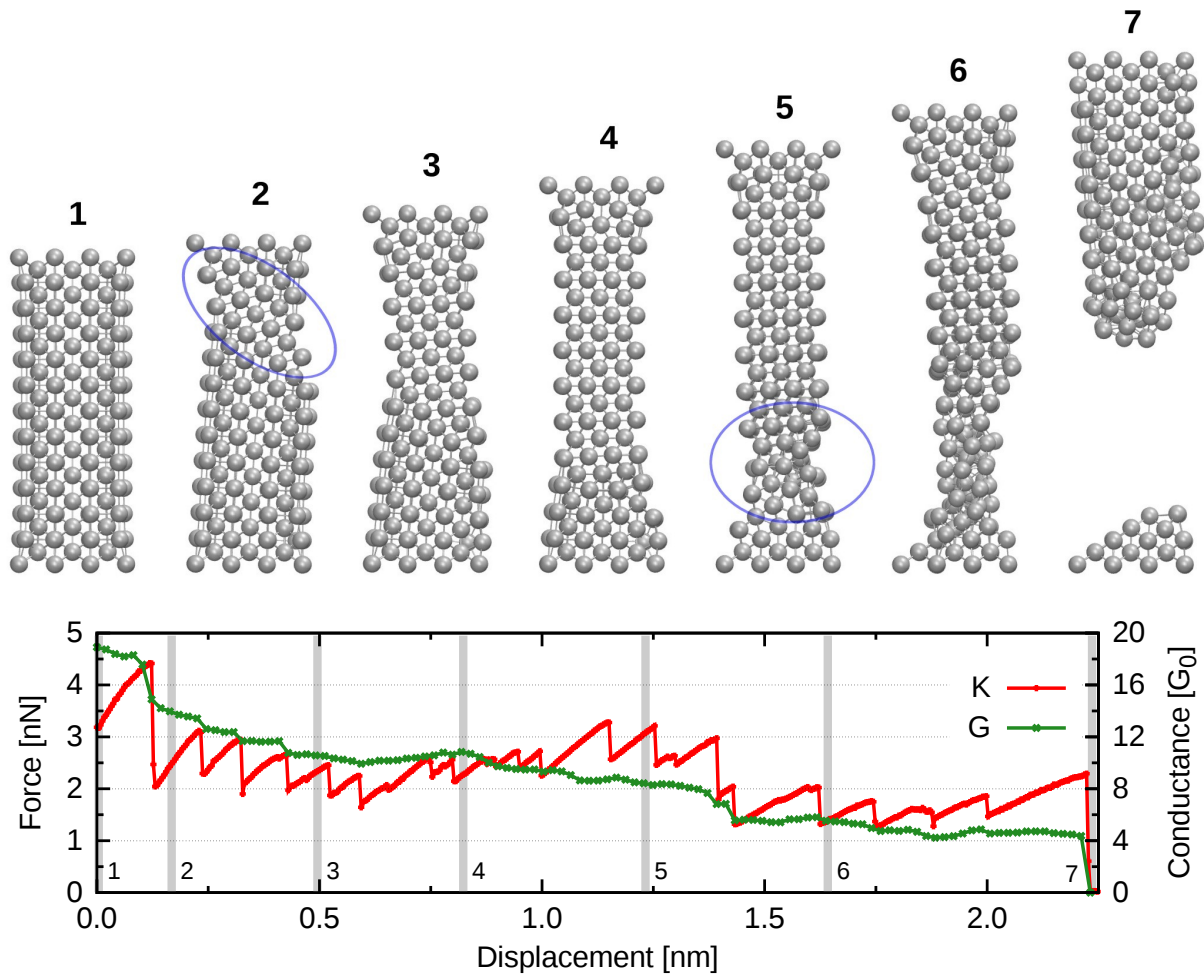


Figure 8.4.: Geometries of an example of an elongation along the  $\langle 110 \rangle$  direction (top) and the corresponding conductance and force curve as function of the displacement (lower part). The positions of the geometries are marked in the lower row by gray bars.

conductance values as function of displacement during elastic or plastic deformations. That is what can be seen at about  $1 G_0$  and  $1.5 G_0$  in the  $\langle 100 \rangle$  and at about  $1.5 G_0$  in the  $\langle 110 \rangle$  direction.

The conductance histograms show further differences between the elongation directions. While in the  $\langle 100 \rangle$  direction a peak every about  $0.8 G_0$  is visible, it is only about every second of them in the  $\langle 110 \rangle$  and  $\langle 111 \rangle$  direction. In experiments (Fig. 8.1) the peaks are separated by about  $1.0 - 1.2 G_0$ . The positions depend on the kind of samples used (thin-film break junctions as used by the group of Elke Scheer contain more disorder and other defects which leads to a broadening of the peaks and a shift to lower values [10]).

The mean channel distributions show a fast saturation of the first channel in the  $\langle 100 \rangle$  direction and a slow one in the  $\langle 111 \rangle$  direction. The  $\langle 110 \rangle$  direction is in between. This is reflected in the suppression of the Fano factor at  $1 G_0$  which is prominent in the  $\langle 100 \rangle$  but not in the other two directions. It still plays a role at higher conductance values leading to different fitting results of the horizontal line to the Fano factor values. The result are  $0.23 \pm 0.04$  ( $\langle 100 \rangle$ ),  $0.27 \pm 0.02$  ( $\langle 110 \rangle$ ) and  $0.27 \pm 0.03$  ( $\langle 111 \rangle$ ).

The experimentally observed slow opening of the first channel and the relative high Fano



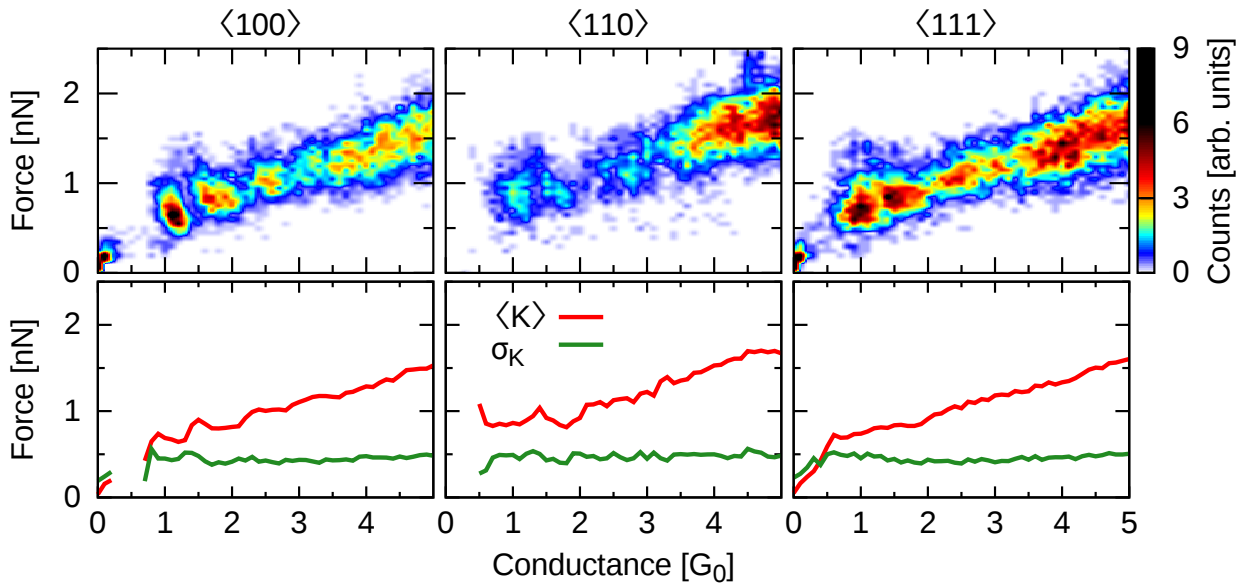


Figure 8.5.: Density of force (upper row) and its mean  $\langle K \rangle$  with standard deviation  $\sigma_K$  (lower row) as function of the total conductance. The densities are normalized to an upper limit of 9.

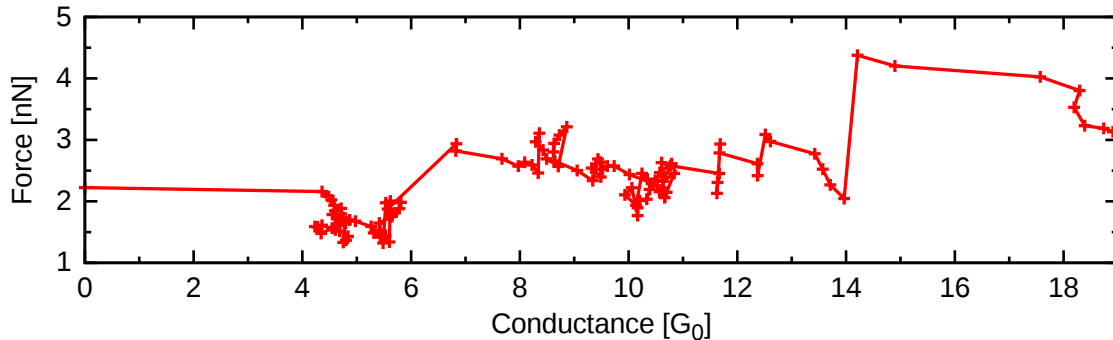


Figure 8.6.: Force vs conductance with the same data as in Fig. 8.4. The data points are ordered according to their appearance during the elongation process.

values without large suppression at  $1 G_0$  (Fig. 8.1) fit best to the  $\langle 111 \rangle$  direction. This is shown in more detail in the channel analysis at  $1 G_0$  in Figs. 8.1 (experiment) and 8.8 (theory). With finite contributions from half open channels and almost no fully open ones the  $\langle 111 \rangle$  direction, different to the other two, fits very well to the results from sample B. In contrast, with a small range of almost closed channels and a broad one of highly up to fully open channels, the  $\langle 100 \rangle$  fits best to the A' sample. The results are consistent with the calculations from Cuevas et al. [10] where an idealized one atom contact in the  $\langle 111 \rangle$  direction was assumed<sup>6</sup>.

The mean thermopower also differs between the three directions: while it is strictly negative or zero in the  $\langle 100 \rangle$  direction, it is about zero with a slight tendency at low conductance values toward negative values in the  $\langle 111 \rangle$  direction and it fluctuates around zero in the  $\langle 110 \rangle$  direction. In all cases  $\sigma_S$  is much larger than the mean value itself.

This behavior can be explained by looking at the energy dependent DOS and transmission

<sup>6</sup>Some statistics was introduced by introducing random fluctuations of the atomic coordinates.

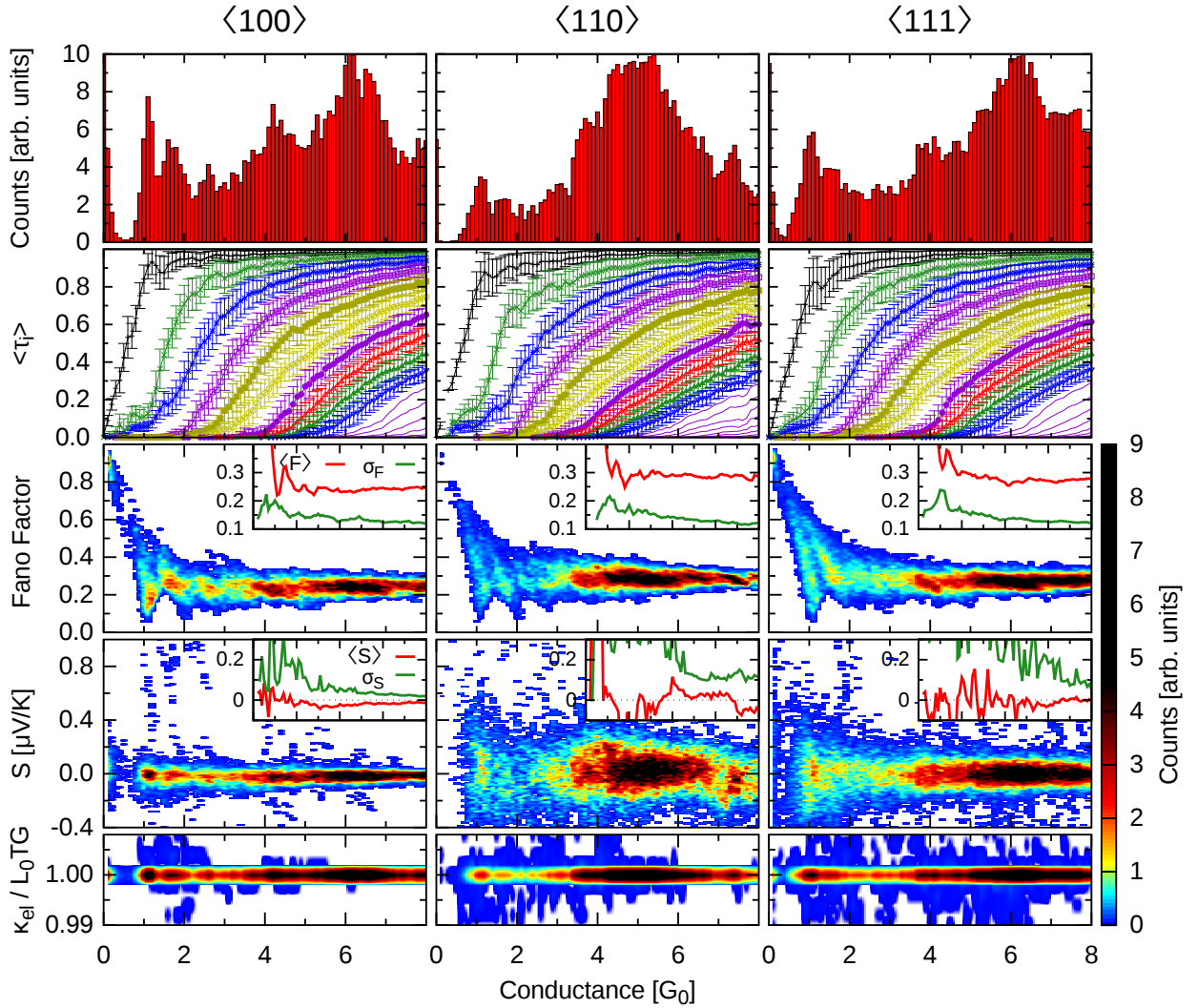


Figure 8.7.: Conductance histograms (first row), mean channel distributions with standard deviations (second row) and density plots of the Fano factor (third row), thermopower (fourth row) and the ratio of  $\kappa_{el}$  to  $G_0 L_0 T K_0$  (fifth row) for Al at 0.25 K (4 K for the thermopower data) with about 300 atoms (288 for  $\langle 100 \rangle$  (first column), 316 for  $\langle 110 \rangle$  (second column), 301 for  $\langle 111 \rangle$  (third column)) in the central wire each as function of the total conductance. The histograms are normalized to an upper limit of 10 and the densities to an upper limit of 9. The standard deviation of the Fano factor ( $\sigma_F$ ) in the insets is shifted upwards by 0.1.

calculations (Fig. 8.9). While the  $s$  orbitals in the dimer examples show a negative energy dependence near the Fermi energy, the  $p$  orbitals show a more complex behavior, compensating each other partially. This leads to a complex energy dependence of the transmission curves. The relative smooth one in the  $\langle 100 \rangle$  direction compared to the other two and its clear positive tendency explains the slightly negative thermopower with the relative small spread of this direction.

The Wiedemann-Franz law (last row in Fig. 8.7) is in all three directions fulfilled.

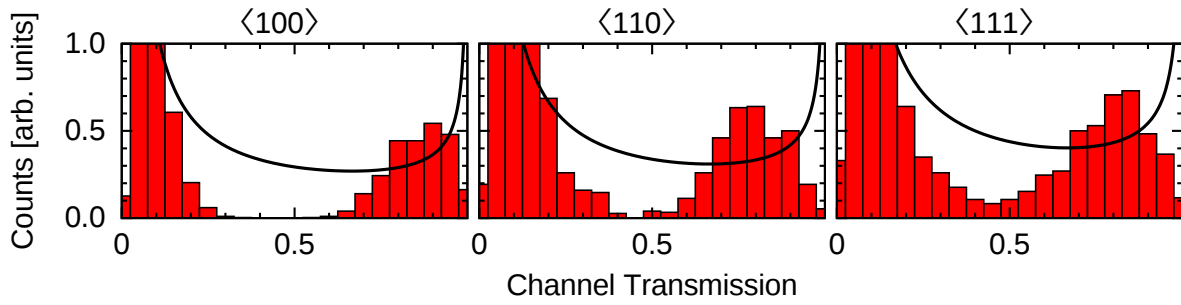


Figure 8.8.: Channel transmission histograms at  $1 \pm 0.125 G_0$  of the three elongation directions together with a fit of the bimodal distribution. The bar at 0 is almost zero because only channels  $> 0$  are included ( $0 < \tau_i < 0.025$ ).

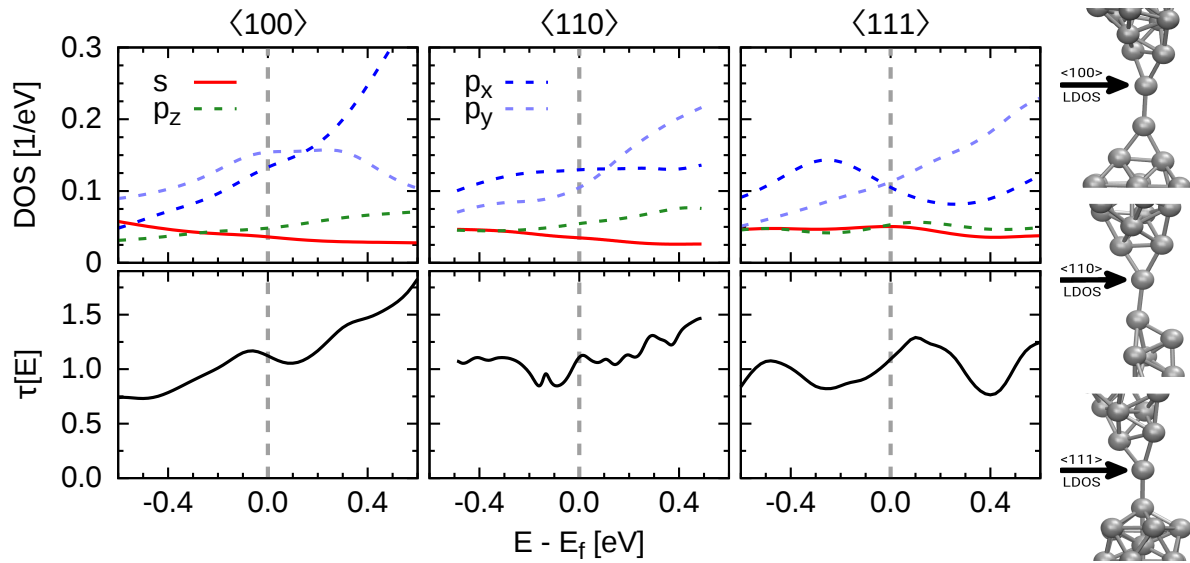


Figure 8.9.: DOS and total transmission calculations as function of the energy for the dimers shown on the right. The top geometry on the right side is from the  $\langle 100 \rangle$ , the middle from the  $\langle 110 \rangle$  and the bottom geometry is from the  $\langle 111 \rangle$  direction. The arrows mark the positions of the atoms where the DOS is calculated from.

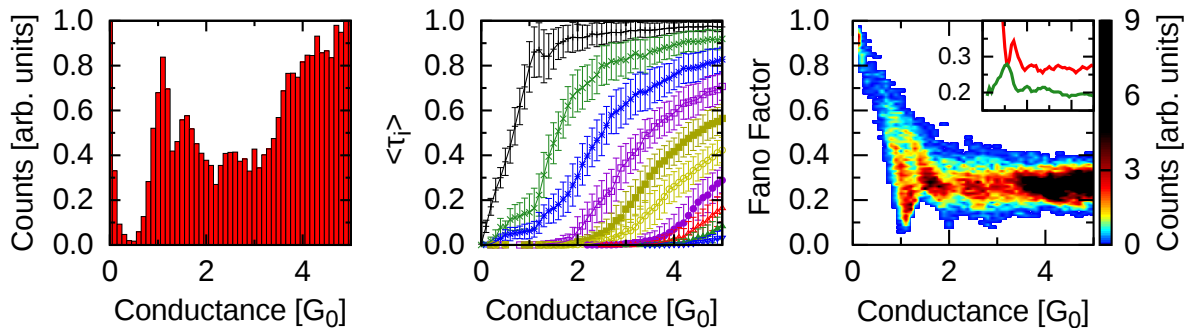


Figure 8.10.: Results of the total data set including all three directions: The conductance histogram (left), the mean channel distribution (middle) and the Fano factor (right) with mean value (red) and standard deviation (green) in the inset.  $\sigma_F$  is shifted upwards by 0.15.

Up to now the electronic properties of the individual directions were discussed but one could argue that in experiments one could have a mixture out of all three directions. One big problem of this argumentation is how one should weight the different directions. In Fig. 8.10 the results for the total of all three directions is presented. That corresponds to an equal weighting of the directions. As the features are very similar in all three directions, it is not astonishing to find them again. But the small differences in the directions also has a blurring effect. So are the peaks in the conductance histograms broader and less pronounced than in the  $\langle 100 \rangle$  and  $\langle 111 \rangle$  direction but at about the same position. Because of the relative large conductance peak at  $1 G_0$  in the  $\langle 100 \rangle$  compared to the other two directions, it dominates the behavior of the mean channel distribution and the Fano factor at around  $1 G_0$ .

### 8.1.1. Conditional MCS and conductance histograms

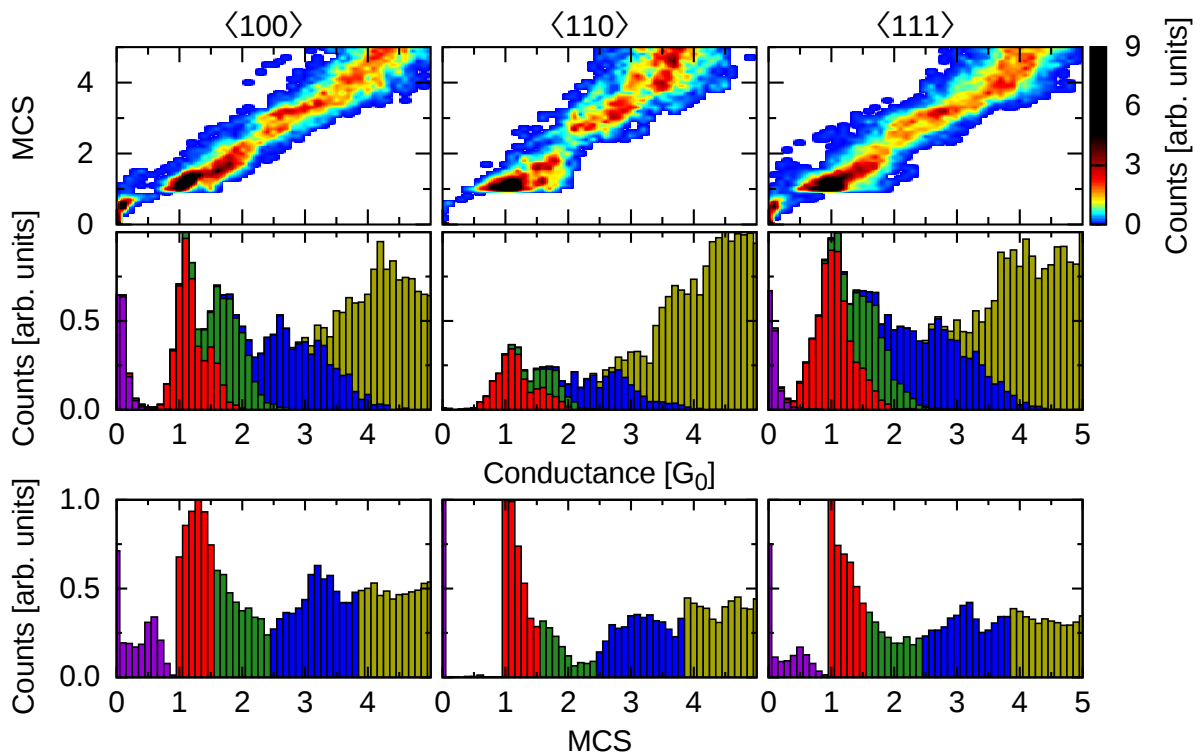


Figure 8.11.: The minimal cross section (MCS) as function of the total conductance (first row), the conductance histogram (second row) and the MCS histogram (third row). The conductance histogram is colored according to the contributions to the corresponding regions in the MCS histogram with the same color.

Besides this purely electronic properties, with Sharvins formula one can connect the total conductance with the minimal cross section (MCS) of a wire, thus a geometric property. This is done in Fig. 8.11 where the connection of both is shown. The colored regions are defined in the MCS histogram and the colored regions in the conductance histogram show the correlated regions. There they are not such well defined because the mapping is not perfect<sup>7</sup>.

<sup>7</sup>This was already discussed in section 6.1.

The red areas (second from left) for example have by definition sharp flanks to the left of 1 in the MCS histograms while the correlated first peaks in the conductance histograms are more Gaussian. The same is true for the other peaks. In this partitioning of the areas the left ones (purple) represent the tunneling regime, the second ones (red) the atomic contacts with a single atom in the narrowest part (monomer, dimer, ...) and the higher ones (green, blue, yellow) are designed to best fit to the peaks in the conductance histogram of the  $\langle 100 \rangle$  direction.

The tunneling regime (purple area) is an interesting part because it is differently populated in the three directions. The  $\langle 100 \rangle$  direction shows as in the MCS histogram a relative sharp left flank at below  $1 G_0$  followed by an increasing number of points going to zero. The  $\langle 111 \rangle$  direction shows a similar behavior but with a larger width of the first peak down to about  $0.5 G_0$  and less data points in the MCS histogram below 1. The  $\langle 110 \rangle$  direction has in contrast to the  $\langle 100 \rangle$  direction a very broad peak around  $1 G_0$  and no data points in the MCS below 1 and therefore no points in the tunneling regime. This means that atomic contacts with a single atom in the narrowest part are always well conducting in the  $\langle 100 \rangle$  direction while the conduction can be reduced with large probability in the  $\langle 110 \rangle$  and  $\langle 111 \rangle$  direction. The reason for the lack of data points in the tunneling regime in the  $\langle 110 \rangle$  direction is the geometric phase (see Fig. 8.4) under tension which leads to a very fast displacement after the breaking of the last bond<sup>8</sup>.

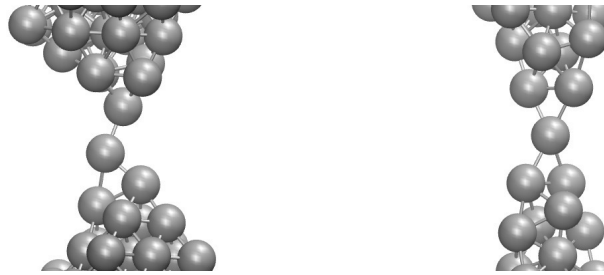


Figure 8.12.: An example for a geometry contributing to the conductance peak in the  $\langle 100 \rangle$  direction at  $1.1 G_0$  (left) and at  $1.5 G_0$  (right). The channel distributions are: 0.82, 0.15, 0.13 (left) and 0.77, 0.55, 0.20 (right).

A third point is the missing feature in the MCS histogram near below 2. This means that the second peak in the conductance histograms of the  $\langle 100 \rangle$  and  $\langle 111 \rangle$  direction are not based upon special minimal cross sections.

Looking at the geometries one finds that mainly dimers contribute to the peak at  $1.1 G_0$  and mainly monomers to the one at  $1.6 G_0$ . Examples are shown in Fig. 8.12. As both cases have only one atom in the bottleneck they can not be separated by simple geometrical means like the MCS. Both cases have three contributing channels as expected from the orbital structure, but while the dimer has one main channel and two minor ones, the monomer has two well contributing channels and one which is only minor.

<sup>8</sup>The geometric phase without tension is shorter than the corresponding one with tension and the transition is very fast.

### 8.1.2. Rising plateaus

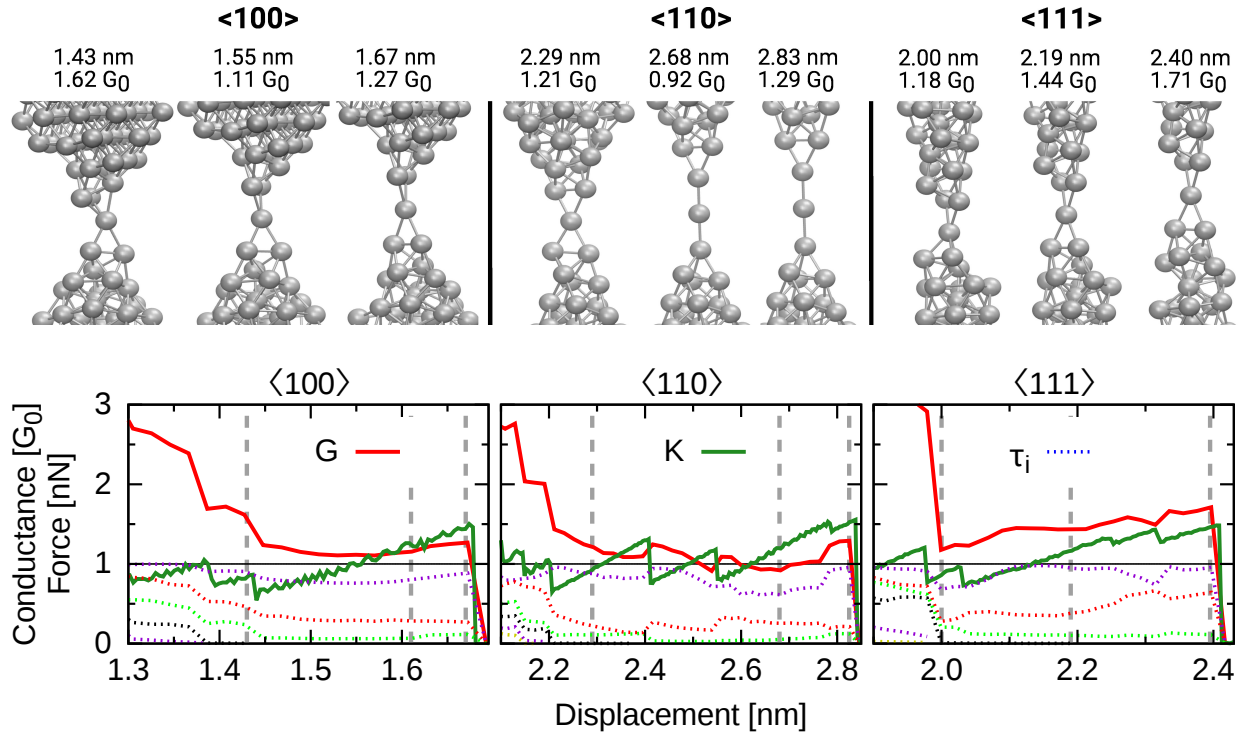


Figure 8.13.: Elongation curves with rising conductance plateaus. One example with three geometries per elongation direction (top) and the corresponding conductance (red), force (green) and channel distribution (dotted) curves (bottom). The resolution of the force in x-direction is five times as high as the one of the conductance. The vertical dashed lines in the graphs mark the positions of the geometries above.

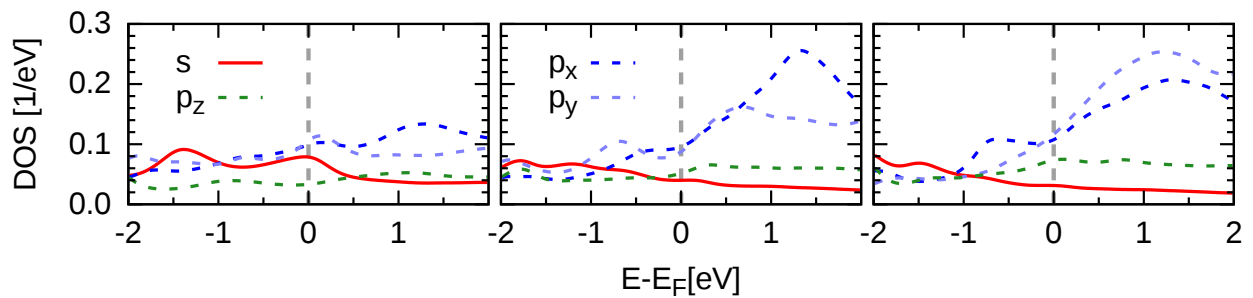


Figure 8.14.: DOS for the central atom of the three geometries of the  $\langle 100 \rangle$  example in Fig. 8.13.

There is an interesting behavior of Al plateaus which was already mentioned in connection with Fig. 8.4 and is well known in experiments (see e.g. [191], [39]) but not that much from other materials<sup>9</sup>. Krans et al. already suggested that this could be due to an optimization of the overlap during the elongation. To analyze this Fig. 8.13 shows one example for each elongation direction. A first interesting remark regarding the geometries is that the leads of the  $\langle 100 \rangle$  examples show a much larger opening angle than the other two directions.

<sup>9</sup>In the paper from Krans et al. [191] they also present Pt measurements which show this behavior.

During the conductance plateaus the force can show several jumps meaning that the wire has geometric reorganizations in the vicinity of the single atom contact (between first and second geometry in the  $\langle 110 \rangle$  example), as well as farther away (between the geometries in the  $\langle 111 \rangle$  and between the second and third geometry in the  $\langle 110 \rangle$  example). The channel distribution is not perfectly comparable, but they have in common that some channels rise while others decrease, so not all are rising.

This can be analyzed deeper by looking at the DOS evolution of an example. In Fig. 8.14 the DOS of the three geometries of the  $\langle 100 \rangle$  example are shown. This example shows first a decrease in the conductance due to the increasing distance between the two leads (geometry one and two). In the DOS this is accompanied or caused by a decrease in the density of the  $s$  orbital. The  $p$  orbitals slightly change their energy dependence and while the  $p_z$  orbital gains density, the two perpendicular orbitals slightly loose some. In the following increase of the conductance gain all  $p$  orbitals density, but most the  $p_z$  one. This means that the  $p$  orbitals get optimized overlaps due to geometric modifications. At the same time the  $s$  orbital still looses density which is compatible with a further elongation of the bonds between the atoms. In total this analysis supplies the theory from Kran et al. that the rising plateaus have their origin in the optimization of orbitals during the elongation process. To finish this part Fig.

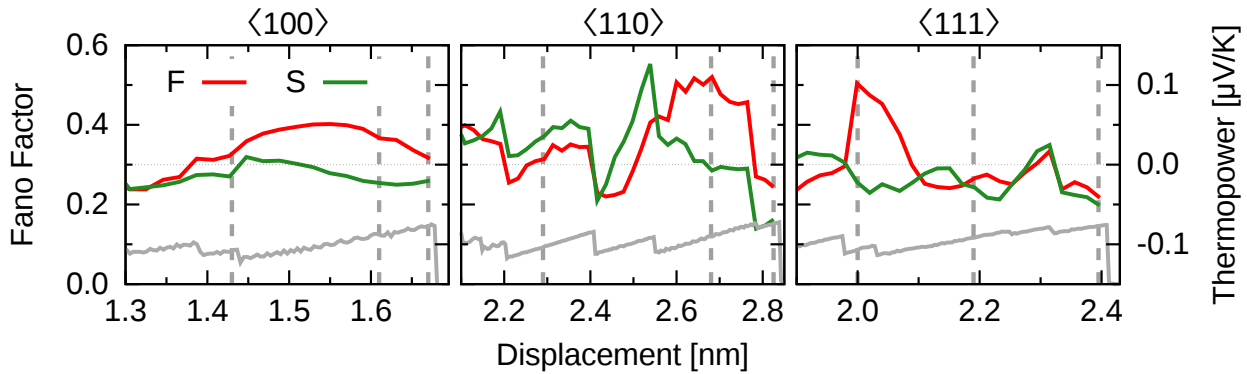


Figure 8.15.: Fano factor (red) and thermopower (green) of the curves shown in Fig. 8.13. The dotted horizontal line in the middle of the plots is a guide for the eye at  $0 \mu\text{V}/\text{K}$ . For better comparison with the figures before the force is added in gray (in arb. units).

8.15 presents the according data of the Fano factor and the thermopower. As the Fano factor and the thermopower are derived values from the channel distribution and energy dependent transmission it is not surprising that they respond to all modifications in the geometry<sup>10</sup>. They are even more sensitive than the total conductance shown in Fig. 8.13. But both properties act like in the mean, while they behave relative smooth with a mainly negative thermopower in the  $\langle 100 \rangle$  direction, they behave more extreme to the geometric modifications in the  $\langle 110 \rangle$  elongation direction and the  $\langle 111 \rangle$  direction is somewhere in between.

<sup>10</sup>Jumps in the force.

## 8.2. Single-atom memory

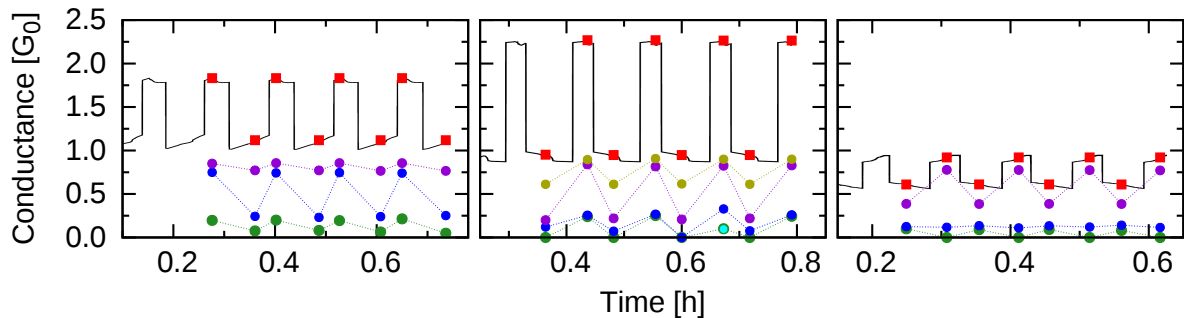


Figure 8.16.: Three experimentally realized bistable switches as function of real time. The black line shows the evolution of the conductance measurement and the filled circles are the channel distributions as numerically determined from the superconducting IV curves. The dotted lines between the circles are only guides for the eyes. The data sets are the same as for Fig. 3 of [14] (left one) and Figs. 7a and 7b from the corresponding supplementary information (central and right).

In the electromigration experiments of Christian Schirm et al. [14]<sup>11</sup> a procedure could be established with which a wire could be switched between two different states with different conductance properties (Fig. 8.16). The procedure used an MCBJ at cryogenic conditions between 250 mK and 1.5 K in a vacuum chamber to thin a wire down to a conductance of a few  $G_0$ . Afterwards current in the order of dozens of  $\mu A$  and hundreds of  $mV$  was used to modify the geometry further. After some cycles where the current direction and amplitude was changed automatically according to jumps in the conductance, eventually a bistable situation was achieved<sup>12</sup>. The wires could be switched hundreds of times by reversing the current direction.

With the help of superconducting leads it was also possible to determine the channel distribution<sup>13</sup>. As the channels are more sensitive to geometric configurations, which was shown in the last section, they can be used to select more precisely the possible geometries for the measured plateaus from the calculated set of elongation curves.

Fig. 8.16 shows prominent examples from the experiments. The effect of the switching onto the channels is very different in the three examples. While in the left example the switching is dominantly effected by the second (blue) channel, in the middle example at least three channels are significantly affected and the number of contributing channels changes from four in the high conductance state to three in the low one. The third example also shows a change in the number of channels, but that time the high one has one channel less than the low one.

With the additional requirement for the selected geometries that they have to be from the same elongation curve such that it is possible to switch between both states, table 8.1 shows

<sup>11</sup>Cooperation paper, parts of our theoretical results shown below are also published there.

<sup>12</sup>They were only called bistable if the wire was stable even without current. Tests achieved up to 10 h.

<sup>13</sup>Multiple Andreev reflection (MAR), for more information see sec. 4.1 and the supplementary information of [14].

<sup>14</sup>The dashes in the line are equally spaced so the length can be estimated by counting the number of dashes (after zooming in).



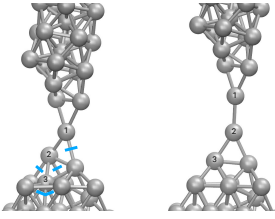
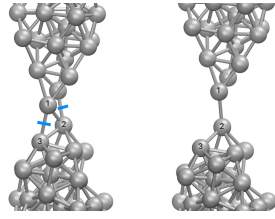
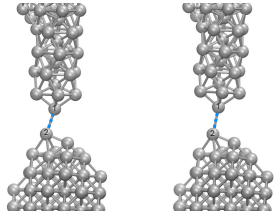
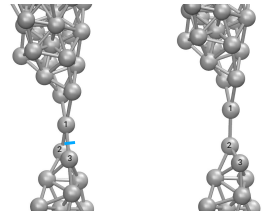
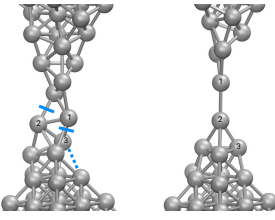
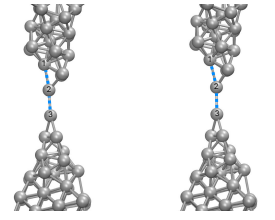
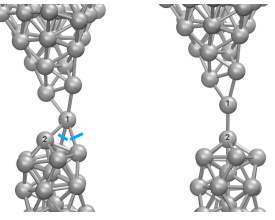
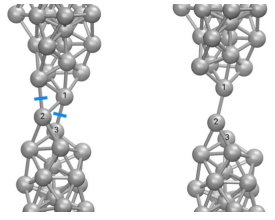
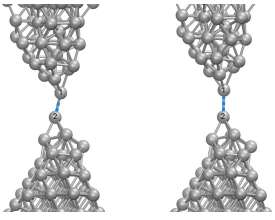
target values	1.84 $G_0$ : 0.86, 0.75, 0.20 1.12 $G_0$ : 0.77, 0.24, 0.07	2.26 $G_0$ : 0.89, 0.84, 0.26, 0.24 0.95 $G_0$ : 0.61, 0.20, 0.12	0.92 $G_0$ : 0.78, 0.12 0.61 $G_0$ : 0.39, 0.12, 0.10
$\langle 100 \rangle$			
sample values	1.82 $G_0$ : 0.89, 0.72, 0.21 1.12 $G_0$ : 0.79, 0.22, 0.10	2.27 $G_0$ : 0.97, 0.67, 0.43, 0.20 0.99 $G_0$ : 0.71, 0.17, 0.11	0.86 $G_0$ : 0.58, 0.22, 0.06 0.69 $G_0$ : 0.55, 0.10, 0.03
$\langle 110 \rangle$			
sample values	1.83 $G_0$ : 0.94, 0.71, 0.17, 0.01 1.11 $G_0$ : 0.80, 0.26, 0.05	2.25 $G_0$ : 1.00, 0.82, 0.27, 0.15 0.94 $G_0$ : 0.83, 0.08, 0.03	0.95 $G_0$ : 0.77, 0.16, 0.03 0.59 $G_0$ : 0.45, 0.11, 0.02
$\langle 111 \rangle$			
sample values	1.83 $G_0$ : 0.99, 0.69, 0.14 1.11 $G_0$ : 0.86, 0.16, 0.09	2.28 $G_0$ : 0.98, 0.73, 0.27, 0.25, 0.04 0.91 $G_0$ : 0.62, 0.20, 0.09	0.94 $G_0$ : 0.73, 0.15, 0.05 0.62 $G_0$ : 0.52, 0.07, 0.03

Table 8.1.: Best matching geometries from each elongation direction for three experimentally prominent jumps (target values). The cyan bars mark bonds which have to be broken going from the left to the right geometry. Interesting bonds are dotted<sup>14</sup> and some atoms are numbered to better find them on both geometries. The dotted line in the left geometry of the second row and second column is special because it gets connected going from left to right.

the best matching geometries from each elongation direction. The resulting geometries show two interesting similarities: The plateaus around 1  $G_0$  are all from dimers while the plateaus at about 1.8  $G_0$  are from monomers. The three geometries of the second example at about 2.3  $G_0$  show also very similar central regions. This result is not unexpected as the neck-hole should dominate roughly the behavior of the contact.

Fig. 8.17 shows the transmission and force data of the  $\langle 111 \rangle$  examples as function of the displacement for a longer range (some geometries during the complete elongation process can be found in table 8.2). It can be nicely seen that the two geometries of the first and

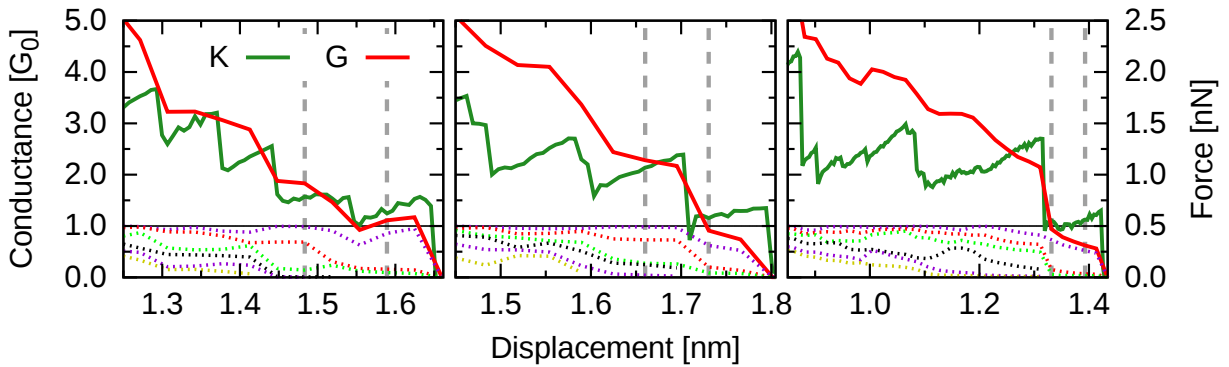


Figure 8.17.: Conductance (red), force (green) and channel transmission as function of the displacement for the  $\langle 111 \rangle$  examples in table 8.1.

second example are separated by one atomic reorganization<sup>15</sup> concerning two bonds (cyan bars in table 8.1). The last example does not contain atomic reorganizations. The two geometries are on the same force and conductance plateau. The main differences between the two geometries are the angle between the two atoms in the neck-hole labeled with '1' and '2' and the length of the bond connecting both changing from 2.9 Å to 3.1 Å (marked by a cyan dashed line<sup>14</sup>).

The observations made for this  $\langle 111 \rangle$  examples are true also for the other two directions, except the first example of the  $\langle 100 \rangle$  direction where six bonds have to be broken during the reorganization of atoms 1 to 3.

In total, with this comparison it could be shown that the switching between the bistable states realized in the experiments from Schirm et al. can be traced back to the reorganization of one up to a few atoms and includes the breaking or forming of only a few bonds.

The experimental and theoretical results were published together in [14].

	sample 1	sample 2	sample 3
$\langle 100 \rangle$			
$\langle 110 \rangle$			
$\langle 111 \rangle$			

Table 8.2.: Snapshots of the elongation process of the geometries in table 8.1.

<sup>15</sup>Jump in the force.

## 9. Additional studies

In the sections till now the properties of different metals was studied at a given temperature, thermostat, elongation speed, statistics, lattice type, system size and starting geometry. But how large is the influence of those fixed parameters and how do they influence the results? This questions will be addressed in the next sections.

### 9.1. NVT versus NVE ensemble

The thermodynamic ensemble in which the atoms of the geometries are evolved in time plays an important role. The reason for this is that the elongation process puts a lot of energy into the system, first of all into the potential energy. But with each rupture process energy flows from the potential energy into the kinetic one leading to an effective heating of the wire.

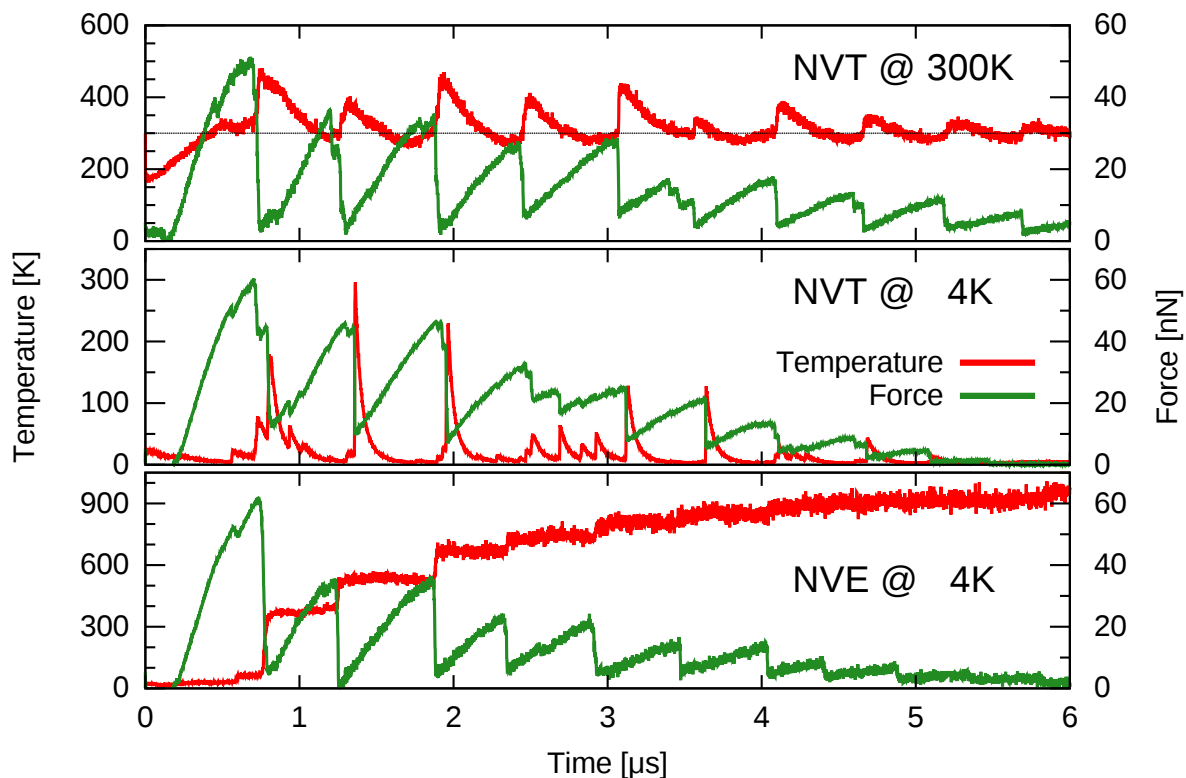


Figure 9.1.: Force and temperature curves for an Fe wire within an NVT ensemble (Nosé-Hoover) at 300 K (first row) and at 4 K (second row) and within an NVE ensemble started at 4 K (third row).

This can be seen in the examples of Fig. 9.1: Each rupture process (green) leads to a sudden increase in the temperature (red). Now having an NVE ensemble where the energy is kept

fix<sup>1</sup> (bottom row) the temperature develops step-wise leading to a very high temperature at the end of the elongation process. Using an NVT ensemble instead, the thermostat tries to keep the temperature fixed. Depending on the thermostat this is not done instantaneously<sup>2</sup>, but with a damping constant or even more enhanced damping mechanism like in the Nosé-Hoover thermostat (see section 2.1.2). The damping leads to an exponential decay of the actual temperature toward the target temperature.

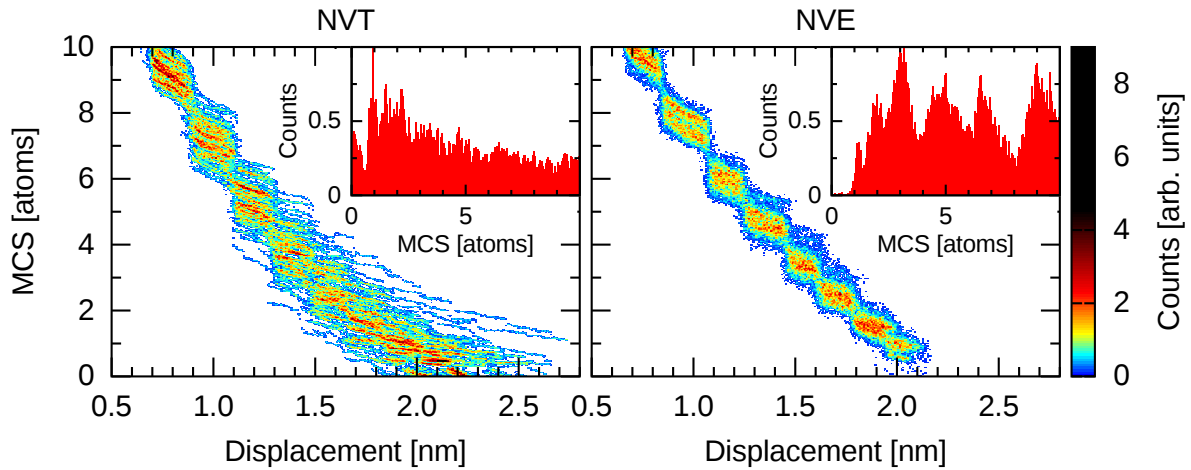


Figure 9.2.: Density plots of the MCS data of 100 elongation curves as function of the displacement of their upper walls to the initial positions for Fe in an NVT ensemble (4K, left) and an NVE ensemble (starting at 4K, right). The densities are normalized to an upper limit of 9. The insets show the corresponding mcs-histograms normalized to an upper limit of 1.

The difference can also be seen in the mcs evolution (Fig. 9.2) and the mcs histogram (insets). While the density plot of the NVT curves shows the usual spread at the end of the elongation process, because of the high temperature the curves in the NVE ensemble behave more fluid like. In this context this means that they behave in the mean more well defined with much less deviations. As a consequence the droplet like behavior which is in the NVT ensemble only visible in the first parts of the elongation process shows up in the NVE ensemble till the end.

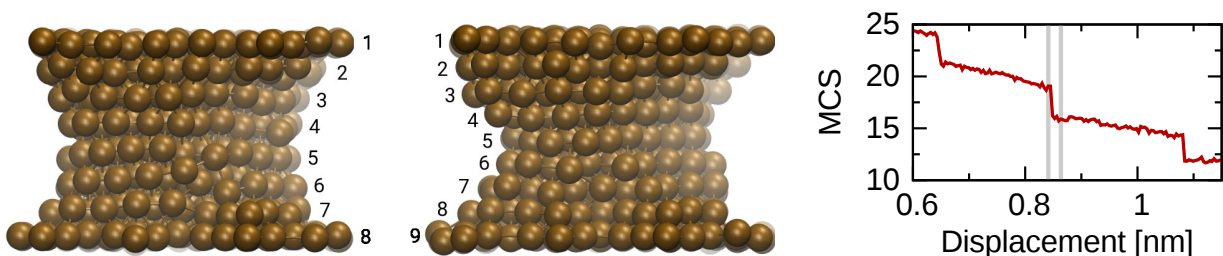


Figure 9.3.: Geometries of an elongation curve before (left) and after (middle) a jump in the MCS curve (right). The gray vertical bars in the MCS graph mark the positions of the two geometries.

<sup>1</sup>The energy included by the elongation process is not considered.

<sup>2</sup>A rescale thermostat could do that, but that would be unphysical.

The reason for this is depicted by an example in Fig. 9.3. Shown is the geometry shortly before and after a jump in the MCS which is equivalent with the jump from one droplet to the next. Before the jump the geometry has eight rows, afterwards it has nine meaning that this droplets just define sections with the same number of rows. The reason why this well defined droplets get lost in the (low temperature) NVT ensemble is the more brittle behavior of the structures leading to more arbitrariness in the breaking process<sup>3</sup>. The regular peaks in the MCS histogram of the NVE ensemble (insets of Fig. 9.2) are just a reflection of this droplets.

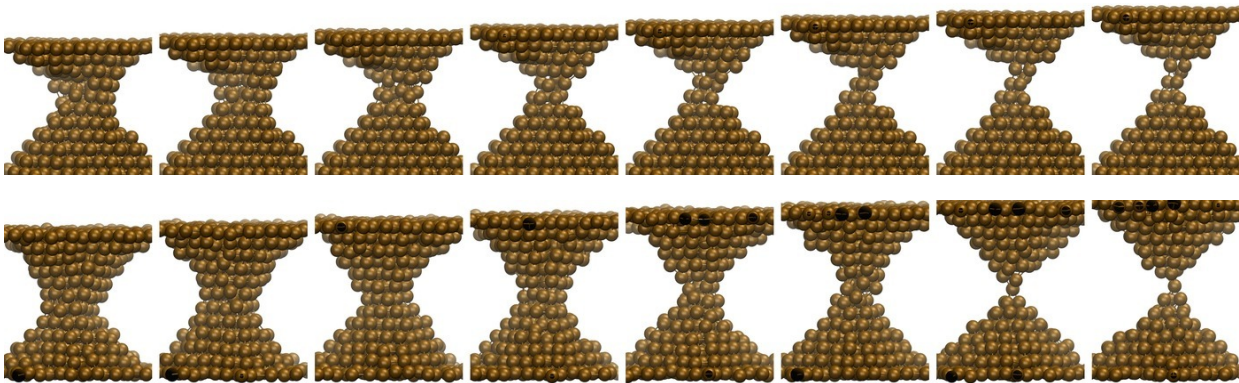


Figure 9.4.: Geometries along an elongation process in the NVT ensemble (top) and in the NVE ensemble (bottom).

An example for the evolution of the geometries during the elongation process is shown in Fig. 9.4. Here one can recognize the points already discussed: The relatively well defined lattice of the NVT example which allows the evolution of a short, view atoms thick wire, leads to a wide spread of possibilities in the histograms. In contrast, the NVE ensemble has due to its relative high temperature<sup>4</sup> a smooth surface. The high mobility of the atoms does not allow the creation of a small, few atoms thick wire as in the NVT example but it leads to a straight forward breaking.

This were the effects of the used thermodynamic ensemble onto the geometric properties. Fig. 9.5 shows the effects onto the transmission values. Here the effects are very similar. The total conductance, coupled via Sharvins formula to the MCS, follows the same trends as function of the displacement (straight in the NVE and with a large spread in the NVT ensemble). The mean values of the other properties behave also quite the same comparing the two thermodynamic ensembles but the spread is much larger in the NVT results compared to the NVE results.

With 16 times less data points as in the mcs histogram the resolution of the conductance histograms are not very good. An interesting point is that the fast breaking due to the high temperature in the NVE ensemble leads to a shift of the first peak to slightly higher values ( $1.3 G_0$  vs.  $1.7 G_0$ ) and that there are almost no points below. As the first peak in the experimental Fe histograms were at about  $2.1 G_0$ , this result could mean that the Fe atoms in the constriction are in the experiments much more mobile than in the theory. A

<sup>3</sup>E.g. breaking in sidearms or building of wires.

<sup>4</sup>Though it also started at 4 K.

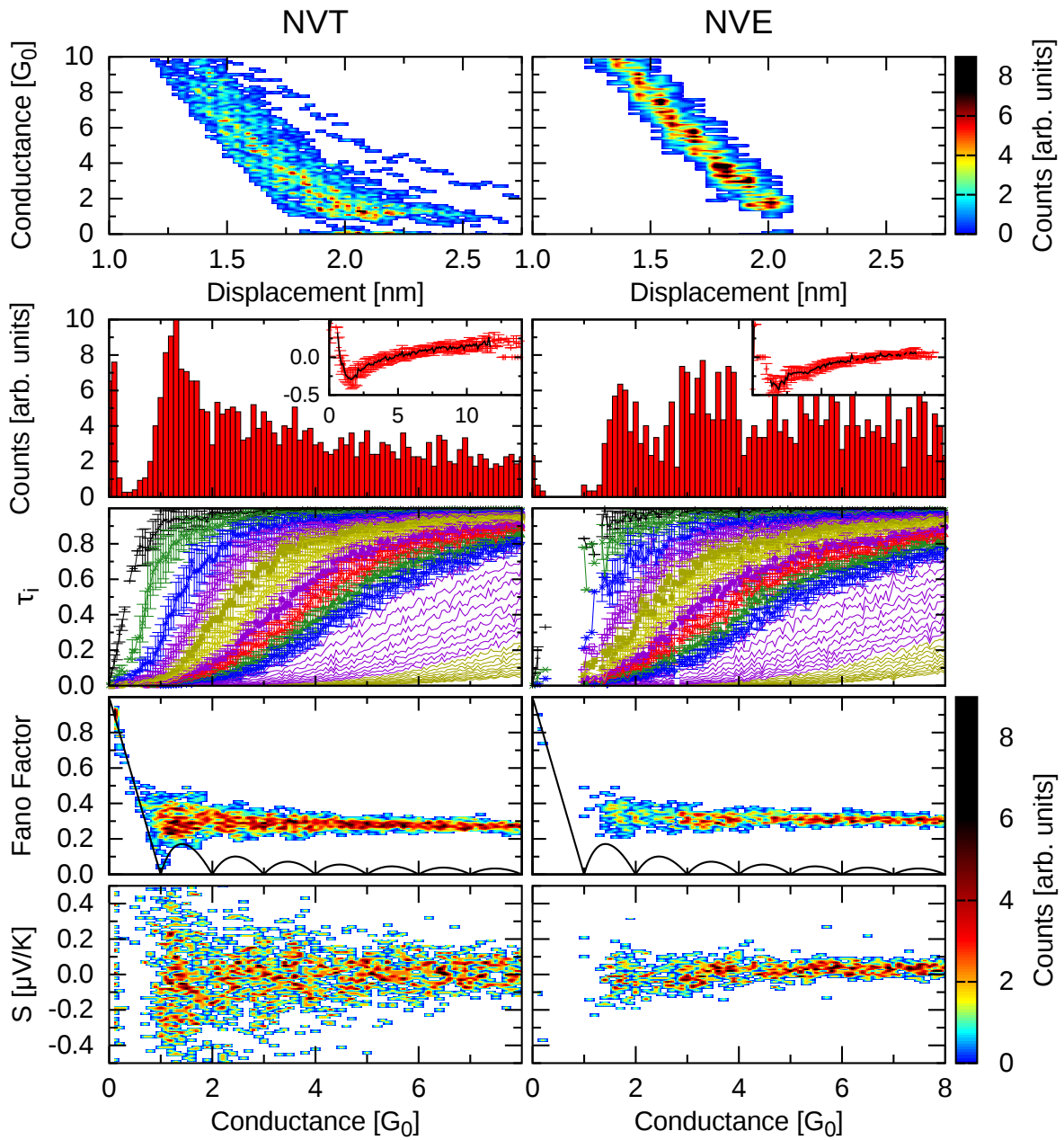


Figure 9.5.: Conductance density plots as function of the displacement (first row), conductance histograms (second row), mean channel distribution (third row), Fano factor (fourth row) and thermopower (sixth row) as function of the total conductance for 50 curves in the NVT (left) and 50 curves in the NVE ensemble (right). Both use an FCC start geometry. For the thermopower a fictive temperature of 4 K was used. The densities are normalized to an upper limit of 9.

reason could lie in a too rigid pseudo potential at low coordination numbers (surface). Local heating could be another point adding to the problem.

## 9.2. Temperature evolution and concept of opening and closing curves

Up to now the results at low temperatures (around 4 K) and at room temperatures (300 K) were discussed. But what happens in between? Is there a continuous transition as one would classically expect? In the following this question will be addressed using small Au wires (56 atoms in the central region).

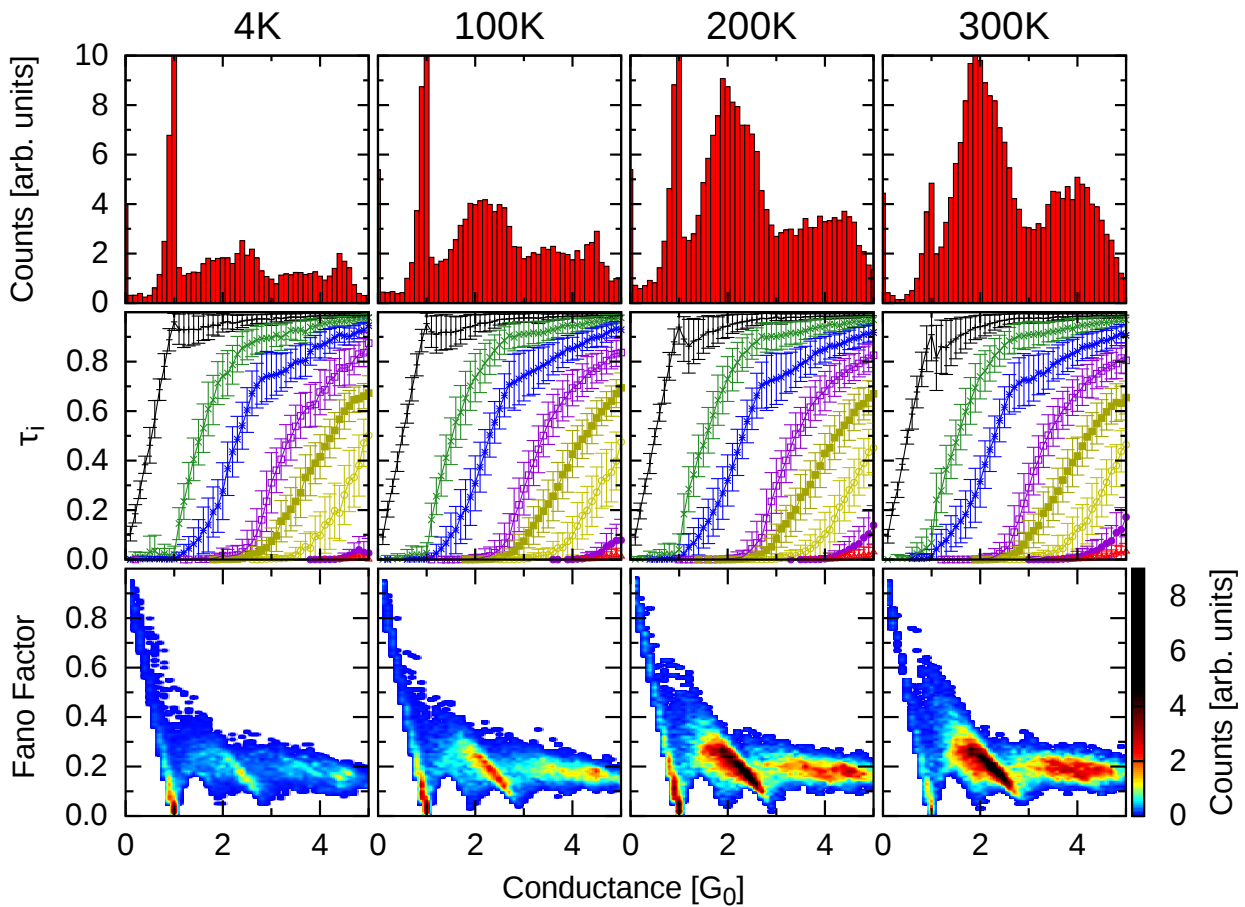


Figure 9.6.: Conductance histograms (first row), mean channel distributions with standard deviations (second row) and density plots of the Fano factor for Au at temperatures between 4 K and 300 K from data of 200 elongation (**opening**) curves with 56 atoms in the central wire each as function of the total conductance. The histograms are normalized to an upper limit of 10 and the densities to an upper limit of 9.

The statistical results for four different temperatures from 4 K to 300 K (Fig. 9.6) show as expected a continuous transition. Because of the size of the contacts the results are not completely identical to the ones already presented <sup>5</sup>.

The conductance histograms (first row) show with increasing temperature a decrease of the first peak at  $1 G_0$  and an increase of the second one at about  $2 G_0$ . To explain this Fig. 9.7 and 9.8 show examples at  $4 G_0$  and  $300 G_0$ , respectively. While at low temperatures the

<sup>5</sup>This point will be addressed later.

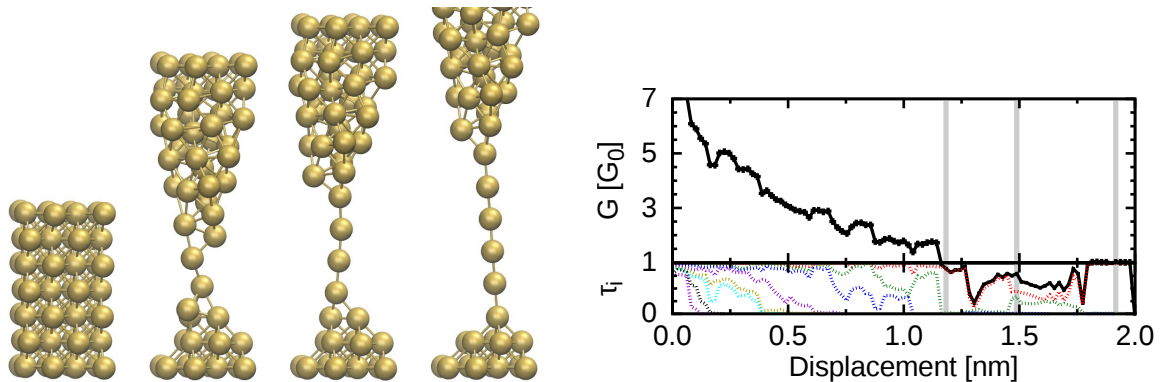


Figure 9.7.: Example for the evolution of a Au geometry at 4K exhibiting a long plateau around  $1 G_0$  by creating a mono-atomic wire (left) and the corresponding conductance (black line) and channel distribution (colored dotted lines) (right). The vertical gray lines mark the positions of the geometries from the left side.

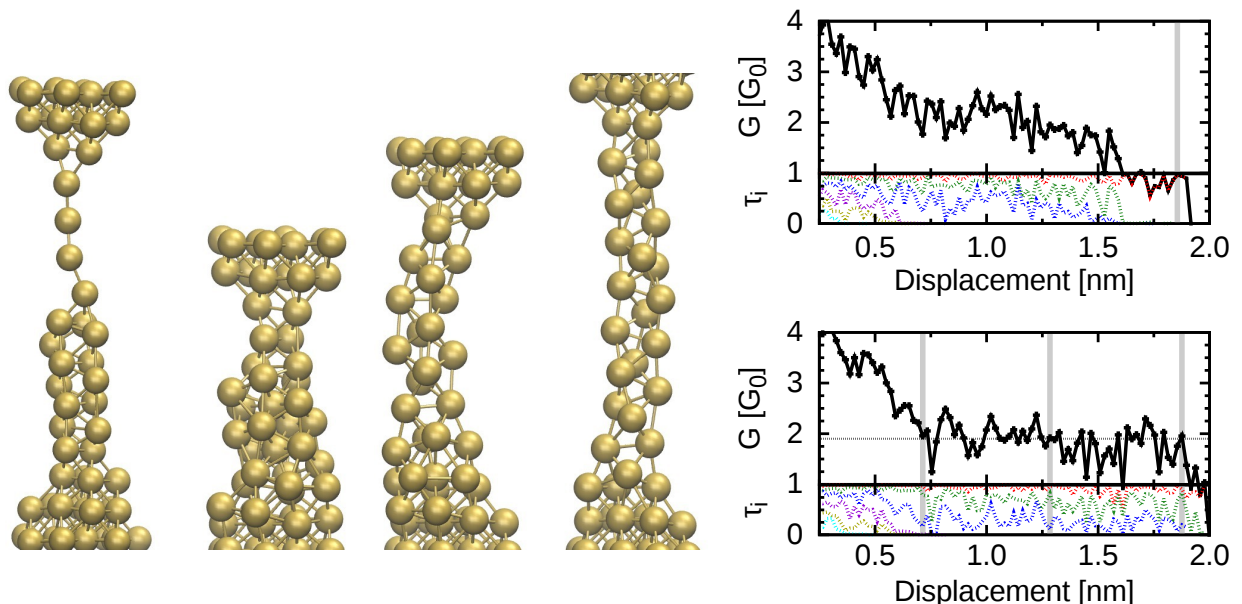


Figure 9.8.: Examples for the evolution of Au geometries at 300K exhibiting a long plateau around  $1 G_0$  (first geometry) and  $2 G_0$  (second to fourth geometry). The corresponding conductances (black line) and channel distributions (colored dotted lines) are shown on the right. Here the upper graph shows the evolution of the curve belonging to the first geometry and the lower one belongs to the other three geometries. The vertical gray lines mark the positions of the geometries from the left side.

wire diameter decays relatively fast to a single atom which forms in the continuing elongation a long wire with roughly  $1 G_0$ , the wires are more flexible at higher temperatures, forming long, few atoms thick wires which break relative sudden. But there are still some configurations at room temperature forming short single atom wires like the first example in Fig. 9.8. This trend was already discussed in earlier sections but here it can be seen very clear.

The channel distributions (second row of Fig. 9.6) show a similar evolution. While in the mean they behave almost identical, the standard deviation above  $1 G_0$  increases with increas-



ing temperature. This is especially visible in the first channel where between 1 and  $2 G_0$  the increasing deviation leads to a decrease in the mean value. That has its representation in the Fano factor (third row) which shows it as increase in the spread within this range. The modifications of the counts (color) in the Fano factor plots are due to the modified conductance histograms.

### 9.2.1. Closing curves

Fig. 9.6 shows the results of the so called ‘opening traces’. But in experiments the samples are opened (elongated) and closed (compressed) in a cyclic manner, resulting in a data set of the opening and one of the closing curves<sup>6</sup>.

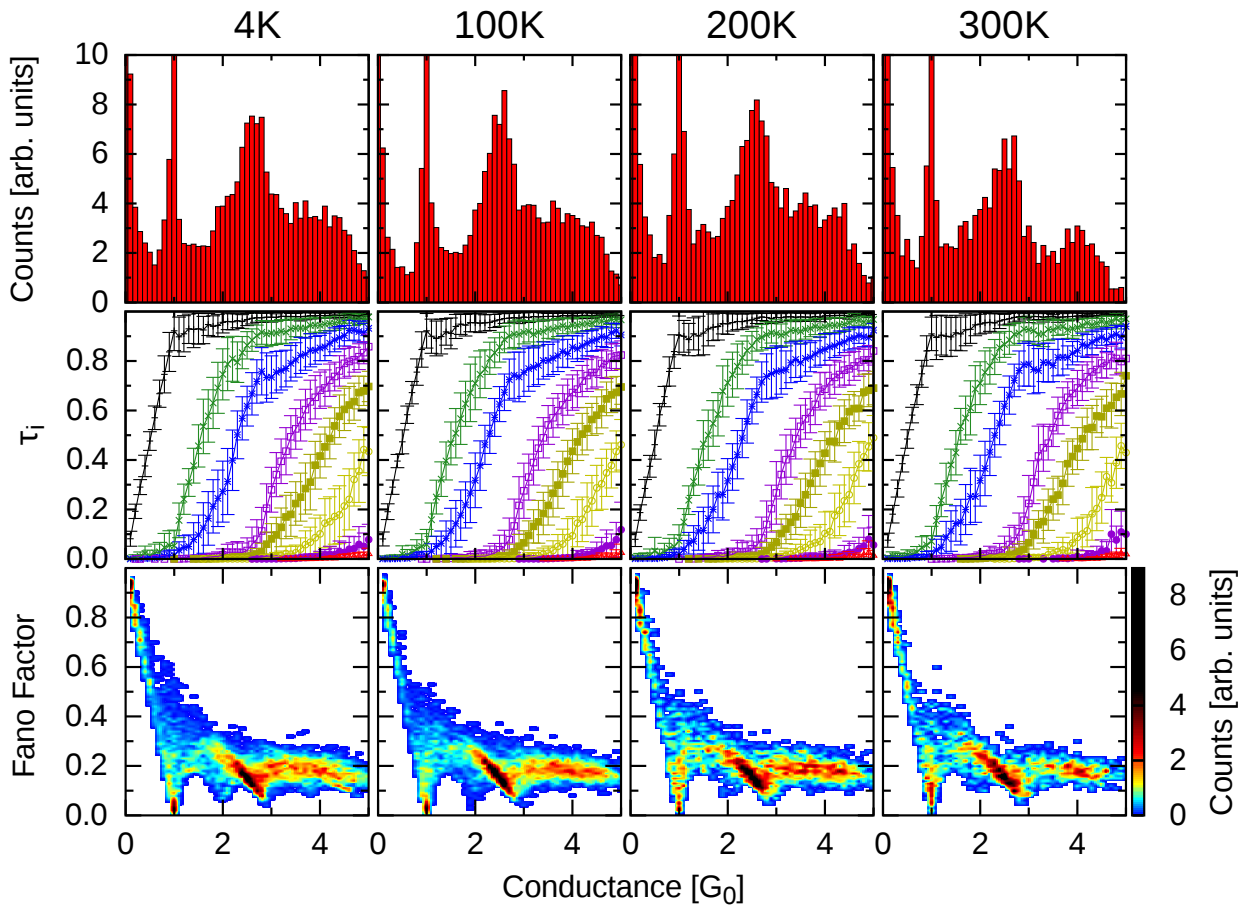


Figure 9.9.: Conductance histograms (first row), mean channel distributions with standard deviations (second row) and density plots of the Fano factor for Au at temperatures between 4 K and 300 K from data of 200 **closing** curves with 56 atoms in the central wire each as function of the total conductance. The histograms are normalized to an upper limit of 10 and the densities to an upper limit of 9.

In Fig. 9.9 the corresponding results of closing curves are shown. Therefore the elongated wires used for Fig. 9.6 were closed again. Comparing the two figures one sees that the

<sup>6</sup>For example in the dissertation of S.Olivier [192] or for Au and Zn in [193].

main differences between the temperatures pointed out above have vanished. The first peak in the conductance histogram is still there but with much less intensity compared to the background<sup>7</sup>. This is at 4 K about 4 times less than in the opening histogram and at 300 K about 2 times less. The second peak has in all four cases about 80 % of the height of the first one which is in total contrast to the opening curves. At 4 K the almost fully open mean first channel at  $1 G_0$  is missing as are the drop of the mean first channel at higher temperatures above  $1 G_0$ . The latter point results in the loss of the shoulder in the Fano factor plots near above  $1 G_0$  at higher temperatures.

What can not be directly seen in this representation is that the total height of the first peak at 4 K is about 2.6 times as high as at 300 K, for the opening curves the factor was about 4.5.

To get a feeling of what happens to cause all this adaptations between the temperatures Fig. 9.10 shows examples of different possibilities of what could happen at 4 K.

The first example shows a dimer forming in the elongation process. The upper part gets in the elongation process elongated in such a way that the dimer does not survive for long, but the orientation of the dips stays stable even after the breaking (geometry two and three). The reconnection is slow due to the well relaxed configuration of the two separated parts leading to relative long plateaus at  $1$  and  $2 G_0$  and a relatively good represented tunneling regime. The geometry of the  $1 G_0$  plateau (fourth geometry) is again a dimer. The final geometry (geometry five at 10 ns) has no well defined crystal structure as the beginning one which leads to an effective decrease in conductance.

The second example has very similar features as the first one but creating a monomer instead of a dimer. The decrease of the conductance plateaus with time after reconnection is due to the fact that the atoms push each other away from the ideal positions with decreasing distance of the walls. During a plateau this dislocations are not far enough to create a geometric reorganization which would lead to steps in the conductance.

The remaining two examples are different. Both configurations form long chains in the elongation process which rip at one end and agglomerate to one side. The difference between those two is how the resulting dips look like, are they more cone like as in example three or more flat as in example four. If they develop cone like dips than the conductance curve can develop steps as in the examples one and two. But if they are flat than no plateaus will be visible.

In total, the closing curves have similar properties as the opening curves but because of the different characteristics of slightly stretched or compressed lattices, they are not identical. Further more, the relaxation processes after the rupture lead to results which have more similarities with high temperatures as with low ones and to a reduction of data points in the low conductance regime.

---

<sup>7</sup>The values between the peaks.

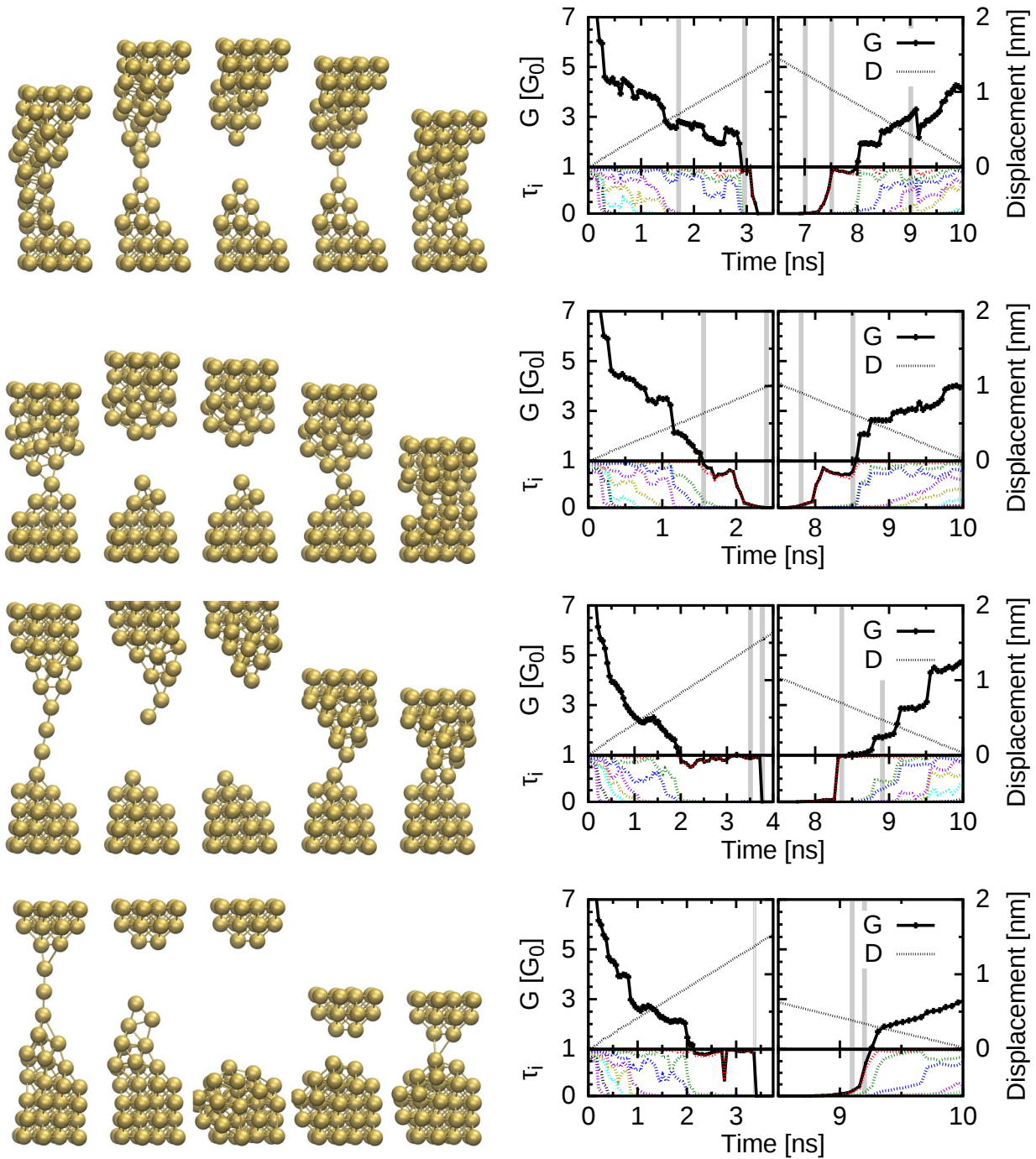


Figure 9.10.: Four examples of the opening and closing of contacts at 4K. The geometries on the left belong to the conductance and channel distribution plots on their right with gray vertical lines marking their positions. The line ‘D’ shows the displacement of the walls according to their original (ideal) positions (right y-axes).

### 9.2.2. Closing curves of Mg, Al and Ag

Equivalent to the proceeding in the last section, the closing of the contacts of the large geometries of Mg, Al and Ag at 4K which were analyzed above (sections 5.1-5.5) were calculated.

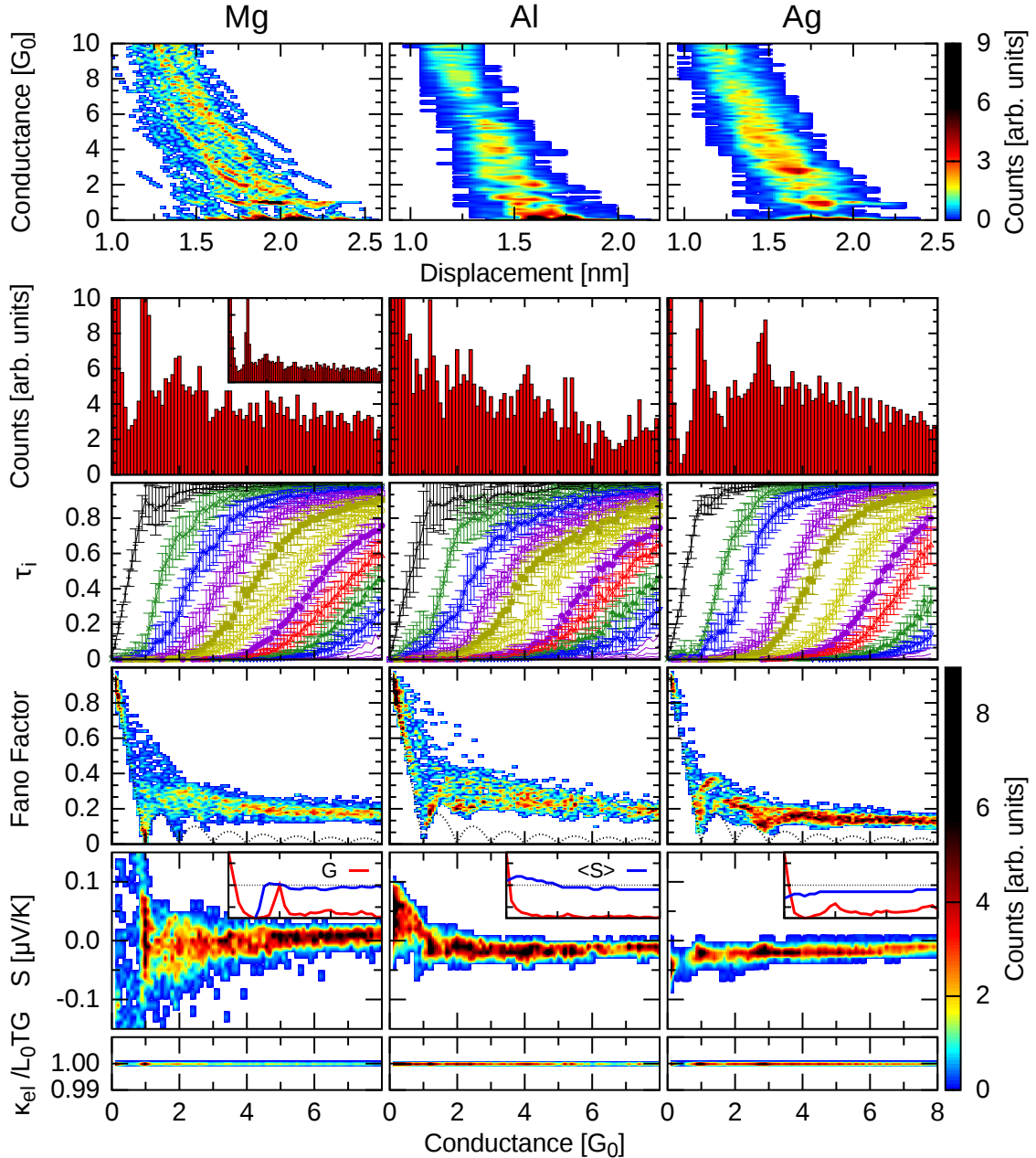


Figure 9.11.: Statistics of 100 closing curves of Mg, Al and Ag at 4K. Density plots of the total conductance as function of the displacement of their upper walls to the initial positions (first row), conductance histograms (second row, Mg only 50 % of total height), mean channel distributions with standard deviations (third row) and density plots of the Fano factor (fourth row), thermopower (fifth row) and the ratio of  $\kappa_{el}$  to  $G_0 L_0 T K_0$  (sixth row) as function of the total conductance. The histograms are normalized to an upper limit of 10 and the densities to an upper limit of 9.

The statistical results of this closing curves are presented in Fig. 9.11. The mean values are again within some error the same as before in the statistics of the opening curves. That is also true for the positions of the peaks in the conductance histograms, but not exactly for their width and relative heights. The Mg peaks are more sharp here than in the opening curves, so are the first peak in the Al histogram at about  $1.1 G_0$  and the third one in Ag at about  $2.9 G_0$ .

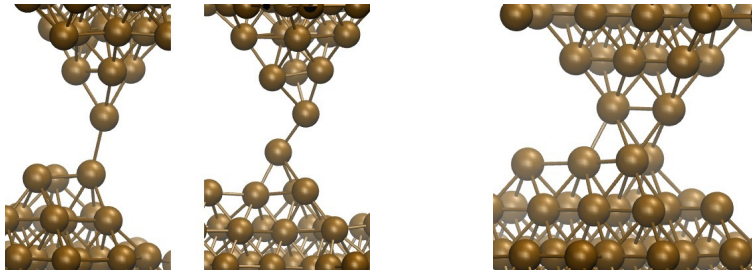


Figure 9.12.: Examples for geometries of Mg contacts with at least four points at the first peak with  $1 \pm 0.1 G_0$  (first and second) and the second one with  $2 \pm 0.1 G_0$  (third). The conductances and highest channels are:  $1.00 G_0$ :  $\tau_1 = 1.00$  (first),  $1.01 G_0$ :  $\tau_1 = 0.99$ ,  $\tau_2 = 0.02$  (second) and  $1.98 G_0$ :  $\tau_1 = 0.97$ ,  $\tau_2 = 0.52$ ,  $\tau_3 = 0.40$ ,  $\tau_4 = 0.09$ ,  $\tau_5 = 0.01$  (third).

The first peak of all three metals consists mainly of dimers and some monomers as shown in Figs. 9.12 and 9.15 for Mg and Ag. The second peak in Mg is slightly more interesting. It consists mainly of geometries with two parallel atoms which lie in their fcc positions<sup>8</sup> as shown on the right of Fig. 9.12.

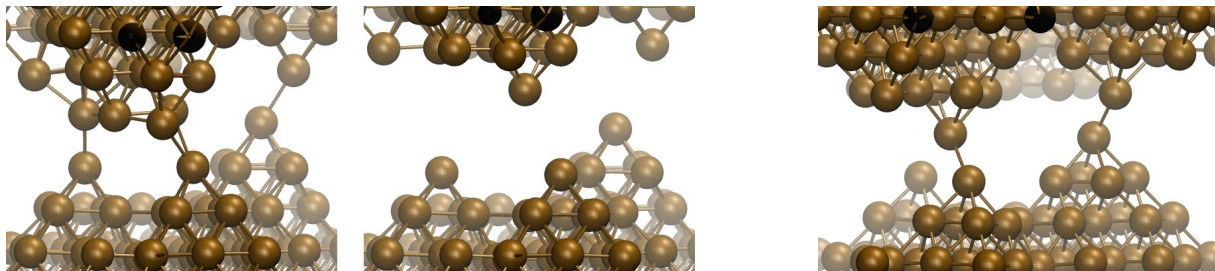


Figure 9.13.: Geometries of a Mg curve with three parallel wires arising during the opening (left) and two during the closing process (right). The second geometry shows the broken contact in-between. The left geometry has a conductance of  $3.1 G_0$ . The five highest channels are  $\tau_1 = 1.00$ ,  $\tau_2 = 0.98$ ,  $\tau_3 = 0.85$ ,  $\tau_4 = 0.23$  and  $\tau_5 = 0.03$ . The right geometry has a conductance of  $2.1 G_0$ . The three highest channels are  $\tau_1 = 0.99$ ,  $\tau_2 = 0.96$ ,  $\tau_3 = 0.07$ .

But one additional geometry was found: Two parallel dimers as known from opening curves of Au (right geometry in Fig. 9.13). The left geometry in Fig. 9.13 shows the corresponding opening curve slightly before rupture. It includes three parallel wires. As Mg does not form chains<sup>9</sup> the wires end up in monomers and dimers. In this case the monomer in the middle and the dimer on the right survive in a similar shape the rupture process and reunite into a

<sup>8</sup>Therefore it looks like a parallelogram.

<sup>9</sup>At least it was never observed here.

similar configuration while the upper atom of the dimer on the left moves upwards (second geometry), prohibiting a reunification into a dimer.

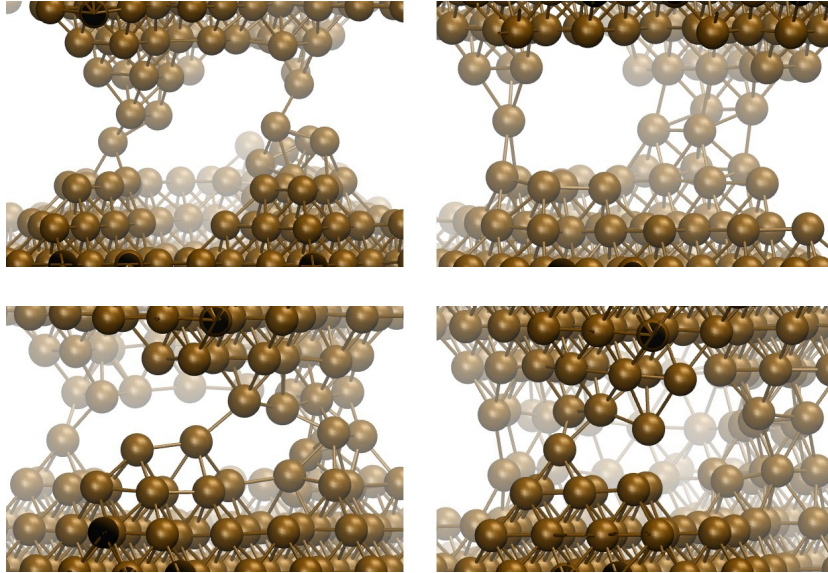


Figure 9.14.: Geometries of Mg of different types of parallel wires. The actual conductance values are  $2.9 G_0$  (upper left),  $4.7 G_0$  (upper right),  $6.7 G_0$  (lower left) and  $14.7 G_0$  (lower right).

Looking back onto the other opening curves shows that parallel wires ending up in parallel monomers and dimers is very seldom. It was only found a second time in the set of 100 curves (upper left geometry in Fig. 9.14). But the case of parallel wires with different minimal cross sections can be found in 7% of the curves (second to fourth geometry in Fig. 9.14). The geometries in the second row show another interesting possibility of parallel wires. Here they are distributed in a circular manner. So the cores are hollowed out while the borders are still in touch. This could be a finite size effect. An according study could shed more light onto this whole point of parallel wires in Mg contacts.

Annotation: It was mentioned above that in experiments there were hints of quantization in Mg. The existence of parallel dimers could be a solution to that.

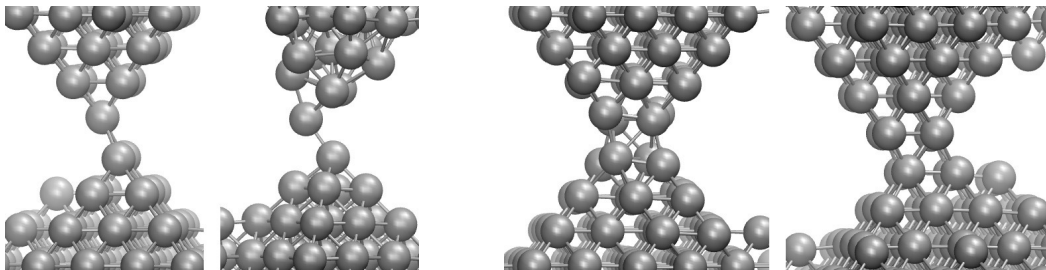


Figure 9.15.: Examples for geometries of Ag contacts with at least five points at the first peak with  $1 \pm 0.1 G_0$  (first and second) and at least four points at the third one with  $2.9 \pm 0.1 G_0$  (third and fourth). The conductances and highest channels are:  $0.99 G_0$ :  $\tau_1 = 0.92$ ,  $\tau_2 = 0.07$  (first),  $0.96 G_0$ :  $\tau_1 = 0.95$ ,  $\tau_2 = 0.08$  (second),  $2.91 G_0$ :  $\tau_1 = 1.00$ ,  $\tau_2 = 0.94$ ,  $\tau_3 = 0.88$ ,  $\tau_4 = 0.05$  (third) and  $2.88 G_0$ :  $\tau_1 = 0.99$ ,  $\tau_2 = 0.96$ ,  $\tau_3 = 0.70$ ,  $\tau_4 = 0.19$ ,  $\tau_5 = 0.04$  (fourth).

In the statistics of Ag the first and third peak in the conductance histogram are specially pronounced, the third one even more than in the opening curves. The first one consists as already mentioned out of monomers and dimers (left half of Fig. 9.15) and the third one out of geometries with four atoms in the minimal cross section (right half of Fig. 9.15). Ag maintains a much higher symmetry than Mg. That is visible in all four examples. But the first example of the  $2.9 G_0$  example has a symmetry break in the connection between the two halves which is relatively stable and leads to a reduction of the conductance<sup>10</sup>. This is different in the second example where the distance between the rows of atoms are different in comparison to one another which leads to a reduction of the conductance. This difference is not visible in the geometry but in the channel distribution which shows two fully open ones and two reduced ones. It is also per definition not stable because the distance is reduced continuously due to the reduction of the distance between the walls.

In total, the statistical results are very similar to their opening counterparts. The differences are smaller than what was shown for the small Au contacts in the last section.

In the following, if not explicitly written different, than only opening curves will be shown as before.

---

<sup>10</sup>Usually it should be  $4 G_0$  with 4 atoms in the MCS.

### 9.3. Influence of velocity

Different to the temperature which can be set arbitrarily within the simulations, the velocity of the walls moving away from their original position has numerical limits. This limit comes due to the problem that in MD calculations one can not parallelize the time<sup>11</sup> and the parallelization in particles has an upper limit<sup>12</sup> and a decrease of the velocity of an order of magnitude leads to an increase in elongation time of about the same order.

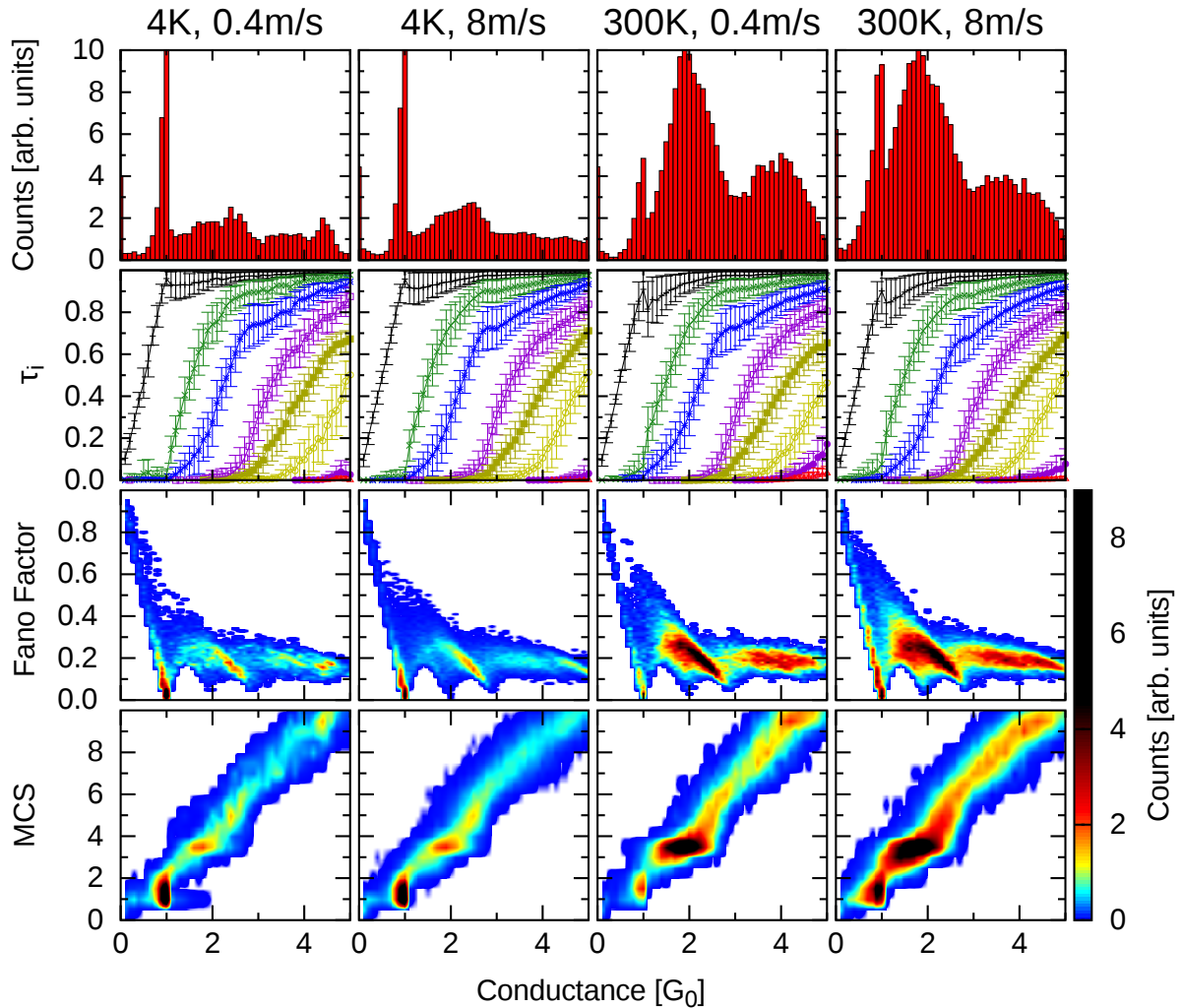


Figure 9.16.: Au data sets of wires with 56 atoms in the central part at 4 K (left half) and at 300 K (right half) at two different velocities of the walls (0.4 m/s and 8 m/s). The sets with 0.4 m/s contain 200 curves each and the sets with 8 m/s contain 1000 curves each. The MCS in the last row is determined by the simple projection method.

A wire with 563 atoms in the central wire needs with a velocity of 0.4 m/s about 1.5 h on 20 cores for the calculation of the elongation process. In experiments velocities in the order

<sup>11</sup>Because of causality.

<sup>12</sup>If one has the same number of cores as particles, which is the upper limit of cores one could imagine to be possible useful, the cores would have to waste a huge amount of time transferring data to one another. Data transfer between cores is very slow, in some cases even slower as if the addressed core would calculate the data itself.



of  $0.1 \mu\text{m/s}$  are used [194] which are six orders of magnitude lower than what was used for the calculations of this work. This difference in timescale can not be bridged from theory side.

So, are this calculations only of academic interest and have nothing to do with reality? The very good agreement between theory and experiments shown in earlier sections does not support this point of view. The reason for this lies in the very high speed of sound in metals which is in the order of  $\text{km/s}$  [195]. This is the upper limit of the movement of atoms and accordingly the timescale in which (small) geometric reorganizations can take place. The argumentation is that as long as the velocity stays far below this limit, the velocity should play no important role. With three orders of magnitude this should be fulfilled.

To analyze this problem in a more quantitative manner Fig. 9.16 presents the results for two different velocities with more than one order of magnitude difference for low and room temperature. As the chosen wires are again very small only the conductance range below about  $4 G_0$  is meaningful, which means in main the first and second peak.

At low temperatures all properties look within some error perfectly the same. At room temperature this is the case except for the peak heights in the conductance histogram and due to this the histograms in the Fano factor and MCS density plots. The peak positions stay the same. The reason is that the higher speed reduces the time for relaxation processes. But at higher temperatures this is what destabilizes thin wires where the one atomic wire is the extreme case, leading to the large decrease of the first peak compared to the other ones. So the effect on the histogram is the same as if reducing the temperature.

In total, within the accessible range of velocities the mean values are velocity independent, but at higher temperatures the velocity has a non negligible effect on the relative peak heights.

## 9.4. Statistical evolution

If one has chosen all the parameters needed for the elongation of a contact (e.g. the size, temperature, elongation direction, speed) the question remains how much elongation curves one needs to get sufficient converged histograms. To get a feeling for this Figs. 9.17 and 9.18 show the evolution of the typical properties studied here with the number of elongation curves for 4 K and 300 K, respectively.

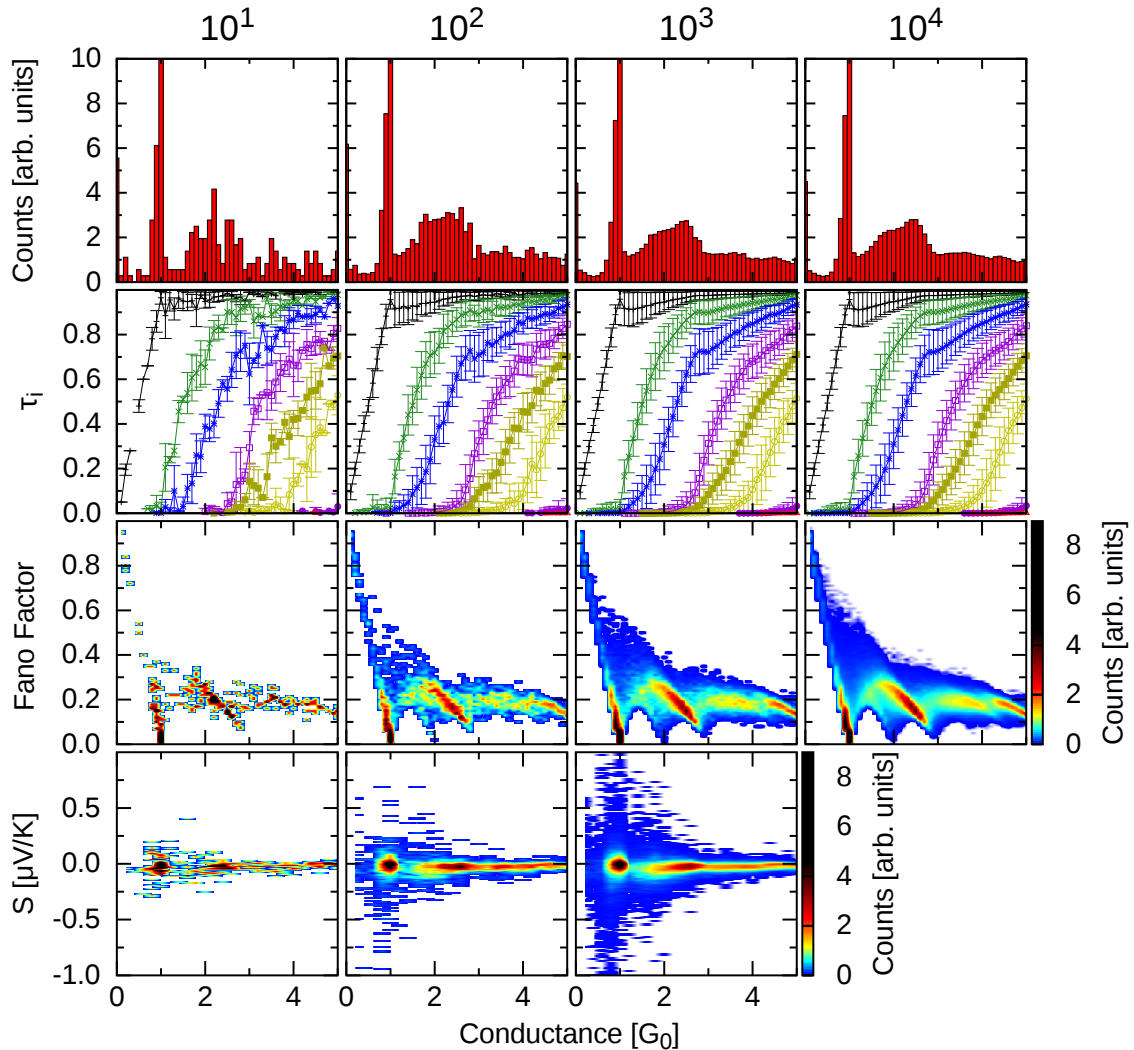


Figure 9.17.: Conductance histograms (first row), mean channel distributions with standard deviations (second row) and density plots of the Fano factor for Au with 56 atoms in the central wire and an elongation speed of 8 m/s at 4 K with statistics ranging from data of 10 elongation curves (first column) up to  $10^4$  elongation curves (fourth column) as function of the total conductance. The thermopower in row four has data from up to  $10^3$  elongation curves. The histograms are normalized to an upper limit of 10 and the densities to an upper limit of 9.

As can be seen, already 10 curves are sufficient to get a noisy but correct representation of the distinctive features. In the conductance histogram (first row) the first and second peak are developed. With 100 curves the histograms are almost perfectly converged. The mean

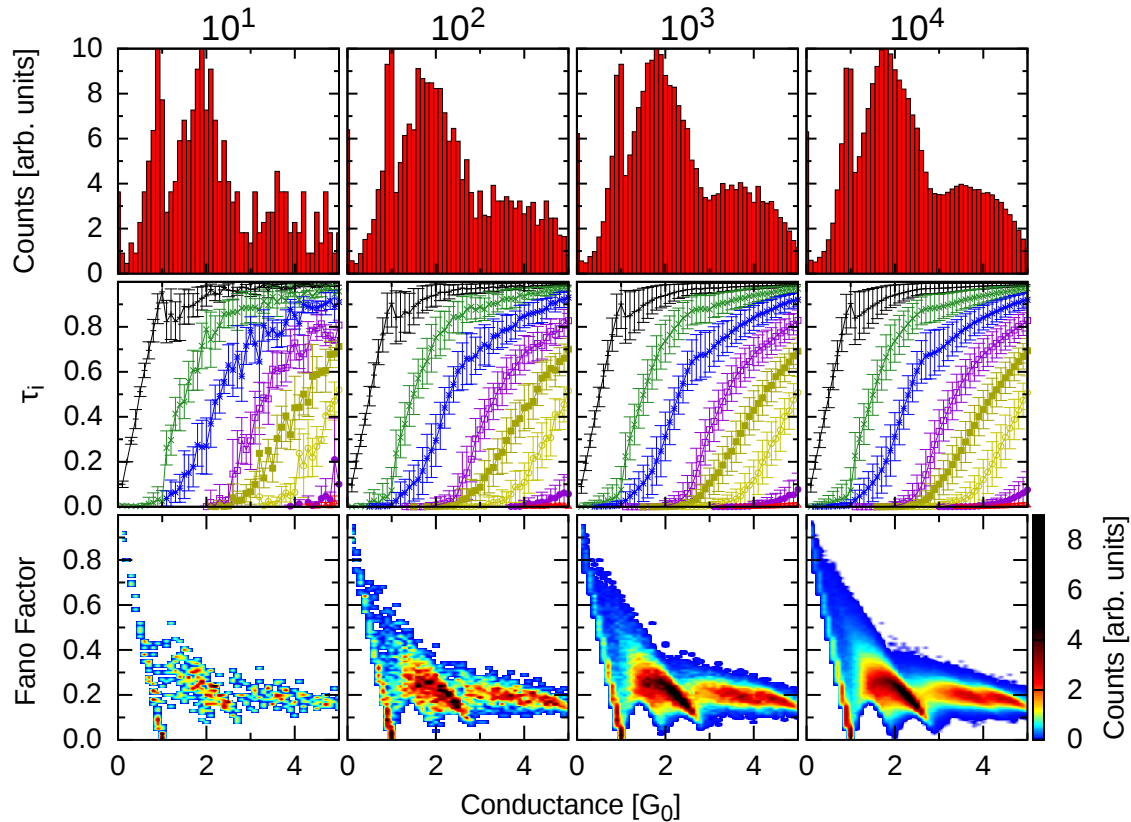


Figure 9.18.: Conductance histograms (first row), mean channel distributions with standard deviations (second row) and density plots of the Fano factor for Au with 56 atoms in the central wire and an elongation speed of 8 m/s at **300 K** with statistics ranging from data of 10 elongation curves (first column) up to  $10^4$  elongation curves (fourth column) as function of the total conductance. The histograms are normalized to an upper limit of 10 and the densities to an upper limit of 9.

channel distribution behaves similar. With 10 curves the rough behavior of the individual channels can be overseen. With 100 curves the mean values have converged. The density plots also behave similar. 10 curves are sufficient to oversee the mean behavior, with 100 curves the configuration space is already roughly sampled. A higher number of elongation curves only samples the configurational space more dense and smooths thereby the resulting histograms.

## 9.5. FCC versus BCC Fe lattice

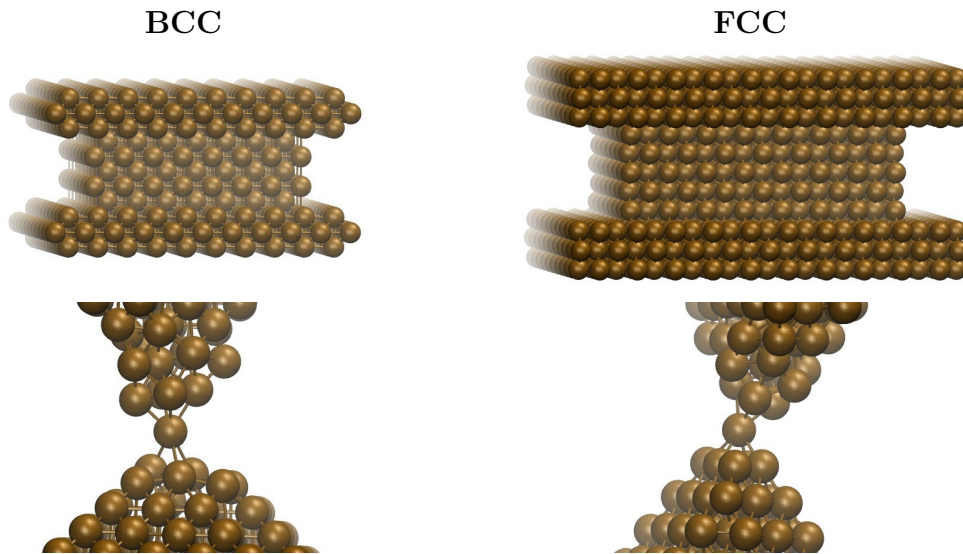


Figure 9.19.: Ideal starting geometries for the bcc (left) and fcc (right) data sets of Fe shown in Fig. 9.20 (top) and one example for each lattice type for a geometry with  $1.5 G_0$  (bottom).

Another property which was briefly mentioned in the context of the Fe results above is the crystal structure. All materials which were investigated here except Fe have an fcc lattice. For Fe the bcc configuration<sup>13</sup> is energetically preferred<sup>14</sup> so it was used for the construction of the ideal starting geometries. Fig. 9.19 shows the two lattice types.

The lattice type of the initial ideal structure is not expected to play an important role because if the wire is large enough and already elongated to some extent, the electric properties should be dominated by the thinnest part of the wire which has enough disorder to forget about its initial lattice structure. An example for this explanation is given in the bottom line of Fig. 9.19 where both geometries shown, the left one coming from a bcc and the right one from an fcc wire, have  $1.5 G_0$ .

To check this assumption in the statistics with respect to the different properties, Fig. 9.20 shows the direct comparison between the two lattice types.

Two main differences can be seen: The delayed decay as function of the displacement and the larger spread in all plots of the fcc configuration compared to the bcc one. The first one is due to the larger number of atoms (about twice as many). The second one is more unclear. The larger number of atoms leads to longer structures which have more possibilities to decay. This leads to more noise and probably also to configurations which are not possible in the relative short bcc wires.

The mean values show within the error bars a perfect agreement.

In total, the lattice type seems not to have a large impact onto the results. It only modifies some details.

<sup>13</sup> [196] references to 'R. Kohlhaas, P. Donner, and N. Schmitz-Pranghe, *Z. Angew. Phys.*, 1967, **23**, 245'

<sup>14</sup>Mg has usually also no fcc structure, but hcp is currently not implemented.

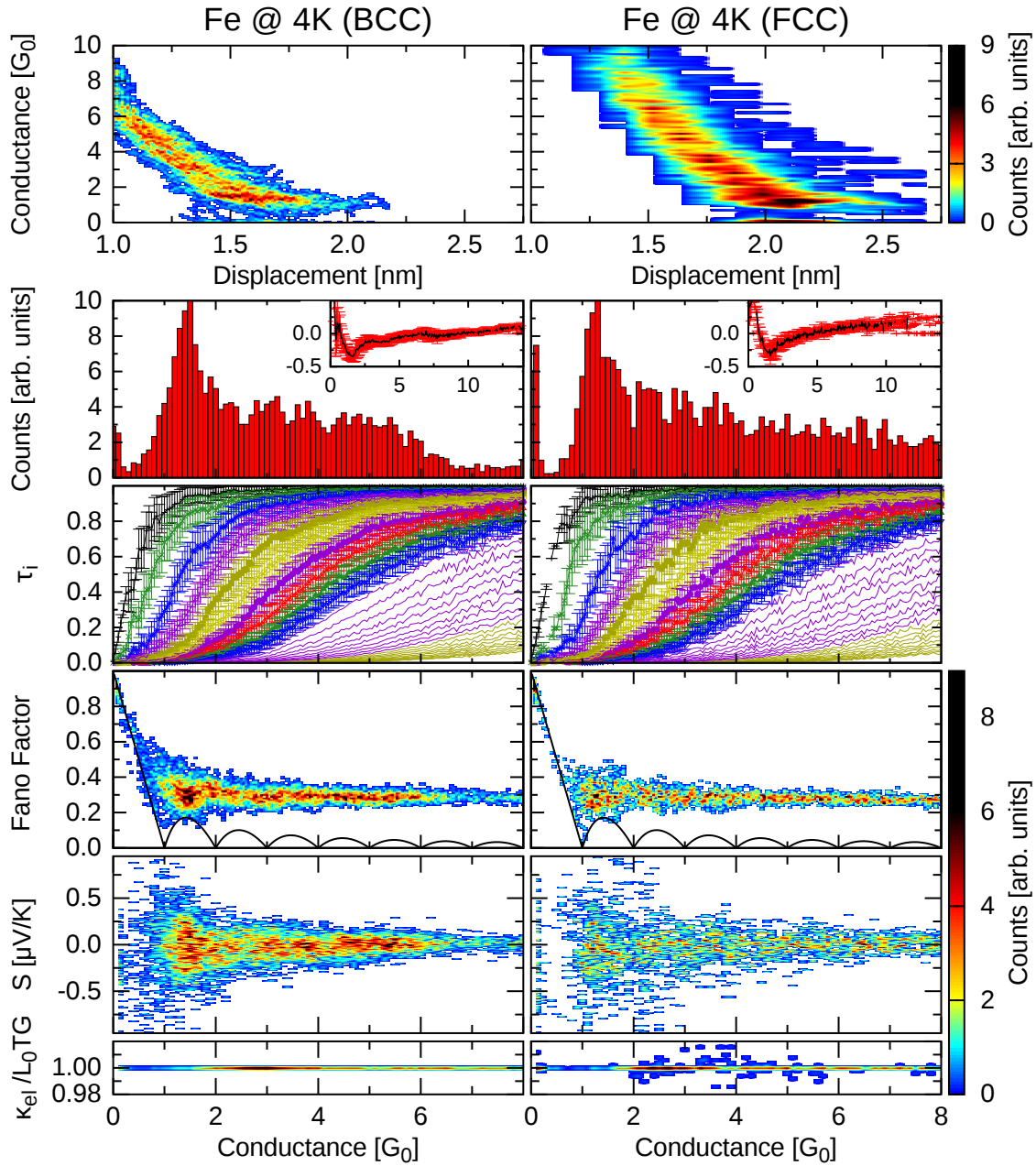


Figure 9.20.: Density plots of the conductance as function of the displacement (first row), conductance histograms (second row), mean channel distributions with standard deviations (third row) and density plots of the Fano factor (fourth row), the thermopower (fifth row) and the ratio of  $\kappa_{el}$  to  $G_0L_0TK_0$  (sixth row) for Fe at 4K with data of 100 elongation curves with 275 atoms (left column) and with data of 50 elongation curves with 563 atoms in the central wire each (right column) as function of the total conductance. The initial geometries are shown in Fig. 9.19. The histograms are normalized to an upper limit of 10 and the densities to an upper limit of 9.

## 9.6. Doubling the size of Au contacts

One of the last questions discussed in this thesis is the question of size. Does the size of the geometry matter? In the last section we saw small differences which could be traced back to the number of atoms in the wire and it is obvious that higher conductance values can only be achieved using large enough wires<sup>15</sup>. There were also differences in the histograms of the small contacts used in earlier sections of this chapter to analyze the effect of for example the statistics or temperature with respect to the ones used in section 5.1. While the differences were not very large, they were sometimes not totally negligible, either.

To get a feeling of how much influence the size and structure of the initial wire has, this section investigates the effect of doubling the number of atoms in the case of Au and in the next section the effect of the shape of different materials will be investigated.

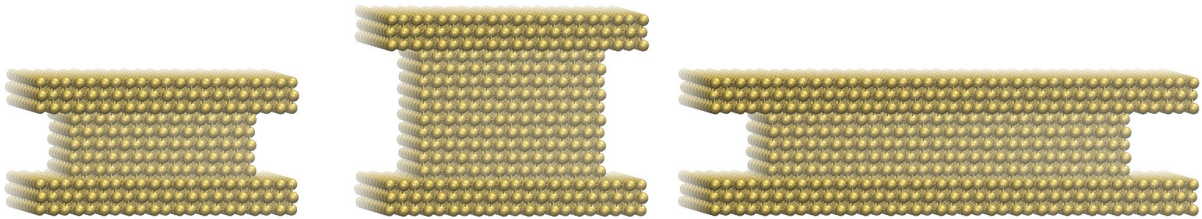


Figure 9.21.: Ideal initial geometries of the three configurations of Au studied in this section. They have 563 (left), 1125 (middle) and 1087 (right) atoms in the central part. They all have the same size in  $y$ -direction (out of paper), but different one in the  $x$ - and  $z$ -directions.

The geometries used in this section are shown in Fig. 9.21. The left one is the one used as standard in earlier sections, the middle one has double its length and the right one has one side doubled perpendicular to the elongation direction. Because of the lattice structure the number of atoms are not doubled perfectly

The results are shown in Fig. 9.22. As in the comparison of the crystal structures above, the mean values seem to be very similar. But in this case the details are important. The most important point in the conductance histogram is the third peak which is not visible in the first and second row, but very clear and sharp in the third one at about  $2.8 G_0$ . The second peak looks very similar in the three cases, but it is highest in the third one and has the largest width in the second row.

This all has its effects onto the mean channel distribution and with it onto the Fano factor and onto the mean thermopower at low conductance values. The peak of the second channel at about  $1/2 G_0$  is also best visible in the third row and least well in the second one and the channels open more and more step like going from the left to the right one mapped onto the Fano factor as increased densities at the dips of the multiple of  $G_0$ . The mean thermopower which missed the experimental found suppression at the maxima of the conductance histogram is now perfectly suppressed for both larger structures (blue lines in the insets of row five).

This can be traced back to points which were already discussed in section 5.3. In short, the result of that section was that parallel wires forming during the elongation process have a large influence onto the behavior of the system leading to effects not possible without. This

<sup>15</sup>At least the cross section has to be large enough.

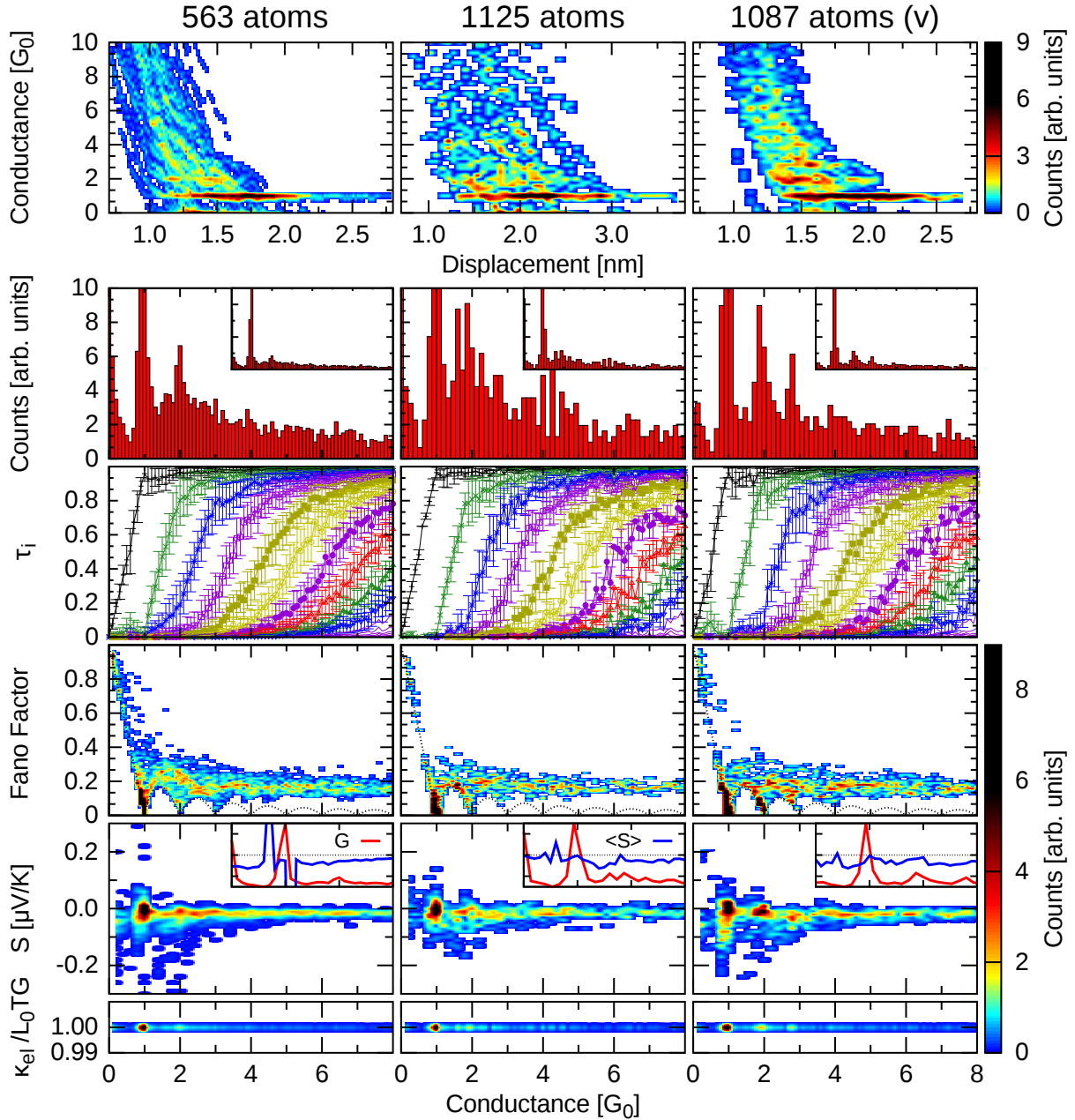


Figure 9.22.: Density plots of the conductance as function of the displacement (first row), conductance histograms (second row), mean channel distributions with standard deviations (third row) and density plots of the Fano factor (fourth row), the thermopower (fifth row) and the ratio of  $\kappa_{el}$  to  $G_0 L_0 T K_0$  (sixth row) as function of the total conductance. The temperature of the Au wires were set to 4 K. The statistics include data of 100 elongation curves of the default size (left column), data of 50 elongation curves with doubled length (middle column) and data of 50 elongation curves with one size perpendicular to the elongation direction doubled (right column). The initial geometries are shown in Fig. 9.19. The histograms are normalized to an upper limit of 40 (see inset for the complete range) and the densities to an upper limit of 9.

was especially important for the explanation of the peak at about  $1/2 G_0$  of the mean second channel and partially for the peak in the conductance histogram at  $2 G_0$ .

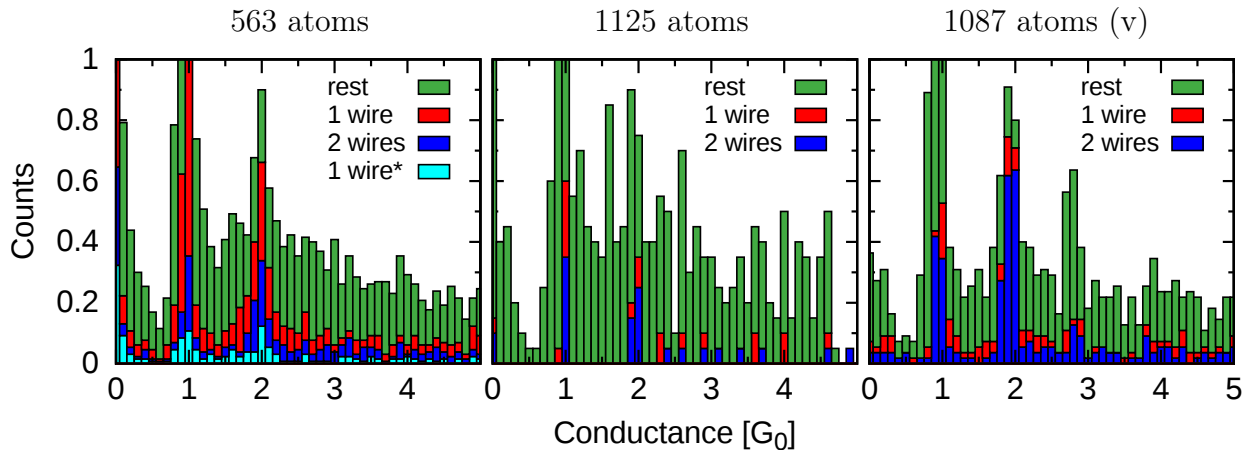


Figure 9.23.: Conditional transmission histograms of Au at 4K according to Fig. 9.22. The total transmission histogram is divided into contributions from single wires (red), two parallel wires (blue) and the rest (green). The condition had to be fulfilled at  $2.0 \pm 0.1 G_0$  for at least 3 data points during the elongation process. The graph for the normal system geometry (left) has an additional part in cyan ('1 wire\*') which shows the histogram of single wires with the additional restriction of only two channels  $\geq 0.2$ . Almost all points of the single wires of the other two geometries fulfill this condition.

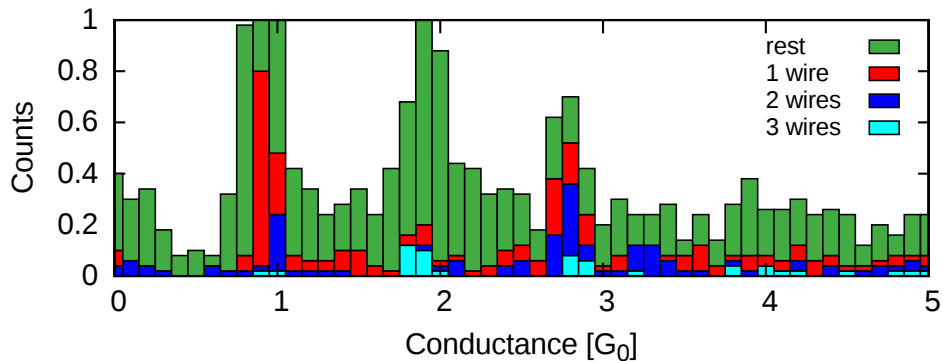


Figure 9.24.: Conditional transmission histograms of the third Au geometry (v) at 4K. The condition had to be fulfilled at  $2.8 \pm 0.1 G_0$  (third peak) for at least 3 data points during the elongation process.

As this are again important points which differ between the three starting geometries, Figs. 9.23 and 9.24 show conditional histograms for parallel wires at  $2 G_0$  and  $2.8 G_0$ , respectively. While the second peak in the original case (left) is slightly dominated by the contributions from plateaus of single wires (red), where about 1/3 of them has mainly two contributing channels, the contribution from this type of wires is only minor in the larger contacts. Even more important as in the original case are the contributions from two parallel wires (blue) which is by far the dominant part for the second peak of the broad contacts (right). As the parallel wires break one by one it is obvious that they also contribute visibly to the first peak but almost not to the points in-between. The histogram of the long wires (middle) do not have such a well defined second peak due to a large background of wires without plateaus.

The third peak (Fig. 9.24) visible only in the right histogram is again dominated by con-



figurations with two parallel wires (four curves, blue) but has also contributions from three parallel wires (one curve, cyan). There are three curves out of fifty of single wires with a plateau at  $2.8 G_0$ . The contacts with two parallel wires do not contribute to the second peak because at least one of the wires has to be thicker than a single atom to sum up to  $3 G_0$ . In contrast, the contact with three parallel wires contributes to the second peak because all three wires have to be of the single atom type<sup>16</sup> and if one breaks than two remain with a total conductance of about  $2 G_0$ . The two wires of that contact break at about the same time such that the contribution to the first peak is vanishing small.

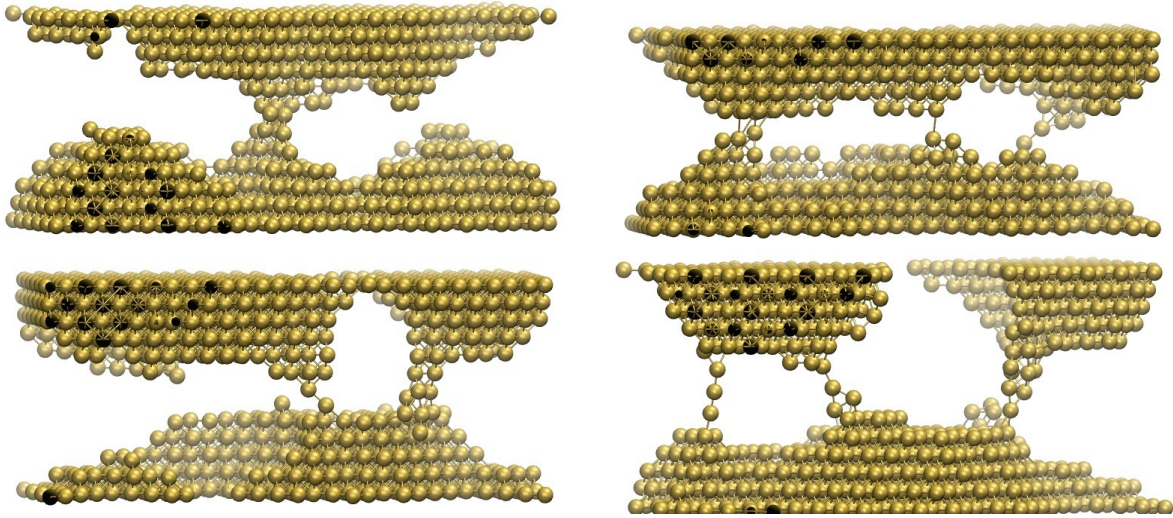


Figure 9.25.: Geometries contributing to the  $3 G_0$  peak in the histogram of the broad (v) double sized Au structures. The values for conductance and Fano factors are:

$$\begin{array}{ll} G = 3.0 G_0, F = 0.15 \text{ (top left),} & G = 2.9 G_0, F = 0.21 \text{ (top right)} \\ G = 2.9 G_0, F = 0.14 \text{ (bottom left),} & G = 2.9 G_0, F = 0.04 \text{ (bottom right)} \end{array}$$

The different types contributing to the third peak are shown in Fig. 9.25: There is the single wire type (top left, red color in the statistics before) which has a Fano factor in the range of the saturation value discussed in section 5.2. The same is true for the geometry with two parallel wires (bottom left, blue color in the statistics before). This is different for the other two shown geometries with three parallel wires: While the one on bottom right has as expected<sup>17</sup> a very small Fano factor while the one on the top right side has a Fano factor much higher than the saturation value. The reason for the high Fano factor in the latter case is that not all three wires are of the single atom type, meaning that the one in the middle is already in the tunneling regime, contributing only with a partially open channel which is compensated by the wire on the right which contributes with more than one channel (it has two fully open channels and two about half open channels). This curve does also not contribute to the cyan histogram in the conditional histogram (Fig. 9.25) because it is only a transient state (one wire is already in the rupture process) and does therefore not fulfill the condition of a plateau with at least three points.

<sup>16</sup>With a diameter of a single atom in the narrowest part, can be cone like or a chain.

<sup>17</sup>Single atom wires usually have one (almost) fully open channel leading to a vanishing Fano factor.

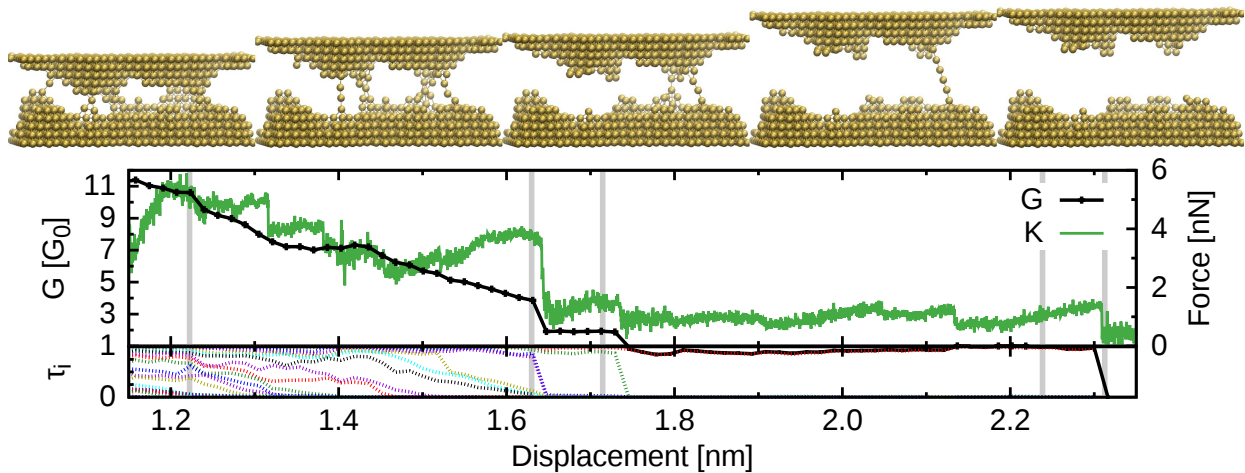


Figure 9.26.: Evolution of a Au contact with 1087 atoms in the central wire. The total conductance (black solid line), the force (green solid line) and the channel distribution (colored dashed lines) are plotted as function of the displacement of the walls from their ideal position. The positions of the geometries shown on top are marked below by gray vertical lines. They have conductance values of  $10.6 G_0$ ,  $3.9 G_0$ ,  $1.9 G_0$ ,  $0.9 G_0$  and  $0 G_0$ .

Fig. 9.26 shows the evolution of such a curve with an extreme number of parallel wires evolving. As it is a nice summary of many things learned so far for the evolution of a Au contact, it should be described here in more detail.

The first snapshot at about  $10.6 G_0$  has five parallel wires which include one monomer and one dimer on the left side. In the following the dimer breaks and the monomer forms a short wire. Each of the four wires in the second snapshot has an (almost) fully open channel and some of them have an additional very small one. Two of the four wires break nearly at the same time leading to a sudden drop in the conductance and a loss of two fully open and two almost closed ones. The two remaining wires are very flexible, leading to a long plateau with a constant conductance and channel distribution. While the dimer in the background breaks at some point, the small wire starts to elongate further, including two more atoms into the wire. At the times the wire is under tension and therefore straight (see green force curve), the first channel is almost perfectly open and therefore the conductance increases to slightly below  $1 G_0$ . At the points where an atom joins the wire, leading to a relaxation of its tension, the first channel and with it the total conductance decreases again. The last time before the rupture the tension in the wire is largest and the conductance reaches  $1.0 G_0$  with a perfectly open first channel.

In summary, the size of the contact has in this special case of Au interesting effects even at low conductance values. The size modifies the possibility of parallel wires which leads to modifications of the mean behaviors of the properties at higher conductance values toward the behavior at low values which has a special impact if most or all of the parallel wires have a single atom in the narrowest part.

As conclusion one would probably come to the end that one has to use only the largest ones.

But the problem is clear, the computer time. While the calculation of a data point with 563 atoms in the central part needs less than 0.2 h on 72 cores<sup>18</sup>, it takes about 1.1 h on 144 cores for the large contacts. Doubling this size further to 2103 atoms leads to an increase of the needed computer time by a factor of 10 to 11 h per data point on 144 cores<sup>19</sup>.

---

<sup>18</sup>Further parallelization leads to a bad parallelization-efficiency.

<sup>19</sup>A further parallelization currently fails due to a bug in a MKL implementation of a scalapack routine which would be needed to replace its OpenMP parallelized version.

## 9.7. Geometry of initial structures of Au, Al and Pb

In section 9.6 a special type of geometric modification was tested for one element. The question was what happens if one doubles the size of the initial Au geometry in two different directions.

This question should now be modified into what happens if one uses a similar number of atoms but having a different initial geometry for different metals. As the second and third configurations of the last section already discussed this question for very large Au geometries at 4 K, the first part here will be a kind of repetition with small contacts.

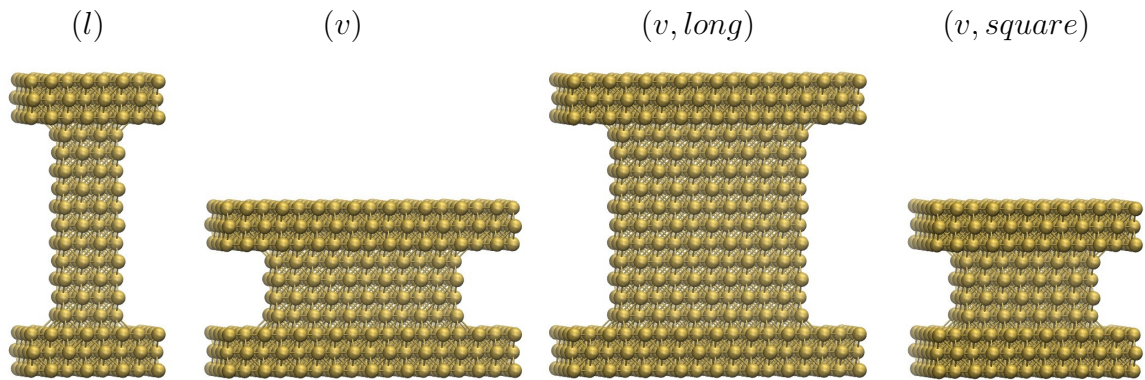


Figure 9.27.: Initial geometries of the long (first), the wide (second, ‘v’ (vertical)), the wide & long (third, ‘v, long’) and the wide & square (fourth, ‘v, square’) wires with 110 (first and second), 303 (third) and 112 (fourth) atoms in the central wire each.

### 9.7.1. Au

Fig. 9.28 shows the results of the long (‘l’) and vertical lying (‘v’) contacts at 4 K. The difference is not so far away from what we already saw in Fig. 9.22 between the two data sets with more than 1000 atoms: The long geometry has besides the first peak a broad second one while the short one has a relative sharp second peak. Because of the small contact size, peaks at higher conductance values are not very meaningful but the mean trends of the other properties are interesting anyway. The second channel (green) has a dip at about  $0.5 G_0$  in the vertical, but not in the long configuration. It also opens more straight between 1 and  $2 G_0$  in the vertical than in the long configuration which also modifies the behavior of the third channel. The mean Fano factor behaves very similar, but again in the range between 1 and  $2 G_0$  the value is largely suppressed in the vertical configuration which is a direct consequence of the behavior of the second channel. It is an interesting remark at that point that the mean values between  $2.5$  and  $3 G_0$  are more suppressed in the long configuration. Because of the many channels in that range this is not easy to see in the channel distribution. The spread in the thermopower values is much larger in the long contacts, leading to large fluctuations in the mean values. This is different in the vertical ones which already show the vanishing mean values at about 1 and  $2 G_0$ . Similar are the results of the thermal conductance values, while the vertical ones fulfill almost perfectly the Wiedemann-Franz law except for a few points between  $0.8$  and  $1.8 G_0$ , there are large deviations in the data set of the long ones up to about  $2.5 G_0$ .

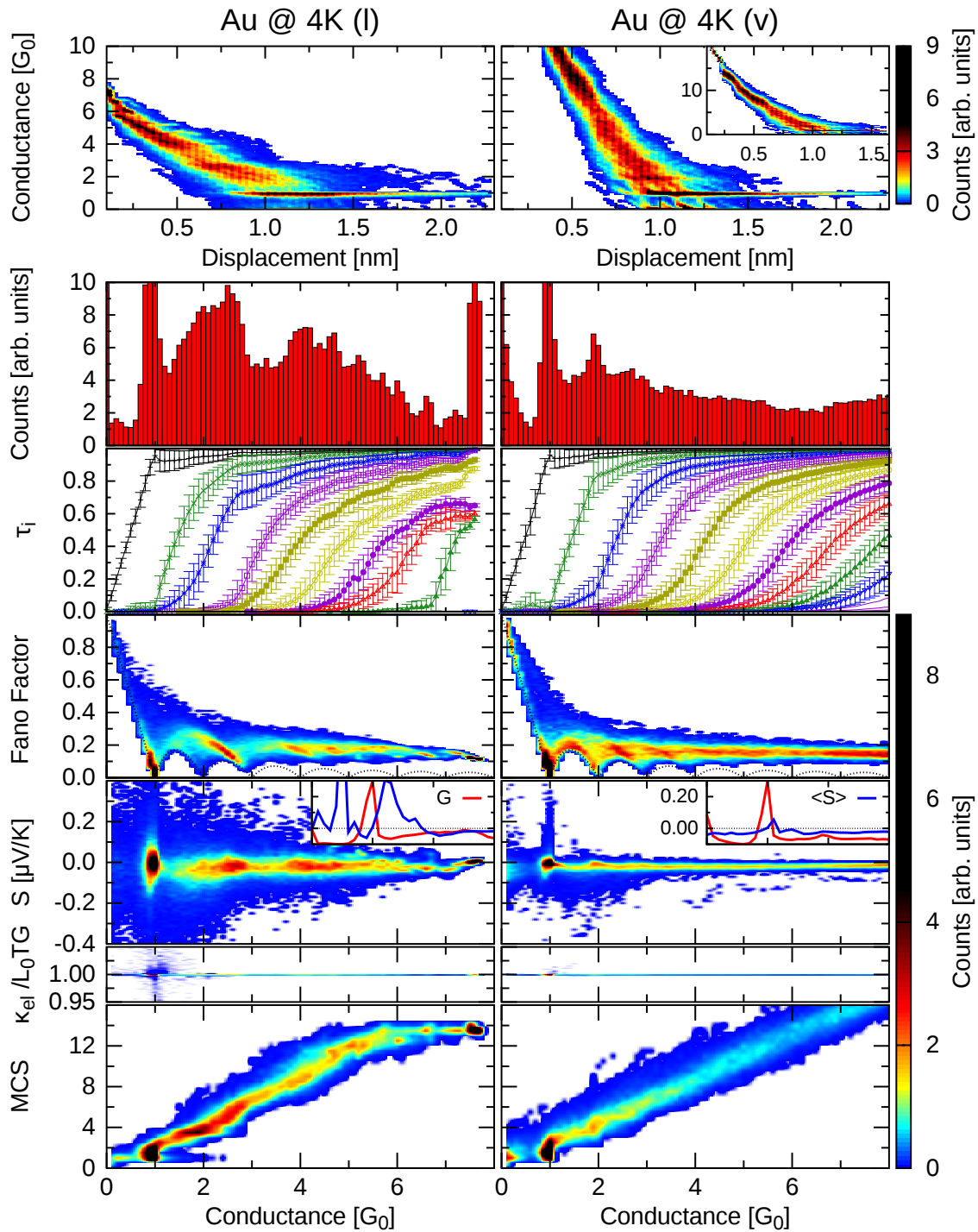


Figure 9.28.: Density plots of the total conductance as function of the displacement of their upper walls to the initial positions (first row), conductance histograms (second row, 25%), mean channel distributions with standard deviations (third row) and density plots of the Fano factor (fourth row), thermopower (fifth row), the ratio of  $\kappa_{el}$  to  $G_0 L_0 T K_0$  (sixth row) and the MCS (seventh row) as function of the total conductance. The Au data are from about 900 elongation curves at 4K with initial geometries as in Fig. 9.27. The histograms are normalized to an upper limit of 10 and the densities to an upper limit of 9.

The density plot of the MCS in the last row is consistent with the conductance histogram. The spread in the long data set is much larger than in the vertical one leading to a mixture of more geometric configurations contributing to the same conductance values which leads to larger spreads in the other properties as seen above.

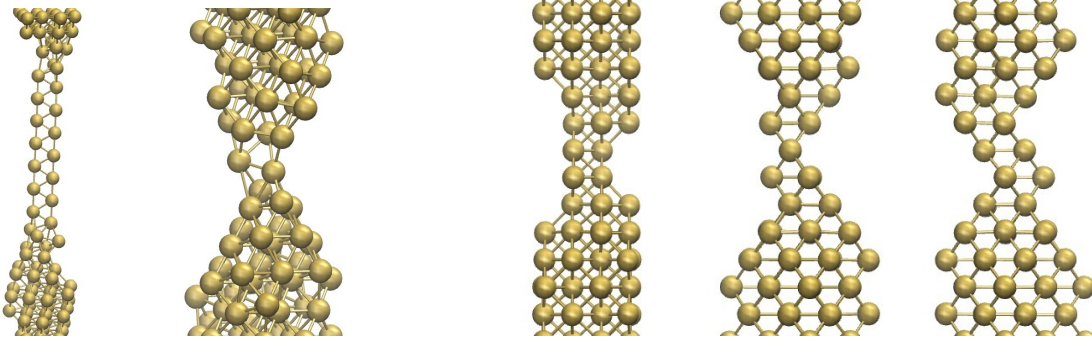


Figure 9.29.: Geometries belonging to the conductance peak of the long 4 K data set of Au at  $2 G_0$ . The three configurations on the right side show the same geometry but from different angles. The conductance and Fano factor values are:  $1.9 G_0:0.04$ ,  $2.0 G_0:0.07$  and  $1.9 G_0:0.22$ .

The two most interesting points in this plots are the conductance peak at  $2 G_0$  with its different channel distributions in the two configurations and the conductance peak (or the part of it) in the long configuration at  $2.5 G_0$  which is not significant in the vertical data set. To have more insights one can search for geometries which have plateaus with this characteristics.

Geometries for the conductance peak of the long wires at  $2 G_0$  are shown in Fig. 9.29. The two geometries on the left side have further more a very low Fano factor which means that the transport is dominated by two almost fully open channels. But only about 6% of the curves contributing to the  $2 G_0$  peak have a such low Fano factor (blue color in the density plot in Fig. 9.28). But whether they have a low Fano factor or not, the right side depicts the reason for the peak from three different angles of the same geometry: The low temperature together with the thin<sup>20</sup> configurations and long<sup>21</sup> geometry support the development of highly symmetric configurations during the elongation process. The example shown on the right in Fig. 9.29 has a relative high Fano factor as have most of the similar geometries building the conductance peak at  $2 G_0$ . The high flexibility of this wires leads to the very broad distribution of the conductance values which leads to the very broad peak at  $2 G_0$  with the lowered second and enhanced third mean channel.

The reason for the conductance peak of the vertical configuration at  $2 G_0$ , which is relative sharp, is a different one. The zigzag structures like the ones shown in Fig. 9.29 for the long configurations also appear if only short and with much reduced probability. Two wires were found with such a structure contributing more than 15 data points<sup>22</sup> to the  $2 G_0$  peak. At

<sup>20</sup>For thicker wires the probability of not regaining a high symmetry after elongating half a unit cell (new line of atoms) gets drastically enhanced because of the decreasing flexibility of the lattice itself.

<sup>21</sup>Short wires are much more rigid, leading to a pyramidal form.

<sup>22</sup>The number of data points is only relevant if one can compare them within a homogeneous data set. To compare to different sets, e.g. between the long and the vertical configurations, one would have to apply some sort of normalization to account at least for the different counting due to different total elongation length.

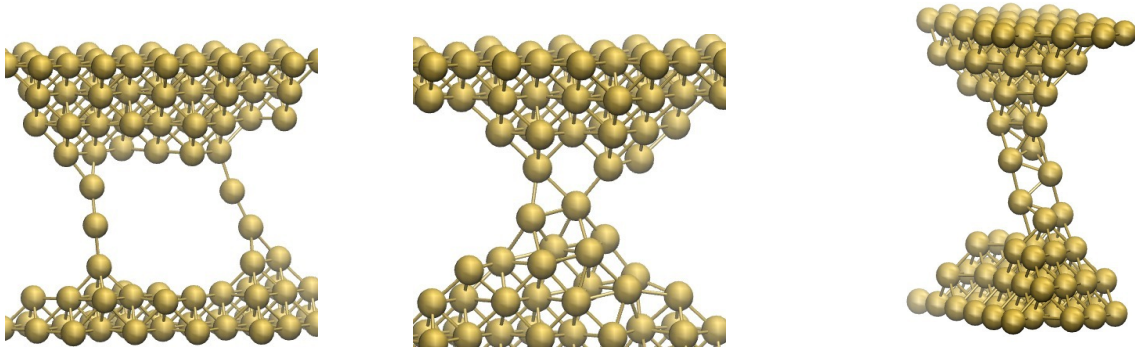


Figure 9.30.: Geometries belonging to the conductance peak of the vertical 4K data set of Au at  $2 G_0$ . The conductance and Fano factor values are:  $2.0 G_0:0.04$ ,  $1.9 G_0:0.06$  and  $1.9 G_0:0.09$ .

the same time 16 wires were found having parallel wires (left geometry in Fig. 9.30). The second geometry in Fig. 9.30 contributes only 10 data points to the conductance peak. But besides the question if one counts it to the parallel wires, it also contributes to the dip of the second mean channel in the statistics at around  $0.5 G_0$ . The reason is that this kind of short structure is very rigid, allowing it to break apart almost as it is now with a second channel carrying at  $0.5 G_0$  still  $1/4$  of the conductance.

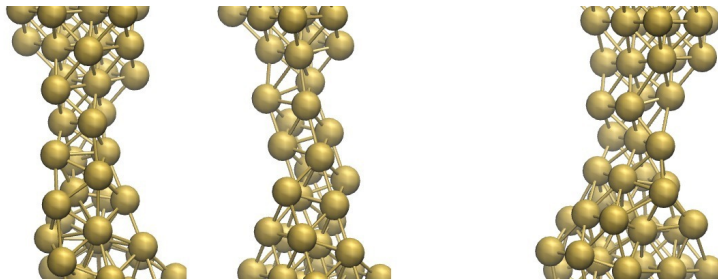


Figure 9.31.: Geometries belonging to the conductance peak of the long 4K Au contacts at  $2.5 G_0$ . The two geometries of the left side are from the same elongation curve and are displaced by  $0.16$  nm. The conductance and Fano factor values are:  $2.5 G_0:0.15$ ,  $2.5 G_0:0.14$  and  $2.5 G_0:0.15$ . All geometries have three channels greater  $0.02$ .

The peak at  $2.5 G_0$  consists of geometries with three atoms in the minimal cross section. They can appear in different forms with more and less symmetry (Fig. 9.31). The first and second geometry in Fig. 9.31, which belong to the same elongation curve, show that the minimal cross section of three atoms stays stable enough for some time to cause neighboring rows of atoms (below) to thin down to compensate the stretching instead of thinning further itself. This type does not directly belong to the one shown on the right of Fig. 9.29 (the process gets modified by the creation of disorder) but it also ends up with a short zigzag structure which also contributes to the peak at  $2 G_0$ .

As this type only modifies the conductance histogram of the long wires, whereas the parallel wires were only seen in the vertical ones, the question remains if it is the cross section that matters, or perhaps the form of the cross section (square or rectangular), or is it the relation between length and cross section that makes the difference?

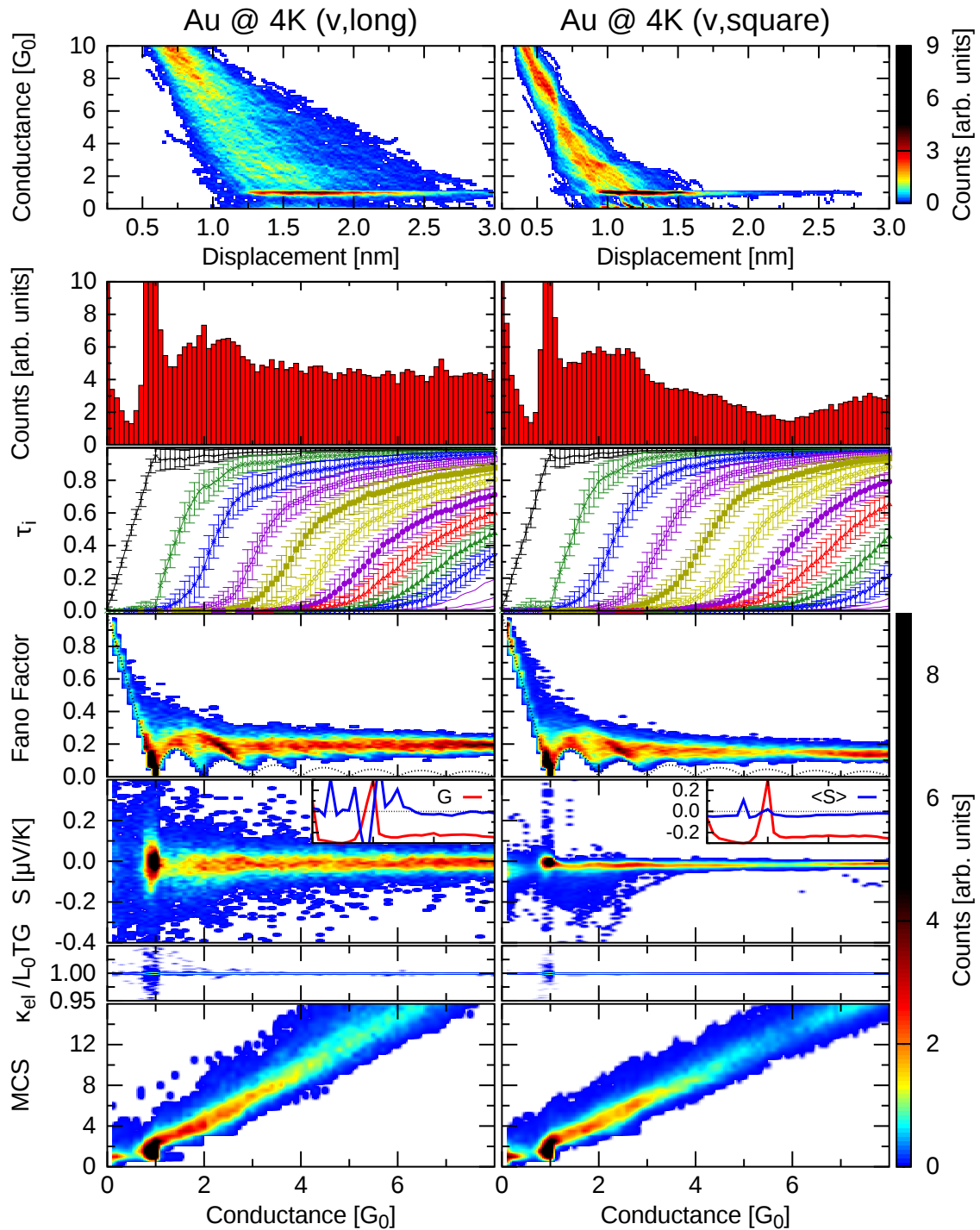


Figure 9.32.: The same as in Fig. 9.28 but for two other geometric configurations (see Fig. 9.27). (25% of first peak in the transmission histograms.) The statistics includes 500 elongation curves.

To go into the direction of an answer Fig. 9.32 shows the results for the vertical-long and vertical-square initial geometries. Interesting is that the length seems to have a strong effect onto the mean values and its scattering, so the mean values of the long wires in Fig. 9.32 are more similar to the ones of the long wires in Fig. 9.28 and the short ones equivalent.



The conductance histograms and some details like the exact evolution of the second mean channel on the other hand seems to be influenced also by the shape of the cross section. So has the conductance peak at  $2 G_0$  in the vertical-square case almost vanished and in the vertical-long case it is overlapped by a very broad peak as seen before in the data set of the long contacts.

Looking onto the geometries one finds that the parallel wires, which mainly determined the conductance peak and the evolution of the second mean channel of the vertical data set, have now almost vanished. From the 16 wires contributing more than 15 data points each during their elongation, only 5 (4) wires with 5 to 10 data points each of the vertical-long (square) remained. Most parallel wires forming in the vertical-square configuration fuse to a single wire or rip in parts or total after a few steps. In the vertical-long configuration one of the pair of parallel evolving wires never survives the dimer configuration, in most cases it already breaks after the evolution of the monomer configuration while the second one sometimes survives long enough to build a chain.

In total, the length of the contact seems to have the most strong effect onto the mean values and their variances, but the form and size of the cross section modifies (important) details.

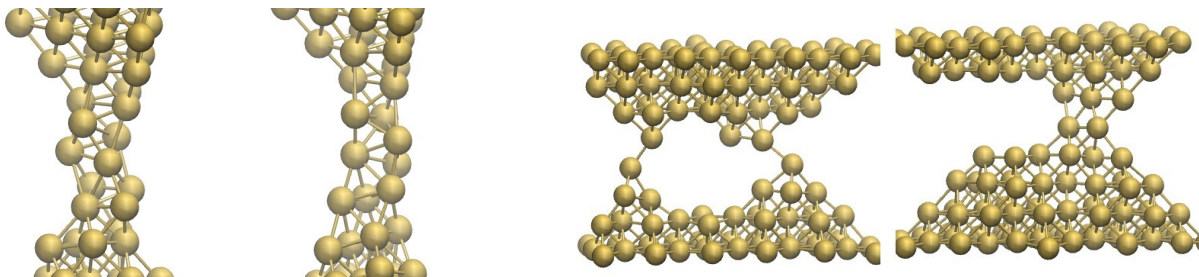


Figure 9.33.: Geometries belonging to the conductance peaks of the 300 K data sets of Au at  $2 G_0$ . On the left side two geometries from the same elongation curve coming from the long (l) starting geometry and on the right side a configuration with two parallel wires and one with two parallel atoms coming from the vertical (v) starting geometry are shown. The conductance and Fano factor values are:  $2.0 G_0:0.53$ ,  $2.1 G_0:0.48$ ,  $2.0 G_0:0.10$  and  $1.9 G_0:0.14$ .

Now one can do the same thing at room temperature. In the data set of the large contacts at room temperature (sec. 7) no parallel wires have been found (only parallel atoms). So the effect of the size is expected to be less pronounced. And indeed the effect is smaller but again not negligible (Fig. 9.34). While the second conductance peak of the vertical configuration looks very like the one of the long configuration at 4 K, the second peak in the long configuration is relative symmetric and dominates the histogram. In contrast to the conductance histograms, the channel distributions and with it the Fano factor are much like their counterparts at low temperature. The most prominent feature in this direction is the evolution of the second and third mean channel. This could imply that there are parallel wires included.

Looking at elongation curves who support at least 5 data points with only two transmission channels each to the peak at  $1.95 \pm 0.1 G_0$  three cases of parallel wires and two cases of

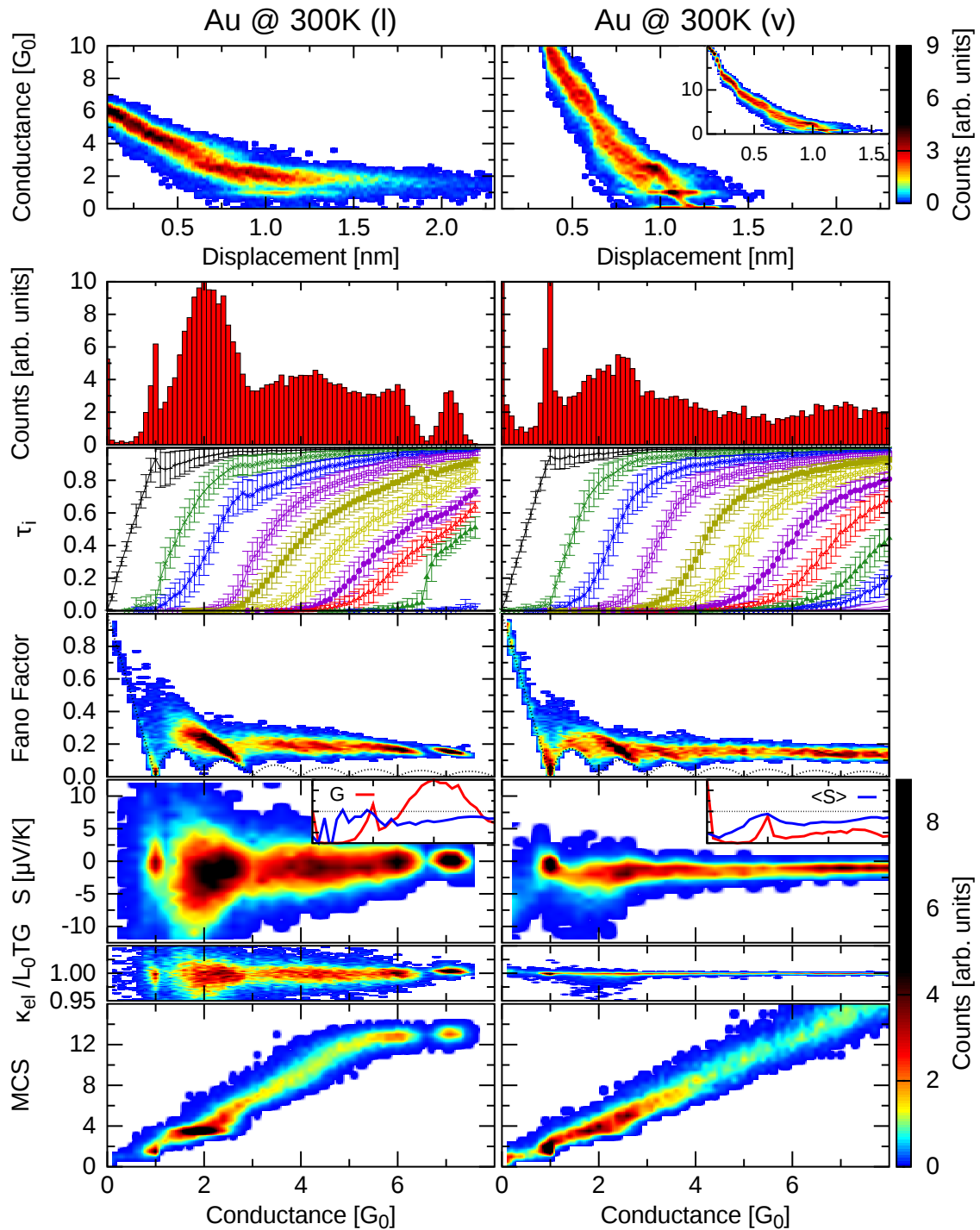


Figure 9.34.: The same as in Fig. 9.28, but for Au at 300 K.

parallel atoms as shown on the right of Fig. 9.33 have been found. In the data set of the long configuration none of those two has been found. This can be explained by the shortness of the geometry in the vertical configuration which means that the walls still have a stabilization effect onto the atoms in the constriction<sup>23</sup>.

<sup>23</sup>But it is not clear if this kind of finite size effect is for the good in comparison with the experiment or not. Comparing this data with large geometries, this effect seems to be positive as the large contacts break

In total, the initial geometry at room temperature has a similar strong effect as at low temperatures for Au.

### 9.7.2. Al

In the last section we have seen that finite size effects modify the results of Au in different manners. But does it play a role in other metals, too?

To answer this question this section analyzes the results for long and vertical contacts at 4 K and 300 K for Al and the next section looks at the equivalent results for Pb.

Fig. 9.35 shows the results for Al at 4 K. This time the results between both configurations seem to be very similar. The scattering is larger in the long than in the vertical configuration as before in Au. Despite the first two peaks, the third one is for the long contacts at about  $2.8 G_0$  and for the vertical ones at about  $3.8 G_0$ .

The peak at  $2.8 G_0$  is mainly build up from zigzag structures (left geometry in Fig. 9.36) and a geometry where each layer in the vicinity of the minimal cross section ('a', 'b') is build up from two atoms which are stacked rotated by  $90^\circ$  toward each other.

The peak at  $3.8 G_0$  is mainly build up by geometries with two parallel atoms in the minimal cross section which are connected on both sides to larger structures (instead of the stacked geometries which are at  $2.8 G_0$ ).

The mean channels are very similar, but at for example  $2 G_0$  the second channel is in mean slightly more open and the third one more close in the long contacts in comparison to the vertical ones. This small deviation is of interest because this point was already discussed in the context of the difference between the crystallographic elongation directions (sec. 8).

Fig. 9.37 shows the differences in more detail by making histograms of the channels at different conductance values. The vertical contacts seem to prefer larger open channels than the long ones. This is already visible at  $1 G_0$  where the vertical data set has a meaningful number of fully open channels ( $\tau_i > 0.95$ ) whereas the long data set has none. At  $2 G_0$  there are three well defined peaks visible in the vertical data set while there are no well defined ones visible in the long data set.

This difference can be explained considering the influence of the length of the contact to the disorder: The longer a contact, the longer is the way between the walls and the more disorder can modify the channel distribution by an increased number of possibilities and therefore larger variances.

In the thermopower the larger spread of the data leads in the long contacts to a larger mean value (at the most conductance values).

This is somewhat different at room temperature (Fig. 9.38) where the data set of the vertical geometries show a very sharp peak at  $1 G_0$ , but not the data set of the long ones. The reason for this peak is the stabilization of the structure by the walls. This can be seen in the high symmetry of the contacts in the vicinity of the minimal cross section of the examples shown in Fig. 9.39.

The channel histograms look very similar to the ones at low temperatures but the two sets are more equal now. For example at  $2 G_0$  both sets show two peaks at semi open channels.

---

often at a tiny place leading to small wires with large stabilizing walls.

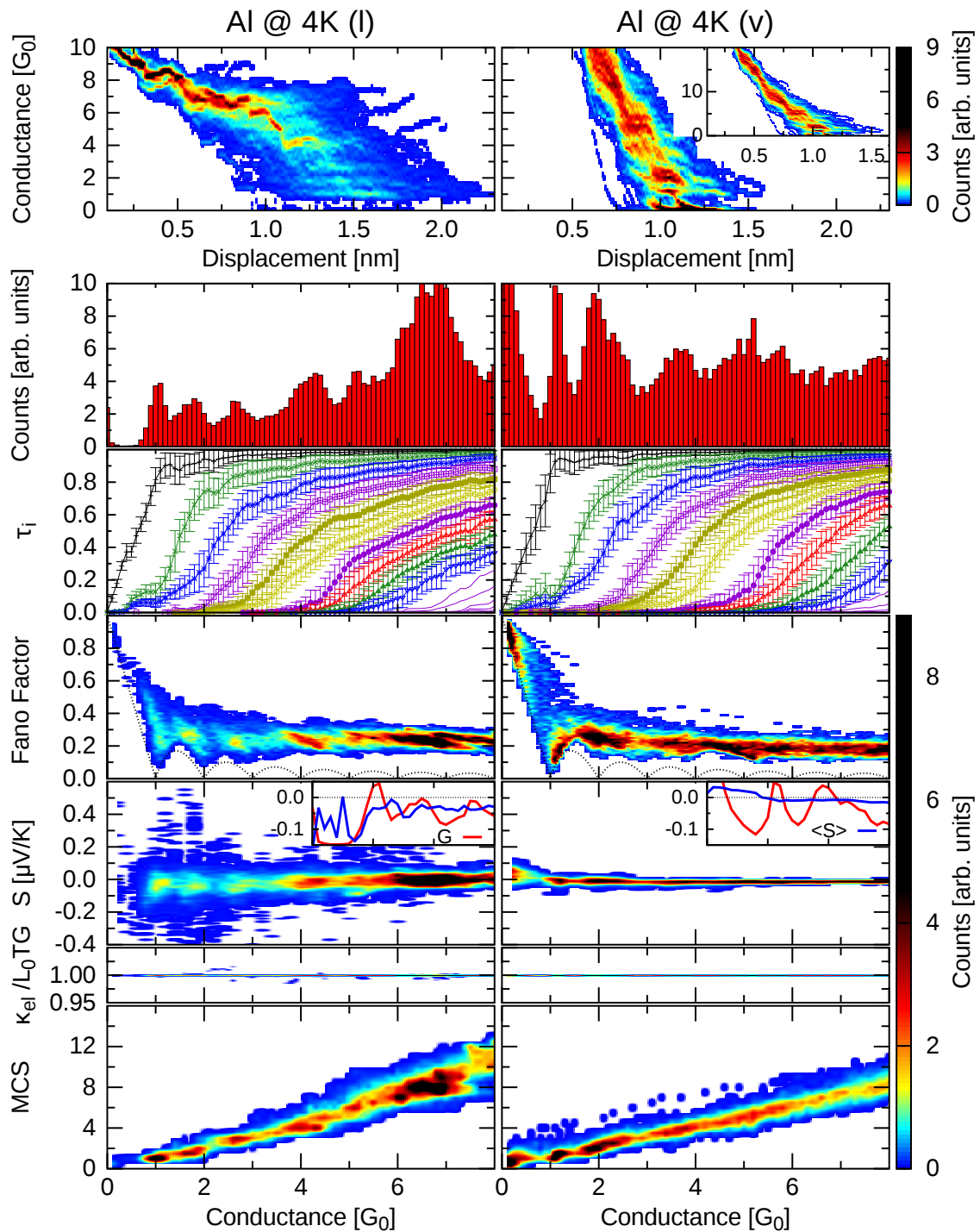


Figure 9.35.: The same as in Fig. 9.28, but for Al at 4 K.

The asymmetry between the different channel openings has increased in both sets so that it is visible in the long one, too.

In total, though the differences between the different initial geometries are not such large as for Au, they still play a non vanishing role.

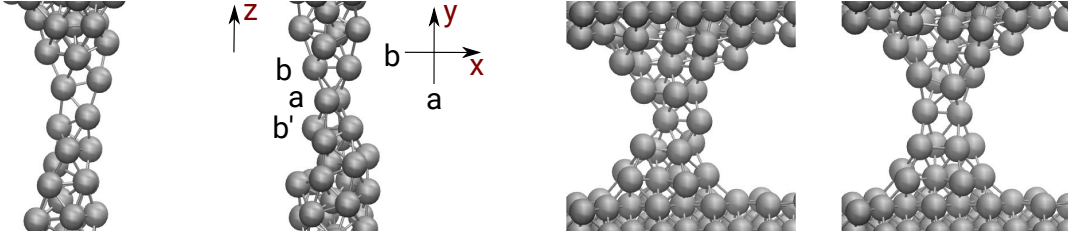


Figure 9.36.: Geometries belonging to the conductance peak of the long 4K Al contacts at  $2.8 G_0$  (left) and to the one of the vertical contacts at  $3.8 G_0$  (right). The conductance and Fano factor values are:  $2.8 G_0:0.19$ ,  $2.8 G_0:0.26$ ,  $3.8 G_0:0.27$  and  $3.8 G_0:0.16$ .

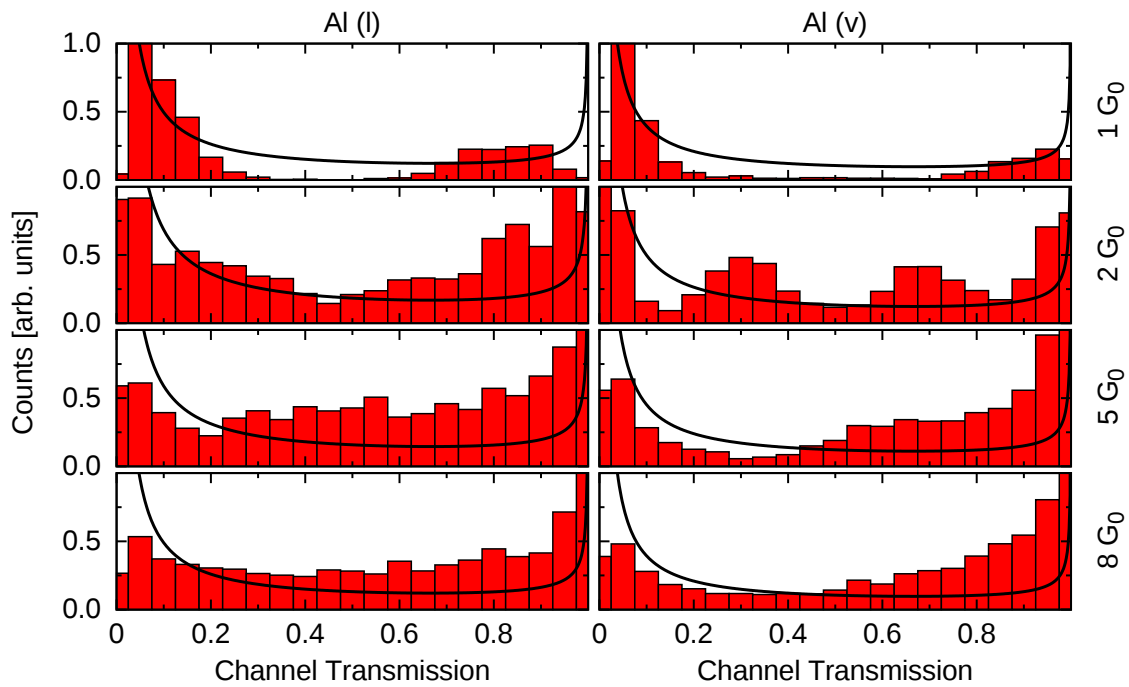


Figure 9.37.: Histograms of the transmission coefficients of the two data sets at 4K at conductance values between 1 and  $8 G_0$  with an uncertainty of  $\pm 0.125 G_0$ . The lines are the fitted bimodal distributions  $P(\tau)$  (equation 5.3).

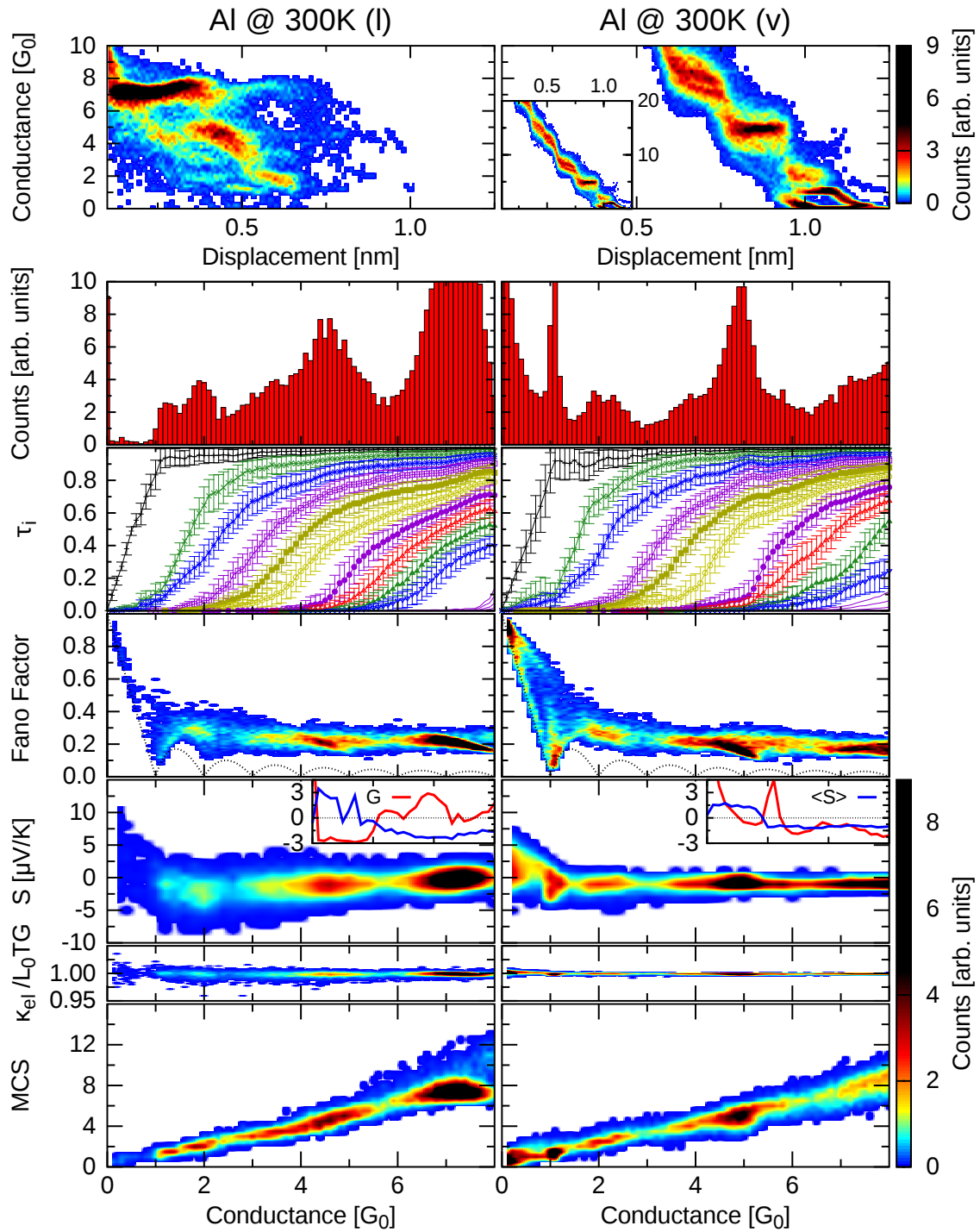


Figure 9.38.: The same as in Fig. 9.28, but for Al at 300 K.

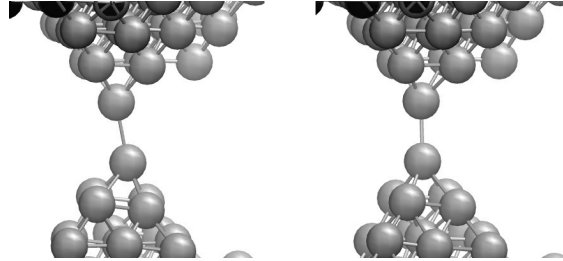


Figure 9.39.: Geometries belonging to the conductance peak of the vertical 300 K Al contacts at  $1 G_0$ . The conductance and Fano factor values are:  $1.0 G_0:0.13$  and  $1.1 G_0:0.08$ .

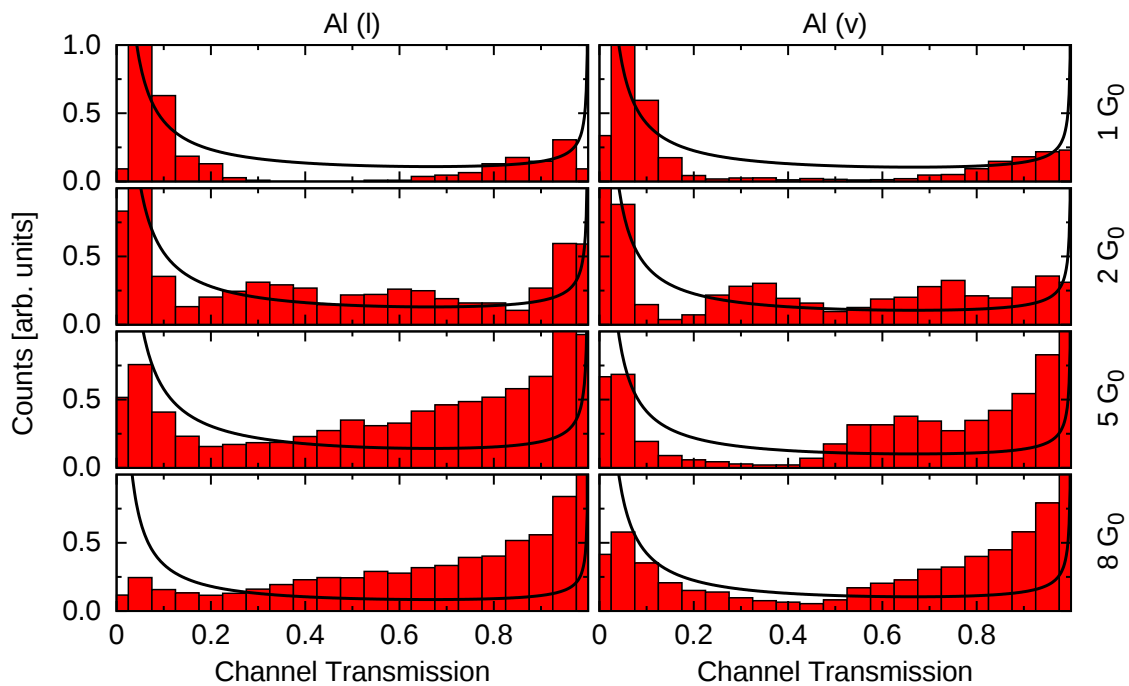


Figure 9.40.: Histograms of the transmission coefficients of the two data sets at 300 K at conductance values between  $2$  and  $8 G_0$  with an uncertainty of  $\pm 0.125 G_0$ . The lines are the fitted bimodal distributions  $P(\tau)$  (equation 5.3).

## 9.7.3. Pb

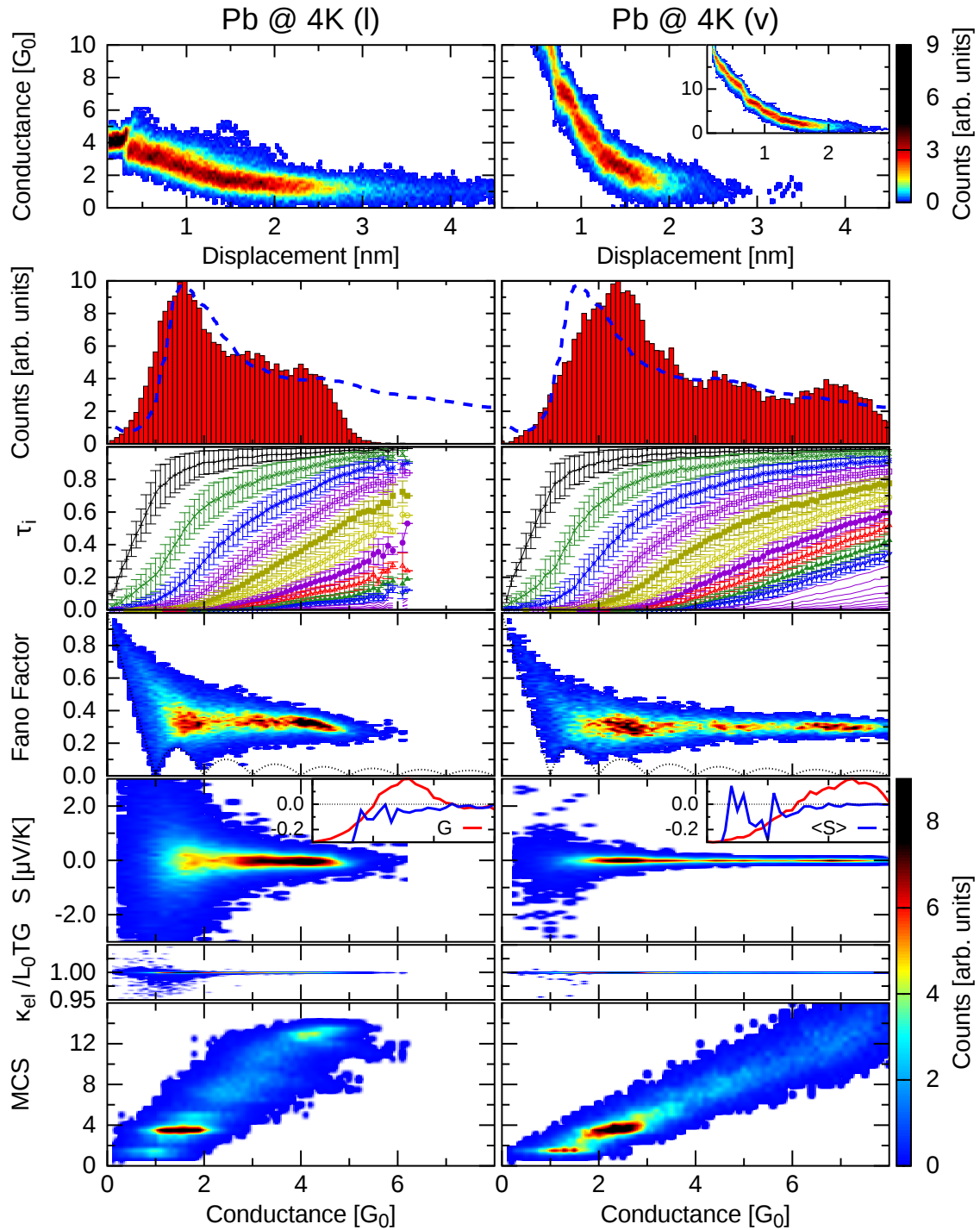


Figure 9.41.: The same as in Fig. 9.28, but for Pb at 4K. The blue curves in the conductance histograms are experimental results from [71].<sup>24</sup>

<sup>24</sup>The experiments were done with the MCBJ technique at liquid-helium temperature ( $T = 2.2 - 4.2$  K) and cryogenic vacuum conditions with high-purity wires.



The mean values of the Pb contacts at 4 K are even less influenced from the initial geometry than the ones of Al but the scattering of the data depends on the initial geometry as before in the other two metals.

The conductance histogram of the long contacts has similar to the experimental findings of Makk et al. [71] (blue dashed line) one peak at about  $1.5 G_0$ . The other one has a shoulder at that position and a peak at about  $1 G_0$  higher.

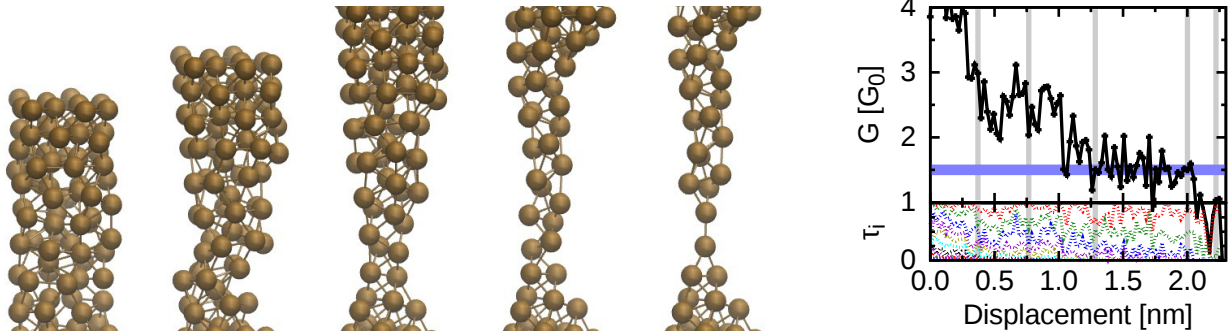


Figure 9.42.: Evolution of a long Pb contact at 4 K. The horizontal blue line is at  $1.5 G_0$ . The positions of the geometries on the left are marked by gray vertical lines in the plot on the right. The conductance and Fano factor values are:  $3.0 G_0:0.43$ ,  $2.0 G_0:0.55$ ,  $2.0 G_0:0.34$ ,  $1.5 G_0:0.43$ ,  $1.5 G_0:0.24$  and  $1.0 G_0:0.11$ .

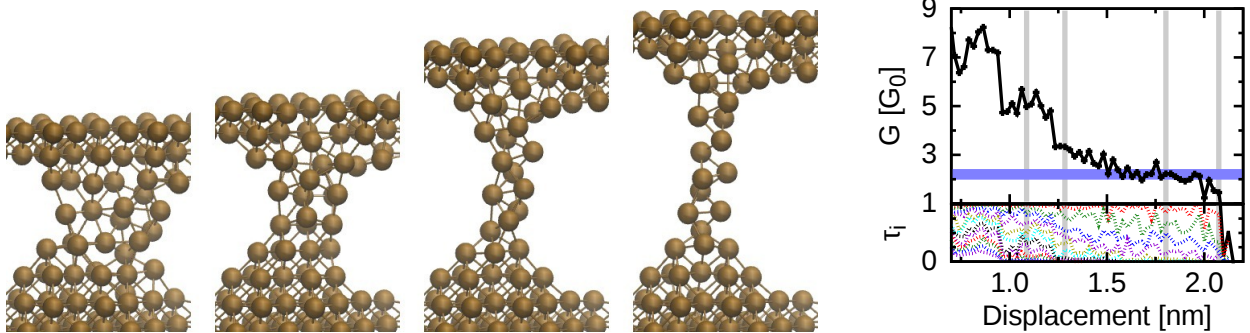


Figure 9.43.: Evolution of a vertical Pb contact at 4 K. The horizontal blue line is at  $2.2 G_0$ . The positions of the geometries on the left are marked by gray vertical lines in the plot on the right. The conductance and Fano factor values are:  $5.0 G_0:0.32$ ,  $3.3 G_0:0.35$ ,  $2.2 G_0:0.35$  and  $1.5 G_0:0.42$ .

A curve belonging to each of the main peaks of the two histograms are shown in Figs. 9.42 and 9.43<sup>25</sup>. The results are both very noisy<sup>26</sup> which is due to the long and thin wires with a large amount of disorder. As the influence of the walls to the ordering of the complete wire is again stronger in the vertical geometries as in the long ones, they have a larger conductance value at the same cross sections (compare geometry three of both figures). This also explains the different slopes of the MCS-G plots in Fig. 9.41<sup>27</sup>.

<sup>25</sup>As it is the first time in the thesis that Pb contacts are shown, the evolution is shown with channel distribution.

<sup>26</sup>The different scaling distorts a bit the viewing.

<sup>27</sup>Note that this effect seems negligible in the other metals (not visible in their MCS-G plots).

In Pb several channels open at once<sup>28</sup> leading to a relative high Fano factor compared to the other metals investigated so far, even slightly higher than Pt (Fig. 5.9).

The thermopower vanishes in the mean above about  $2 G_0$  (blue lines in insets of Fig. 9.41), below it has an oscillatory behavior with a tendency toward negative values.

The Wiedemann-Franz law is relative good fulfilled except for very few points below  $2 G_0$  in the data set of the vertical contacts and a larger number in the set of the long ones. It has a tendency toward smaller values, meaning that the electric thermal conductance is less than expected from the linear approximation.

The room temperature results (Fig. 9.44) are slightly different for the vertical contacts as expected, e.g. the contacts break slightly faster (about 0.5 nm) due to the higher mobility of the atoms, but the results of the long contacts are totally different. The contacts thin down rapidly till they reach a plateau at about  $0.8 G_0$ . This has an effect not only onto the histograms but also onto the mean channel distribution where the second and higher channels are suppressed in comparison to the other data sets and to the Wiedemann-Franz law were the electric contribution to the thermal conductance is for a large number of points significantly suppressed, down to about half what is expected from the linear approximation.

To see what happens in the long contacts, Fig. 9.45 shows the elongation process of a curve which contributes significantly to the first peak at around  $0.8 G_0$  which has not only shifted down by about half the conductance compared to the corresponding peak at 4 K, but got also sharper. As can be seen in the first geometry it is not mainly the sinning down of the wire which causes the fast decrease of the conductance for this already thin wires, but the fast increase in disorder. Nevertheless, the wire thins down very fast, reaching at one point the size of about two to three atoms (geometry three). At that point the wire does not shrink any further in minimal diameter. In contrast, the thicker parts thin down during the further elongation process and the thin part converts to a higher symmetry (geometry four). They present two layers of zigzag structures stacked above one another and shifted by half a period against each other. This is depicted on the left side of geometry four where the neighboring atoms within one zigzag structure are connected with black lines and the ones of different ones with blue (back) and red (front) lines. This phase does not stretch through the whole wire, but it can be found locally in almost every part. It has an mcs value of about 3.8 though it looks like two atoms in diameter. The reason for this high value is that because of the contribution of all four atoms in the neighborhood<sup>29</sup>. The channel distribution on the right shows that the longer this tube gets, the more the higher channels are suppressed. This is why in the mean they have this drop near below  $1 G_0$ .

The vertical (short) contacts (Fig. 9.46) do not show this phase with the double zigzag structure. They also do not have the possibility of creating such large structures because the influence of the walls, which is much larger here onto the middle part of the central wire because of the small distance between the walls, keeps most of the atoms in a slightly more symmetric configuration throughout the complete elongation process<sup>30</sup>. This is also the reason why the difference to the low temperature results are much smaller than for the long wires.

<sup>28</sup>Electronic configuration:  $[Xe]4f^{14}5d^{10}6s^2p^2$ .

<sup>29</sup>The mcs value of a zigzag structure depends on the angle between the atoms.

<sup>30</sup>Referenced to as finite size effect.

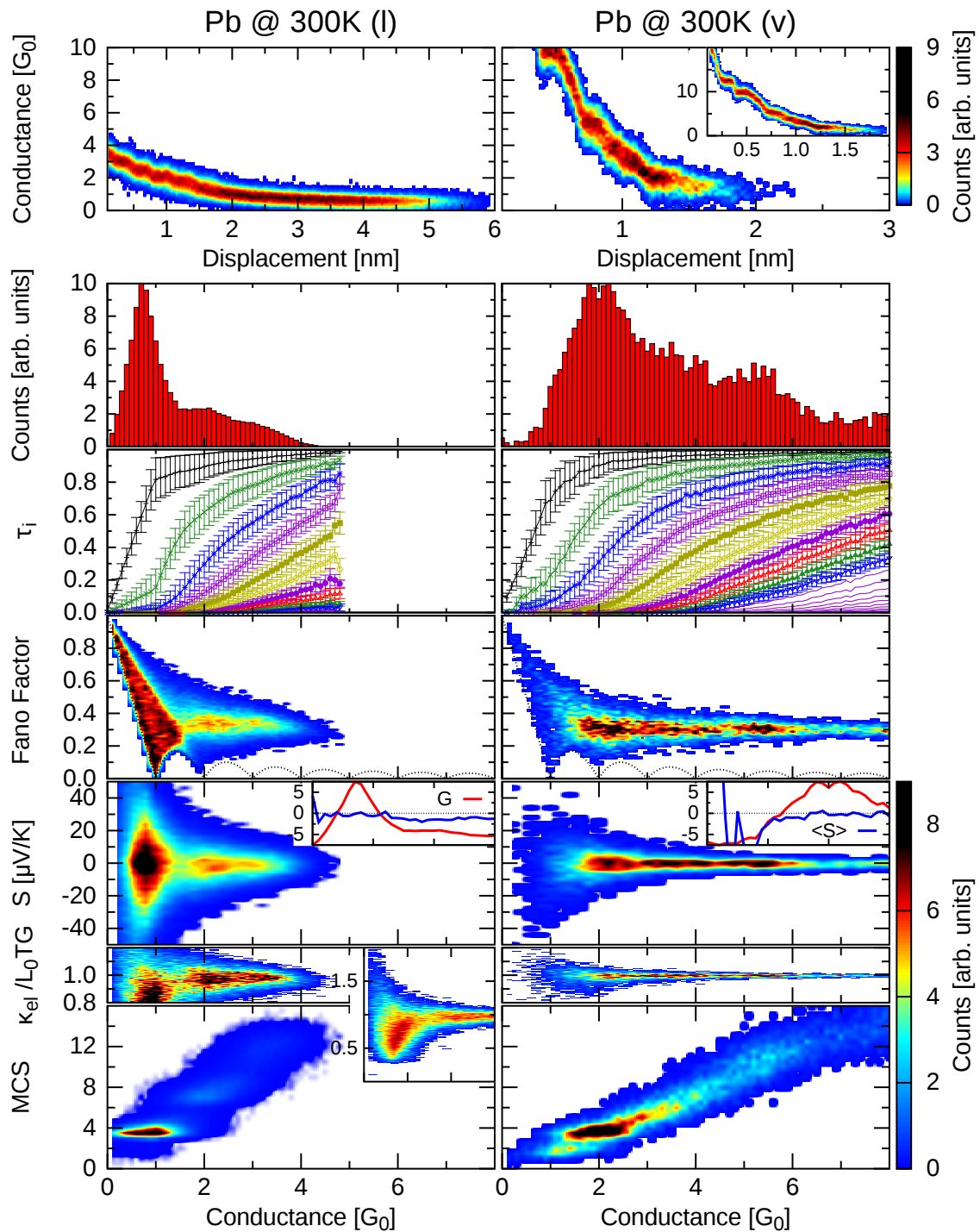


Figure 9.44.: The same as in Fig. 9.28, but for Pb at 300 K.

In total, for Pb the shape has a very large effect, much larger than for the other metals which were investigated. As not only the histograms are affected, one has to be very carefully with the statistical results.

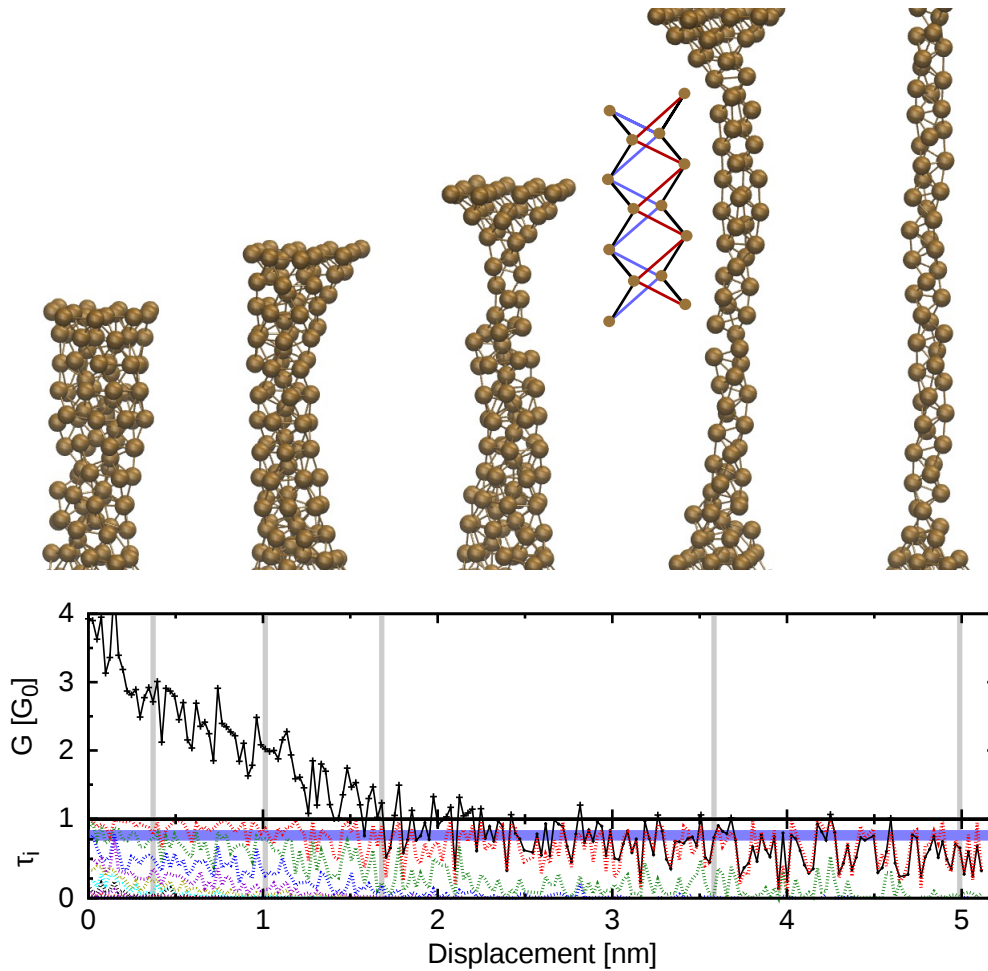


Figure 9.45.: Evolution of a long Pb contact at 300 K. The horizontal blue line is at  $0.8 G_0$ . The positions of the geometries on the left are marked by gray vertical lines in the plot on the right. The conductance and Fano factor values are:  $2.8 G_0:0.40$ ,  $2.1 G_0:0.30$ ,  $1.3 G_0:0.30$ ,  $0.8 G_0:0.32$  and  $0.6 G_0:0.42$ .

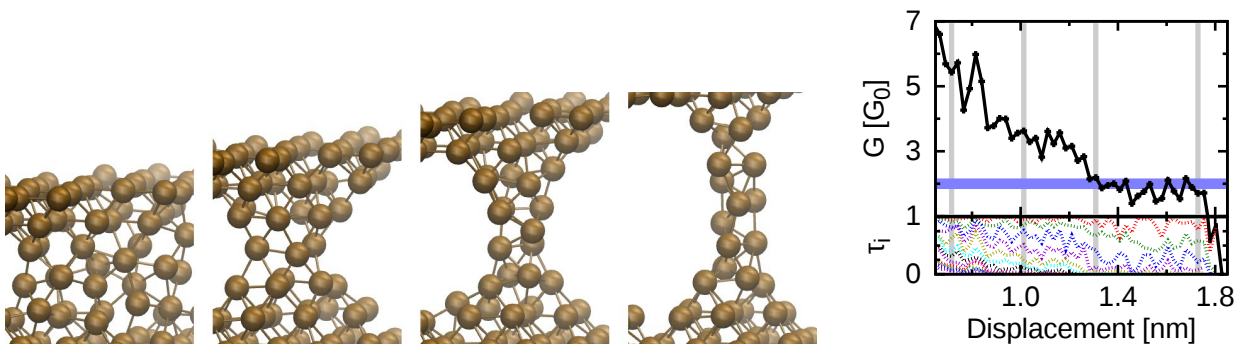


Figure 9.46.: Evolution of a vertical Pb contact at 300 K. The horizontal blue line is at  $2.0 G_0$ . The positions of the geometries on the left are marked by gray vertical lines in the plot on the right. The conductance and Fano factor values are:  $5.4 G_0:0.31$ ,  $3.6 G_0:0.28$ ,  $2.2 G_0:0.30$  and  $1.7 G_0:0.41$ .

## 10. Summary

In this work mechanical and electrical properties of various metals were investigated. The comparison with experiments showed very good agreement in most metals with most properties.

For example the thermopower results from Evangeli et al. [16] where they found that the sign of the mean was different for Au and Pt and between bulk and atomic sized wires. Both could be traced back to the different orbital structures of the metals which differ between Au and Pt and between bulk and single atom contacts. A second point in their results was an oscillation of the thermopower of Au with minima at the maxima of the corresponding conductance histogram<sup>1</sup>, which was traced back to the channel saturation at that points. In the publication with Evangeli et al. we were only able to show this for the first peak. A later analysis of even larger structures was able to reproduce it also for the second and third peak.

Similar results from Chen et al. [15] for the shot noise of Au, namely the suppression of the shot noise at the maxima of the conductance histogram, could be traced back to the openings of the channels. The second observation of them was that at about  $G_0/2$  in some samples at least two channels had to contribute to the conductance contradicting the knowledge of Au at that point. That observation could be explained by the appearance of parallel wires which ripped off at about the same time. While at low temperatures parallel wires up to several atoms in length each have been found, only atoms from parallel surfaces were found to contribute multiple channels at about  $G_0/2$  at room temperatures.

The saturation of the Fano factor at higher conductance values could be shown to originate from a relatively constant relation between open and semi-open channels which is specific for each metal and similar within groups, for example the monovalent metals. The impression that Mott's model of ferromagnetic metals at those scales could be incorrect could be confirmed. While the majority spins are dominated by  $s$  orbitals consistent with Mott's theory, the minority spins are dominated by  $d$  orbitals which drastically enhance the contribution to the conductance via additional channels compared to the majority spins, thus leading to a negative spin polarization. The resulting noise of these ferromagnetic materials is therefore a superposition of the majority spins which behave more like monovalent metals like Au and the minority spins which behave very similar to Pt, which is dominated by the  $d$  orbitals.

The first peaks of the conductance histogram of the low temperature experiments of Mg from Smit et al. [13] could be roughly reproduced. No signature of conductance quantization was apparent in the corresponding channel distribution or noise calculations. But indications were found that parallel wires could play a role, similar to Au, where parallel wires lead to an enhancement of the higher peaks in the conductance histogram. This could probably explain the experimental conductance histogram of Mg, too.

The conductance values and channel distributions of the plateaus of the bistable switches from Schirm et al. [14] were compared with the results from the calculated elongation pro-

---

<sup>1</sup>At about integers of  $G_0$ .

cesses of Al in three different elongation (or growin) directions ( $\langle 100 \rangle$ ,  $\langle 110 \rangle$  and  $\langle 111 \rangle$ ). Best comparison with the whole experimental data set (not only the plateaus) was found in the  $\langle 111 \rangle$  direction, but examples where both plateaus (the upper and lower one) were achieved during one elongation process have been found in all three directions. All examples examined showed a transition between the two states involving only up to four bonds which had to be broken or established.

As already mentioned there are also a few points which do not fit very well to the experimental findings. The most relevant discrepancies found during this work are the conductance histogram of Fe and that higher peaks in most histograms could not be reproduced very well. The reason for the first one is still unclear, a possible problem could be the MD potentials though different ones were tested. The problem of the higher peaks is most likely a consequence of the still relatively small system size compared to experiments.

Other results of the work are that

- the velocity of the elongation speed is not very important (at least within some range),
- the histograms and mean values evolve smoothly and not somehow steplike with temperature between 4 K and room temperature,
- the thermostating is important to not drastically heat up (or even melt) the wire,
- (at least for Fe) the crystal structure (fcc or bcc) does not drastically modify the results,
- the closing curves are less sensitive to temperature as the opening ones and
- accordingly the distribution and mean values of the closing curves even at room temperature behave more like the low temperature results of the closing curves except that the very long plateaus at  $1 G_0$  are missing (Au),
- a statistics of 10 curves is already sufficient (but very noisy) to see most features of the histograms and mean values where it is at room temperatures better converged than at low temperatures and
- the initial geometry and size of the contacts can modify the results drastically (specially in Au where it additionally modifies the possibility of the appearance of parallel wires).

## Publications

The results of the work found their way into several publications. Those are:

- C. Schirm, M. Matt, F. Pauly, J. C. Cuevas, P. Nielaba, and E. Scheer, “A current-driven single-atom memory,” *Nat. Nanotechnol.*, vol. 8, no. 9, pp. 645–648, Sep 2013. <http://www.nature.com/nnano/journal/v8/n9/abs/nnano.2013.170.html>
- R. Chen, M. Matt, F. Pauly, P. Nielaba, J. C. Cuevas, and D. Natelson, “Shot noise variation within ensembles of gold atomic break junctions at room temperature,” *Journal of Physics: Condensed Matter*, vol. 26, no. 47, p. 474204, 2014. <http://stacks.iop.org/0953-8984/26/i=47/a=474204>

- C. Evangeli, M. Matt, L. Rincón-García, F. Pauly, P. Nielaba, G. Rubio-Bollinger, J. C. Cuevas, and N. Agraït, “Quantum thermopower of metallic atomic-size contacts at room temperature,” *Nano Letters*, vol. 15, no. 2, pp. 1006–1011, 2015.  
<http://dx.doi.org/10.1021/nl503853v>
- R. Vardimon, M. Matt, P. Nielaba, J. C. Cuevas, and O. Tal, “Orbital origin of the electrical conduction in ferromagnetic atomic-size contacts: Insights from shot noise measurements and theoretical simulations,” *Phys. Rev. B*, vol. 93, p. 085439, Feb 2016.  
<http://link.aps.org/doi/10.1103/PhysRevB.93.085439>
- M. Beck, A. Haller, D. Kawetzki, M. Matt, M. Pütz, M. Ring, R. Schmid, K. Scholz, U. Siems, P. Nielaba, “Structures and Phases in (Nano-) Systems in Confined Geometry,” *NIC Symposium 2016, ISBN: 978-3-95806-109-5*
- L. Cui, W. Jeong, S. Hur, M. Matt, J.C. Klöckner, F. Pauly, P. Nielaba, J.C. Cuevas, E. Meyhofer, and P. Reddy, “Quantized thermal transport in single-atom junctions,” *Science*, vol. 355, no. 6330, pp. 1192–1195, 2017.  
<http://science.sciencemag.org/content/355/6330/1192>

In preparation are:

- M. Matt, C. Schirm, O. Schecker, T. Böhler, E. Scheer, J. C. Cuevas, P. Nielaba, and F. Pauly, “Mechanical, electrical and thermoelectrical properties of Al nanocontacts”
- Y. H. Wang, M. Bürkle, J. C. Mao, M. Matt, Z. L. Peng, Y. Shao, X. S. Zhou, W. Hong, F. Pauly, D. Bowler, T. Miyazaki, Y. Asai, B. W. Mao, E. Scheer “Fine tuning transistor of single atomic contact” and

## Open questions

This work could not close the subject from theoretical side completely. Open questions are for example the influence of the system size onto the results. The tests made in this work showed that there are finite-size effects which can be large for some details (for example the frequency of appearance of parallel wires in Au).

Parallel wires are an interesting point on their own. They have been found in Au and a few in Mg but not in the other metals. In Au the appearance of parallel wires was found to be drastically influenced by the system size and by the initial geometry. Therefore one could ask the question, whether there is a critical size at which parallel wires could also appear in other materials? And a related question is if one could trigger the appearance of parallel wires through finite size effects by choosing special initial geometries?

A correlated question is the influence of the found parallel structures in Mg (very rare appearance of parallel wires) onto its mean properties and if this influence could be found in experiments, too.

A different question not asked in this work contains the influence of mechanical waves with long wavelength onto the electrical properties. For example what is the time-dependent conductance of an oscillating bridge? Ignoring electron-phonon interaction this question could be analyzed using the same programs and methods.





# A. Appendix

## A.1. Examples

In the following examples the spin index  $\sigma$  which could be appended almost everywhere will be omitted. The same for the superindex  $r,a$  of the retarded and advanced Green's functions  $\mathbf{G}^{r,a} \rightarrow \mathbf{G}$  and of the energy  $E^{r,a} = E \pm i\eta \rightarrow E$ .

### A.1.1. Example 1: $\text{H}_2$

The following example is a short summary of chapter 5.3.1 of [4].

The tight-binding Hamiltonian for a hydrogen molecule without spin can be written in second quantisation as

$$\mathbf{H} = \sum_i \varepsilon_i \mathbf{c}_i^\dagger \mathbf{c}_i + \sum_{i \neq j} t_{ij} \mathbf{c}_i^\dagger \mathbf{c}_j \quad (\text{A.1})$$

where  $i, j$  are the orbital sites,  $\mathbf{c}_i^\dagger$  and  $\mathbf{c}_i$  are the creation and annihilation operators of a particle (electron) on site  $i$ ,  $\varepsilon_i$  is the onsite energy of site  $i$  and  $t_{ij}$  is the hopping parameter (coupling) between site  $i$  and  $j$ . This Hamiltonian reduces in our case to

$$\mathbf{H} = \varepsilon_0 (\mathbf{n}_1 + \mathbf{n}_2) + t (\mathbf{c}_1^\dagger \mathbf{c}_2 + \mathbf{c}_2^\dagger \mathbf{c}_1) \quad (\text{A.2})$$

$$= \varepsilon_0 \begin{pmatrix} 1 & 0 \\ 0 & 1 \end{pmatrix} + t \begin{pmatrix} 0 & 1 \\ 1 & 0 \end{pmatrix} \quad (\text{A.3})$$

where  $\mathbf{n}_i = \mathbf{c}_i^\dagger \mathbf{c}_i$  is the number operator which counts the number of electrons on site  $i$ . The Green's functions can now be calculated in three different ways: with (i) the direct definition (2.48), with (ii) the spectral representation (2.49) and (iii) with Dyson's equation.

(i) the direct definition:

$$\mathbf{G}(E) = \lim_{\eta \rightarrow 0} [E\mathbf{1} - \mathbf{H}]^{-1} \quad (\text{A.4})$$

$$= \begin{pmatrix} E - \varepsilon_0 & -t \\ -t & E - \varepsilon_0 \end{pmatrix}^{-1} \quad (\text{A.5})$$

$$G_{11}(E) = \frac{E - \varepsilon_0}{(E - \varepsilon_0)^2 - t^2} \quad (\text{A.6})$$

$$= \frac{1}{2} \left[ E - \underbrace{(\varepsilon_0 + t)}_{\varepsilon_+} \right]^{-1} + \frac{1}{2} \left[ E - \underbrace{(\varepsilon_0 - t)}_{\varepsilon_-} \right]^{-1} \quad (\text{A.7})$$

$$= \frac{1}{2} \left( \frac{1}{E - \varepsilon_+} + \frac{1}{E - \varepsilon_-} \right). \quad (\text{A.8})$$

Here  $\varepsilon_+$  and  $\varepsilon_-$  are the energies of the bonding and antibonding states of the hydrogen molecule.

And the density of states projected onto site 1 follows up to

$$\varrho_1(E) = \mp \frac{1}{\pi} \Im \{G_{11}(E)\} \quad (\text{A.9})$$

$$= \frac{1}{2} \delta(E - \varepsilon_+) + \frac{1}{2} \delta(E - \varepsilon_-) \quad (\text{A.10})$$

(ii) the spectral representation:

Using the eigenfunctions of the bonding ( $|\Psi_+\rangle$ ) and antibonding ( $|\Psi_-\rangle$ ) states with eigenvalues  $\varepsilon_{\pm}$ :

$$|\Psi_{\pm}\rangle = \frac{1}{\sqrt{2}} (|1\rangle + |2\rangle) \quad (\text{A.11})$$

$$G_{11}(E) = \langle 1 | \mathbf{G} | 1 \rangle \quad (\text{A.12})$$

$$= \sum_{n=\pm} \frac{\langle 1 | \Psi_n \rangle \langle \Psi_n | 1 \rangle}{E - \varepsilon_n} \quad (\text{A.13})$$

$$= \sum_{n=\pm} \frac{|\langle 1 | \Psi_n \rangle|^2}{E - \varepsilon_n} \quad (\text{A.14})$$

$$= \frac{1}{2} \left( \frac{1}{E - \varepsilon_+} + \frac{1}{E - \varepsilon_-} \right). \quad (\text{A.15})$$

(iii) Dyson's equation:

Here one has to divide the Hamilton matrix ( $\mathbf{H}$ ) into an unperturbed part ( $\mathbf{H}_0$ ) and a

perturbation ( $\mathbf{V}$ ). The perturbation is chosen to be the coupling between the two states:

$$\mathbf{G}(E) = \mathbf{g}(E) + \mathbf{g}(E)\mathbf{V}\mathbf{G}(E) \quad (\text{A.16})$$

$$\mathbf{H} = \mathbf{H}_0 + \mathbf{V} = \varepsilon_0 \begin{pmatrix} 1 & 0 \\ 0 & 1 \end{pmatrix} + t \begin{pmatrix} 0 & 1 \\ 1 & 0 \end{pmatrix} \quad (\text{A.17})$$

$$\mathbf{g}(E) = [E\mathbb{1} - \mathbf{H}_0]^{-1} = [E - \varepsilon_0]^{-1} \mathbb{1} \quad (\text{A.18})$$

$\mathbf{g}$  is the Green's function of the unperturbed system.

Now taking into account, that  $\mathbf{g}$  is diagonal while  $\mathbf{V}$  is purely off-diagonal, one ends up with:

$$G_{21}(E) = g_{22}(E)V_{21}G_{11}(E) \quad (\text{A.19})$$

$$G_{11}(E) = g_{11}(E) + g_{11}(E)V_{12}G_{21}(E) \quad (\text{A.20})$$

$$= g_{11}(E) + g_{11}(E)V_{12}g_{22}(E)V_{21}G_{11}(E) \quad (\text{A.21})$$

$$= g_{11}(E) + g_{11}(E)\Sigma_{11}(E)G_{11}(E) \quad (\text{A.22})$$

$$= \frac{1}{E - \varepsilon_0 - \Sigma_{11}(E)} \quad (\text{A.23})$$

$$= \frac{1}{2} \left( \frac{1}{E - \varepsilon_+} + \frac{1}{E - \varepsilon_-} \right). \quad (\text{A.24})$$

$\Sigma$  is the so called self-energy, which modifies the unperturbed system (position ( $\varepsilon_0$ ) and lifetime of the energy levels) due to perturbations like the interaction between different states (e.g. atoms).

Dyson's equation does not look very handy, and indeed, in this example it isn't. But in other cases it will be the only feasible way to go. The next example will be such a case.

### A.1.2. Example 2: Semi-infinite linear chain

The following example is a short summary of chapter 5.3.2 of [4].

The tight-binding Hamiltonian of a semi-infinite linear chain is almost identical to the one of the  $\text{H}_2$  molecule except that one does not have only two atoms (states), but infinitely many of them:

$$\mathbf{H} = \varepsilon_0 \sum_i \mathbf{n}_i + t \sum_i \left( \mathbf{c}_i^\dagger \mathbf{c}_{i+1} + \mathbf{c}_{i+1}^\dagger \mathbf{c}_i \right) \quad (\text{A.25})$$

where  $i = 1, 2, \dots$  is the index of the atom (state).

To calculate the Green's function with the direct definition or the spectral representation seems to be impracticable because one would have to handle infinite large matrices. For Dyson's equation one can divide the system into two subsystem: a single atom and a semi-infinite linear chain. The perturbation is coupling between both, as in the case of our  $\text{H}_2$

example. This leads us to

$$\mathbf{H} = \mathbf{H}_0 \mathbf{V} = \begin{pmatrix} \varepsilon_0 & 0 \\ 0 & \mathbf{H}' \end{pmatrix} + t \begin{pmatrix} 0 & 1 \\ 1 & 0 \end{pmatrix} \quad (\text{A.26})$$

where  $\mathbf{H}'$  is the Hamiltonian of the unperturbed subsystem 2 which is equal to  $\mathbf{H}$ , because 1 atom more or less does not modify the infinite system.

Dyson's equation now reads again:

$$G_{11}(E) = g_{11}(E) + g_{11}(E)V_{12}G_{21}(E) \quad (\text{A.27})$$

$$G_{21}(E) = g_{22}(E)V_{21}G_{11}(E) \quad (\text{A.28})$$

$$g_{11}(E) = 1/(E - \varepsilon_0) \quad (\text{A.29})$$

The difference is now, that  $g_{22} = G_{11}$  the unperturbed Green's function of subsystem 2  $g_{22}$  is equal to the surface Green's function  $G_{11}$  of the semi-infinite linear chain.

Putting everything together one ends up with

$$G_{11}(E) = \frac{1}{E - \varepsilon_0} + \frac{t^2}{E - \varepsilon_0} G_{11}^2(E) \quad (\text{A.30})$$

$$= \frac{1}{t} \left[ \frac{E - \varepsilon_0}{2t} - \sqrt{\left(\frac{E - \varepsilon_0}{2t}\right)^2 - 1} \right] \quad (\text{A.31})$$

$$= \frac{1}{t} \left[ \frac{E - \varepsilon_0}{2t} \mp i \sqrt{1 - \left(\frac{E - \varepsilon_0}{2t}\right)^2} \right] \quad (\text{A.32})$$

$$\varrho_1(E) = \frac{1}{\pi} \Im \{G_{11}(E)\} \quad (\text{A.33})$$

$$= \frac{1}{\pi t} \sqrt{1 - \left(\frac{E - \varepsilon_0}{2t}\right)^2}, \quad |E - \varepsilon_0| \leq 2|t| \quad (\text{A.34})$$

In contrast to the  $H_2$  example, there is an infinite number of states within the energy band of the semi-infinite linear chain of  $2t$  around  $\varepsilon_0$ , the energy of the unperturbed atom (state).

### A.1.3. Example 3: A single level coupled to electrodes

The following example is a short summary of chapter 5.3.3 of [4].

This last example is the one closest to our calculations. The aim is to couple two infinite leads (like the semi-infinite chain before) to a single level (atom) with energy  $\varepsilon_c$  in the center between the electrodes.

In the 'real' calculations one replaces the single level in the center by a couple of atoms with orbitals. The (electron) orbitals are then coupled to the electrodes as the single level here.

The Hamiltonian for this example can be written as (without spin)

$$\mathbf{H} = \mathbf{H}_L + \mathbf{H}_R + \mathbf{H}_C + \mathbf{V}_{CL} + \mathbf{V}_{CR} \quad (\text{A.35})$$

$$= \mathbf{H}_L + \mathbf{H}_R + \varepsilon_c \mathbf{c}_C^\dagger \mathbf{c}_C + t_L \left( \mathbf{c}_C^\dagger \mathbf{c}_L + \mathbf{c}_L^\dagger \mathbf{c}_C \right) + t_R \left( \mathbf{c}_C^\dagger \mathbf{c}_R + \mathbf{c}_R^\dagger \mathbf{c}_C \right). \quad (\text{A.36})$$

$\mathbf{H}_{L/R/C}$  are the Hamiltonians of the unperturbed left, right and center system (leads/single level) and  $\mathbf{V}_{CL/CR}$  are the couplings between the center system and the two leads.

Now, as already indicated, one can use the results of the example with the semi-infinite chain to get the element of the Green's function for the central part to derive the local density of states:

$$G_{CC}(E) = g_{CC}(E) + g_{CC}(E)V_{CL}G_{CL}(E) + g_{CC}(E)V_{CR}G_{CR}(E) \quad (\text{A.37})$$

$$G_{LC}(E) = g_{LL}(E)V_{LC}G_{CC}(E) \quad (\text{A.38})$$

$$G_{RC}(E) = g_{RR}(E)V_{RC}G_{CC}(E) \quad (\text{A.39})$$

$$g_{CC}(E) = 1/(E - \varepsilon_c). \quad (\text{A.40})$$

Here one has to add a coupling term to each electrode (instead of only one in total like in the previous examples).

With the couplings  $V_{CL/CR} = t_{L/R}$ , where  $t_{L/R}$  are the hopping parameters to the left/right electrodes, one gets

$$G_{CC}(E) = g_{CC}(E) + g_{CC}(E)V_{CL}g_{LL}(E)V_{LC}G_{CC}(E) \quad (\text{A.41})$$

$$+ g_{CC}(E)V_{CR}g_{RR}(E)V_{RC}G_{CC}(E) \quad (\text{A.42})$$

$$= g_{CC}(E) + g_{CC}(E) (t_L^2 g_{LL}(E) + t_R^2 g_{RR}(E)) G_{CC}(E) \quad (\text{A.43})$$

$$= g_{CC}(E) + g_{CC}(E)\Sigma_{CC}(E)G_{CC}(E) \quad (\text{A.44})$$

$$= \frac{1}{E - \varepsilon_c - \Sigma_{CC}(E)} \quad (\text{A.45})$$

with the self-energy  $\Sigma_{CC}$  which moves the energy level  $\varepsilon_c$  by an amount of  $\text{Re}\{\Sigma_{CC}(E)\}$  and introduces a finite 'energy width' to the non interacting level by its imaginary part  $\text{Im}\{\Sigma_{CC}(E)\}$ .

In the wide-band approximation ( $g_{LL/RR}$  is independent of  $E$  and purely imaginary near  $\varepsilon_c$ ), one can replace  $\Sigma_{CC} = \mp i\Gamma = \mp i(\Gamma_L + \Gamma_R)$  with  $\Gamma_{L/R} \approx \pm t_{L/R}^2 g_{LL/RR}$ , the scattering rates between leads and the central part. Within this approximation one ends up with

$$G_{CC}(E) = \frac{1}{E - \varepsilon_c \pm i\Gamma} \quad (\text{A.46})$$

$$\varrho_C(E) = \frac{1}{\pi} \Im \{G_{11}(E)\} = \frac{1}{\pi} \frac{\Gamma}{(E - \varepsilon_c)^2 + \Gamma^2} \quad (\text{A.47})$$

$\rho_C(E)$  is now a Lorentzian function with half-width at half-maximum  $\Gamma$  which describes as imaginary part of  $\Sigma$  the finite 'energy width' of the energy level due to its interactions to the leads.

The inverse ( $\hbar/\Gamma$ ) gives a timescale which can be interpreted as time an electron needs to jump from one state to the other (also mentioned as finite lifetime of the resonant level).

## A.2. Program specific data

As this work was the first one in the group using LAMMPS, the following input file was the basis for several Bachelor and Master theses in the area of mechanical and thermal properties of nano scale wires, bridges and membranes (for example in [197–199]).

```
#####
# elongation of initially ideal wire via LAMMPS #
#####

# units and boundary conditions
units          metal
atom_style     atomic
boundary       s s s

# create domains
lattice        fcc 4.0780 origin 0          0          0
region         mdbox      block  -7.0 7.0    -3.5 3.5    -1.5 1.5
region         wallu      block  -9.5 9.5    -5.0 5.0    1.5 2.5
region         walld      block  -9.5 9.5    -5.0 5.0    -2.5 -1.5
region         regun      union 3 wallu walld mdbox

create_box     1 regun
create_atoms   1 region regun

# specify internal/ghost atoms
group          internal region regun
group          bu region wallu
group          bd region walld
# make group without wall atoms
group          internalsu subtract internal bu bd

# specify inter-atomic potential with element string for output
pair_style     eam/fs
pair_coeff     * * ../Au.eam.fs Au
variable       element string 79

# keep wall-atoms fixed for equilibration, units box [A], else [a0]
fix           flb bu move linear 0.0 0.0 0.0 units box
fix           frb bd move linear 0.0 0.0 0.0 units box

# specify neighbor/re-neighbor parameters
neighbor       0.3 bin
neigh_modify   every 10 delay 0 check no

# setup thermal output and make some special calculations
```

```

compute vwire    internalsu stress/atom NULL virial
compute vwir    internalsu reduce sum c_vwire[3]
compute mytemp  internalsu temp

variable        vw equal c_vwir/vol
variable        fw equal c_vwir/lz*10^(-6)

# print every 100 steps: step-number, E_pot, E_kin, p, box-size,
# virial, p_zz, force, internal T, own definition of temperature
thermo          100
thermo_style    custom step pe ke press lx ly lz v_vw pzz v_fw temp c_mytemp

# create initial velocities with gaussian distribution at T=300K
velocity        internalsu create 300 2269839 dist gaussian

# time integrator of NVT ensemble at T=300K (Nose-Hoover thermostat)
fix             NVT internalsu nvt temp 300 300 100

# time in ps, works fine with 0.0001
timestep        0.001

# equilibrate MD field
run             100000

# define output: all, wire, walls; redefine element number
dump           d0 all          xyz 10000 wire_total.xyz
dump           d1 internalsu xyz 10000 wire.xyz
dump           d2 bu          xyz 10000 wall_u.xyz
dump           d3 bd          xyz 10000 wall_d.xyz

dump_modify    d0 element ${element}
dump_modify    d1 element ${element}
dump_modify    d2 element ${element}
dump_modify    d3 element ${element}

# stretch system (opening curve)
#for each atom vl/vr, 1 means 1A/1ps = 10^{-10}m/10^{-12}s = 100 m/s
fix           flb bu move linear 0.0 0.0 0.001 units box
run           7500000

# get system to a halt and relax
fix           flb bu move linear 0.0 0.0 0.000 units box
run           100000

# shrink system (closing curve)
fix           flb bu move linear 0.0 0.0 -0.001 units box
run           7500000

```

Listing A.1: LAMMPS input script

```

#####
# TB transport code - input file #
#####
# remark: most options have default values, so they are not needed here, #
# (n) = needed #
#####

element      = Al          # (n) name of element
TBinfile     = al_par      # (n) TB parameter file
coordinates_c = wire.xyz    # central wire where the transmission is
                        # to be calculated in xyz format
coordinates_u = wall_u.xyz  # upper wall in xyz format
coordinates_d = wall_d.xyz  # lower wall in xyz format
plane_direction = 100      # elongation direction, possible are
                        # 100, 110, 111
spin_pol     = F          # is transport spin polarized? Needs extra
                        # parameters in TBinfile if true
num_c_atoms  = 288        # (n) atoms in the center (nca)
num_u_atoms  = 392        # (n) atoms in the left wall (nla)
num_d_atoms  = 392        # (n) atoms in the right wall (nra)
n_xy_cells   = 10         # electrode fcc-100-plane construction
n_z_cells    = 3          # electrode fcc-100-plane construction
i_max_read_xy = 15        # i_max for G-bulk-construction (-> cutoff)
i_max_read_z  = 0         # i_max for G-bulk-construction (-> cutoff)
g_select     = s          # [b=bulk/s=surface]
compute_mode = rxx        # 1: [c: compute, r: read, g: generate],
                        # 2: [s: stop after generation],
                        # 3: [d: rm glead_dir], x: !s,!d
glead_dir    = glead_dir_al # location of lead greens functions to be
                        # saved on desk (huge, up to several 10 GB,
                        # should be saved locally; reusable)
calc_channels = T         # calculate different channels?
parallel_eloop = T        # parallelization sceem of energy loop

# frame infos:
first_stretchconfig = 1    # first stretchconfig
last_stretchconfig  = 501  # last stretchconfig to be computed
stepsize            = 2    # stepsize for stretching (in frames)
step_geoinfo        = 1    # frame for geo information

# energy:
reference_occ       = 1.5   # (n) reference occupation of element
read_Ef            = T     # use fermi Energy from Ef_read
Ef_precision       = 1.0E-8 # precision for determination of E Fermi
E_lower            = 0.20   # upper border of E Fermi
E_upper            = 0.40   # lower border of E Fermi
Ef_max_it          = 20     # max iteration steps before error
Ef_read            = 0.309352607 # Fermi energy
Delta_E_around_Ef = 0.000502 # Delta E (Ryd) with [E_f-D, E_f+D] (4.0K)
n_E_around_Ef     = 5      # energy points around E_fermi, devide
                        # 2*D into 2n intervals with 2n+1 points
intpts_gen_str     = file   # read integration points from file or
                        # use equally spaced points (file/genp)
intpts_file        = intpts.dat # file with integration points
int_pts            = 149    # number of integration points if genp

```



```

eta_int      = 0.0001
eta_xx      = 0.02
eta_cx      = 0.00
eta_cc      = 1E-8

# charge neutral loop:
# (optimal values depend on material, size and shape of contact)
charge_neutral_itmax = 120      # max iterations in charge neutrality
use_shifts      = T            # use old shifts as starting point
min_damp_value  = 5.01E-02     # minimal damping value
diff_damp_value = 1.01E-02     # damping values (internal modification)
n_cs_damp_arr   = 1 0.350     # damping values: iteration-step value
n_cs_damp_arr   = 2 0.250     # the iteration step has to increase
n_cs_damp_arr   = 5 0.100
n_cs_damp_arr   = 10 0.010

# RAM optimization:
sprdim         = 0.8          # (1-sprdim) is sparseness of matrix (central wire)
,
,
,
spxcdim        = 0.8          # the larger the contact the more sparse the matrix
# (wire-walls), (program will fail if too small)
spmulf         = 2.0          # modification value during run, should be >= 1.0
save_steps     = 200          # save energy dependent results on disk all x steps

# LDOS:
LDOS_out       = T            # calculate LDOS (time consuming): T/F
LDOS_array_atom = 17          # line number of atom in wire file (starts
# with 1, other programs like vmd start with 0)
LDOS_array_atom = 51          # up to num_c_atoms possible
LDOS_array_eta = 0.01001     # energy eta for calculation
# (low/high value: high noise / low resolution)

# accuracy for internal checks:
eps_geocheck   = 1E-3         # accuracy for position of wall atoms
eps_decimation = 1E-8         # accuracy of convergency in decimation

# output:
out_transmission = Transmission.dat # all valuable informations,
# if spinpol, X_sp1 and X_sp2 are added
n_Ti_out        = 50          # number of channels saved in out-file
min_Ti          = 1E-2         # minimal value of channel to be counted
time_file       = time.out    # time data during run

# output of matrices for testing:
HS_out          = F
Hsk_out         = F
G_0jab_out     = F

# end:
eps_broken_contact = 1E-2     # minimal transmission before stopping
stop_after_break  = T         # end after breaking or after last_stretchconfig
cleaning_up      = T         # erase temporal files

```

Listing A.2: Transport code input script

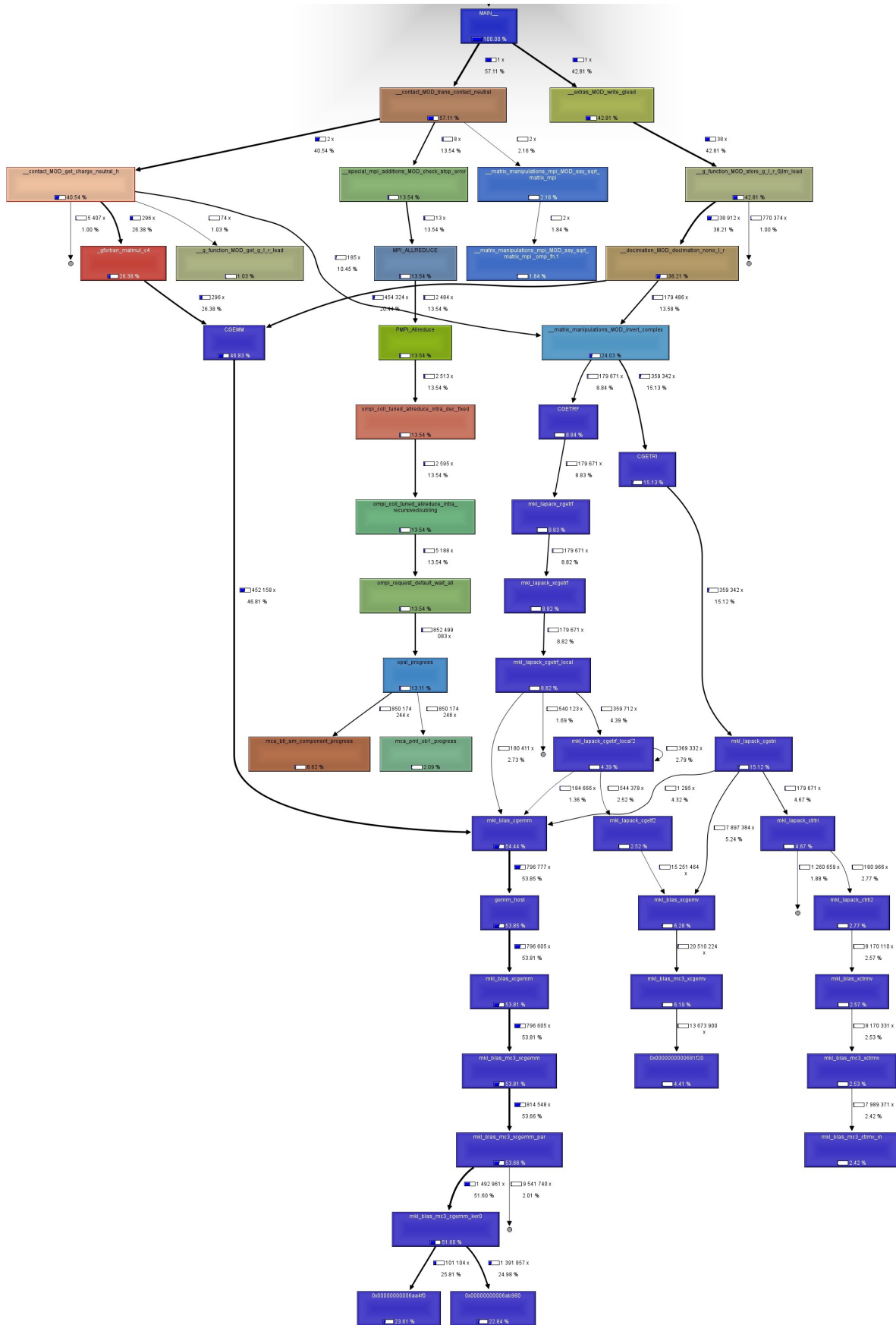


Figure A.1.: Call-graph from callgrind (resolution in pdf sufficient for scaling).

### A.3. Au multiwire geometries

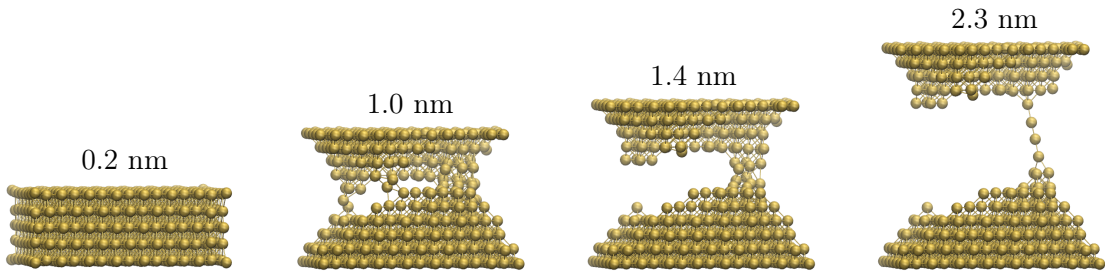


Figure A.2.: Au geometries: 83.0(98),8.7(14),2.8(4),0.93(2:0.92,0.01)

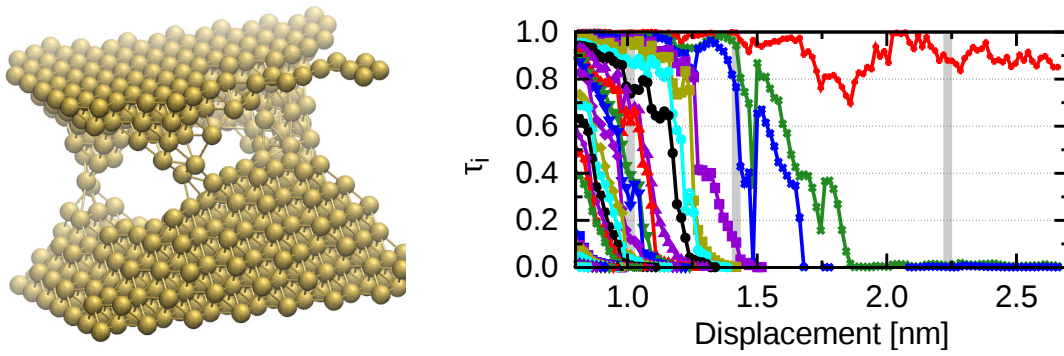


Figure A.3.: Au: Left: again geometry at 1.0 nm from a different angle, with total transmission  $8.7G_0$  and 14 channels. Right: channel distribution with marks at the above geometries.

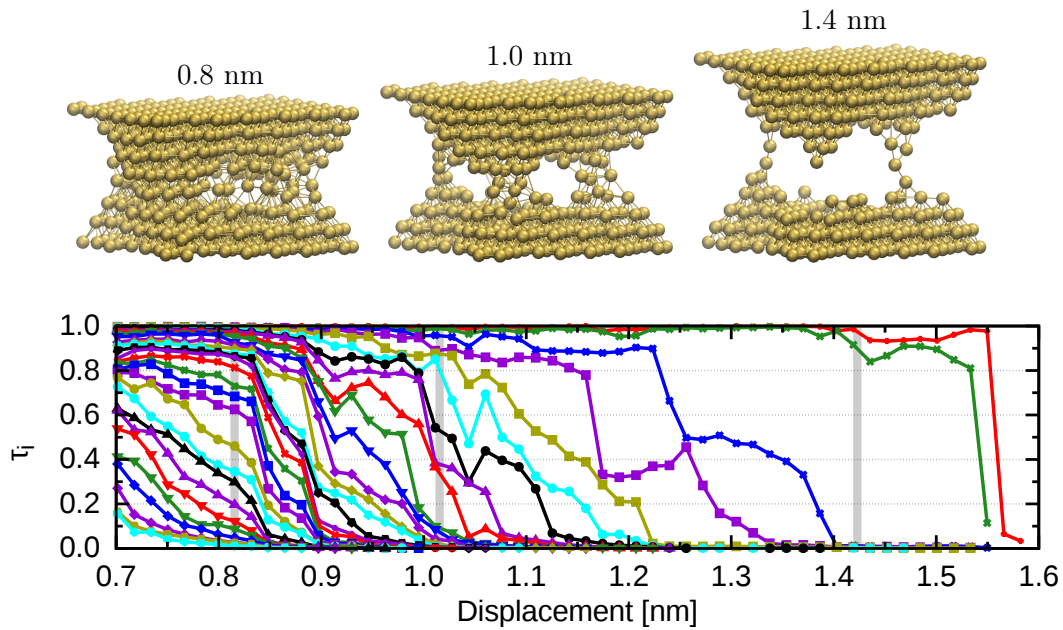


Figure A.4.: 19.7(31),6.9(13),1.85(2:1.0,0.84)

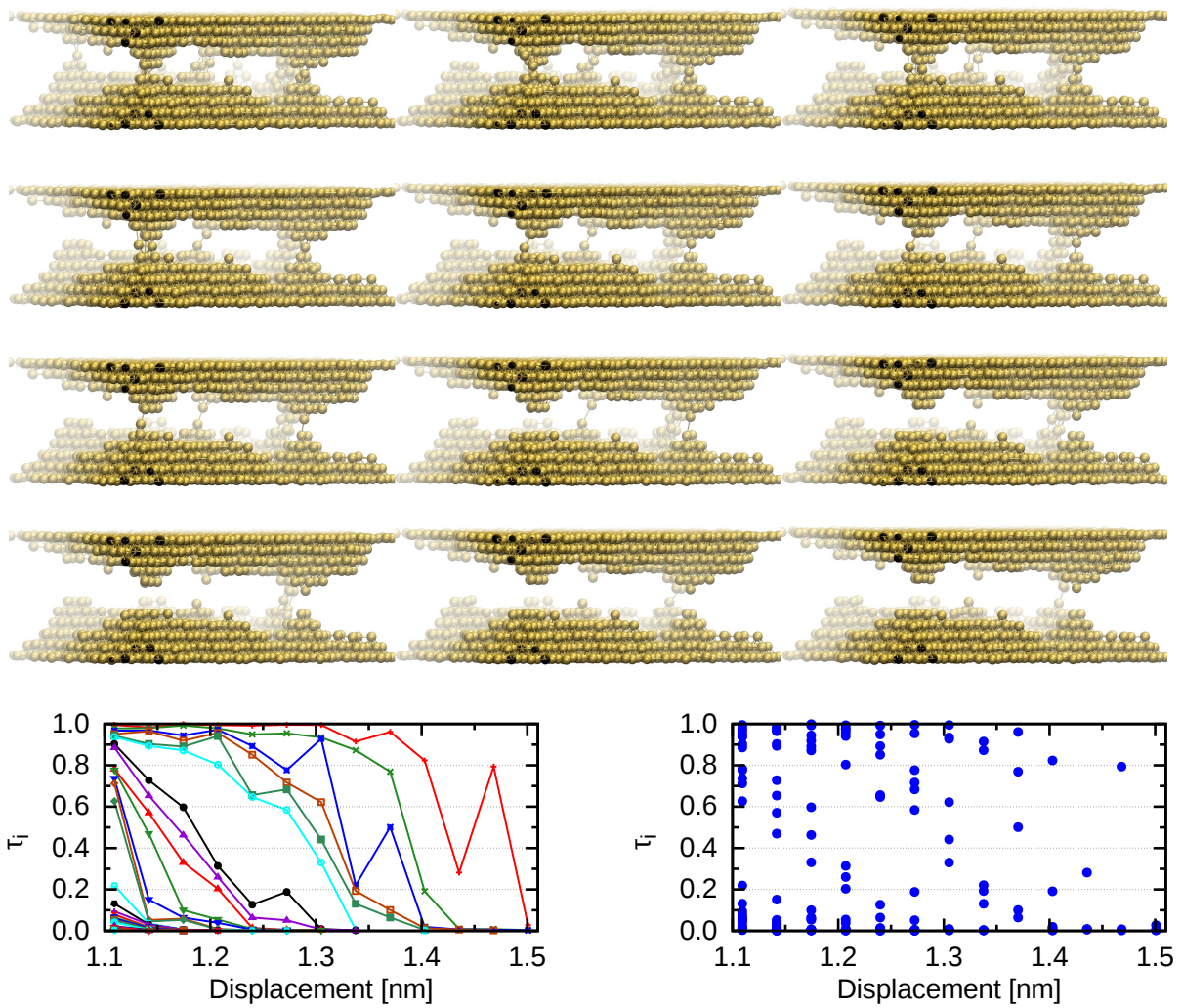


Figure A.5.: Geometries of an elongation process of Au with 2103 atoms at 4 K and the corresponding channel distribution.

## A.4. Al geometries

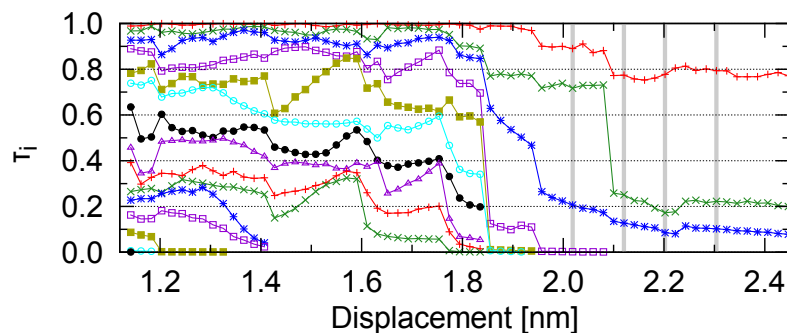
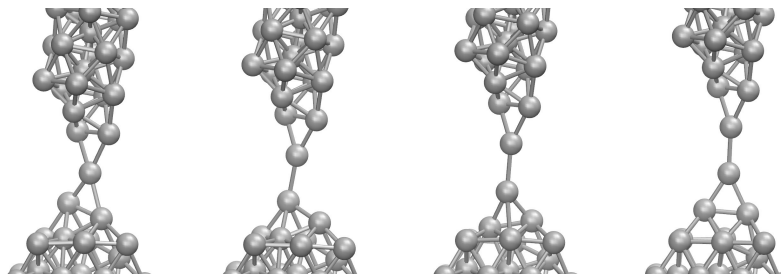


Figure A.6.: Same geometry as the upper left figure in table 8.1, but with two additional geometries in-between. Below: channel distribution during the elongation process with the four geometries marked.

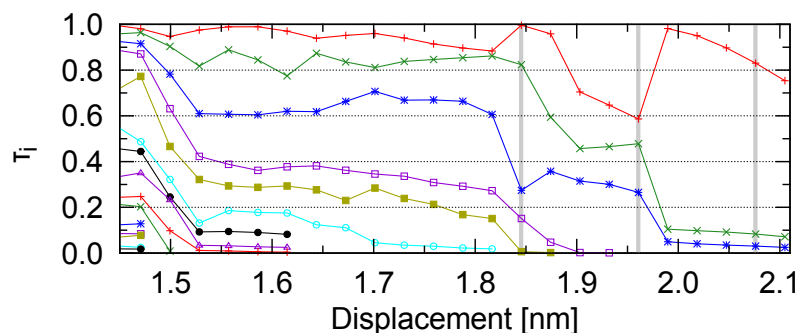
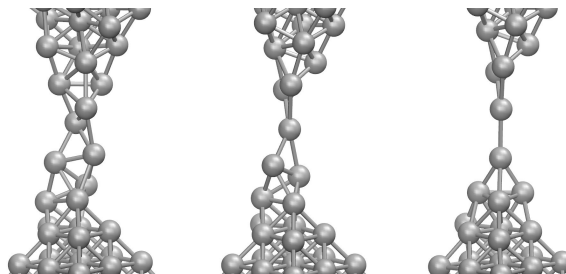


Figure A.7.: Same geometry as the center center figure in table 8.1, but with one additional geometries in-between. Below: channel distribution during the elongation process with the four geometries marked.

## A.5. Histograms of channel transmissions

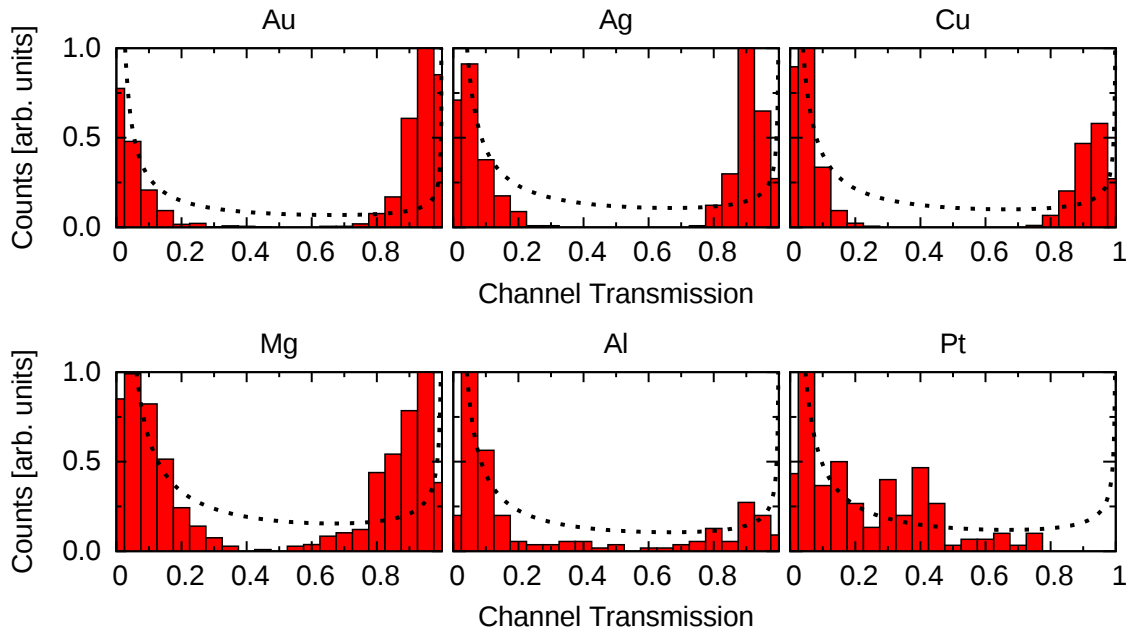


Figure A.8.: Histogram of the transmission coefficients at a conductance of  $1 G_0$

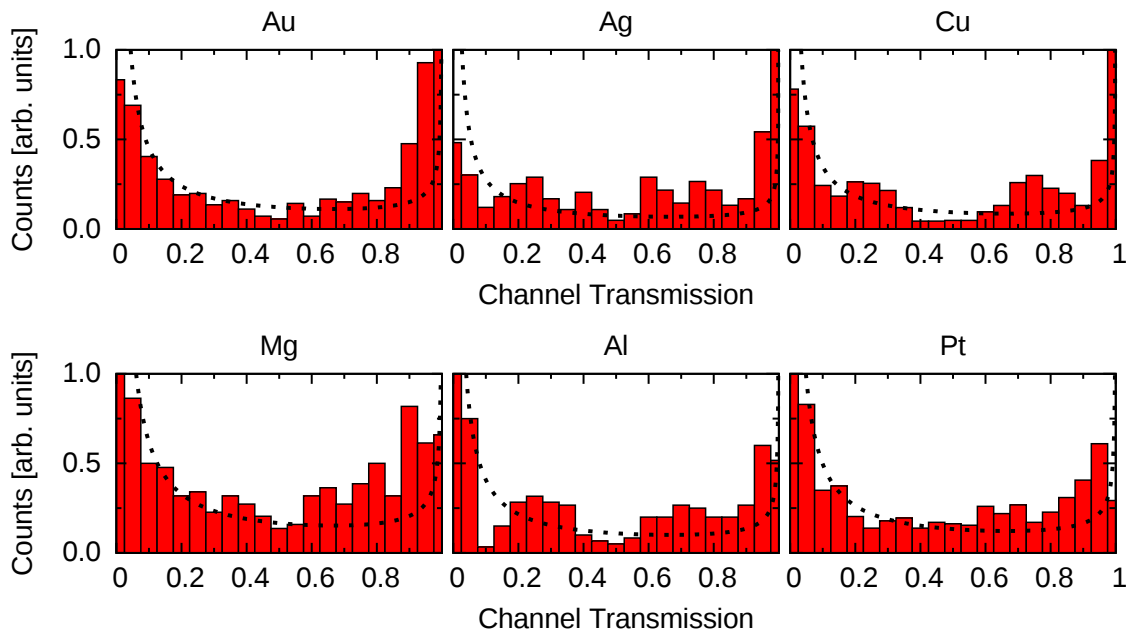


Figure A.9.: Histogram of the transmission coefficients at a conductance of  $2 G_0$

## A.6. Fano factor convergence values - overview

metal	small 4 K	300 K	large 4 K	300 K	4 K (close)	giants 4 K
Au (l)	$0.15 \pm 0.03$	$0.17 \pm 0.02$	-	-	-	$0.16 \pm 0.02$
Au (v)	$0.13 \pm 0.03$	$0.13 \pm 0.03$	$0.16 \pm 0.02$	$0.15 \pm 0.02$	-	$0.16 \pm 0.03$
Al (l)	$0.24 \pm 0.03$	$0.22 \pm 0.03$	-	-	-	-
Al (v)	$0.17 \pm 0.03$	$0.17 \pm 0.03$	$0.14 \pm 0.02$	-	$0.18 \pm 0.03$	-
Pb (l)	$0.32 \pm 0.03$	$0.32 \pm 0.04$	-	-	-	-
Pb (v)	$0.29 \pm 0.03$	$0.30 \pm 0.02$	-	-	-	-
Ag (v)	-	-	$0.12 \pm 0.02$	-	$0.12 \pm 0.02$	-
Cu (v)	-	-	$0.14 \pm 0.02$	-	-	-
Mg (v)	-	-	$0.18 \pm 0.02$	-	$0.17 \pm 0.03$	-
Pt (v)	-	-	$0.27 \pm 0.03$	$0.27 \pm 0.02$	-	-

Table A.1.: Overview of the fitted values for the convergence of the Fano values for high conductance values.

metal	total	spin up	spin down
Fe (4 K)	$0.28 \pm 0.02$	$0.21 \pm 0.02$	$0.35 \pm 0.02$
Co (4 K)	$0.27 \pm 0.02$	$0.21 \pm 0.02$	$0.30 \pm 0.02$
Ni (4 K)	$0.24 \pm 0.02$	$0.16 \pm 0.03$	$0.28 \pm 0.02$
Ni (300 K)	$0.25 \pm 0.02$	$0.16 \pm 0.02$	$0.29 \pm 0.02$

Table A.2.: Overview of the fitted values for the convergence of the Fano values for high conductance values of spin dependent materials.

## A.7. Experimental results

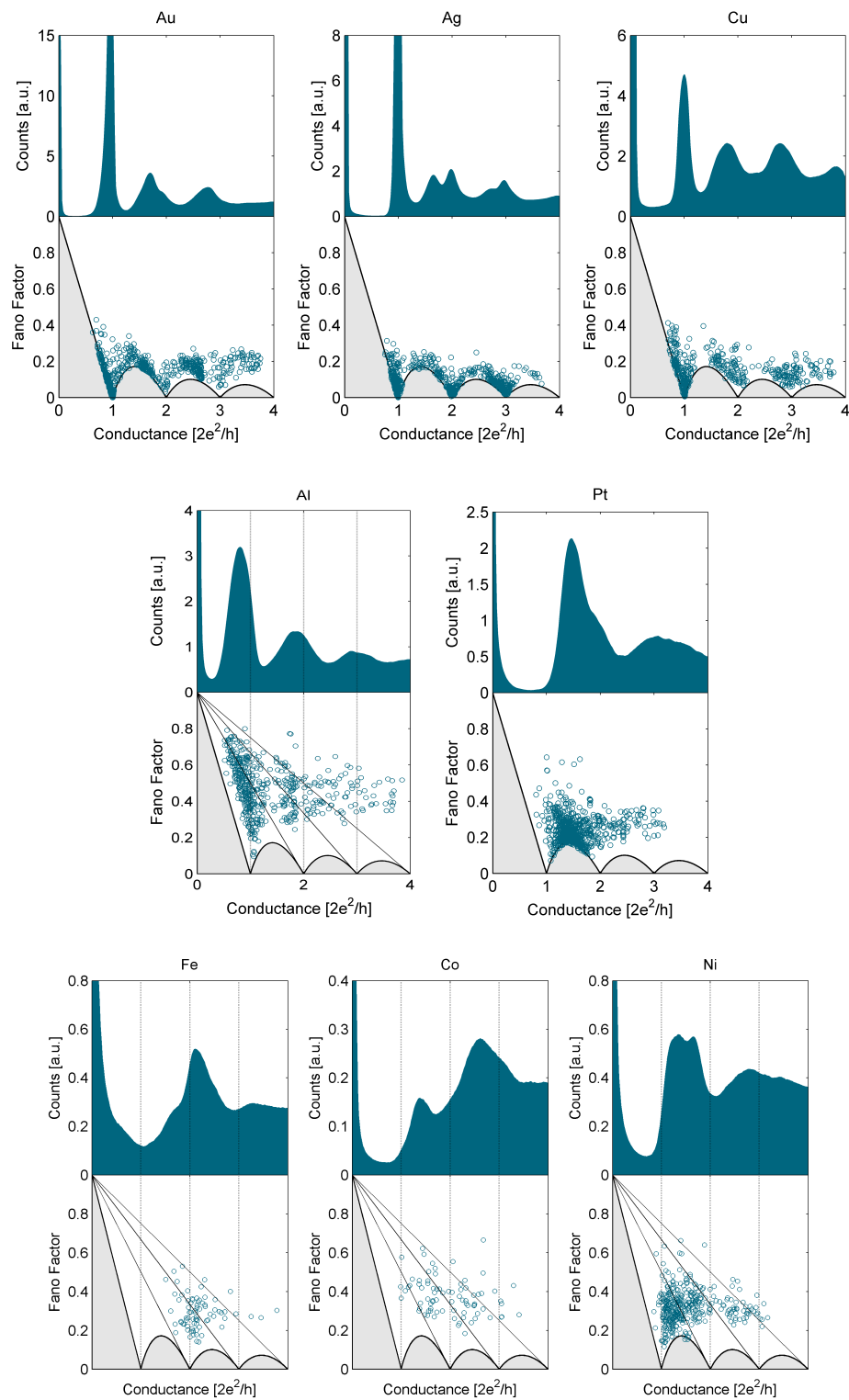


Figure A.10.: Experimental results done by Ran Vardimon from the group of Oren Tal, Weizmann Institute of Science, Israel (private communication). The experiments were done in cryogenic vacuum at about  $10^{-5}$  mbar and 4.2 K.



# Acknowledgments

In the following I would like to thank everyone who accompanied me on the long way here and who made it possible for me to write this thesis. Specially I want to thank Prof. Dr. Peter Nielaba, Prof. Dr. Juan Carlos Cuevas and Junior-Prof. Dr. Fabian Pauly my first, second and third order Ph.D. supervisors. There have been a lot of very interesting and fruitful discussions and we still have common open projects. Without them the project PHD wouldn't have been possible for me.

There were also a lot of interesting and fruitful discussions with other scientists within common projects and beyond. In this context I want to specially thank Prof. Dr. Elke Scheer and Dr. Ran Vardimon and of course the whole working groups of LS Nielaba and AG Nowak.

Last but not least I would like to thank my family, friends and my beloved girlfriend Steffi for their enduring encouragement and support.



# Bibliography

- [1] “Intel TOCK BLOCK: 10nm Cannonlake delayed to 2017, bonus 14nm Kaby Lake to ’16.” [Online]. Available: [http://www.theregister.co.uk/2015/07/16/intel\\_10nm\\_14nm\\_plans/](http://www.theregister.co.uk/2015/07/16/intel_10nm_14nm_plans/)
- [2] “14 nanometer.” [Online]. Available: [https://en.wikipedia.org/wiki/14\\_nanometer](https://en.wikipedia.org/wiki/14_nanometer)
- [3] “Samsung 10nm.” [Online]. Available: <http://www.sammobile.com/2016/10/17/samsung-announces-industry-first-mass-production-of-system-on-chip-with-10nm-finfet-technology/>
- [4] J. Cuevas and E. Scheer, *Molecular Electronics : An Introduction to Theory and Experiment*. World Scientific, 2010.
- [5] N. Agraït, A. Levy Yeyati, and J. M. van Ruitenbeek, “Quantum properties of atomic-sized conductors,” *Physics Reports*, vol. 377, no. 2–3, pp. 81 – 279, 2003. [Online]. Available: <http://www.sciencedirect.com/science/article/pii/S0370157302006336>
- [6] J. K. Gimzewski and R. Möller, “Transition from the tunneling regime to point contact studied using scanning tunneling microscopy,” *Phys. Rev. B*, vol. 36, pp. 1284–1287, Jul 1987. [Online]. Available: <http://link.aps.org/doi/10.1103/PhysRevB.36.1284>
- [7] U. Dürig, O. Züger, and D. W. Pohl, “Observation of metallic adhesion using the scanning tunneling microscope,” *Phys. Rev. Lett.*, vol. 65, pp. 349–352, Jul 1990. [Online]. Available: <http://link.aps.org/doi/10.1103/PhysRevLett.65.349>
- [8] C. J. Muller, J. M. van Ruitenbeek, and L. J. de Jongh, “Conductance and supercurrent discontinuities in atomic-scale metallic constrictions of variable width,” *Phys. Rev. Lett.*, vol. 69, pp. 140–143, Jul 1992. [Online]. Available: <http://link.aps.org/doi/10.1103/PhysRevLett.69.140>
- [9] T. N. Todorov and A. P. Sutton, “Jumps in electronic conductance due to mechanical instabilities,” *Phys. Rev. Lett.*, vol. 70, pp. 2138–2141, Apr 1993. [Online]. Available: <http://link.aps.org/doi/10.1103/PhysRevLett.70.2138>
- [10] J. C. Cuevas, A. L. Yeyati, and A. Martín-Rodero, “Microscopic origin of conducting channels in metallic atomic-size contacts,” *Phys. Rev. Lett.*, vol. 80, pp. 1066–1069, Feb 1998. [Online]. Available: <http://link.aps.org/doi/10.1103/PhysRevLett.80.1066>
- [11] F. Pauly, “Phase-coherent electron transport through metallic atomic-sized contacts and organic molecules,” Ph.D. dissertation, TH Karlsruhe, 2007.
- [12] M. Dreher, “Untersuchung elektronischer Eigenschaften komplexer Materialien mittels Computer-Simulationen,” Ph.D. dissertation, Universität Konstanz, 2008.

- [13] R. H. M. Smit, A. I. Mares, M. Häfner, P. Pou, J. C. Cuevas, and J. M. van Ruitenbeek, “Metallic properties of magnesium point contacts,” *New Journal of Physics*, vol. 11, no. 7, p. 073043, Jul. 2009.
- [14] C. Schirm, M. Matt, F. Pauly, J. C. Cuevas, P. Nielaba, and E. Scheer, “A current-driven single-atom memory,” *Nat. Nanotechnol.*, vol. 8, no. 9, pp. 645–648, Sep 2013. [Online]. Available: <http://www.nature.com/nano/journal/v8/n9/abs/nano.2013.170.html>
- [15] R. Chen, M. Matt, F. Pauly, P. Nielaba, J. C. Cuevas, and D. Natelson, “Shot noise variation within ensembles of gold atomic break junctions at room temperature,” *Journal of Physics: Condensed Matter*, vol. 26, no. 47, p. 474204, 2014. [Online]. Available: <http://stacks.iop.org/0953-8984/26/i=47/a=474204>
- [16] C. Evangeli, M. Matt, L. Rincón-García, F. Pauly, P. Nielaba, G. Rubio-Bollinger, J. C. Cuevas, and N. Agraït, “Quantum thermopower of metallic atomic-size contacts at room temperature,” *Nano Letters*, vol. 15, no. 2, pp. 1006–1011, 2015. [Online]. Available: <http://dx.doi.org/10.1021/nl503853v>
- [17] N. F. Mott, “The electrical conductivity of transition metals,” *Proceedings of the Royal Society of London A: Mathematical, Physical and Engineering Sciences*, vol. 153, no. 880, pp. 699–717, 1936. [Online]. Available: <http://rspa.royalsocietypublishing.org/content/153/880/699>
- [18] R. Vardimon, M. Matt, P. Nielaba, J. C. Cuevas, and O. Tal, “Orbital origin of the electrical conduction in ferromagnetic atomic-size contacts: Insights from shot noise measurements and theoretical simulations,” *Phys. Rev. B*, vol. 93, p. 085439, Feb 2016. [Online]. Available: <http://link.aps.org/doi/10.1103/PhysRevB.93.085439>
- [19] J. Park, A. Pasupathy, J. Goldsmith, C. Chang, Y. Yaish, J. Petta, M. Rinkoski, J. Sethna, H. Abruna, P. McEuen, and D. Ralph, “Coulomb blockade and the kondo effect in single-atom transistors.” *Nature*, vol. 417, p. 722–725, 2002.
- [20] W. Liang, M. P. Shores, M. Bockrath, J. R. Long, and H. Park, “Kondo resonance in a single-molecule transistor.” *Nature*, vol. 417, p. 725–729, 2002.
- [21] S. e. a. Kubatkin, “Single-electron transistor of a single organic molecule with access to several redox states.” *Nature*, vol. 425, p. 698–701, 2003.
- [22] K. Moth-Poulsen and T. Bjornholm, “Molecular electronics with single molecules in solid-state devices.” *Nature Nanotech.*, vol. 4, p. 551–556, 2009.
- [23] A. R. Champagne, A. N. Pasupathy, and D. C. Ralph, “Mechanically adjustable and electrically gated single-molecule transistors.” *Nano Lett.*, vol. 5, p. 305–308, 2005.
- [24] C. A. Martin, R. H. M. Smit, H. S. J. van der Zant, and J. M. van Ruitenbeek, “A nanoelectromechanical single-atom switch.” *Nano Lett.*, vol. 9, p. 2940–2945, 2009.
- [25] S. Ballmann and H. B. Weber, “An electrostatic gate for mechanically controlled single-molecule junctions.” *New J. Phys.*, vol. 14, p. 123028, 2012.

- [26] M. e. a. Fuechsle, “A single-atom transistor.” *Nature Nanotech.*, vol. 7, p. 242–246, 2012.
- [27] M. Fujihira, K. Nishiyama, and H. Yamada, “Photoelectrochemical responses of optically transparent electrodes modified with langmuir-blodgett films consisting of surfactant derivatives of electron donor, acceptor, and sensitizer molecules.” *Thin Solid Films*, vol. 132, p. 77, 1985.
- [28] R. Avriller and T. Frederiksen, *Phys. Rev. B*, vol. 86, p. 155411, 2012.
- [29] Z. Wu, S. Wu, S. Oberholzer, M. Steinacher, M. Calame, and C. Schönenberger, *Phys. Rev. B*, vol. 78, p. 235421, 2008.
- [30] W. Lee, K. Kim, W. Jeong, L. Zotti, F. Pauly, J. Cuevas, and P. Reddy, *Nature*, vol. 498, p. 209, 2013.
- [31] K. Itakura, K. Yuki, S. Kurokawa, H. Yasuda, and A. Sakai, *Phys. Rev. B*, vol. 60, p. 11163, 1999.
- [32] M. Kiguchi, O. Tal, S. Wohlthat, F. Pauly, M. Krieger, D. Djukic, J. Cuevas, and J. van Ruitenbeek, “Highly conductive molecular junctions based on direct binding of benzene to platinum electrodes.” *Phys. Rev. Lett.*, vol. 101, p. 046801, 2008.
- [33] F. Pauly, J. Viljas, J. Cuevas, and G. Schön, “Density-functional study of tilt-angle and temperature-dependent conductance in biphenyl dithiol single-molecule junctions.” *Phys. Rev. B*, vol. 77, p. 155312, 2008.
- [34] N. Agraït, C. Untiedt, G. Rubio-Bollinger, and S. Vieira, “Onset of energy dissipation in ballistic atomic wires,” *Phys. Rev. Lett.*, vol. 88, p. 216803, May 2002. [Online]. Available: <http://link.aps.org/doi/10.1103/PhysRevLett.88.216803>
- [35] M. Kumar, R. Avriller, A. L. Yeyati, and J. M. van Ruitenbeek, “Detection of vibration-mode scattering in electronic shot noise,” *Phys. Rev. Lett.*, vol. 108, p. 146602, Apr 2012. [Online]. Available: <http://link.aps.org/doi/10.1103/PhysRevLett.108.146602>
- [36] I. K. Yanson, O. I. Shklyarevskii, S. Csonka, H. van Kempen, S. Speller, A. I. Yanson, and J. M. van Ruitenbeek, “Atomic-size oscillations in conductance histograms for gold nanowires and the influence of work hardening,” *Phys. Rev. Lett.*, vol. 95, p. 256806, Dec 2005. [Online]. Available: <http://link.aps.org/doi/10.1103/PhysRevLett.95.256806>
- [37] V. L., K. J.E., T. I.W., N. C., H. M.S., and S. M.L., *Nano Lett.*, vol. 6, p. 458, 2006.
- [38] J. C. Cuevas, A. Levy Yeyati, A. Martín-Rodero, G. Rubio Bollinger, C. Untiedt, and N. Agraït, “Evolution of conducting channels in metallic atomic contacts under elastic deformation,” *Phys. Rev. Lett.*, vol. 81, pp. 2990–2993, Oct 1998. [Online]. Available: <http://link.aps.org/doi/10.1103/PhysRevLett.81.2990>
- [39] E. Scheer, P. Joyez, D. Esteve, C. Urbina, and M. Devoret, “Conduction channel transmissions of atomic-size aluminum contacts,” *Phys. Rev. Lett.*, vol. 78, pp. 3535–3538, May 1997. [Online]. Available: <http://link.aps.org/doi/10.1103/PhysRevLett.78.3535>

- [40] J. M. J. W. Ekin, *J. Appl. Phys.*, vol. 58, p. 3888, 1985.
- [41] C. J. Muller, J. M. van Ruitenbeek, and L. J. de Jongh, *Physica C*, vol. 191, p. 485, 1992.
- [42] N. Agraït, J. G. Rodrigo, and S. Vieira, “Conductance steps and quantization in atomic-size contacts.” *Phys. Rev. B*, vol. 47, pp. 12 345–12 348, 1993.
- [43] J. I. Pascual, J. Méndez, J. Gómez-Herrero, A. M. Baró, N. García, and V. T. Binh, *Phys. Rev. Lett.*, vol. 71, p. 1852, 1993.
- [44] L. Olesen, E. Lagsgaard, I. Stensgaard, F. Besenbacher, J. Schiøtz, P. Stoltze, K. W. Jacobsen, and J. K. Nørskov, *Phys. Rev. Lett.*, vol. 74, p. 2147, 1995.
- [45] C. Sirvent, J. G. Rodrigo, S. Vieira, L. Jurczyszyn, N. Mingo, and F. Flores, *Phys. Rev. B*, vol. 53, p. 16086, 1996.
- [46] L. Limot, J. Kröger, R. Berndt, A. Garcia-Lekue, and W. A. Hofer, *Phys. Rev. Lett.*, vol. 94, p. 126102, 2005.
- [47] N. Néel, J. Kröger, L. Limot, K. Palotas, W. A. Hofer, and R. Berndt, *Phys. Rev. Lett.*, vol. 98, p. 016801, 2007.
- [48] G. Rubio, N. Agraït, and S. Vieira, “Atomic-sized metallic contacts: Mechanical properties and electronic transport,” *Phys. Rev. Lett.*, vol. 76, pp. 2302–2305, Mar 1996. [Online]. Available: <http://link.aps.org/doi/10.1103/PhysRevLett.76.2302>
- [49] A. I. Yanson, J. M. van Ruitenbeek, G. R. Bollinger, H. E. van den Brom, and N. Agraït, “Formation and manipulation of a metallic wire of single gold atoms,” *Nature*, vol. 395, no. 6704, pp. 783–785, 1998.
- [50] H. Ohnishi, Y. Kondo, and K. Takayanagi, “Quantized conductance through individual rows of suspended gold atoms,” *Nature*, vol. 395, no. 6704, pp. 780–783.
- [51] H. Park, A. K. L. Lim, A. P. Alivisatos, J. Park, and P. L. McEuen, “Fabrication of metallic electrodes with nanometer separation by electromigration,” *Applied Physics Letters*, vol. 75, no. 2, pp. 301–303, 1999. [Online]. Available: <http://scitation.aip.org/content/aip/journal/apl/75/2/10.1063/1.124354>
- [52] J. L. Costa-Krämer, *Phys. Rev. B*, vol. 55, p. 4875, 1997.
- [53] H. Park, J. Park, A. Lim, E. Anderson, A. Alivisatos, and P. McEuen, “Nanomechanical oscillations in a single-c 60 transistor.” *Nature*, vol. 407, p. 57, 2000.
- [54] T. Hasegawa, K. Terabe, T. Tsuruoka, and M. Aono, “Atomic switch: atom/ion movement controlled devices for beyond von-neumann computers.” *Adv. Mater.*, vol. 24, p. 252–267, 2012.
- [55] S. J. Van der Molen and P. Liljeroth, “Charge transport through molecular switches.” *J. Phys.*, vol. 22, p. 133001, 2010.

- [56] S. Quek, M. Kamenetska, M. Steigerwald, H. Choi, S. Louie, M. Hybertsen, J. Neaton, and L. Venkataraman, “Mechanically controlled binary conductance switching of a single-molecule junction.” *Nature Nanotechnol.*, vol. 4, pp. 230–234, 2009.
- [57] D. P. E. Smith, “Quantum point contact switches.” *Science*, vol. 269, p. 371–373, 1995.
- [58] K. Terabe, T. Hasegawa, N. T., and M. Aono, “Quantized conductance atomic switch.” *Nature*, vol. 433, p. 47–50, 2005.
- [59] G. A. et al., “From stochastic single atomic switch to nanoscale resistive memory device.” *Nanoscale*, vol. 3, p. 1504–1507, 2011.
- [60] J. M. Krans, J. M. van Ruitenbeek, V. V. Fisun, I. K. Yanson, and L. J. de Jongh, “The signature of conductance quantization in metallic point contacts,” *Nature*, vol. 375, pp. 767–769, Jun 1995. [Online]. Available: <http://dx.doi.org/10.1038/375767a0>
- [61] Z. Gai, Y. He, H. Yu, and W. S. Yang, *Phys. Rev. B*, vol. 53, p. 1042, 1996.
- [62] A. M. Bratkovsky, A. P. Sutton, and T. N. Todorov, “Conditions for conductance quantization in realistic models of atomic-scale metallic contacts,” *Phys. Rev. B*, vol. 52, pp. 5036–5051, Aug 1995. [Online]. Available: <http://link.aps.org/doi/10.1103/PhysRevB.52.5036>
- [63] J. C. Cuevas, A. Martín-Rodero, and A. L. Yeyati, “Hamiltonian approach to the transport properties of superconducting quantum point contacts,” *Phys. Rev. B*, vol. 54, pp. 7366–7379, Sep 1996. [Online]. Available: <http://link.aps.org/doi/10.1103/PhysRevB.54.7366>
- [64] E. Scheer, N. Agraït, J. C. Cuevas, A. L. Yeyati, B. Ludoph, A. Martín-Rodero, G. Rubio, J. M. van Ruitenbeek, and C. Urbina, “The signature of chemical valence in the electrical conduction through a single-atom contact.” *Nature (London)*, vol. 394, p. 154–157, 1998.
- [65] A. Martín-Rodero, A. L. Yeyati, and J. Cuevas, “Transport properties of normal and ferromagnetic atomic-size constrictions with superconducting electrodes,” *Physica C: Superconductivity*, vol. 352, no. 1–4, pp. 67 – 72, 2001. [Online]. Available: <http://www.sciencedirect.com/science/article/pii/S0921453400016798>
- [66] T. Todorov, “Tight-binding simulation of current-carrying nanostructures.” *J. Phys.: Condens. Matter*, vol. 14, p. 3049, 2002.
- [67] J. Cuevas, J. Heurich, F. Pauly, W. Wenzel, and G. Schön, “Theoretical description of the electrical conduction in atomic and molecular junctions.” *Nanotechnology*, vol. 14, p. R29, 2003.
- [68] M. Dreher, F. Pauly, J. Heurich, J. C. Cuevas, E. Scheer, and P. Nielaba, “Structure and conductance histogram of atomic-sized Au contacts,” *Phys. Rev. B*, vol. 72, p. 075435, Aug 2005. [Online]. Available: <http://link.aps.org/doi/10.1103/PhysRevB.72.075435>

- [69] F. Pauly, M. Dreher, J. K. Viljas, M. Häfner, J. C. Cuevas, and P. Nielaba, “Theoretical analysis of the conductance histograms and structural properties of ag, pt, and ni nanocontacts,” *Phys. Rev. B*, vol. 74, p. 235106, Dec 2006. [Online]. Available: <http://link.aps.org/doi/10.1103/PhysRevB.74.235106>
- [70] M. Häfner, J. K. Viljas, D. Frustaglia, F. Pauly, M. Dreher, P. Nielaba, and J. C. Cuevas, “Theoretical study of the conductance of ferromagnetic atomic-sized contacts,” *Phys. Rev. B*, vol. 77, p. 104409, Mar 2008. [Online]. Available: <http://link.aps.org/doi/10.1103/PhysRevB.77.104409>
- [71] P. Makk, S. Csonka, and A. Halbritter, “Effect of hydrogen molecules on the electronic transport through atomic-sized metallic junctions in the superconducting state,” *Phys. Rev. B*, vol. 78, p. 045414, Jul 2008. [Online]. Available: <http://link.aps.org/doi/10.1103/PhysRevB.78.045414>
- [72] M. Häfner, J. Viljas, and J. Cuevas, “Theory of anisotropic magnetoresistance in atomic-sized ferromagnetic metal contacts.” *Phys. Rev. B*, no. 79, p. 140410, 2009.
- [73] F. Pauly, J. K. Viljas, M. Bürkle, M. Dreher, P. Nielaba, and J. C. Cuevas, “Molecular dynamics study of the thermopower of ag, au, and pt nanocontacts,” *Phys. Rev. B*, vol. 84, p. 195420, Nov 2011. [Online]. Available: <http://link.aps.org/doi/10.1103/PhysRevB.84.195420>
- [74] P. Makk, D. Visontai, L. Oroszlány, D. Z. Manrique, S. Csonka, J. Cserti, C. Lambert, and A. Halbritter, “Advanced simulation of conductance histograms validated through channel-sensitive experiments on indium nanojunctions,” *Phys. Rev. Lett.*, vol. 107, p. 276801, Dec 2011. [Online]. Available: <http://link.aps.org/doi/10.1103/PhysRevLett.107.276801>
- [75] P. Makk, D. Tomaszewski, J. Martinek, Z. Balogh, S. Csonka, M. Wawrzyniak, M. Frei, L. Venkataraman, and A. Halbritter, *ACS Nano*, vol. 6, p. 3411, 2012.
- [76] C. J. Vineis, A. Shakouri, A. Majumdar, and M. G. Kanatzidis, “Nanostructured thermoelectrics: Big efficiency gains from small features.” *Adv. Mater.*, vol. 22, pp. 3970–3980, 2010.
- [77] A. Bulusu and D. G. Walker, “Review of electronic transport models for thermoelectric materials.” *Superlattices Microstruct.*, vol. 44, pp. 1–36, 2008.
- [78] P. Pichanusakorn and P. Bandaru, “Nanostructured thermoelectrics.” *Mater. Sci. Eng. R*, vol. 67, pp. 19–63, 2010.
- [79] Y. Dubi and M. Di Ventra, “Colloquium: Heat flow and thermoelectricity in atomic and molecular junctions.” *Rev. Mod. Phys.*, vol. 83, pp. 131–155, 2011.
- [80] B. Ludoph and J. M. v. Ruitenbeek, “Thermopower of atomic-size metallic contacts,” *Phys. Rev. B*, vol. 59, pp. 12 290–12 293, May 1999. [Online]. Available: <http://link.aps.org/doi/10.1103/PhysRevB.59.12290>
- [81] M. Tsutsui, T. Morikawa, A. Arima, and M. Taniguchi, “Thermoelectricity in atomic-sized junctions at room temperatures.” *Sci. Rep.*, vol. 3, p. 3326, 2013.



- 
- [82] R. Vardimon, M. Klionsky, and O. Tal, “Experimental determination of conduction channels in atomic-scale conductors based on shot noise measurements,” *Phys. Rev. B*, vol. 88, p. 161404, Oct 2013. [Online]. Available: <http://link.aps.org/doi/10.1103/PhysRevB.88.161404>
- [83] K. I. Bolotin, F. Kuemmeth, A. N. Pasupathy, and D. C. Ralph, *Nano Lett.*, vol. 6, p. 123, 2006.
- [84] A. Sokolov, E. Y. Tsymbal, J. Redepenning, and B. Doudin, *Nat. Nanotechnol.*, vol. 2, p. 171, 2007.
- [85] N. Néel, J. Kröger, and R. Berndt, *Phys. Rev. Lett.*, vol. 102, p. 086805, 2009.
- [86] S. Egle, C. Bacca, H. F. Pernau, M. Hübner, D. Hinzke, U. Nowak, and E. Scheer, *Phys. Rev. B*, vol. 81, p. 134402, 2010.
- [87] F. Strigl, C. Espy, M. Bückle, E. Scheer, and T. Pietsch, *Nature Comm.*, vol. 6, p. 6172, 2015.
- [88] R. Vardimon, M. Klionsky, and O. Tal, *Nano Lett.*, vol. 15, p. 3894, 2015.
- [89] K. Hansen, E. Laegsgaard, I. Stensgaard, and F. Besenbacher, *Phys. Rev. B*, vol. 56, p. 2208, 1997.
- [90] F. Ott, S. Barberan, J. G. Lunney, J. M. D. Coey, P. Berthet, A. M. de Leon-Guevara, and A. Revcolevschi, *Phys. Rev. B*, vol. 58, p. 4656, 1998.
- [91] H. Oshima and K. Miyano, *Appl. Phys. Lett.*, vol. 73, p. 2203, 1998.
- [92] T. Ono, Y. Ooka, H. Miyajima, and Y. Otani, *Appl. Phys. Lett.*, vol. 75, p. 1622, 1999.
- [93] F. Komori and K. Nakatsuji, *J. Phys. Soc. Jap.*, vol. 68, p. 3786, 1999.
- [94] N. García, M. Muñoz, and Y.-W. Zhao, *Phys. Rev. Lett.*, vol. 82, p. 2923, 1999.
- [95] B. Ludoph and J. M. van Ruitenbeek, *Phys. Rev. B*, vol. 61, p. 2273, 2000.
- [96] A. I. Yanson, Ph.D. dissertation, Universiteit Leiden, 2001.
- [97] M. Viret, S. Berger, M. Gabureac, F. Ott, D. Olligs, I. Petej, J. F. Gregg, C. Fermon, G. Francinet, and G. L. Goff, *Phys. Rev. B*, vol. 66, p. 220401(R), 2002.
- [98] F. Elhoussine, S. Mátéfi-Tempfli, A. Encinas, and L. Piraux, *Appl. Phys. Lett.*, vol. 81, p. 1681, 2002.
- [99] M. Shimizu, E. Saitoh, H. Miyajima, and Y. Otani, *J. Magn. Magn. Mat.*, vol. 239, p. 243, 2002.
- [100] D. Gillingham, I. Linington, and J. Bland, *J. Phys.: Condens. Matter*, vol. 14, 2002.
- [101] V. Rodrigues, J. Bettini, P. C. Silva, and D. Ugarte, *Phys. Rev. Lett.*, vol. 91, p. 96801, 2003.

- 
- [102] D. Gillingham, C. Müller, and J. Bland, *J. Phys.: Condens. Matter*, vol. 15, 2003.
- [103] D. Gillingham, I. Linington, C. Müller, and J. Bland, *J. Appl. Phys.*, vol. 93, p. 7388, 2003.
- [104] C. Untiedt, D. M. T. Dekker, D. Djukic, and J. M. van Ruitenbeek, *Phys. Rev. B*, vol. 69, p. 081401(R), 2004.
- [105] M. Gabureac, M. Viret, F. Ott, and C. Fermon, *Phys. Rev. B*, vol. 69, p. 100401(R), 2004.
- [106] C.-S. Yang, C. Zhang, J. Redepenning, and B. Doudin, *Appl. Phys. Lett.*, vol. 84, p. 2865, 2004.
- [107] J. L. Costa-Krämer, M. Díaz, and P. A. Serena, *Appl. Phys. A*, vol. 81, p. 1539, 2005.
- [108] K. I. Bolotin, F. Kuemmeth, A. N. Pasupathy, and D. C. Ralph, *Nano Lett.*, vol. 6, p. 123, 2006.
- [109] Z. K. Keane, L. H. Yu, and D. Natelson, *Appl. Phys. Lett.*, vol. 88, p. 062514, 2006.
- [110] M. Viret, M. Gabureac, F. Ott, C. Fermon, C. Barreateau, G. Autés, and R. Guirardo-Lopez, *Eur. Phys. J. B*, vol. 51, p. 1, 2006.
- [111] M. R. Calvo, J. Fernández-Rossier, J. J. Palacios, D. Jacob, D. Natelson, and C. Untiedt, *Nature*, vol. 458, p. 1150, 2009.
- [112] A. Halbritter, P. Makk, S. Mackowiak, S. Csonka, M. Wawrzyniak, and J. Martinek, *Phys. Rev. Lett.*, vol. 105, p. 266805, 2010.
- [113] Y. Moriguchi, K. Yamauchi, S. Kurokawa, and A. Sakai, *Surf. Sci.*, vol. 606, p. 928, 2012.
- [114] A. von Bieren, A. K. Patra, S. Krzyk, J. Rhensius, R. M. Reeve, L. J. Heyderman, R. Hoffmann-Vogel, and M. Kläui, *Phys. Rev. Lett.*, vol. 110, p. 067203, 2013.
- [115] J. Velez, R. F. Sabirianov, S. S. Jaswal, and E. Y. Tsymbal, *Phys. Rev. Lett.*, vol. 94, p. 127203, 2005.
- [116] A. Martín-Rodero, A. L. Yeyati, and J. C. Cuevas, *Physica C*, vol. 352, p. 67, 2001.
- [117] S. Krstić, X.-G. Zhang, and W. H. Butler, *Phys. Rev. B*, vol. 66, p. 205319, 2002.
- [118] A. Smogunov, A. D. Corso, and E. Tossati, *Surf. Sci.*, vol. 507, p. 609, 2002.
- [119] A. Smogunov, A. D. Corso, and E. Tossati, *Surf. Sci.*, vol. 532, p. 549, 2003.
- [120] A. Delin and E. Tosatti, *Phys. Rev. B*, vol. 68, p. 144434, 2003.
- [121] J. Velez and W. H. Butler, *Phys. Rev. B*, vol. 69, p. 094425, 2004.
- [122] A. Bagrets, N. Papanikolaou, and I. Mertig, *Phys. Rev. B*, vol. 70, p. 064410, 2004.

- 
- [123] A. R. Rocha and S. Sanvito, *Phys. Rev. B*, vol. 70, p. 094406, 2004.
- [124] D. Jacob, J. Fernández-Rossier, and J. J. Palacios, *Phys. Rev. B*, vol. 71, p. 220403(R), 2005.
- [125] M. Wierzbowska, A. Delin, and E. Tosatti, *Phys. Rev. B*, vol. 72, p. 035439, 2005.
- [126] H. Dalglish and G. Kirczenow, *Phys. Rev. B*, vol. 72, p. 155429, 2005.
- [127] P. A. Khomyakov, G. Brocks, V. Karpan, M. Zwierzycki, and P. J. Kelly, *Phys. Rev. B*, vol. 72, p. 035450, 2005.
- [128] J. Fernández-Rossier, D. Jacob, C. Untiedt, and J. J. Palacios, *Phys. Rev. B*, vol. 72, p. 224418, 2005.
- [129] A. Smogunov, A. D. Corso, and E. Tosatti, *Phys. Rev. B*, vol. 73, p. 075418, 2006.
- [130] D. Jacob and J. J. Palacios, *Phys. Rev. B*, vol. 73, p. 075429, 2006.
- [131] G. Autés, C. Barreteau, D. Spanjaard, and M. C. Desjonquères, *J. Phys.: Condens. Matter*, vol. 18, p. 6785, 2006.
- [132] K. Xia, M. Zwierzycki, M. Talanana, P. J. Kelly, and G. E. W. Bauer, *Phys. Rev. B*, vol. 73, p. 064420, 2006.
- [133] A. R. Rocha, T. Archer, and S. Sanvito, *Phys. Rev. B*, vol. 76, p. 054435, 2007.
- [134] J. C. Tung and G. Y. Guo, *Phys. Rev. B*, vol. 76, p. 094413, 2007.
- [135] A. Bagrets, N. Papanikolaou, and I. Mertig, *Phys. Rev. B*, vol. 75, p. 235448, 2007.
- [136] G. Autés, C. Barreteau, M.-C. Desjonquères, D. Spanjaard, and M. Viret, *Europhys. Lett.*, vol. 83, p. 17010, 2008.
- [137] D. Jacob, J. Fernández-Rossier, and J. J. Palacios, *Phys. Rev. B*, vol. 77, p. 165412, 2008.
- [138] K. Tao, I. Rungger, S. Sanvito, and V. S. Stepanyuk, *Phys. Rev. B*, vol. 82, p. 085412, 2010.
- [139] B. Hardrat, N.-P. Wang, F. Freimuth, Y. Mokrousov, and S. Heinze, *Phys. Rev. B*, vol. 85, p. 245412, 2012.
- [140] Y. q. Xie, Q. Li, L. Huang, X. Ye, and S.-H. Ke, *Appl. Phys. Lett.*, vol. 101, p. 192408, 2012.
- [141] M. Calvo, D. Jacob, and C. Untiedt, *Phys. Rev. B*, vol. 86, p. 075447, 2012.
- [142] Z. Tan, X. l. Zheng, X. Ye, Y. q. Xie, and S.-H. Ke, *Appl. Phys. Lett.*, vol. 114, p. 063711, 2013.
- [143] K. Nagaev, “On the shot noise in dirty metal contacts,” *Phys. Lett. A*, vol. 169, no. 1-2, pp. 103–107, Sep 14 1992.

- [144] C. W. J. Beenakker and M. Büttiker, “Suppression of shot noise in metallic diffusive conductors,” *Phys. Rev. B*, vol. 46, pp. 1889–1892, Jul 1992. [Online]. Available: <http://link.aps.org/doi/10.1103/PhysRevB.46.1889>
- [145] D. Frenkel and B. Smit, *Understanding molecular simulation: from algorithms to applications*. San Diego [u.a.]: Academic Press, 2002, vol. 1.
- [146] S. Nosé, “A molecular dynamics method for simulations in the canonical ensemble,” *Molecular Physics*, vol. 52, no. 2, pp. 255–268, 1984. [Online]. Available: <http://dx.doi.org/10.1080/00268978400101201>
- [147] W. G. Hoover, “Canonical dynamics: Equilibrium phase-space distributions,” *Phys. Rev. A*, vol. 31, pp. 1695–1697, Mar 1985. [Online]. Available: <http://link.aps.org/doi/10.1103/PhysRevA.31.1695>
- [148] “LAMMPS.” [Online]. Available: <http://lammmps.sandia.gov>
- [149] M. Parrinello and A. Rahman, “Polymorphic transitions in single crystals: A new molecular dynamics method,” *Journal of Applied Physics*, vol. 52, no. 12, pp. 7182–7190, 1981. [Online]. Available: <http://scitation.aip.org/content/aip/journal/jap/52/12/10.1063/1.328693>
- [150] W. Shinoda, M. Shiga, and M. Mikami, “Rapid estimation of elastic constants by molecular dynamics simulation under constant stress,” *Phys. Rev. B*, vol. 69, p. 134103, Apr 2004. [Online]. Available: <http://link.aps.org/doi/10.1103/PhysRevB.69.134103>
- [151] M. E. Tuckerman, J. Alejandre, R. L.-R. andrea L Jochim, and G. J. Martyna, “A liouville-operator derived measure-preserving integrator for molecular dynamics simulations in the isothermal–isobaric ensemble,” *Journal of Physics A: Mathematical and General*, vol. 39, no. 19, p. 5629, 2006. [Online]. Available: <http://stacks.iop.org/0305-4470/39/i=19/a=S18>
- [152] G. J. Martyna, M. L. Klein, and M. Tuckerman, “Nosé–hoover chains: The canonical ensemble via continuous dynamics,” *The Journal of Chemical Physics*, vol. 97, no. 4, pp. 2635–2643, 1992. [Online]. Available: <http://scitation.aip.org/content/aip/journal/jcp/97/4/10.1063/1.463940>
- [153] M. W. Finnis and J. E. Sinclair, “A simple empirical n-body potential for transition metals,” *Philosophical Magazine A*, vol. 50, no. 1, pp. 45–55, 1984. [Online]. Available: <http://dx.doi.org/10.1080/01418618408244210>
- [154] M. S. Daw and M. I. Baskes, “Semiempirical, quantum mechanical calculation of hydrogen embrittlement in metals,” *Phys. Rev. Lett.*, vol. 50, pp. 1285–1288, Apr 1983. [Online]. Available: <http://link.aps.org/doi/10.1103/PhysRevLett.50.1285>
- [155] M. S. Daw and M. I. Baskes, “Embedded-atom method: Derivation and application to impurities, surfaces, and other defects in metals,” *Phys. Rev. B*, vol. 29, pp. 6443–6453, Jun 1984. [Online]. Available: <http://link.aps.org/doi/10.1103/PhysRevB.29.6443>

- [156] H. W. Sheng, M. J. Kramer, A. Cadien, T. Fujita, and M. W. Chen, “Highly optimized embedded-atom-method potentials for fourteen fcc metals,” *Phys. Rev. B*, vol. 83, p. 134118, Apr 2011. [Online]. Available: <http://link.aps.org/doi/10.1103/PhysRevB.83.134118>
- [157] X. D. Dai, Y. Kong, J. H. Li, and B. X. Liu, “Extended finniss–sinclair potential for bcc and fcc metals and alloys,” *Journal of Physics: Condensed Matter*, vol. 18, no. 19, p. 4527, 2006. [Online]. Available: <http://stacks.iop.org/0953-8984/18/i=19/a=008>
- [158] R. E. Cohen, M. J. Mehl, and D. A. Papaconstantopoulos, “Tight-binding total-energy method for transition and noble metals,” *Phys. Rev. B*, vol. 50, pp. 14 694–14 697, Nov 1994. [Online]. Available: <http://link.aps.org/doi/10.1103/PhysRevB.50.14694>
- [159] F. Guinea, C. Tejedor, F. Flores, and E. Louis, “Effective two-dimensional hamiltonian at surfaces,” *Phys. Rev. B*, vol. 28, pp. 4397–4402, Oct 1983. [Online]. Available: <http://link.aps.org/doi/10.1103/PhysRevB.28.4397>
- [160] D. Averin and A. Bardas, “ac josephson effect in a single quantum channel,” *Phys. Rev. Lett.*, vol. 75, pp. 1831–1834, Aug 1995. [Online]. Available: <http://link.aps.org/doi/10.1103/PhysRevLett.75.1831>
- [161] S. Plimpton, “Fast parallel algorithms for short-range molecular dynamics,” *Journal of Computational Physics*, vol. 117, no. 1, pp. 1 – 19, 1995. [Online]. Available: <http://www.sciencedirect.com/science/article/pii/S002199918571039X>
- [162] M. Brandbyge, N. Kobayashi, and M. Tsukada, “Conduction channels at finite bias in single-atom gold contacts,” *Phys. Rev. B*, vol. 60, pp. 17 064–17 070, Dec 1999. [Online]. Available: <http://link.aps.org/doi/10.1103/PhysRevB.60.17064>
- [163] C. Muller, J. Krans, T. Todorov, and R. M.A., *Phys. Rev. B*, vol. 53, p. 1022, 1996.
- [164] I. A. Yanson and J. M. van Ruitenbeek, “Do histograms constitute a proof for conductance quantization?” *Phys. Rev. Lett.*, vol. 79, p. 2157–2160, 1997.
- [165] M. Kamenetska, M. Koentopp, A. Whalley, Y. Park, M. Steigerwald, M. Nuckolls, C. Hybertsen, and L. Venkataraman, *Phys. Rev. Lett.*, vol. 102, p. 126803, 2009.
- [166] H. Vazquez, R. Skouta, S. S., M. Kamenetska, R. Breslow, L. Venkataraman, and M. Hybertsen, *Nature Nanotechnol.*, vol. 7, p. 663, 2012.
- [167] E. Lörtscher, H. Weber, and H. Riel, *Phys. Rev. Lett.*, vol. 98, p. 176807, 2007.
- [168] C. Guédon, H. Valkenier, T. Markussen, K. Thygesen, J. Hummelen, and S. van der Molen, *Nature Nanotechnol.*, vol. 7, p. 305, 2012.
- [169] P. Darancet, J. Widawsky, H. Choi, L. Venkataraman, and J. Neaton, *Nano Lett.*, vol. 12, p. 6250, 2012.
- [170] N. Fournier, C. Wagner, C. Weiss, R. Temirov, and F. Tautz, *Phys. Rev. B*, vol. 84, p. 035435, 2011.

- [171] S. Aradhya, M. Frei, A. Halbritter, and L. Venkataraman, *ACS Nano*, vol. 7, p. 3706, 2013.
- [172] R. Waser, “Nanoelectronics and information technology,” *Wiley-VCH*, 2003.
- [173] Y. Kurui, Y. Oshima, M. Okamoto, and K. Takayanagi, “Conductance quantization and dequantization in gold nanowires due to multiple reflection at the interface,” *Phys. Rev. B*, vol. 79, p. 165414, Apr 2009. [Online]. Available: <http://link.aps.org/doi/10.1103/PhysRevB.79.165414>
- [174] L. Saminadayar, D. C. Glattli, Y. Jin, and B. Etienne, “Observation of the  $e/3$  fractionally charged Laughlin quasiparticle,” *Phys. Rev. Lett.*, vol. 79, pp. 2526–2529, Sep 1997. [Online]. Available: <http://link.aps.org/doi/10.1103/PhysRevLett.79.2526>
- [175] Y. M. Blanter and M. Büttiker, “Shot noise in mesoscopic conductors,” *Phys. Rep.*, vol. 336, pp. 1–166, Sep. 2000.
- [176] C. W. J. Beenakker, “Random-matrix theory of quantum transport,” *Rev. Mod. Phys.*, vol. 69, pp. 731–808, Jul 1997. [Online]. Available: <http://link.aps.org/doi/10.1103/RevModPhys.69.731>
- [177] S.-F. Shi and D. C. Ralph, *Nat. Nanotechnol.*, vol. 2, p. 522, 2007.
- [178] S.-F. Shi, K. I. Bolotin, F. Kuemmeth, and D. C. Ralph, *Phys. Rev. B*, vol. 76, p. 184438, 2007.
- [179] E. Scheer, P. Joyez, D. Esteve, C. Urbina, and M. H. Devoret, *Phys. Rev. Lett.*, vol. 78, p. 3535, 1997.
- [180] R. Meservey and P. M. Tedrow, “Spin-polarized electron tunneling,” *Physics Reports*, vol. 238, no. 4, pp. 173–243, 1994.
- [181] A. Burtzloff, A. Weismann, M. Brandbyge, and R. Berndt, “Shot noise as a probe of spin-polarized transport through single atoms,” *Phys. Rev. Lett.*, vol. 114, p. 016602, Jan 2015. [Online]. Available: <http://link.aps.org/doi/10.1103/PhysRevLett.114.016602>
- [182] F. J. Blatt, P. A. Schroeder, C. L. Foiles, and D. Greig, “Thermoelectric power of metals.” *Plenum Press: New York*, 1976.
- [183] P. Wheeler, J. Russom, K. Evans, N. King, and D. Natelson, *Nano Lett.*, vol. 10, p. 1287, 2010.
- [184] R. Chen, P. Wheeler, and D. Natelson, *Phys. Rev. B*, vol. 85, p. 235455, 2012.
- [185] R. Chen, P. Wheeler, M. Di Ventra, and D. Natelson, *Sci. Rep.*, vol. 4, p. 4221, 2014.
- [186] Y. Moriguchi, K. Yamauchi, S. Kurokawa, and A. Sakai, “Conductance of atom-sized contacts of transition metals at room temperature,” *Surface Science*, vol. 606, no. 11–12, pp. 928 – 932, 2012. [Online]. Available: <http://www.sciencedirect.com/science/article/pii/S003960281200060X>

- [187] Copyright 1993-2016 Mark Winter [The University of Sheffield and WebElements Ltd, UK], “Au thermochemistry data,” accessed: 2016-07-06. [Online]. Available: <https://www.webelements.com/gold/thermochemistry.html>
- [188] E. Scheer, T. Böhler, A. Edtbauer, S. Egle, A. Erbe, and T. Pietsch, “Switchable zero-bias anomaly in individual c60 molecules contacted with tunable aluminum electrodes,” *Low Temperature Physics = Fizika Nizkich Temperatur*, vol. 39, no. 3, pp. 335–342, 2013.
- [189] B. Ludoph and J. M. v. Ruitenbeek, “Conductance fluctuations as a tool for investigating the quantum modes in atomic-size metallic contacts,” *Phys. Rev. B*, vol. 61, pp. 2273–2285, Jan 2000. [Online]. Available: <http://link.aps.org/doi/10.1103/PhysRevB.61.2273>
- [190] H. E. van den Brom and J. M. van Ruitenbeek, *Shot Noise Suppression in Metallic Quantum Point Contacts*. Berlin, Heidelberg: Springer Berlin Heidelberg, 2000, pp. 114–122. [Online]. Available: [http://dx.doi.org/10.1007/3-540-45557-4\\_11](http://dx.doi.org/10.1007/3-540-45557-4_11)
- [191] J. M. Krans, C. J. Muller, I. K. Yanson, T. C. M. Govaert, R. Hesper, and J. M. van Ruitenbeek, “One-atom point contacts,” *Phys. Rev. B*, vol. 48, pp. 14 721–14 724, Nov 1993. [Online]. Available: <http://link.aps.org/doi/10.1103/PhysRevB.48.14721>
- [192] O. Schecker, “Von punktkontakten zu nano-elektro-mechanischen systemen,” Ph.D. dissertation, Universität Konstanz, 2008.
- [193] T. Böhler, J. Grebing, A. Mayer-Gindner, H. v. Löhneysen, and E. Scheer, “Mechanically controllable break-junctions for use as electrodes for molecular electronics,” *Nanotechnology*, vol. 15, no. 7, p. S465, 2004. [Online]. Available: <http://stacks.iop.org/0957-4484/15/i=7/a=054>
- [194] E. Scheer, P. Konrad, C. Bacca, A. Mayer-Gindner, H. v. Löhneysen, M. Häfner, and J. C. Cuevas, “Correlation between transport properties and atomic configuration of atomic contacts of zinc by low-temperature measurements,” *Phys. Rev. B*, vol. 74, p. 205430, Nov 2006. [Online]. Available: <http://link.aps.org/doi/10.1103/PhysRevB.74.205430>
- [195] J. L. Rose, *Ultrasonic waves in solid media*. Cambridge Univ. Press, 2004.
- [196] “webelements.com.” [Online]. Available: [https://www.webelements.com/iron/crystal\\_structure.html](https://www.webelements.com/iron/crystal_structure.html)
- [197] M. Ring, “Computer simulations of the dynamics of nanomembranes,” Master’s thesis, University of Konstanz, 2013.
- [198] R. Schmid, “Computersimulationen von nanobrücken mit fehlstellen,” Bachelor’s thesis, University of Konstanz, 2012.
- [199] J. Nieswand, “Wärmetransport in goldnanostrukturen,” Bachelor’s thesis, University of Konstanz, 2016.